A First 2 MW-Class (136)/170/204 GHz Multi-Frequency Gyrotron Pre-Prototype for DEMO: Design, Construction and Key Components Verification

Zur Erlangung des akademischen Grades eines

DOKTORS DER INGENIEURWISSENSCHAFTEN (Dr.-Ing.)

von der KIT-Fakultät für Elektrotechnik und Informationstechnik des

Karlsruher Instituts für Technologie (KIT)

genehmigte

DISSERTATION

von

M.Sc. Tobias Ruess
geb. in Ulm

Tag der mündlichen Prüfung:	30.05. 2023
Referent:	Prof. Dr.-Ing. John Jelonnek
Korreferent:	Assoc. Prof. Dr.-Ing. Konstantinos Avramidis

Kurzfassung

DEMO soll das erste Fusions-Demonstrationskraftwerk sein, das die Erzeugung von Elektrizität durch den Einsatz des Tokamak-Konzepts demonstriert. Die Reaktionen finden in einem magnetisch eingeschlossenen Plasma zwischen Deuterium und Tritium bei einer erforderlichen Temperatur von etwa 120 Millionen Kelvin statt. Eine mögliche Heizmethode ist die Elektron-Zyklotron-Resonanzheizung (ECRH). Durch den nicht-induktiven Strombetrieb mittels ECRH können potentielle Plasmainstabilitäten kontrolliert werden. Als potentielle Quellen sind bisher nur Hochleistungs-Vakuumröhren (Gyrotrons) bekannt. Sie arbeiten mit Ausgangsleistungen im MW-Bereich und bei Frequenzen im Mikrowellen- bis sub-THz-Bereich. Die für die vorliegende Arbeit relevanten Anforderungen an das europäische (EU) DEMO sind Erweiterungen der bereits für ITER gestellten Anforderungen. Diese beinhalten eine Erhöhung der Ausgangsleistung pro Einheit von 1 MW auf 2 MW, den Betrieb bei mehreren Frequenzen (136/170/204 GHz) statt nur bei 170 GHz und eine stufenweise Durchstimmbarkeit der Frequenz in einer Bandbreite von ± 10 GHz in Schritten von $2 - 3$ GHz.

In dieser Arbeit soll das erste 2 MW 170/204 GHz Kurzpuls-Gyrotron in koaxialer Geometrie entworfen und auf der Basis eines existierenden 2 MW 170 GHz Kurzpuls-Gyrotrons gebaut werden. Der Elektronenstrahlerzeuger, der koaxiale Resonator und das quasi-optische Auskoppelsystem sollen an das Magnetfeldprofil eines neuen 10.5 T supraleitenden Magneten und für den Betrieb bei 170 GHz und 204 GHz adaptiert werden. Die $TE_{40,23}$-Mode wird als geeignete Betriebsmode für 204 GHz ausgewählt, während die $TE_{34,19}$-Mode für den Betrieb bei 170 GHz verwendet wird. Die Optimierung des koaxialen Resonators wird mittels eines adaptierten systematischen Verfahrens durchgeführt. Der neu entworfene koaxiale Resonator erreicht die geforderte Ausgangsleistung von ≥ 2 MW bei 170 GHz und 204 GHz. Außerdem wird ein neues quasi-optisches Auskoppelsystem für 170 GHz und 204 GHz vorgestellt, das den Anforderungen an ein Gauß'sches Profil

für den Ausgangsstrahl von besser als 95 % erfüllt. Abschließend zeigen Simulationen der genannten Schlüsselkomponenten einen prinzipiellen Betrieb bei 136 GHz, wobei die DEMO-Anforderungen erfüllt sind.

Die stufenweise Durchstimmbarkeit der Frequenz von koaxialen Resonatoren wird systematisch untersucht. Bei der Auswahl der Moden wird erstmals die Belastung an der Innenwand berücksichtigt. Es wird eine neue Modenserie vorgestellt, die einen Sprung im azimutalen Modenindex von der $TE_{m,p}$ Betriebsmode zur $TE_{m+2,p-1}$-Mode enthält. Die vorgeschlagene Modenserie reduziert die Abweichung des relativen Kaustikradius im Vergleich zur bestehenden Modenserien um den Faktor zwei. Simulationen zeigen, dass die Betriebsfrequenzen schrittweise von hohen zu niedrigen Frequenzen und umgekehrt abgestimmt werden können. Dabei variiert die Ausgangsleistung um maximal 5 % bei der Mittenfrequenz von 170 GHz und 18 % bei 204 GHz.

Die bestehenden Messeinrichtungen am KIT werden für den Betrieb von Gyrotrons über 200 GHz und für die Validierung von Komponenten optimiert. Die maximale Betriebsfrequenz der Systeme wird von 175 GHz auf 260 GHz erhöht. Insbesondere der für die Verifikation des quasi-optischen Auskoppelsystems notwendige quasi-optische Modenerzeuger wird optimiert. Mechanisch verstellbare Einheiten werden durch hochpräzise computergesteuerte Lineartische und ein Goniometer ersetzt. Eine autonome Messroutine mit einem Algorithmus zur Modenbestimmung wird implementiert. Diese Optimierungen verkürzen die benötige Zeit zur Anregung der gewünschten Gyrotronmode von Monaten auf wenige Tage. Die beiden relevanten Betriebsmoden bei 170 GHz und 204 GHz speisen das neue 170/204 GHz quasi-optische Auskoppelsystem zur Verifikation in kalten Messungen. Die Messungen zeigen eine gute Übereinstimmung mit den Simulationen. Die $TE_{40,23}$-Mode hat den weltweit höchsten Eigenwert einer jemals in kalten Messungen angeregten Mode.

Schließlich werden neue Modenserie untersucht, bei denen eine erhöhte Wandbelastung von 2.5 kW/cm^2 durch eine optimierte Kühlung der Resonatorwand akzeptiert wird. Diese Modenserien profitieren von einer Reduzierung der Abweichung des relativen Kaustikradius von bisher ca. 5 % auf nun 0.3 %.

Abstract

DEMO is planned to be the first DEMOnstration fusion power plant that will proof the production of electricity by facilitating the Tokamak concept. The fusion reaction takes place in a magnetically confined plasma that consists of Deuterium and Tritium. A temperature of up to 120 million Kelvin is required for the reaction. Electron Cyclotron Resonance Heating and Current Drive (ECRH&CD) is a possible method to heat and to control the plasma. The sources are high-power vacuum gyrotrons that produce microwave power at MW-levels in the microwave and sub-THz range. The European (EU) DEMO requirements associated with this work are adapted from those of ITER, from 1 MW to 2 MW output power per unit, from 170 GHz single-frequency operation to 136/170/204 GHz multi-frequency / multi-purpose operation and the ability to tune the frequency within a bandwidth of ± 10 GHz around the center frequency in steps of $2-3$ GHz.

In this work, the first 2 MW 170/204 GHz dual-frequency coaxial-cavity short-pulse pre-prototype has been designed and built on the basis of an existing 2 MW 170 GHz coaxial-cavity short-pulse pre-prototype. The Magnetron Injection Gun, the coaxial cavity and the quasi-optical output coupler are adapted to the magnetic field profile of a new 10.5 T SC magnet and to the operation at 204 GHz. Existing components, such as the cathode shall be used. The $TE_{40,23}$ mode is identified as the operating mode at 204 GHz. The mode fits to the parameters that are already determined by the $TE_{34,19}$ mode at 170 GHz. A new coaxial cavity is designed using an adapted systematic procedure. This design provides an output power of 2.1 MW at 204 GHz, which is an increase of about 20 %. The design allows an output power up to 2.6 MW at 170 GHz. In addition, a new 170/204 GHz dual-frequency quasi-optical output coupler has been developed providing a Gaussian mode content of > 95 %. Finally, simulations at 136 GHz show a principle operation satisfying the DEMO requirements.

Frequency step-tunability around the given center frequencies has been investigated for the first time considering the insert loading constraint during the mode selection process. A novel mode series is presented that includes a jump in the azimuthal mode index from the nominal $TE_{m,p}$ mode to the $TE_{m+2,p-1}$ mode. The proposed mode series reduces the deviation of the relative caustic radii by a factor of two compared to classical approaches. Simulations are performed to tune the gyrotron in steps from high to low frequency and reverse. The deviation of the output power is in maximum 5 % at 170 GHz and 18 % at 204 GHz.

An update of the frequency measurement system for gyrotron operation at KIT is performed to verify gyrotrons and their key components operating above 200 GHz. They are upgraded from the current frequency limitation of 175 GHz to at least 260 GHz. Particularly, the quasi-optical mode generator is optimized. It is used to validate the quasi-optical output coupler. The mechanically controlled linear drivers are replaced by high-precision computer-controlled linear drivers. A goniometer has been added for a full electronically adjustment. A novel automated measurement procedure with mode evaluation algorithms is implemented. The optimizations reduce the time needed to excite the desired gyrotron mode with higher quality from months to a few days. The excited cavity modes operating at 170 GHz and 204 GHz feed the 170/204 GHz dual-frequency quasi-optical output coupler for verification in cold measurement. A comparison shows an excellent agreement with simulations. The $TE_{40,23}$ mode at 204 GHz is the mode with the highest eigenvalue ever excited in cold measurements.

Finally, a study on alternative mode series is performed considering an extended wall loading constraint of up to 2.5 kW/cm^2. These mode series benefit from low deviation of the relative caustic radius. One identified mode series has a beam radius and an insert radius, which is almost identical to the existing mode series. The result is that the most complicated and costly components to manufacture (insert and MIG) can be reused and do not need to be modified. A fast verification of the proposed mode series using several existing components is proposed.

Contents

Abbreviations and Symbols

Abbreviations

CD	Current Drive
CTS	Collective Thomson Scattering
CVD	Chemical Vapour Deposition
CW	Continuous Wave
DEMO	DEMOnstration Power Plant
DUT	Device Under Test
ECRH	Electron Cyclotron Resonance Heating
EU	European Union
EM	Electromagnetic
FEM	Frequency Extension Module
FFP	Future Fusion Power Plant
FULGOR	Fusion Long Pulse Gyrotron Laboratory
GMC	Gaussian Mode Content
HV	High-Voltage
IHM	Institute for Pulsed Power and Microwave Technology
iMIG	Inverse Magnetron Injection Gun
KIT	Karlsruher Institute of Technology
LP	Long-Pulse

MIG	Magnetron Injection Gun
NBI	Neutral Beam Injection
NTM	Neoclassical Tearing Mode
OFHC	Oxygen-Free High Conductivity
q.-p.	Quasi-Parabolic
RF	Radio Frequency
SC	Super-Conducting
SMC	Scattering-Matrix Code
SP	Short-Pulse
TE	Transverse Electric
TM	Transverse Magnetic
VNA	Vector Network Analyzer
W7-X	Wendelstein 7-X

Constants

π	Pi: ≈ 3.14159265
c_0	Speed of light: 299 792 458 m/s
A_0	Richardson constant: ≈ 1202 mA/mm^{2}K^2
k_B	Boltzmann constant: $1.380649 \cdot 10^{-23}$ J/K

Latin variables

b	Magnetic compression
B_{emt}	Magnetic field strength at emitter
B_{cav}	Magnetic field strength at cavity
$B_{3\,\mathrm{dB}}$	3 dB bandwidth
D	Diameter
d_{window}	Thickness of gyrotron output window
e	Elementary charge
E	Electrical field
f	Operation frequency
f_c	Relativistic electron cyclotron frequency
f_{cut}	Cut-off frequency
F	Focal length
$Ge_{m,p}$	Beam wave coupling coefficient of mode $\mathrm{TE}_{m,p}$
I_{beam}	Beam current
J_s	Current density of emission
k	Wave number
$k_\perp, k_\parallel$	Transverse and axial components of the wave number
L_{mid}	Interaction midsection length
L_{tot}	Total cavity length
m_e	Electron rest mass
m	Azimuthal mode index
P_{RF}	RF output power
P_Ω	Power of ohmic losses

p	Radial mode index
$Q_{\mathrm{diff}}, Q_{\Omega}, Q_{\mathrm{tot}}$	Diffractive, ohmic and total quality factor
r_{beam}	Electron beam radius
r_{c}	Caustic radius
r_{cav}	Radius of the interaction section
r_{i}	Radius of the insert
r_{emt}	Radius of the emitter
r_{E}	Emitter radius
r_{L}	Larmor radius
R	Reflection factor
s	Harmonic of the gyrotron interaction
S	Inner cavity surface
$\tan\delta$	Loss tangent
T_{emt}	Temperature of heated emitter
T	Transmission factor
v	Velocity
$v_{\perp}, v_{\parallel}$	Transverse and axial component of the velocity
V_{c}	Accelerating voltage applied at the cathode
V_{b}	Voltage applied at the body
V_{a}	Voltage applied at the anode
V_{i}	Voltage applied at the coaxial insert
W_{kin}	Kinetic energy
W_E	Work function of the emitter material

U_{beam}	Electron beam energy
ΔU	Voltage depression
ΔE	Kinetic energy spread
Q	Fusion power gain

Greek variables

α	Pitch factor or velocity ratio ($\alpha = \beta_\perp / \beta_\parallel$)
β	Normalized velocity ($\beta = v/c$)
$\beta_\perp, \beta_\parallel$	Transverse and axial component of the normalized velocities
γ	Relativistic Lorentz factor
Γ	Reflection coefficient
δ	Skin depth of conducting material
$\Delta\alpha$	Spread of the pitch factor
$\delta\beta_\perp$	Spread of the perpendicular velocities
ϵ_r	Relative permittivity
η	Interaction efficiency
θ_{B}	Brillouin angle
λ	Wavelength
μ_0	Permeability of free space
ρ_Ω	Cavity wall-loading
σ	Electrical conductivity
$\chi_{m,p}$	Eigenvalue of $\text{TE}_{m,p}$ mode
Ω_c	Relativistic angular electron cyclotron frequency

1 Introduction

Nine billion people are expected to live on Earth by 2050 [1]. That are at least 1 billion people more than today. As the population grows, so does the world's demand for energy. In addition, currently common energy sources such as gas, oil and coal are to be replaced by renewable ones. Nuclear fission is currently being phased out in Germany. However, solar and wind energy are dependent on changing environmental conditions and may not be reliable base energies [2]. An alternative promising approach is to generate energy in a controlled nuclear fusion reaction using a magnetically confined plasma. Recently, the role of nuclear fusion in the industry is increasing providing several start-ups with billion-dollar budgets emerging around the world, like Tokamak Energy Ltd., UK, Commonwealth Fusion Systems, US and TAE Technologies, US. Amongst them are German start-ups as for example Gauss Fusion.

1.1 Fundamentals of Fusion and EC RH&CD

Fusion reactions are running in the sun by fusing atomic nuclei. The most effective fusion reaction under terrestrial conditions takes place with Deuterium $\left({}^{2}_{1}\mathrm{D}\right)$ and Tritium $\left({}^{3}_{1}\mathrm{T}\right)$:

$$ {}^{2}_{1}\mathrm{D} + {}^{3}_{1}\mathrm{T} \rightarrow {}^{4}_{2}\mathrm{He} + n \quad . \tag{1.1} $$

The resulting helium atom is lighter than Deuterium and Tritium together. Thus, according to Einstein's postulation [3], energy E is generated by the difference of the electron rest mass Δm_e:

$$ E = \Delta m_e \cdot c^2 \quad . \tag{1.2} $$

The fusion reaction gains 17.6 MeV, divided into 14.1 MeV of kinetic energy of the neutron n and 3.5 MeV of the helium atom. The base material Deuterium

can be extracted from water, while Tritium must be gained from specific breeding blankets by a reaction of neutrons with lithium [4].

$$ {}^{6}_{1}\mathrm{Li} + n \rightarrow \alpha_{\mathrm{rad}} + {}^{2}_{1}\mathrm{T} + 4.78\,\mathrm{MeV} \tag{1.3} $$

The Lawson criterion specifies a minimum value for a triple product that the reaction proceeds by itself [5]. This triple product consists of the temperature, the particle density and the energy confinement time. A temperature of $\approx 120-150$ Mio. K and a pressure of about several bars are necessary for the reaction between Deuterium and Tritium on earth. This corresponds to a kinetic energy of $\approx 10-13$ keV, which is required to overcome the Coulomb barrier. A powerful heating system is needed to achieve such high plasma temperatures. Known heating methods are:

- Ohmic heating [6]
- Neutral Beam Injection (NBI) [7]
- Ion Cyclotron Resonance Heating (ICRH) [8]
- Electron Cyclotron Resonance Heating (ECRH) [9]

The ECRH describes a mechanism in which the microwave energy is transferred to electrons in the form of thermal kinetic energy. It is based on the cyclotron interaction. ECRH has several advantages compared to the other heating methods. An example is the low-loss microwave transmission via waveguides [10] or via quasi-optical mirror lines[11]. This allows the sources to be located far from the plasma vessel. In addition, the launching mirrors or antennas might be steered by small steps in frequency. Resulting in a power absorption at different locations in the plasma. This effect can eliminate plasma instabilities [12]. Additionally, the high operating frequencies lead to smaller port sizes.

Today, MW-class gyrotrons are available for the required high microwave power for ECRH. Gyrotrons are vacuum electron tubes producing microwave output powers of up to 2 MW [13] at frequencies from below 100 GHz up to 300 GHz. In addition to ECRH, gyrotrons can be used for plasma start-up, non-inductive Current Drive (CD) [14], Collective Thomson Scattering (CTS) [15] and plasma stability control [16].

Today, the largest ECRH system is installed at the stellarator Wendelstein 7-X (W7-X) in Greifswald, Germany. A total of ten 1 MW CW (1800 s) gyrotrons operate at 140 GHz [17, 18]. The tokamak project ITER in Cadarache, France, is currently under construction. ITER will be equipped with a total of 24 gyrotrons, each providing 1 MW output power at 170 GHz in CW (3600 s) [19]. Other fusion experiments using gyrotrons are WEST, France [20], ASDEX, Germany [21], DTT, Italy [22], TCV, Switzerland [23], DIII-D, US [24], KSTAR, South Korea [25], JT-60SA, Japan [26], J-TEXT, China [27] and T-15 MD, Russia [28].

1.2 Requirements for Future Fusion Gyrotrons

The DEMOnstration power plant (DEMO) shall be the first fusion power plant the demonstrates the generation of electricity. It is predicted that European (EU) DEMO will generate approximately 2 GW of thermal power [29] and 750 MW of electrical power [30]. A second major objective of EU DEMO is to demonstrate the reliability of a CW fusion power plant and its components for commercial Future Fusion Power plants (FFP). A complete list of all gyrotron requirements for the EU DEMO is described in [31]. A brief summary is given here for completeness. The gyrotrons used in recent fusion experiments such as W7-X and ITER operate at a single frequency such as 140 GHz or 170 GHz. However, first experimental fusion test facilities have already been equipped with gyrotrons, which are able to operate at multiple frequencies [21]. These multi-frequency gyrotrons can be used for multiple purposes, such as start-up, bulk heating, and non-inductive current drive. This advantage is also intended for the EU DEMO. It shall be equipped with multi-frequency/multi-purpose gyrotrons operating at 136 GHz, 170 GHz, 204 GHz, and 238 GHz. In addition, a bandwidth of ± 10 GHz shall be covered around each center frequency in steps of $2-3$ GHz. Gyrotron frequency tuning can be used for remote steering with a fixed launcher or mirror for plasma stability control. Additionally, the microwave output power per gyrotron shall be increased from 1 MW (W7-X, ITER) to 2 MW in CW operation. Increasing the microwave output power per

gyrotron unit results in fewer gyrotrons and associated infrastructure, such as superconducting (SC) magnets. Hence, reducing the number of units reduces the overall cost and the space required. A third major gyrotron requirement is the efficiency of the tube. The total gyrotron efficiency of $> 60\,\%$ requires a beam-wave interaction efficiency in the cavity of $> 35\,\%$.

1.3 State of the Art

State of the art fusion gyrotrons produce 1 MW microwave output power at 140 GHz and 170 GHz in long pulse operation at W7-X and ITER. Those gyrotrons are manufactured by Thales Group, France [32], Gycom Ltd., Russia [33], Canon Electron Tubes & Devices Co., Ltd., Japan [34] and Communication and Power Industries (CPI), US [35]. In [36], short-pulse experiments of a hollow-cavity gyrotron providing 1.5 MW output power at 140 GHz are presented. A CW gyrotron based on the short-pulse design has been fabricated and is currently being validated in experiments. At Karlsruhe Institute of Technology (KIT), the world record in microwave output power of 2.2 MW at 170 GHz in short-pulse operation was achieved with a coaxial-cavity gyrotron [13]. The gyrotron has been upgraded to operate with longer-pulses up to 50 ms [37] and is currently further upgraded for even longer pulses up to 1 s. In parallel, Russian researchers are currently working on injection locking [38, 39] to increase the microwave output power in hollow-cavity gyrotrons to $1.5 - 2$ MW.

Besides the intention to increase the output power per tube, the multi-frequency operation of gyrotrons is a major part in research and development (R&D). Several fusion experiments are already employing multi-frequency gyrotrons, e.g. ASDEX Upgrade is equipped with eight gyrotrons operating at either 105 GHz or 140 GHz. At JT-60SA the gyrotrons are able to operate at 82 GHz, 110 GHz or 138 GHz and at TCV at 84 GHz or 126 GHz. In addition, theoretical designs and first experiments up to 2 s have been published for multi-frequency operation at 104 GHz, 136 GHz, 170 GHz, 203 GHz using the hollow-cavity technology [40]. A theoretical design operating at 170 GHz, 204 GHz and 238 GHz using a coaxial cavity is published in [41]. In addition,

the frequency step-tunability is part of the research, too. First experiments for stepwise tuning of a hollow-cavity and coaxial-cavity gyrotron at KIT has been successfully performed over a large frequency range in [42, 43] and [44], respectively.

Fusion gyrotrons can also be used for plasma diagnostics using CTS, where an exact frequency is required. Therefore, frequency locking is used to stabilize the frequency as discussed in [45, 46].

A third major topic in gyrotron R&D is the increase of the total efficiency. It is defined by the ratio from the output power to the DC power applied to the gyrotron. The total efficiency can be separated into the interaction efficiency and the collector efficiency. The interaction efficiency can be increased by a highly optimized cavity design. In [36], an interaction efficiency of up to ≈ 40 % has been achieved. The total efficiency is typically increased by a Single-Stage Depressed Collector which can result in a total efficiency of around 50 %. At KIT, a Multi-Stage Depressed Collector is currently being prepared for initial experiments [47]. It shall allow a total gyrotron efficiency of > 60 % in future.

1.4 Scope of the Work

The scope of the work is to build a first 2 MW multi-frequency / multi-purpose coaxial-cavity pre-prototype. The operating frequencies should be 136 GHz, 170 GHz and 204 GHz. Particularly, the focus is on gyrotron operation at 170 GHz and 204 GHz. The design of the multi-frequency pre-prototype gyrotron bases on the existing 2 MW 170 GHz single-frequency coaxial-cavity pre-prototype, which is designed to operate in the existing SC magnet. A magnetic field strength of ≈ 8.3 T that is required for operating at 204 GHz cannot be provided by the existing SC magnet. Therefore, a new 10.5 T SC magnet is ordered. The magnetic profile of this new SC magnet is considered in this work. The upgrade of the gyrotron shall considers minimum modifications from the existing tube.

The main key components, namely the coaxial cavity, the Magnetron Injection Gun (MIG) and the quasi-optical output coupler, are investigated. An optimized design has to be provided for the pre-prototype that operates at multiple-frequencies. The cathodes of the existing MIGs shall be reused because it is the primary cost driver. All MIGs available at KIT are investigated if the electron beam requirements are satisfied at 170 GHz and 204 GHz using the new magnetic field profile. In addition to the ability to operate at multiple frequencies, also frequency step-tunability in a bandwidth of ± 10 GHz and in steps of $2 - 3$ GHz is investigated at the given center frequencies.

The pre-prototype design presented in this work will be the first gyrotron at KIT operating above 200 GHz. Three different frequency and mode measurement systems are available at KIT. They are used either for the verification of gyrotron components or for recording their behavior during operation. These measurement test stands are the quasi-optical mode generator used for the verification of the quasi-optical output coupler, the gyrotron output window measurement test arrangement and the frequency diagnostic system. All of these have been upgraded from the current limitation of 175 GHz up to a minimum of 260 GHz. A major modification is planned for the upgrade of the quasi-optical mode generator test facility. It was previously adjusted by hand considering usually months of work for adjustment. Electronic linear drivers and evaluation algorithms shall be installed and implemented to reduce the adjustment time drastically.

2 Fundamentals and Challenges

In the first part of this chapter, the working principle of gyrotron oscillators and their key components are discussed. In the second part, the challenges for a DEMO-relevant design are presented. Three subjects are noted, (i) the wall loading constraints of the cavity and the coaxial insert, (ii) the mode competition, and (iii) the ability to operate the gyrotron at multiple frequencies.

2.1 Gyrotron Operation Principle

Gyrotron oscillators are vacuum tubes that produce MW-level output power at microwave and sub-THz frequencies. A schematic of a coaxial-cavity gyrotron is shown in Fig. 2.1. A hollow electron beam is emitted by the emitter of the MIG and is accelerated by a DC voltage of up to 90 kV. The electrons are guided from the MIG through a beam tunnel to the interaction area (cavity) by an axial magnetic field. By slowly increasing the magnetic flux in the beam tunnel the guiding center radius of the electrons is compressed and the axial kinetic energy is transferred to transverse kinetic energy. This follows from the Bush theorem considering conservation of energy [48]. The electrons gyrate around the magnetic field lines on helical trajectories [49]. The interaction bases on a weakly relativistic electron beam and a transverse electric $TE_{m,p}$ mode. m describes the azimuthal and p the radial mode index. The maximum magnetic field strength is related to the operating frequency of that $TE_{m,p}$ mode. The generated electromagnetic (EM) field is separated after the interaction from the electron beam using a quasi-optical output coupler. It transforms the high-order rotating $TE_{m,p}$ mode into a Gaussian beam. This beam can be further collimated and coupled out radially. Finally, the energy of the spent electron beam is dissipated in the collector.

The interaction mechanism in gyrotrons is called electron-cyclotron interaction and is discussed in detail in [51, 52]. The energy exchange takes place

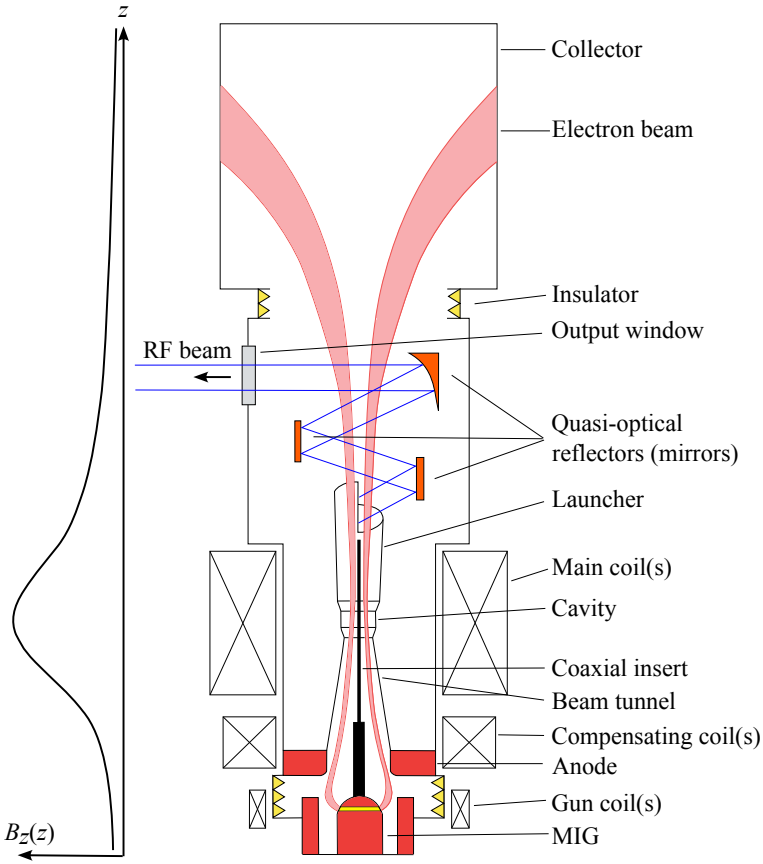

Fig. 2.1: Schematic of the KIT 2 MW 170 GHz short-pulse coaxial-cavity pre-prototype [50].

close to the angular electron cyclotron frequency Ω_c of the electrons, which can be derived from the Lorentz force equation. The Lorentz factor γ has to be considered in the equation due to the high electron energy.

$$\frac{\Omega_c}{2\pi} = f_c = \frac{1}{2\pi}\frac{q_e B_{cav}}{m_e \gamma} \approx \frac{28 \cdot B_{cav}}{\gamma} \tag{2.1}$$

The unit of Ω_c is GHz, if B_{cav} is given in T. f_c describes the electron cyclotron frequency. B_{cav} is the maximum magnetic field strength at the center of

the midsection of the cavity, m_e the electron rest mass and q_e the electron charge. The relativistic Lorentz factor is described by,

$$\gamma = \frac{1}{\sqrt{1-(v/c_0)^2}} = 1 + \frac{W_{\mathrm{kin}}}{m_e c_0^2} \approx 1 + \frac{W_{\mathrm{kin}}}{511\,[\mathrm{keV}]} \tag{2.2}$$

with the kinetic energy of the electron W_{kin}, the velocity v of the electron and c_0 the speed of light in vacuum. The distance between the trajectories and the electron guiding center radius is described by the Larmor radius r_L.

$$r_L = \frac{\gamma m_e v_\perp}{q_e B_{\mathrm{cav}}} \tag{2.3}$$

$v_\perp$ is the transverse component of the velocity.

The electrons are accelerated or decelerated depending on their relative phase position by the presence of a synchronous EM field in the interaction region. An example for both cases (accelerating and decelerating phases) is presented in Fig. 2.2. In the accelerating phase (top graph of Fig. 2.2) the kinetic energy increases, which leads to an increase of γ according to Eq. 2.2. Therefore, the electron cyclotron frequency is decreased according to Eq. 2.1. Those electrons move towards a favorable phase position [52]. In the decelerating phase, the electrons transfer a part of the kinetic energy to the EM field and become lighter. Thus, the electron cyclotron frequency Ω_c increases. If the electron cyclotron frequency is chosen to be slightly below the angular frequency of the EM wave, the difference between the frequencies ($\omega - \Omega_c$) decreases. Therefore, the electrons stay longer in the deceleration phase. As a result, the electrons in the decelerating field accumulate at the decelerating phase. Finally, net energy is transferred coherently to the EM wave. The accumulation of the electrons is called bunching [53]. The electrons can recover energy from the EM field region, which is called over-bunching [54], if the interaction region is too long.

Through the movement of the electrons along the EM field, the frequency is shifted by a Doppler term $k_\parallel v_\parallel$ [54]. The resonance condition is defined by

$$\omega - k_\parallel v_\parallel \geq s \cdot \Omega_c\,. \tag{2.4}$$

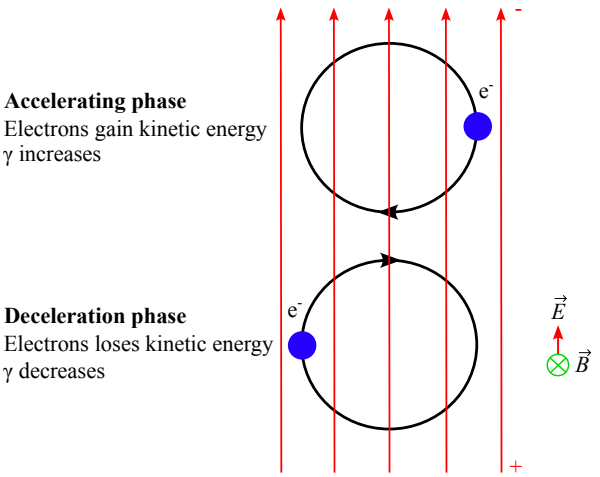

Fig. 2.2: Principle of electron cyclotron interaction mechanism in a gyrotron cavity.

The wavenumber k is given by

$$k = \frac{2\pi}{\lambda} = \frac{2\pi f}{c_0}\,, \tag{2.5}$$

$$k^2 = k_{\parallel}^2 + k_{\perp}^2\,. \tag{2.6}$$

$k_{\parallel}$ and $k_{\perp}$ are the axial and transverse components of the wavenumber. Equation 2.4 is valid for gyrotrons operating at the fundamental ($s = 1$) of the electron cyclotron frequency or at a harmonic ($s > 1$) . The resonance condition between the transversal electrical $\mathrm{TE}_{m,p}$ mode and the electron beam can be illustrated using the Brillouin diagram [55]. In that diagram, the relation between ω and k is given by,

$$\omega = c_0\sqrt{k_{\parallel}^2 + k_{\perp}^2}\,. \tag{2.7}$$

The beamline follows the condition

$$\omega - k_{\parallel} v_{\parallel} = s \cdot \Omega_c\,. \tag{2.8}$$

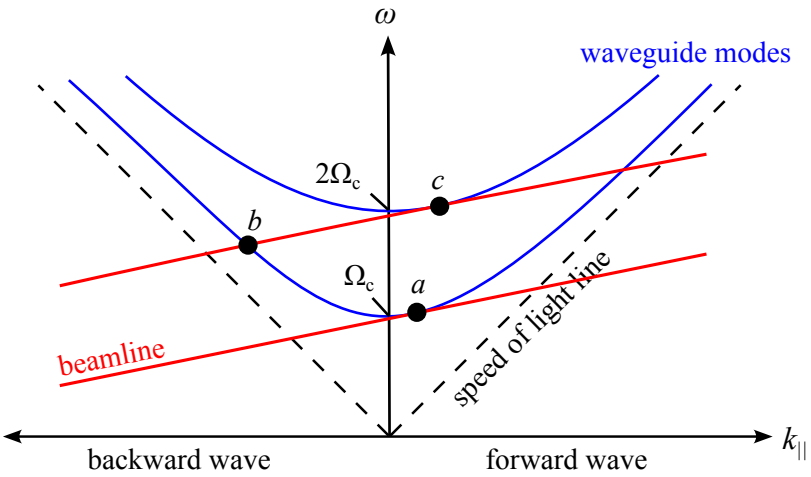

Fig. 2.3: Dispersion diagram of possible operating modes with the electron beamline (red).

A Brillouin diagram is shown in Fig. 2.3. The hyperbolas represent the dispersion curves of two different TE modes (blue lines). The intersection points between the dispersion curves and the beamline (red) represent points of possible interaction. In this example, three different intersection points are marked with "a", "b" and "c". Point "a" highlights a typical point of a gyrotron interaction at the first harmonic. The operating frequency is very close to the cut-off frequency. Point "b" represents a backward wave with $k_{\parallel} \ll 0$. Point "c" indicates an interaction at the second harmonic cyclotron frequency.

2.2 Gyrotron Key Components

In the following, the gyrotron key components relevant to this work are discussed. A detailed explanation of all gyrotron sub-components are discussed in [52].

2.2.1 Magnetron Injection Gun

The hollow electron beam is generated by a Magnetron Injection Gun (MIG). There are two major configurations in the MIG design, namely diode-type and triode-type. The basic schematics of the two classic configurations in coaxial-cavity technology are shown in Fig. 2.4. MIGs built in coaxial-cavity technology contain an insert that passes through the cathode. The diode-type MIG has the advantage of a simple and robust design. Only one high-voltage potential is required for the principal operation or two in the depressed collector operation. However, the electron beam parameters can be controlled only by the applied acceleration voltage $V_{\mathrm{acc}} = |V_{\mathrm{c}} - V_{\mathrm{b}}|$. MIGs built in triode configuration have an additional modulation anode. It can be used to control the electric field at the emitter. The triode configuration requires an additional power supply and ramp-up, which slightly increases its complexity and cost. In addition, a third configuration, the Inverse Magnetron Injection Gun (iMIG) exist, which is described in [57, 58, 59].

In the following, the basic operation of the emitter is discussed. The electrons are emitted by thermionic emission, where electrons are released from the heated emitter due to its sufficient high temperature T_{emt} [52]. The MIG

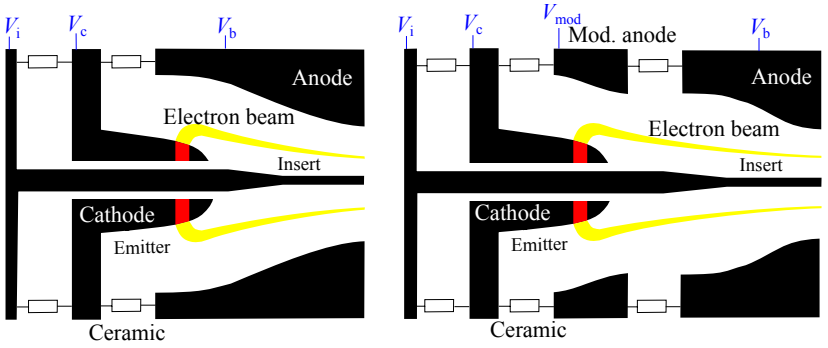

Fig. 2.4: Schematic view of the structure of a coaxial diode-type (left) and triode-type (right) Magnetron Injection Gun [56]. In a triode configuration, the voltages applied are at the cathode V_{c}, the anode V_{b}, the insert V_{i} and at the modulation anode V_{mod}.

operates in the temperature limited emission area. The total beam current is described by the Richardson-Dushman equation:

$$J_s = A_0 T_{\mathrm{emt}}^2 \exp^{-\frac{W_E}{k_B T_{\mathrm{emt}}}} . \tag{2.9}$$

J_s is the current density of the emission, A_0 is the Richardson constant, W_E is the work function of the emitter material and k_B is the Boltzmann constant. An electric field E at the emitter surface is formed due to the negatively biased emitter of the MIG. The resulting Schottky-Effect lowers the work function of the surface barrier by ΔW. Therefore, the Richardson-Dushman equation must be modified to:

$$J_s = A_0 T_{\mathrm{emt}}^2 \exp^{-\frac{W_E - \Delta W}{k_B T}} , \tag{2.10}$$

where ΔW is given by

$$\Delta W = \sqrt{\frac{q_e^3 \cdot E}{4\pi\varepsilon_0}} . \tag{2.11}$$

ε_0 is the permittivity of vacuum. Today's emitters for fusion gyrotrons are specified with a maximum current density of $4 - 5$ A/cm^2 at an emitter surface temperature of around 1000 °C resulting in a lifetime of about 10^4 hours [60]. Thermionic emitters are manufactured from porous tungsten with an impregnated emitter surface to reduce the work function [61]. Commonly, the pores of the emitting tungsten ring are filled with Al_2O_3, BaO and CaO in a certain mixture [56].

The emitted electrons have a transverse velocity $v_\perp$ and an axial velocity $v_\parallel$ component. The velocity ratio, or pitch factor α, is defined by

$$\alpha = \frac{v_\perp}{v_\parallel} = \frac{\beta_\perp}{\beta_\parallel} , \tag{2.12}$$

with the normalized transverse electron velocity $\beta_\perp = v_\perp / c$ and parallel electron velocity $\beta_\parallel = v_\parallel / c$. A high pitch factor is favored leading to a possible higher interaction efficiency [62], since the interacting transverse component contains more energy. Typical values for the pitch factor are in

the range of $\alpha = 1.1-1.3$ for fusion gyrotrons. It can be varied at the nominal acceleration voltage using a modulation anode in triode-type configuration. Realistic electron beams contain spreads for e.g. the pitch factor $\Delta\alpha$, the kinetic energy ΔE_{kin} and the electron beam radius Δr_{beam}. The pitch factor and the kinetic energy spread are defined by the standard deviation

$$\Delta\alpha = \frac{1}{\alpha_{\mathrm{mean}}} \cdot \sqrt{\frac{1}{N}\sum_{i=1}^{N}(\alpha_i - \alpha_{\mathrm{mean}})^2} \tag{2.13}$$

$$\Delta E_{\mathrm{kin,\,mean}} = \frac{1}{E_{\mathrm{kin}}} \cdot \sqrt{\frac{1}{N}\sum_{i=1}^{N}(E_{\mathrm{kin},i} - E_{\mathrm{kin,\,mean}})^2} \tag{2.14}$$

α_{mean} and $E_{\mathrm{kin,\,mean}}$ are the mean value of the velocity ratio and $\Delta\alpha$ and ΔE_{kin} are the root-mean-square(rms) values of the spreads. In contrast, the spread of the electron beam radius is uniformly distributed with

$$\Delta r_{\mathrm{beam}} = \frac{r_{\mathrm{emt,\,max}} - r_{\mathrm{emt,\,min}}}{b^{1/2}} \tag{2.15}$$

The electron motion considers the adiabatic approximation. The adiabatic approximation describes a slow change of the electric and magnetic field [63] along the gyrotron axis and is valid for a small variation of the electric and magnetic field [64]. The condition

$$\frac{p_\perp^2}{B} = \text{const.} \tag{2.16}$$

is an invariant of motion [63]. As presented in Fig. 2.4, the electron beam is compressed from the average emitter radius r_{emt} to the beam radius at the cavity section r_{beam}. This effect is due to the adiabatic compression according to the Busch Theorem [48] with respect to the changing magnetic field flux along the gyrotron axis, between the emitter B_{emt} and the cavity B_{cav}. The magnetic compression ratio b is defined by

$$b = \frac{B_{\mathrm{cav}}}{B_{\mathrm{emt}}} = \left(\frac{r_{\mathrm{emt}}}{r_{\mathrm{beam}}}\right)^2 . \tag{2.17}$$

2.2.2 Cavity

The cavity is a straight circular waveguide (midsection) with a down-taper at the input and an up-taper at the output with an angle of 5° in maximum. Thus, it forms an open cavity. Figure 2.5 depicts a schematic of the two different types of cavities, the hollow-type cavity and coaxial-type cavity. The coaxial cavity has an additional corrugated insert installed. Main energy is transferred from the electron beam to the electromagnetic wave in the midsection. The maximum magnetic field of the SC magnet is located at the center of the midsection.

Advantages of Coaxial-Cavity Technology

The main benefit of the coaxial configuration is the reduced mode competition, which gets even more relevant for increasing mode eigenvalues at higher operating frequencies [65, 66]. The eigenvalue of a given mode in the coaxial cavity depends on the ratio of the cavity radius to the insert radius. Longitudinal impedance corrugations on the insert lead to an adjustment of the quality factors of the neighboring modes and hence to a reduced mode competition [67]. The second benefit is the lower voltage depression in the coaxial-cavity technology. Voltage depression describes the effect of decelerating electrons due to the space charge of the electrons along the beam

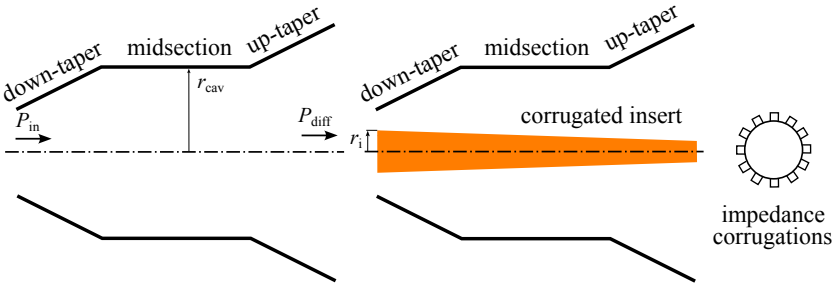

Fig. 2.5: Schematic of a hollow-cavity (left) and coaxial cavity (right). Both consist of down-taper, midsection and up-taper. The coaxial-cavity is equipped with a corrugated insert additionally.

path. This creates a negative potential. The voltage depression ΔV reduces the accelerating voltage V_{acc} to the beam potential V_{beam}. It corresponds to the electron energy at the entrance of the cavity. The voltage depression for a coaxial-cavity is described by [52].

$$\Delta V = |V_{\mathrm{acc}} - V_{\mathrm{beam}}| \tilde{=} 60 \frac{I_{\mathrm{beam}}}{\beta_{\parallel}} \ln\left(\frac{r_{\mathrm{cav}}}{r_{\mathrm{beam}}}\right) \frac{\ln\left(\frac{r_{\mathrm{beam}}}{r_{\mathrm{i}}}\right)}{\ln\left(\frac{r_{\mathrm{cav}}}{r_{\mathrm{i}}}\right)} \tag{2.18}$$

I_{beam} is the beam current. The cavity and coaxial insert radius is given by r_{cav} and r_{insert}, respectively.

Mode Propagation in Circular Waveguides

The interaction takes place between an electron beam and a mode, which is very close to its cut-off. In a cylindrical waveguide, several different types of modes can propagate. Those are the $\mathrm{TE}_{m,p}$ and $\mathrm{TM}_{m,p}$ modes. In case of the coaxial structure the additionally the TEM-mode can propagate. The field components E_{φ} and E_{r} of a $\mathrm{TM}_{m,p}$ mode vanishes operating close to cut-off. Hence, the energy transfer from an electron beam to a TM mode can be neglected [68]. The TEM mode can also be neglected because it provides a very low quality factor. This is due to the fact that the modes do not have a cut-off frequency. Only the $\mathrm{TE}_{m,p}$ modes show a stable operation and an efficient interaction with the electron beam. The azimuthal and radial electrical field components for a $\mathrm{TE}_{m,p}$ mode can be described by [69].

$$E_r = -\frac{m}{r_{\mathrm{cav}}} \cdot J_m\left(\frac{\chi_{m,p} \cdot r}{r_{\mathrm{cav}}}\right) \cdot e^{-jm\varphi} e^{-jk_z z} \tag{2.19}$$

$$E_{\varphi} = j\frac{\chi_{m,p}}{r_{\mathrm{cav}}} \cdot J'_m\left(\frac{\chi_{m,p} \cdot r}{r_{\mathrm{cav}}}\right) \cdot e^{-jm\varphi} e^{-jk_z z} \tag{2.20}$$

$$E_z = 0 \tag{2.21}$$

$$E = \sqrt{E_r^2 + E_{\varphi}^2} \tag{2.22}$$

The cut-off frequency f_{cut} of the operating mode can be calculated by

$$f_{\mathrm{cut}} = c_0 \frac{\chi_{m,p}}{2\pi r_{\mathrm{cav}}}. \tag{2.23}$$

The eigenvalue $\chi_{m,p}$ is described by the p-th root of the derivative of the Bessel function (J'_m). The beam-wave coupling is given by [67]

$$Ge_{m,p} = \frac{J_{m\mp1}\left(k_{\perp,m,p} r_{\text{beam}}\right)}{J_m\left(\chi_{m,p}\right)\sqrt{\pi\left(\chi_{m,p}^2 - m^2\right)}}. \tag{2.24}$$

The highest mode coupling is achieved at the beam/guiding center radius r_{beam}

$$r_{\text{beam}} = \frac{r_{\text{cav}}\chi_{m\mp1,1}}{\chi_{m,p}}. \tag{2.25}$$

The "-" and "+" in the formula defines the maximum coupling to the co- and counter-rotating mode with respect to the gyrating electron. In general, in this work, a co-rotating mode is defined by a positive azimuthal mode index and a counter-rotating mode by a negative.

Wall Loading Constraints

The quality factor Q_{tot} of a resonator can be divided into two parts, namely the ohmic Q_Ω and the diffractive quality factor Q_{dif}. The total quality factor can be calculated by

$$\frac{1}{Q_{\text{tot}}} = \frac{1}{Q_\Omega} + \frac{1}{Q_{\text{dif}}}. \tag{2.26}$$

The Ohmic quality factor is described by [64]

$$Q_\Omega \approx \frac{r_{\text{cav}}}{\delta}\left(1 - \frac{m^2}{\chi_{m,p}^2}\right). \tag{2.27}$$

δ is the skin depth defined by $\delta = 1/\sqrt{\pi f \mu_0 \sigma}$. The diffractive quality factor is expressed by [64]

$$Q_{\text{dif}} \approx \frac{4\pi K}{n^2}\left(\frac{L_{\text{eff}}}{\lambda_0}\right)^2. \tag{2.28}$$

Where n is the longitudinal mode index (typical $n = 1$), L_{eff} the effective length of the cavity and K is a constant defined by the reflection coefficients $\Gamma_{1,2}$ at the down- and up-taper [70] described by

$$K/n \approx \frac{1}{1 - |\Gamma_1| \cdot |\Gamma_2|} \,. \tag{2.29}$$

A major challenge in the gyrotron design is to achieve low ohmic wall losses, which can be estimated by [64]

$$P_\Omega \approx 2c_0 \sqrt{\frac{\pi f}{\mu_0 \sigma}} Q_{\text{dif}} P_{\text{out}} \frac{\chi_{m,p}}{1 - m^2/\chi_{m,p}^2} \,, \tag{2.30}$$

Assuming the cavity surface S, the cavity wall loading is given by [71]

$$\rho_\Omega = \frac{P_\Omega}{S} = \frac{Q_{\text{dif}} \cdot P_{\text{dif}}}{Q_\Omega \cdot S} \approx \frac{2\sqrt{\pi}}{c_0^3 \sqrt{\mu_0 \sigma}} \frac{f^{2.5} \cdot Q_{\text{dif}}}{L_{\text{eff}}/\lambda \left(\chi_{\text{m,p}}^2 - m^2\right)} P_{\text{dif}} \,. \tag{2.31}$$

The strong dependency of the wall loading and the resonance frequency is given by $\rho_\Omega \sim f^{2.5}$.

Efficiency

The efficiency $\eta_\perp$ of the power transfer from the kinetic electron beam to the electromagnetic field is given by

$$\eta_\perp = \frac{P_{\text{elec}}}{P_\perp} \,. \tag{2.32}$$

$P_\perp$ is the perpendicular power of the electron beam and P_{elec} the generated microwave power in the cavity. The theoretical maximum of $\eta_\perp$ is at $\approx 72\,\%$ [72]. The total electrical efficiency η_{elec} describing the total energy transfer from the electrons to the TE mode is given by

$$\eta_{\text{elec}} \approx \frac{\alpha^2}{1 + \alpha^2} \cdot \eta_\perp \,. \tag{2.33}$$

2.2.3 Quasi-Optical Output Coupler

A detailed description of the quasi-optical output coupler can be found in [50]. In this section, the main working principle is discussed. The quasi-optical output coupler decouples the electron beam from the EM wave. The EM wave is radially coupled out of the gyrotron, while the electron beam is dissipated in the collector. Such a quasi-optical output coupler consists of a launcher acting like a waveguide antenna, and several mirrors. The first launchers were proposed in [73, 74]. Several additional designs have been developed, which are summarized and compared in [75]. The quasi-optical output coupler converts the operating gyrotron cavity mode into a linearly polarized Gaussian mode, which has low transmission losses in free-space and in a corrugated waveguide. It is used to guide the electromagnetic wave to the plasma vessel.

In a highly oversized waveguide, the transmission of the EM field can be approximated using geometric optics [76, 77]. Considering this assumption, a representation of a high-order rotating gyrotron mode is shown in Fig. 2.6. The angle between the unit vector in azimuthal direction ($\vec{e}_\varphi$) and the ray (direction of Poynting vector) is given by the spreading angle

$$\cos\theta = \frac{m}{\chi_{m,p}}\,. \tag{2.34}$$

The rays are reflected by the metallic wall and are all intersecting at the caustic radius r_c. The caustic radius is defined by [52]

$$r_\mathrm{c} = r_\mathrm{cav}\cos\theta = \frac{m}{\chi_{m,p}} r_\mathrm{cav}\,. \tag{2.35}$$

Propagation in z-direction, along the gyrotron axis, is represented in the geometrical optics with the Brillouin angle θ_B

$$\theta_\mathrm{B} = \arcsin\left(\frac{\chi_{m,p}}{k\cdot r_\mathrm{cav}}\right)\,. \tag{2.36}$$

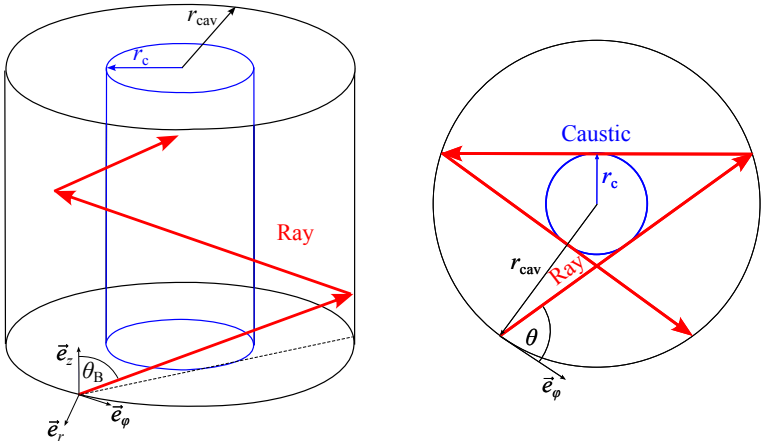

Fig. 2.6: Schematic view of quasi-optical propagation in z-direction, along the gyrotron axis, in the left graph and the cross section of the circular waveguide at the right [50]. The red colored arrows describe the rays, which are all intersecting the caustic radius r_c (blue).

2.3 Challenges Towards a DEMO Relevant Design

Challenges regarding the design and operation of a hollow-cavity gyrotron for EU DEMO are already discussed and summarized in [31]. In this section, some major challenges with respect to a DEMO-relevant design considering a multi-MW coaxial-cavity gyrotron are discussed.

Cavity and Insert Wall-Loading

Today, the maximum acceptable cavity wall loading is 2 kW/cm^2 and of the insert loading is 0.2 kW/cm^2 [78]. The ohmic loading becomes more challenging at higher frequencies with $\rho_\Omega \sim f^{2.5}$ as it is foreseen for an EU DEMO-relevant design. Simulations show that the nominal operation parameters, and thus the resulting performance, degrade if the cavity radius stays constant at higher frequencies. In contrast, increasing the cavity radius leads to operating modes with higher eigenvalues, resulting in an increased mode competition and a reduced mode stability. Hence, a major challenge in future DEMO-relevant gyrotron designs is to find an appropriate trade-off

between performance and mode stability at frequencies above 200 GHz. An alternative approach is to improve the cavity cooling system to relax the wall loading constraints. The maximum limit is given by the utilized cooling technology [79]. However, it is estimated that a maximum wall loading of 2.5 kW/cm^2 could be accepted using a mini-channel cooling [56].

Mode Competition

The eigenvalue of the $TE_{34,19}$ mode, which is considered as operating mode at 170 GHz, is $\chi_{34,19} = 105.2$. It is presently the highest operating mode in a gyrotron. This mode, together with a cavity radius of 29.55 mm, meets the gyrotron design requirements providing an output power of 2 MW at 170 GHz with a wall loading below the limit of 2 kW/cm^2. However, the number of propagable modes N in a waveguide increases with increasing frequency, which can be estimated with

$$N \approx 2.55 \cdot (2r_{\mathrm{cav}}/\lambda)^2 \ . \tag{2.37}$$

Keeping the existing cavity radius r_{cav} constant, the eigenvalues of the modes operating at 204 GHz or even higher are far above 100. The coaxial-cavity technology benefits from the insert by reduced mode competition. But, it still requires a precise cavity design and fabrication for such high-order gyrotron modes.

Multi-Frequency/Multi-Purpose Operation with Fast Frequency Step-Tunability

A major part of this work is to design a pre-prototype gyrotron operating at multiple frequencies with the ability to tune the frequencies in steps. The possibility in operating the gyrotron at multiple-frequencies is called in the following multi-frequency operation. Multi-purpose means that the gyrotrons can be used for e.g. start-up, bulk heating, and non-inductive current drive. Several gyrotron key components, such as the MIG, the coaxial cavity with insert and the quasi-optical output coupler must be optimized for operation at different modes and frequencies. A key aspect is the mode

selection process, which shall identify modes with similar relative caustic radii for the given center frequencies, e.g. at 136/170/204/238 GHz. In the case of frequency step-tunability the relative caustic radius cannot be similar, but should be in a range of < 4 %. The change of the relative caustic radius makes it more challenging to design a quasi-optical output coupler for those modes. Furthermore, a fast frequency tuning should be possible, which is determined by the change of the maximum magnetic field [12].

3 Design of a First Multi-Frequency Pre-Prototype Gyrotron

In this chapter, the upgrade of the existing 2 MW 170 GHz $TE_{34,19}$ mode coaxial-cavity short-pulse pre-prototype gyrotron is considered theoretically towards multi-frequency operation. The relevant gyrotron key components are discussed in detail. The gyrotron has to be updated towards an operation at either 170 GHz or 204 GHz using off-the-shelf components with best possible performance. For the first time, frequency-step tunability is studied at those center frequencies considering the insert loading in the mode selection process. In addition, first studies regarding the possibility of cavity operation at 136 GHz are performed, too.

3.1 Requirements for Multi-Frequency Operation

Multi-frequency gyrotrons can be used for different purposes in a nuclear fusion experiment, like plasma start-up, bulk heating, non-inductive current drive and plasma stabilization. There are two main design criteria for a multi-frequency operation. First, the corresponding operating frequencies should fit to the natural transmission maxima of the gyrotron output window, and second, the launcher should be able to operate properly with all selected gyrotron modes.

3.1.1 Determination of the Main Frequencies

A transparent window is required to couple the microwave beam out of the vacuum tube with a minimum of losses and reflection. There are various vacuum window materials that can be used for gyrotrons, such as BeO, Silicon, SiC or chemical-vapor deposition (CVD) diamond [80, 81]. Megawatt-class

gyrotrons operating at long pulses are equipped with a CVD-diamond window. CVD diamond has a high microwave power transmission capability and a low loss tangent of tan $\delta \approx 2 \cdot 10^{-5}$. Its thermal conductivity of about 2000 W/mK is very high and is needed for edge cooling of the window disk [82]. The resonance frequencies f_{op} are defined by the equation [83]

$$f_{\mathrm{op}} = n \cdot \frac{\lambda_m}{2} = \frac{n \cdot c_0}{2 \cdot d_{\mathrm{window}} \cdot \sqrt{\epsilon_r'}} \quad \forall n = 1, ..., \infty \,, \tag{3.1}$$

where λ_m is the wavelength in the medium (CVD diamond) , n an integer number, d_{window} the thickness of the window and ϵ_r' the relative permittivity of the material ($\epsilon_r' = 5.67$ for CVD-diamond) [82]. Figure 3.1 presents the transmission and reflection of a CVD-diamond disk with a thickness of 1.85 mm. This disk is used for the gyrotron and torus windows at ITER [84]. The natural resonances of this disk are at 136.1 GHz, 170.01 GHz, 204.2 GHz and 238.2 GHz in the given frequency range, which corresponds to $4/2\lambda_m$, $5/2\lambda_m$, $6/2\lambda_m$, and $7/2\lambda_m$, respectively.

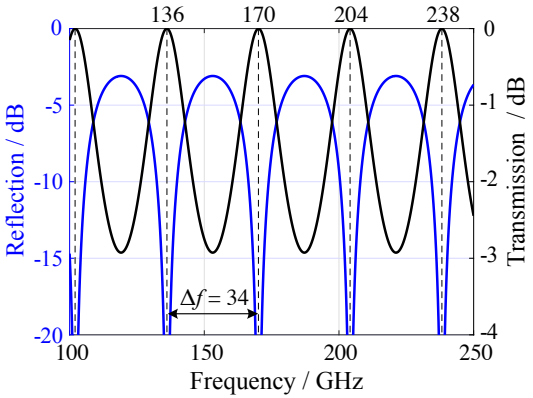

Fig. 3.1: Calculated transmission and reflection of a single CVD-diamond disk ($\epsilon_r' = 5.67$, $d_{\mathrm{window}} = 1.85$ mm) in the relevant range from 100 − 250 GHz.

Research is currently ongoing to install a diamond disk at the Brewster angle for broadband operation. This means that one polarization direction does not show a resonance behavior and thus the operating frequency does not depend on the CVD-diamond disk [85]. Broadband gyrotron output windows are mandatory for the ability to step-tune the frequency in a range of ± 10 GHz in $2 - 3$ GHz steps around the center frequencies.

3.1.2 Mode Selection Process

Operating modes have to be identified in the mode selection process, which fit to the output window and offer a small deviation in the caustic radii. In [86], a maximum deviation in caustic radii of 2.6 % is proposed to guarantee a proper operation. However, the given launcher is not optimized for multi-frequency operation. According to simulations at KIT, a deviation in the relative caustic radii of the selected modes in the mode series of < 4 % is required to guarantee a proper operation of the launcher [41]. Since the upgrade towards a multi-frequency pre-prototype is based in this work on the existing 2 MW coaxial-cavity pre-prototype, the first mode in the mode series has been defined by the already operating $TE_{34,19}$ mode at 170 GHz [13]. Therefore, the identification of suitable mode candidates operating at 136 GHz, 204 GHz and 238 GHz are limited. The identified candidates are the $TE_{28,15}$ mode operating at 136 GHz, the $TE_{40,23}$ mode at 204 GHz and the $TE_{48,26}$ mode at 238 GHz. The properties for these modes are summarized in Tab. 3.1. The $TE_{28,15}$ mode and the $TE_{40,23}$ mode operating at 136 GHz and 204 GHz operate very closely to the resonance frequency of the diamond disk. It results in a very low reflection at the gyrotron window and thus a high transmission. The deviation of the relative caustic radius is in total above 4 %. However, relative to the mode at 170 GHz, the difference is within the requirements. A study of possible alternative mode series, which are designed from scratch, is discussed in Chapter 6. In the following studies, the main focus is set on a dual-frequency 170/204 GHz operation.

The E-field patterns of the chosen $TE_{m,p}$ modes at 170 GHz and 204 GHz are presented in Fig. 3.2. The mode indices of the $TE_{m,p}$ mode are given by

the azimuthal mode index $m = 34$ and $m = 40$ and the radial mode index by $p = 19$ and $p = 23$ for 170 GHz and 204 GHz, respectively. The graphs in Fig. 3.2 are plotted in absolute values. The radius of the field maxima is smaller in the case of the $TE_{40,23}$ mode and the number of maxima in the azimuthal direction is higher.

Table 3.1: Summary of key parameters of suitable modes for the operation at 136 GHz, 170 GHz, 204 GHz and 238 GHz.

Mode	$TE_{28,15}$	$TE_{34,19}$	$TE_{40,23}$	$TE_{48,26}$
Frequency / GHz	135.81	170.0	204.18	237.24
Window reflection / %	0.030	0	0.026	0.472
Rel. caustic radius	0.3333	0.3232	0.3167	0.3270
Diff. in caustic radius / %	3.09	0	-2.01	+1.18
Eigenvalue	84.0	105.2	126.3	146.8

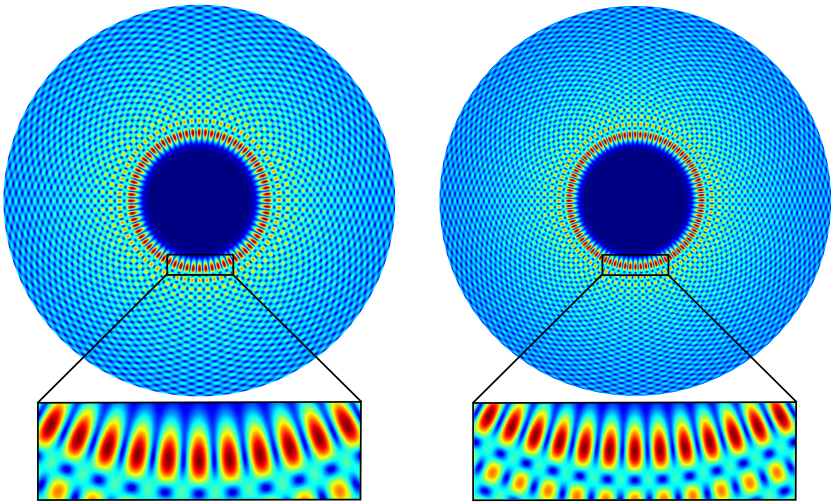

Fig. 3.2: *E*-field intensity patterns of the non-rotating $TE_{34,19}$ mode at 170 GHz (left) and the $TE_{40,23}$ mode at 204 GHz (right).

3.2 Verifying the Existing Pre-Prototype Gyrotron

The performance of the relevant gyrotron key components of the existing 170 GHz single-frequency pre-prototype design are studied at 204 GHz with the $TE_{40,23}$ mode. The investigated key components are the coaxial cavity and the quasi-optical output coupler. This study provides an indication about the required modification to achieve a 170/204 GHz dual-frequency gyrotron providing 2 MW output power at both frequencies.

3.2.1 Influence of Magnetic Field Profiles

The existing SC magnet from Oxford Instruments, Abingdon, UK cannot provide the required $\approx$ 8.3 T to operate the gyrotron at 204 GHz. Simulations presented in this work are based on the dimensions and magnetic field profile of a future 10.5 T SC magnet. This SC magnet is longer in z-direction due to the higher magnetic field forces. The distance between the emitter and the center of the cavity is extended from 367 mm for the existing magnet to 400 mm. This implicit that the gyrotron components have to be adapted accordingly. Simulations show that operating the gyrotron without an adaption to the SC magnet leads to a drastic increase of the velocity spreads above 40 % [41]. The electron beam trajectory of the existing SC magnet is compared in Fig. 3.3 to the one of the new 10.5 T SC magnet exemplarily for the iMIG. The distance between the electron beam and the body is increased. The effect of trapped electrons can occur as a consequence. In terms of the longer main coil of the future 10.5 T SC magnet, the magnetic field profile in the cavity area is more flat and the magnetic field compression is increased. As a result, all available MIGs at KIT have to be validated with the new magnetic field profile and, if necessary, modified accordingly.

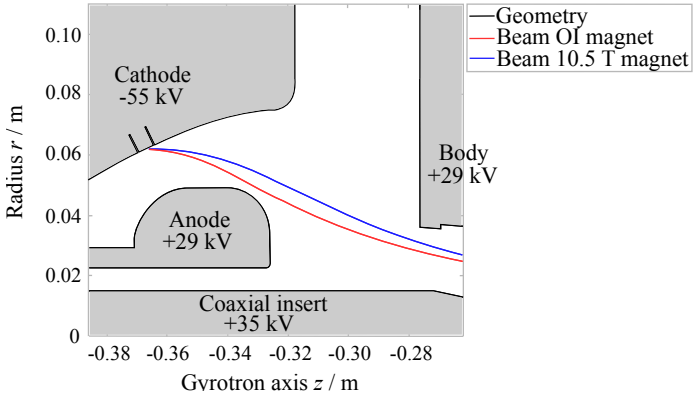

Fig. 3.3: Comparison of the electron beam trajectories of the existing Oxford Instruments (OI) SC magnet and the new 10.5 T SC magnet.

3.2.2 Operating the Existing 170 GHz Single-Frequency Pre-Prototype at 204 GHz

In addition, the coaxial cavity and the quasi-optical output coupler of the 170 GHz single-frequency design are validated for an operation at 204 GHz.

Coaxial Cavity

The design of the existing 170 GHz single-frequency coaxial cavity has been investigated whether a principle operation at 204 GHz without any modification is possible. For this study, the electron beam parameters of the existing MIG are not needed. Nevertheless, in order to be as realistic as possible, an adiabatic start-up is performed in the interaction simulations carried out with the code package EURIDICE [87]. A general description of the code is given in [88] and in Appendix A.1. A kinetic energy spread of $\Delta E = 0.2\,\%$ rms and a relatively large velocity spread of $\Delta\alpha = 20\,\%$ rms is considered. These values correspond to a worst-case approximation according to [31].

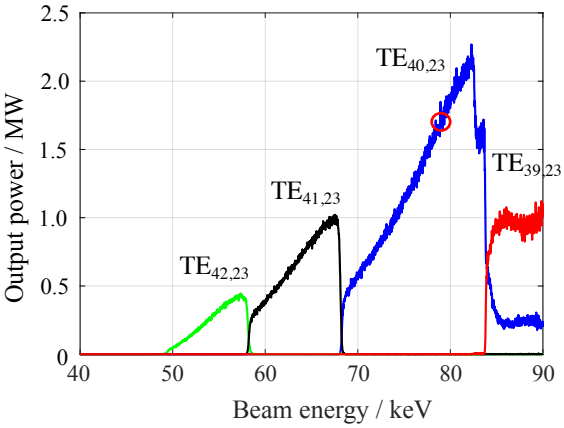

Fig. 3.4: Adiabatic start-up scenario at 204 GHz with the existing coaxial cavity, originally designed for 170 GHz single-frequency operation. The circle indicates the operation point of the nominal $TE_{40,23}$ mode at a beam energy of 79 keV, a beam current of $I_{\text{beam}} = 70$ A and a magnetic field strength of 8.15 T .

Initial simulations show that the pitch factor needs to be reduced from the nominal $\alpha = 1.3$ to $\alpha = 1.2$ for operation at 204 GHz to avoid parasitic oscillations. Figure 3.4 presents an adiabatic start-up scenario at 204 GHz. The interaction simulation shows an output power of 1.66 MW and an interaction efficiency of 31.2 %. The nominal operation point is at a beam energy of 79 keV and a beam current of 70 A. The operation parameters and thus the performance is limited by the wall loading of 2 kW/cm^2. An insert loading of 0.06 kW/cm^2 has been obtained, which is far below the limit. Operation of the existing 170 GHz coaxial cavity is possible at 204 GHz, however, the EU DEMO requirement of 2 MW output power at all possible frequencies is not fulfilled. Therefore, the coaxial cavity must be modified as proposed in Section 3.3.2.

Quasi-Optical Output Coupler

The existing quasi-optical output coupler is designed for 170 GHz single-frequency operation [89] providing a Gaussian mode content of 96.3 %. It has been verified by simulations using TWLDO [90] and the commercial 3D full-wave code SURF3D [91]. The fundamental Gaussian mode content of the single-frequency design operating at 204 GHz has been calculated to be only 91.6 %, which is below the desired 95 %. Figure 3.5 presents the E-field intensity distribution of the nominal $TE_{34,19}$ mode at 170 GHz and the $TE_{40,23}$ mode at 204 GHz in the window plane. The differences in the quality of the microwave output beam at the two frequencies are obvious. Therefore, the 170 GHz single-frequency design of the quasi-optical output coupler is not suited for gyrotron operation at 204 GHz. A modification of the quasi-optical output coupler is discussed in Section 3.3.3.

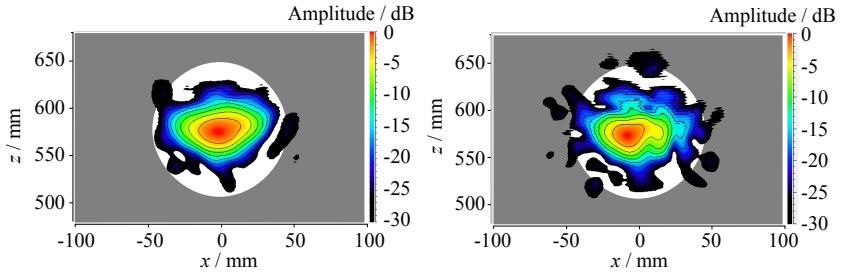

(a) 170 GHz (b) 204 GHz

Fig. 3.5: E-field intensity distribution of the output beam in the window plane at a) 170 GHz and b) 204 GHz. A gyrotron output window with 49 mm radius is indicated in gray.

3.3 Optimization Towards a 170/204 GHz Pre-Prototype Gyrotron

First simulations show that the MIGs available at KIT have to be modified and adapted to the geometry of the new 10.5 T SC magnet. This step is required to locate the emitter at the correct position in the magnetic field profile. Other gyrotron key components, such as the coaxial cavity and the quasi-optical output coupler, could in principle be operated at 204 GHz. However, modification of these components is mandatory. In the following, the MIGs are investigated using the magnetic field profile of the new 10.5 T SC magnet. The resulting electron beam parameters are considered in interaction simulations with the optimized coaxial cavity. A new quasi-optical output coupler is designed for proper operation at 170 GHz and 204 GHz. Finally, a detailed study about frequency step-tunability is performed considering the optimized coaxial cavity and quasi-optical output coupler.

3.3.1 MIG Adaption to New Magnetic Field Profile

Currently, three different MIGs are available at KIT, namely the inverse Magnetron Injection Gun (iMIG) [59], the coaxial Magnetron Injection Gun with non-emissive coating of the emitter edges (cMIG) [92] and a coaxial MIG [93]. The iMIG and cMIG are built in a triode configuration, the coaxial MIG is designed in diode configuration. All 3 MIGs are investigated to assess whether the resulting quality of the electron beam is sufficient for an operation at 170 GHz and 204 GHz in the new magnetic field profile. The simulations are performed with the self-consistent, electrostatic trajectory 3D in-house code-package ARIADNE [94]. The objectives of the simulations are to meet the following design criteria:

(i) the existing cathode shall be reused,

(ii) the distance between electron beam and metallic wall shall be > 2 mm,

(iii) the pitch factor α shall be around 1.2 at 204 GHz and 1.3 at 170 GHz,

(iv) the transverse velocity spread shall be $\delta\beta_t < 3$ %.

Optimization of the Coaxial Magnetron Injection Gun

The performance of the existing coaxial diode MIG is validated at 170 GHz and 204 GHz. The diode MIG benefits from its relatively simple construction and operation, since only the acceleration voltage is applied. The coaxial diode MIG that exists at KIT was originally designed and optimized for the magnetic field profile of the existing SC magnet. Here, only the anode is redesigned to make efficient use of the available components. Therefore, existing components, such as the cathode, are re-used. The modification includes an elongation of the anode shape to adapt the gyrotron to the geometrical configuration of the new 10.5 T SC magnet.

The nominal pitch factors are defined by interaction simulations to be $\alpha_{170\,\mathrm{GHz}} = 1.3$ and $\alpha_{204\,\mathrm{GHz}} = 1.23$ and are thus almost equal [95]. An anode shape optimized for 170 GHz operation reduces the pitch factor to $\alpha_{204\,\mathrm{GHz}} \approx 1.0$ at 204 GHz, which is too low for an efficient operation. A diode MIG is published in [96, 97] that can operate at two different frequencies. The proposed approach is to use co-rotating modes at one frequency and counter-rotating modes at the other. Therefore, a new anode shape is designed that provides the mentioned pitch factors at both frequencies using the counter-rotating $\mathrm{TE}_{-34,19}$ mode at 170 GHz and the co-rotating $\mathrm{TE}_{40,23}$ mode at 204 GHz. The counter-rotating $\mathrm{TE}_{-34,19}$ mode has a beam radius of $r_{\mathrm{beam}} = 10.58$ mm and is larger compared to the co-rotating $\mathrm{TE}_{34,19}$ mode with $r_{\mathrm{beam}} = 10.00$ mm. This means that the effect of lowering the pitch factor by increasing the beam radius using a counter-rotating mode at the lower frequency is beneficial for dual-frequency operation. However, the polarity of the SC magnet has to be reversed in experiments using a co-rotating mode at the one and a counter-rotating mode at the other frequency. The change of the polarity of the magnetic field is required to allow a proper operation of the same quasi-optical output coupler. The use of co-rotating and counter-rotating modes is required for the diode MIG only. The nominal parameters like the beam radius r_{beam} and magnetic field strength B_{cav} are summarized in Tab. 3.2.

Table 3.2: Summary of beam radius r_{beam} and magnetic field strength B_{cav} for the $\text{TE}_{\pm 34,19}$ operating at 170 GHz and $\text{TE}_{40,23}$ mode at 204 GHz.

Mode	$\text{TE}_{34,19}$	$\text{TE}_{-34,19}$	$\text{TE}_{40,23}$
Beam radius (r_{beam}/ mm)	10.00	10.58	9.77
Magnetic field strength (B_{cav}/ T)	6.86	6.86	8.27

Figure 3.6 presents a schematic of the optimized anode profile. In addition, the magnetic field lines and the corresponding electron beam trajectories are illustrated for the $\text{TE}_{40,23}$ mode. The halo shield (i. e. the last part of the anode) is optimized according to the magnetic field lines of the 10.5 T SC magnet. It is used to prevent trapped secondary electrons emitted from the upper rear part of the cathode. The distance between the electron beam and the halo shield is 2.9 mm for the $\text{TE}_{40,23}$ mode, 2.2 mm for the $\text{TE}_{-34,19}$ mode and 1.5 mm for the $\text{TE}_{34,19}$ mode. Therefore, the requirement for the distance between the electron beam and the wall is satisfied for the $\text{TE}_{-34,19}$ and $\text{TE}_{40,23}$ modes.

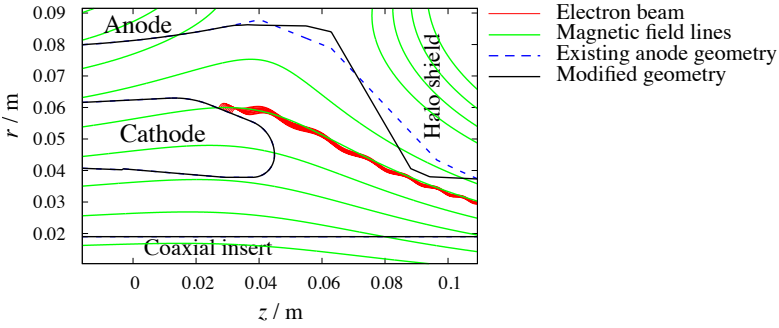

Fig. 3.6: Magnetic field lines (green) of the 10.5 T SC magnet between the MIG (left) and the beam tunnel (right). The electron beam (red) is emitted from the cathode (not modified). A comparison of the shape of the existing (blue dashed) and modified anode (black) is shown.

Two main MIG design criteria are defined in [93]. These are 1) the avoidance of trapped electrons in terms of the emission of secondary electrons from the cathode surface and 2) about potential wells. The avoidance of possible trapped secondary electrons will be discussed first. The insert is mounted to the bottom of the gyrotron in the coaxial-cavity technology. It adds several challenges to the MIG design. Firstly, it implies that the insert passes through the cathode. Secondly, the gyrotron body and the anode are on the same potential, which creates a high electric field in the inner region and outer region of the cathode. That can cause significant difficulties in satisfying the first design criterion. The secondary electrons emitted from the cathode surface are affected by the magnetic compression. They could be guided into the cavity section and can cause issues during operation. This effect can be investigated by using the procedure published in [93] where the whole cathode surface is defined as emitter, as shown in Fig. 3.7. Some of the electrons emitted from the cathode nose are collected by the insert and some of those emitted from the upper rear part are collected by the anode. The effect of possible trapped electrons from the upper part of the cathode can be controlled by the correct choice of the halo shield. The blue dots in Fig. 3.7 indicate the position of emitted electrons that are guided into the cavity and are not collected by a metallic wall (anode or insert). The most critical electrons are those guided into the interaction region. The pitch factor in the cavity is shown as a function of the position of the electron emission (the ones highlighted in blue in Fig. 3.7) in Fig. 3.8 for all three proposed operating modes. Safe operation without electron trapping by the magnetic mirror can be expected, if the maximum pitch factor of all the different electrons are smaller than $\alpha_{\max} \leq 3$ [93].

The second MIG design criterion is the prevention of potential wells. A potential well is formed, if the electrical equipotential lines cross the magnetic field lines twice. Then, the electrons are trapped in such an area. The design presented in this work has two potential wells. Neither the cathode nor the anode shape can be modified accordingly. However, this is not critical because of the planned operation with short pulses for the proof-of-principal.

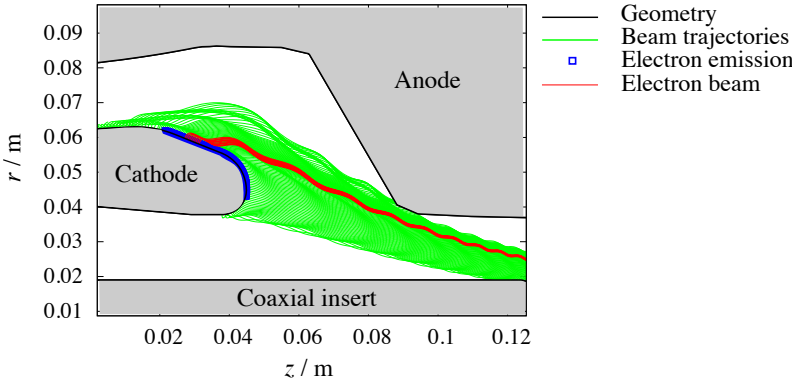

Fig. 3.7: Trajectories of electrons emitted from the cathode surface at 204 GHz. The green lines present the electron trajectories. The blue dots mark the position of emitted electrons reaching the cavity.

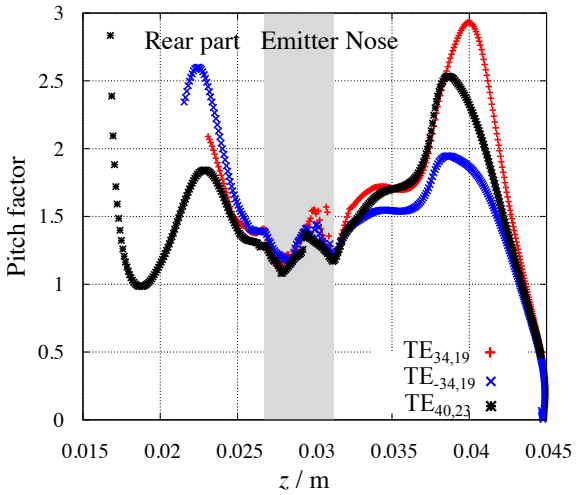

Fig. 3.8: Pitch factor α at the cavity versus the axial position of the emitting point on the surface of the cathode. The surface area marked in blue in Fig. 3.7 is selected and the main operating modes at 170 GHz and 204 GHz are considered.

The revised coaxial diode MIG is studied for the nominal operating parameters. The pitch factor α and the transverse velocity spread $\delta\beta_t$ of the $TE_{-34,19}$ mode and the $TE_{40,23}$ mode are plotted in a wide range of magnetic compression and magnetic field angles at the emitter in Fig. 3.9 and Fig. 3.10, respectively. The magnetic field angle and the magnetic compression can be varied independently in experiments. As shown in the graphs, the transverse velocity spread is not significantly affected by varying the beam radius. However, the pitch factor increases with decreasing beam radius in terms of a larger magnetic compression. A summary of the nominal operation parameters is given in Tab. 3.3.

Table 3.3: Summary of the pitch factor α and the transverse velocity spread $\delta\beta_t$ at 170 GHz and 204 GHz using the coaxial diode MIG for a magnetic field angle of $-0.5°$.

Mode	$TE_{-34,19}$	$TE_{40,23}$
Beam energy (U_{beam} / keV)	92.8	89.9
Beam current (I_{beam} / A)	75	68
Pitch factor (α)	1.30	1.23
Transverse velocity spread ($\delta\beta_t$ / %)	2.28	2.41

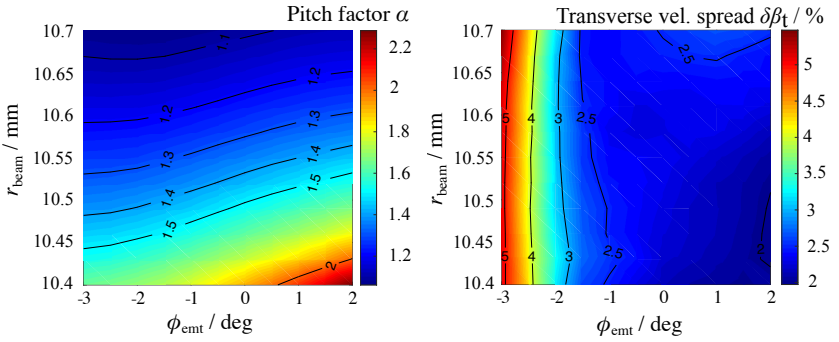

(a) Pitch factor α. (b) Transverse velocity spread $\delta\beta_t$.

Fig. 3.9: a) Pitch factor α and b) transverse velocity spread $\delta\beta_t$ of the $TE_{-34,19}$ mode at 170 GHz in a wide range of magnetic compression and magnetic field angles at the emitter ϕ_{emt}.

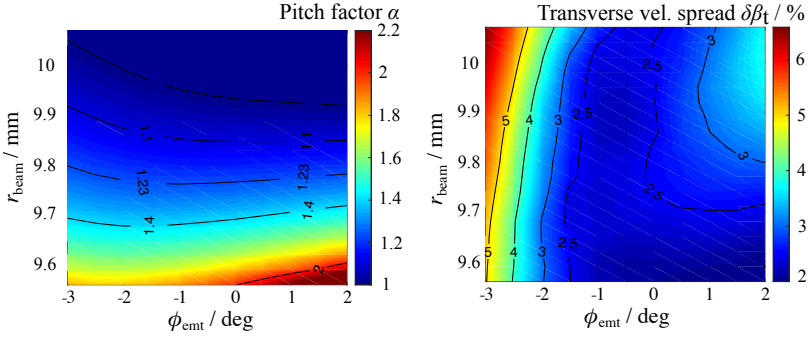

(a) Pitch factor α. (b) Transverse velocity spread $\delta\beta_t$.

Fig. 3.10: a) Pitch factor α and b) transverse velocity spread $\delta\beta_t$ of the $TE_{40,23}$ mode at 204 GHz versus the magnetic compression and magnetic field angles at the emitter ϕ_{emt}.

Figure 3.11 shows a tolerance analysis considering anode displacement in the radial and axial direction. Axial displacement does not significantly affect the pitch factor and the velocity spread due to the flat anode shape around the emitter area. The tolerance for positive axial displacements is limited to 1 mm by secondary electrons. The geometry of the anode itself limits the tolerance to negative displacements to −1.4 mm to keep the distance of the electron beam to the anode above 2 mm. The influence of the radial displacement is more significant. A radial shift of up to 0.5 mm is accepted. For larger radial shift, the pitch factor is too high and mode instability can occur. Again, secondary electrons limit the tolerance to positive radial misalignment to 0.3 mm and the negative misalignment is limited by the geometry to −0.5 mm.

The anode with the optimum shape is fabricated. The coaxial diode MIG will be used for the first proof-of-principal experiments of the 170/204 GHz coaxial-cavity pre-prototype. A measurement with a 3D measurement arm shows manufacturing tolerances of $< 60\ \mu$m, which is below the specified tolerances defined in the simulations.

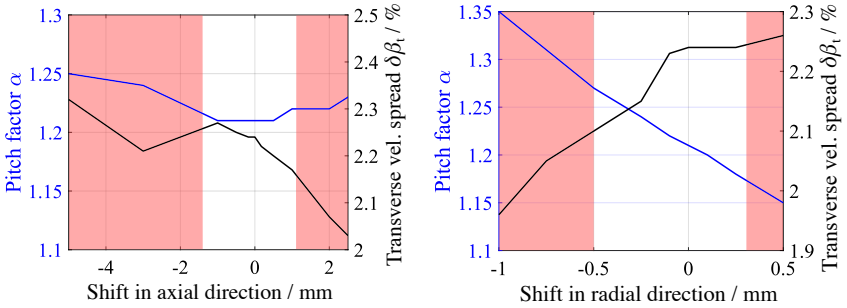

(a) Shift in axial direction.

(b) Shift in radial direction.

Fig. 3.11: Analysis of the tolerances for a shift in a) axial and b) radial direction at 204 GHz.

The diode MIG will be replaced by a triode MIG after the first proof-of-principle experiments. A MIG in triode configuration is intended for a future EU DEMO-relevant design as it provides more flexibility in setting the electron beam parameters. The additional modulation anode in a triode configuration can eliminate the issue of maintaining the pitch factor at nominal operating parameters at different frequencies. This allows operating modes that rotate in the same direction to be used for multi-frequency operation. Therefore, the polarity of the magnetic field does not have to be reversed. Two triode MIGs are discussed below.

Magnetron Injection Gun with Coated Non-Emissive Layer (cMIG)

The design of the triode-type cMIG has been published in [92]. The schematic and the emitted electron beam are presented in Fig. 3.12. It assumes the magnetic field profile of the new 10.5 T SC magnet. The applied nominal voltages are a cathode voltage of $V_c = -55$ kV, insert and body voltage of $V_b = V_i = 35$ kV. The potential of the modulation anode is set to ground. The existing cMIG meets all defined design requirements according to the simulations. But, the geometry still needs to be adapted to fit into the new 10.5 T SC magnet.

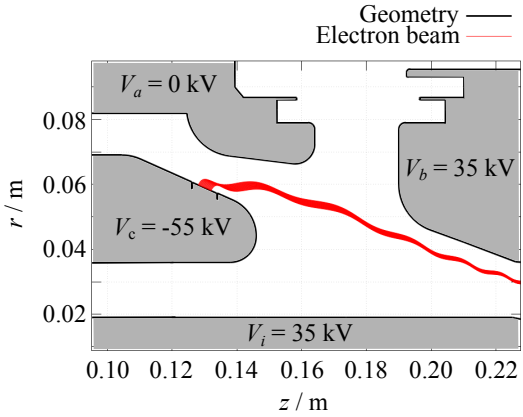

Fig. 3.12: Schematic of the cMIG.

Figure 3.13 presents the pitch factor during start-up with increasing acceleration voltage. The kinetic beam energy is used at the x-axis for better compatibility. The resulting pitch factor is $\alpha = 1.3/1.25$ and the transverse velocity spread is $\delta\beta_t = 2.2/2.5$ % at a beam energy of 90.0/87.5 keV, a beam current of 75/68 A and a maximum magnetic field strength of 6.86/8.27 T for the operation at 170/204 GHz, respectively. The results are summarized in Tab. 3.4. In general, the performance of the cMIG is slightly better than that of the diode MIG.

Table 3.4: Summary of the pitch factor α and the transverse velocity spread $\delta\beta_t$ at 170 GHz and 204 GHz using the cMIG.

Mode	$TE_{-34,19}$	$TE_{40,23}$
Beam energy (U_{beam} / keV)	90.0	87.5
Beam current (I_{beam} / A)	75	68
Pitch factor (α)	1.30	1.25
Transverse velocity spread ($\delta\beta_t$ / %)	2.20	2.51

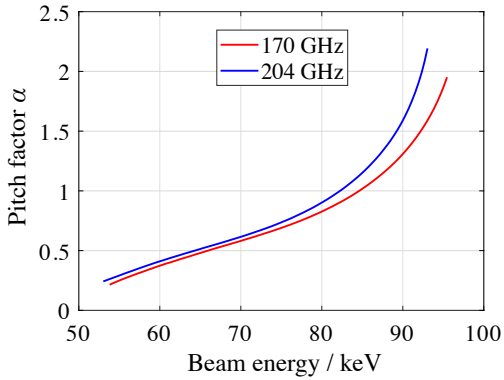

Fig. 3.13: Pitch factor for the start-up of the cMIG.

Inverse Magnetron Injection Gun (iMIG)

The emitter of the iMIG is placed at the outer wall of the MIG. Figure 3.14 presents a schematic of an iMIG [59]. The emitter ring can be much larger without increasing the overall diameter of the MIG design. A larger emitter radius is able to handle higher beam currents, while the maximum current density still does not exceed ≈ 4 A/cm^2. Therefore, a longer lifetime can be expected at similar beam currents. In addition, a more compact MIG can be constructed because the modulation anode is placed inside resulting in a decreased borehole of the SC magnet. This leads to a better field homogeneity and reduced magnet cost [98]. Another advantage is the improved cooling, since the heated emitter and the heated surrounding can be cooled by the outer wall. An iMIG was developed in 2015 at KIT for the operation in the existing SC magnet [59]. This iMIG has an average emitter radius of 62 mm and is 3 mm larger than in the other coaxial MIGs at KIT.

The iMIG is a favored configuration for future EU DEMO-relevant fusion gyrotrons. Therefore, the iMIG is adapted to the magnetic field profile of the new 10.5 T SC magnet. The beamline of the existing and new SC magnet is depicted in Fig. 3.14. The distance of the electron beam trajectories to the

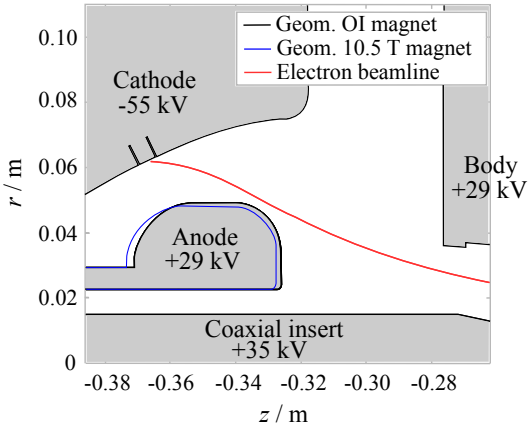

Fig. 3.14: Schematic view of the different geometries of the iMIG of the existing design and a modification according to the magnetic field profile of a 10.5 T SC magnet.

modulation anode is below 2 mm using the new magnetic field profile. A modification of the modulation anode is performed.

The construction of the modulation anode consists of two parts. One is the modulation anode itself, which is made of molybdenum. The other is a holder made of copper. The new design takes into account that the two parts of the modulation anode can be reworked. The copper rear part has to be shortened to bring the front part closer to the emitter part. At the other part, the rounding at the rear of the modulation anode has to be increased to ensure a small velocity spread. In addition, the radius is decreased to provide a distance of in minimum 2 mm to the electron beam. The resulting pitch factor and the transverse velocity spread at 170 GHz and 204 GHz are presented in Fig. 3.15 and Fig. 3.16. The graphs show the effect of a large range of magnetic compression and the angle of the electron beam at the emitter surface onto the pitch factor and the transversal velocity spread. The results are summarized in Tab. 3.5 for the nominal operation point marked with a red circle. There are combinations with lower velocity spreads providing almost similar pitch factors. However,

simulations on secondary electrons show that these combinations can offer trapped secondary electrons.

Table 3.5: Summary of the simulation results of the pitch factor α and the transverse velocity spread $\delta\beta_t$ at the nominal operation point at 170 GHz and 204 GHz using the iMIG.

Mode	$TE_{34,19}$	$TE_{40,23}$
Beam energy (U_{beam} / keV)	91.0	90.0
Beam current (I_{beam} / A)	75	68
Magnetic field angle (ϕ_{emt} / deg)	-4	0
Beam radius (r_{beam} / mm)	10.00	9.85
Pitch factor (α)	1.30	1.28
Transverse velocity spread ($\delta\beta_t$ / %)	2.14	2.10

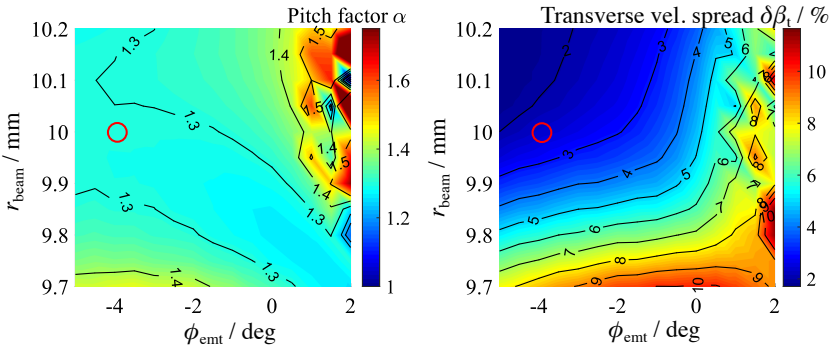

(a) Pitch factor α.

(b) Transverse velocity spread $\delta\beta_t$.

Fig. 3.15: a) Pitch factor α and b) transverse velocity spread $\delta\beta_t$ of the $TE_{34,19}$ mode at 170 GHz in a wide range of magnetic compression and magnetic field angles at the emitter ϕ_{emt} using the iMIG. The nominal operation points are marked with a red circle.

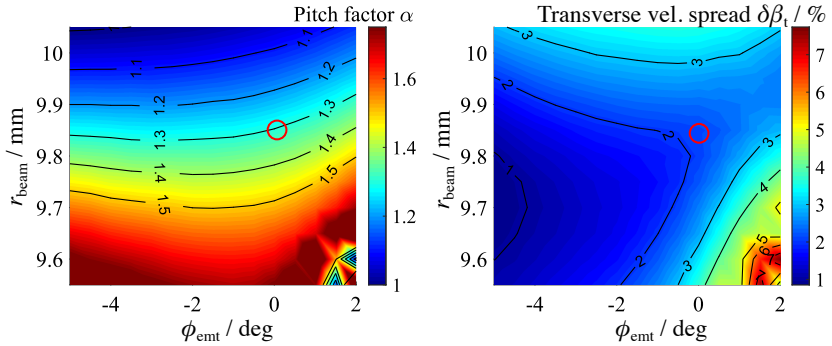

(a) Pitch factor α.

(b) Transverse velocity spread $\delta\beta_t$.

Fig. 3.16: a) Pitch factor α and b) transverse velocity spread $\delta\beta_t$ of the $TE_{40,23}$ mode at 204 GHz over a wide range of magnetic compression and magnetic field angles at the emitter ϕ_{emt} using the iMIG. The nominal operation points are marked with a red circle.

3.3.2 Design of a New Dual-Frequency Coaxial Cavity

An optimization of the coaxial cavity is required to achieve > 2 MW output power at both frequencies. The optimization considers following requirements:

(i) The operating mode at 170 GHz is fixed to the $TE_{34,19}$ mode. It allows to keep the available MIGs.

(ii) The cavity radius is fixed to $r_{cav} = 29.55$ mm. Thus, the $TE_{34,19}$ mode still fits to the window resonance.

(iii) The total length of the cavity is kept identical to the original cavity ($L_{tot} = 120$ mm). It allows to fit the cavity into the existing tube.

(iv) The constraint of the wall loading is carefully kept to be below 2 kW/cm^2 and the insert loading is kept to be below 0.2 kW/cm^2 [99, 100].

(v) The maximum output power and interaction efficiency at 170 GHz and 204 GHz shall be achieved.

Figure 3.17 presents a schematic of the coaxial cavity. It consists of a straight midsection L_{mid}, a down-taper and an up-taper forming an open resonator. The different sections are connected by parabolic smoothing to reduce unwanted mode conversion at the transitions [101].

The existing 170 GHz single-frequency design achieves a maximum output power of up to 1.7 MW at 204 GHz. A limiting factor is the wall loading constraint of 2 kW/cm^2 that limits the applied acceleration voltage and beam current. This effect results from the dependency of the wall loading and the operating frequency given by $\rho_\Omega \sim f^{2.5}$. This effect becomes worse at operating frequencies much higher than 200 GHz. A reduction of the wall loading can be achieved by increasing the cavity radius or by choosing a higher volume mode with higher eigenvalues. In both cases, the operating frequencies would not longer fit to the resonances of the gyrotron output window. In addition, the mode spectrum becomes more dense. An alternative method is to consider the proportionality between the diffractive quality factor and the wall loading, as given in Eq. 2.31. The approach is to tune the diffractive quality factor by the geometrical shape of the coaxial cavity to reduce the wall loading. With reduced wall loading, the nominal operating parameters can be increased. Thus, the interaction efficiency and the output

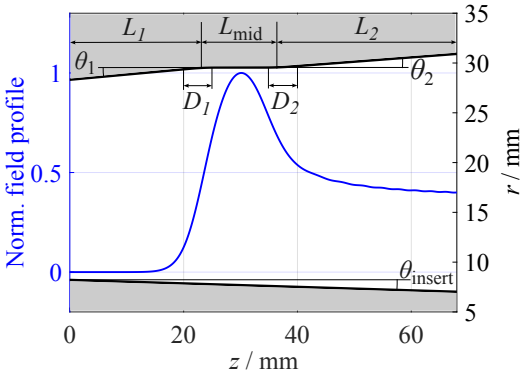

Fig. 3.17: Geometry of the coaxial cavity with the normalized transverse electric field profile.

power can be increased. In addition, a trade-off must be considered in the cavity design for the operation at 170 GHz and 204 GHz.

A systematic hollow-cavity design approach is published in [31]. This approach has been adapted for cavities with a coaxial insert. The proposed design steps are:

- Step 1: Calculate the midsection radius and electron beam radii using equations from Section 2.2.2 for the selected operating modes.
- Step 2: Estimate the initial cavity geometry with the parameters L_1, L_{mid}, L_2, θ_1, θ_2, D_1, D_2, r_{insert}, θ_{insert} based on existing designs.
- Step 3: Perform the initial gyrotron interaction simulations at different center frequencies to identify an optimum midsection length. The operating parameters like the beam voltage, beam current, magnetic field, etc. have to optimized accordingly.
- Step 4: Optimize the insert radius r_{insert}, the insert angle θ_{insert}, the number of corrugations and the corrugation depth for all center frequencies.
- Step 5: Optimize the input θ_1 and output angle θ_2 to maximize power and efficiency according to the defined length in step 3.
- Step 6: Optimize the down-taper length L_1 and the smoothing D_1 to maximize the reflection of the operating mode while minimizing the mode conversion.
- Step 7: Optimize up-taper length L_2 and smoothing D_2 to have maximum power transmission to the quasi-optical output coupler with reduced mode conversion. In addition, a non-linear up-taper has to be designed to adapt the wall radius to that of the launcher.

To step 1: The cavity radius at the midsection is fixed to $r_{\mathrm{cav}} = 29.55$ mm as given in the requirements. The electron beam radii of the two operating modes are calculated with Eq. 2.25 to be $r_{\mathrm{beam}} = 10.00$ mm for the $\mathrm{TE}_{34,19}$ mode operating at 170 GHz and $r_{\mathrm{beam}} = 9.77$ mm for the $\mathrm{TE}_{40,23}$ mode operating at 204 GHz.

Table 3.6: Initial geometrical parameters for the coaxial-cavity design.

Length L_1 / mm	22
Input angle θ_1 °	3
Smoothing length D_1 / mm	2
Length L_{mid} / mm	16
Radius r_{cav} / mm	29.55
Length L_2 / mm	30
Output angle θ_2 / °	2.5
Smoothing length D_2 / mm	2
Length L_{insert} / mm	68
Insert radius r_{insert} / mm	7.9
Insert angle θ_{insert} / °	-1
Number of corrugations	76
Corrugation depth d / mm	0.44

To step 2: The existing coaxial-cavity is chosen as the basis for optimization. A summary of the physical parameters is given in Tab. 3.6.

To step 3: A study on the variation of the interaction length is presented in Fig. 3.18 for the $\mathrm{TE}_{34,19}$ mode at 170 GHz and the $\mathrm{TE}_{40,23}$ mode at 204 GHz. The output power, interaction efficiency and diffractive quality factor are depicted along the variation of the midsection length. The study starts from the initial midsection length of $L_{\mathrm{mid}} = 16$ mm down to $L_{\mathrm{mid}} = 11$ mm. This study has been performed for single- and multi-mode operation considering the main competing modes listed in Tab. 6.4. The simulations do not consider parameter spreads. The operating parameters are selected individually at each step to fulfill the wall-loading limitation of 2 kW/cm^2 and have been optimized for the multi-mode simulations. This explains the better performance compared to single-mode simulations. The performance is increased by reducing the midsection length and thus the diffractive quality factor. However, at a midsection length below 13 mm the performance at 170 GHz is decreasing strongly, where the diffractive quality factor is close to $Q_{\mathrm{diff}} \approx 1000$. At 204 GHz the mode competition increases strongly with a

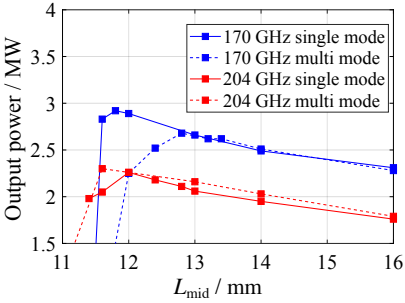

(a) Output power.

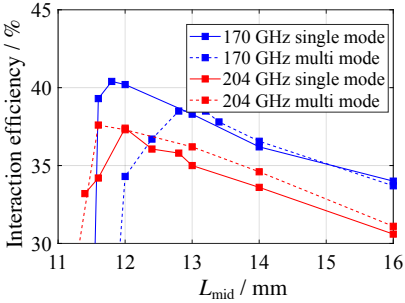

(b) Interaction efficiency.

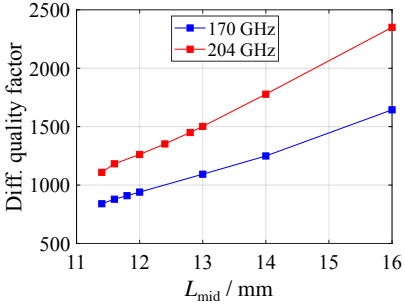

(c) Diffractive quality factor.

Fig. 3.18: Output power, interaction efficiency and diffractive quality factor for different mid-section lengths L_{mid} from 11 mm to 16 mm. The operating parameters are selected individually at each step to fulfill the wall-loading limitation of 2 kW/cm^2 and to achieve maximum output power.

mid-section length below 13 mm. The nominal midsection length is defined for the further study to be 13.6 mm including some safety margin.

To step 4: The corrugation depth of the existing insert is $d = 0.44$ mm. This corresponds to $\lambda_0/4$ at 170 GHz. A detailed analysis about longitudinal insert corrugations and insert misalignment is published in [88]. Simulations show that the influence of the existing corrugations depth is not critical for

an operation at 204 GHz. There is not a significant improvement using a corrugation depth of $d = 0.36$ mm corresponding to $\lambda_0/4$ at 204 GHz. The minor improvement in performance does not justify a new insert for the first proof-of-principal experiments at 170 GHz and 204 GHz.

To step 5: The input angle θ_1 and output angle θ_2 of the down-taper and up-taper are investigated considering a midsection length of $L_{\text{mid}} = 13.6$ mm. Figure 3.19 presents the effect of the input and output angle onto the output power, efficiency and ohmic wall loading. Simulations have been performed using the similar operation parameters. The values in the red box indicates angles with high performance while keeping the ohmic wall loading around 2 kW/cm^2. Further simulations with varied operation parameters have been performed using the angles in the highlighted area. Highest performance is achieved for the angles at $\theta_1 = 2.5°$ and $\theta_2 = 2.5°$. About 0.5 % points in the interaction efficiency and about 50 kW are gained by changing the down-taper angle from the initial 3° to 2.5°. Considering velocity, guiding center and kinetic energy spreads, the interaction is much more robust using a down-taper angle of $\theta_1 = 2.5°$ instead of $\theta_1 = 3.0°$. An input angle in this range can lead to backward waves, which can reduce the performance.

To step 6 and 7: The smoothing length of the down-taper D_1 and up-taper D_2 has to be optimized and selected to be $D_1 = D_2 = 2.2$ mm to reduce any conversion into competing modes. They are 200 µm longer than in the design of the 170 GHz single-frequency coaxial cavity. The length of the down-taper L_1 and up-taper L_2 are fixed according to the design requirements. The diffractive quality factor Q_{diff} of the optimized coaxial-cavity design is given by 1094 and 1647 at 170 GHz and 204 GHz, respectively. An output power of 2.15 MW at an interaction efficiency of 35.8 % at 204 GHz is achieved in single-mode simulations. The wall loading is kept to 2 kW/cm^2 and the maximum insert loading is 0.05 kW/cm^2. The nominal operation parameters are a beam energy of $U_{\text{beam}} = 87.2$ keV, beam current of $I_{\text{beam}} = 68$ A, magnetic field strength at cavity midsection of $B_{\text{cav}} = 8.23$ T and a pitch factor of $\alpha = 1.23$.

In addition, a non-linear up-taper is required. It connects the end of the up-taper of the cavity smoothly to the launcher [102]. The wall radius is increased up to 32 mm of the launcher. The allowable mode conversion is

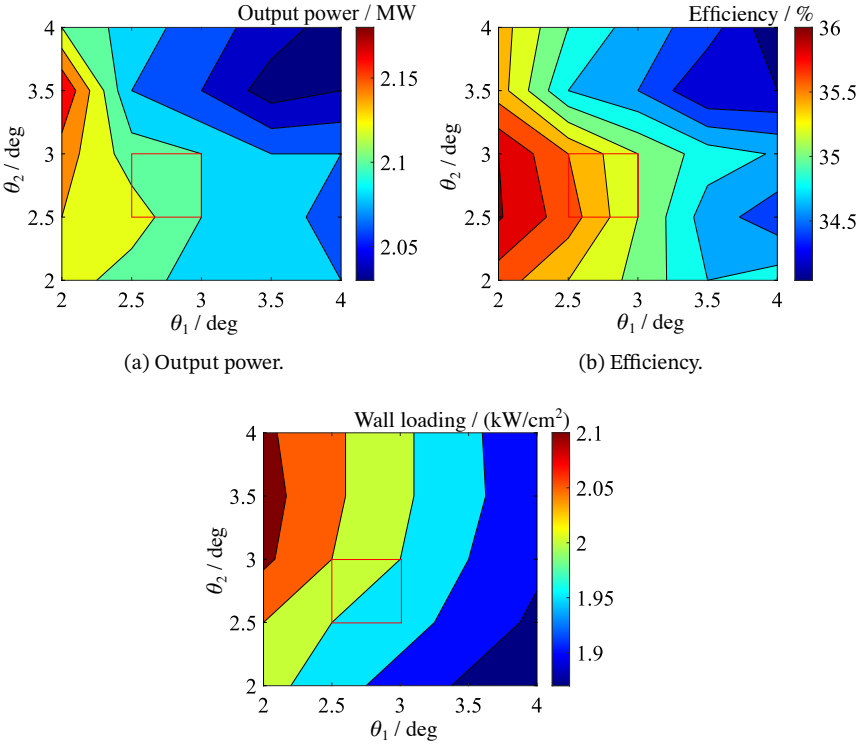

(a) Output power.

(b) Efficiency.

(c) Wall loading.

Fig. 3.19: Influence of the input θ_1 and output angle θ_2 of the down-taper and up-taper for the a) output power, b) efficiency and c) resistive wall loading considering the $TE_{40,23}$ mode at 204 GHz. The area of the red box indicate the best choice regarding the trade-off between high performance and keeping the ohmic wall loading in the limitation.

limited by 0.1 %. The non-linear up-taper of the existing 170 GHz single-frequency design shows a mode conversion of 0.6 % at 204 GHz from the $TE_{40,23}$ main mode to the lower order $TE_{40,22}$ mode. A modification of the geometry reduces the mode conversion to 0.05 % at 204 GHz and keeps it below 0.1 % at 170 GHz. The geometry of the optimized non-linear up-taper is presented in Fig. 3.20.

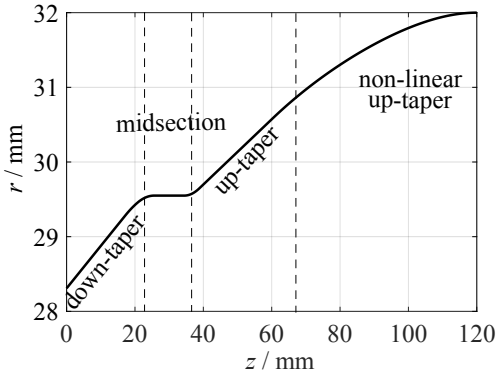

Fig. 3.20: Geometry of the modification of the non-linear up-taper to reduce mode conversion.

At last, the final physical parameters of the geometry are presented in Tab. 3.7.

Multi-Mode Time-Dependent Simulations

Multi-mode simulations are performed with the optimized coaxial cavity and ideal electron beam parameters, i.e. velocity, guiding center and kinetic energy spreads are not included. The start-up scenarios of the given modes are presented in Fig. 3.21a and Fig. 3.21b. In total 63 modes at 170 GHz and 74 modes at 204 GHz are considered. Modes are considered in interaction simulation if their relative coupling is above 0.5 and their operating frequency is in the range between -5 % to $+10$ % of the center mode frequency. The most dangerous competitors appear in this range. The nominal operation points are indicated with a red circle. The points are defined by the maximum allowed wall loading limit of 2 kW/cm^2. The wall loading are plotted in Fig. 3.21c and Fig. 3.21d, accordingly. The nominal operation points are characterized by a beam energy of 91.7 keV and 89.5 keV, a beam current of 77 A and 70 A and a maximum magnetic field strength of 6.88 T and 8.27 T for the operation at 170 GHz and 204 GHz, respectively. The optimized coaxial cavity provides an output power of 2.61 MW and an inter-

Table 3.7: Geometrical parameters for the coaxial-cavity design used for the simulations of 170/204 GHz multi-frequency operation towards a first proof-of-principal experiment.

Down-taper	
Length L_1 / mm	23.2
Input angle θ_1 / °	2.5
Smoothing length D_1 / mm	2.2
Midsection	
Length L_{mid} / mm	13.6
Radius r_{cav} / mm	29.55
Up-taper	
Length L_2 / mm	31.2
Output angle θ_1 / °	2.5
Smoothing length D_1 / mm	2.2
Non-linear up-taper to launcher input	
Length L_{upt} / mm	52.0
Insert	
Length L_{insert} / mm	68
Insert radius r_{insert} / mm	7.8
Insert angle θ_{insert} / °	-1
Number of corrugations	76
Corrugation depth d / mm	0.44

action efficiency of 38.4 % at 170 GHz and 2.22 MW and 37.0 % at 204 GHz. The results demonstrate that the optimized coaxial cavity is able to generate > 2 MW output power at both frequencies using an ideal electron beam.

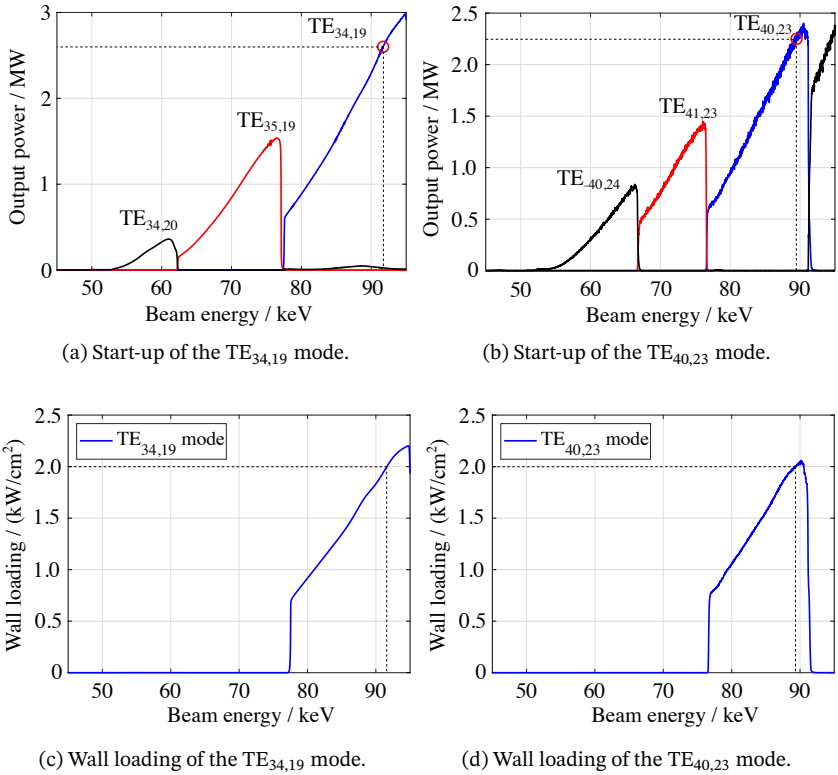

(a) Start-up of the $TE_{34,19}$ mode.

(b) Start-up of the $TE_{40,23}$ mode.

(c) Wall loading of the $TE_{34,19}$ mode.

(d) Wall loading of the $TE_{40,23}$ mode.

Fig. 3.21: Oscillation start-up for the optimized coaxial cavity considering an ideal electron beam for the a) $TE_{34,19}$ mode at 170 GHz and b) $TE_{40,23}$ mode at 204 GHz. The operation points are indicated with the red circles. They are defined by the wall loading sown in c) and d).

In the following steps, an analysis of the variation of the electron beam radius and the impact of different qualities of electron beams are studied. Finally, the electron beam parameters from the previous MIG simulations are included into the interaction simulations.

Analysis of Parameter Tolerances

Firstly, a variation of the electron beam radius is investigated. The electron beam radius of 10.00 mm for the $TE_{34,19}$ mode operating at 170 GHz was chosen in previous works [13]. Therefore, this study is focused on the $TE_{40,23}$ mode. The highest theoretical coupling between the electron beam and the $TE_{40,23}$ mode is according to Fig. 3.22 at an electron beam radius of $r_{\mathrm{beam}} = 9.77$ mm. The graph has several maxima corresponding to the radial mode index $p = 23$. However, the maximum interaction efficiency can only be achieved at the highest coupling.

The mode spectra of the main competing modes at an electron beam radius of $r_{\mathrm{beam}} = 9.70/9.77/9.85$ and 10.00 mm are investigated. The results are presented in Fig. 3.23. A frequency range of $-2\,\%$ and $+3\,\%$ around the center frequency of 204.15 GHz is selected. The coupling to the next counter-rotating modes, namely the $TE_{-(m-3),n+1}$ ($TE_{-37,24}$) and $TE_{-(m-2),n+1}$ ($TE_{-38,24}$), decrease with increasing electron beam radius. This behavior is a favorable condition for a proper excitation of the main operating mode. In addition, the coupling to the azimuthally neighboring co-rotating modes with an azimuthal mode index $m > 40$ increases with increasing electron beam

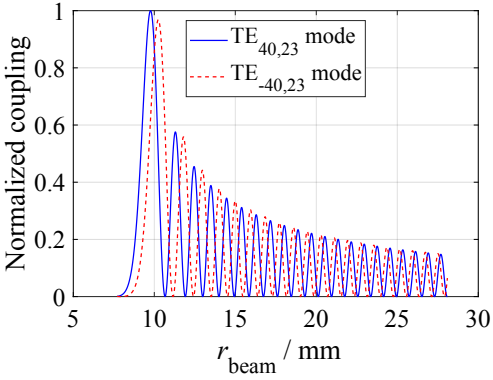

Fig. 3.22: Normalized coupling of the electron beam to the $TE_{40,23}$ mode and $TE_{-40,23}$ mode along the radius.

radius. The coupling of the co-rotating $TE_{40,23}$ mode and counter-rotating $TE_{-40,23}$ mode is almost identical at an electron beam radius of 10.00 mm, according to Fig. 3.22 and Fig. 3.23d. Therefore, an electron beam radius of $r_{beam} = 10.00$ mm sets the upper limit for the beam radii variation. The lower limit is set to $r_{beam} = 9.70$ mm. It is defined by the increase of the insert loading in terms of the closer distance of the electron beam to the insert.

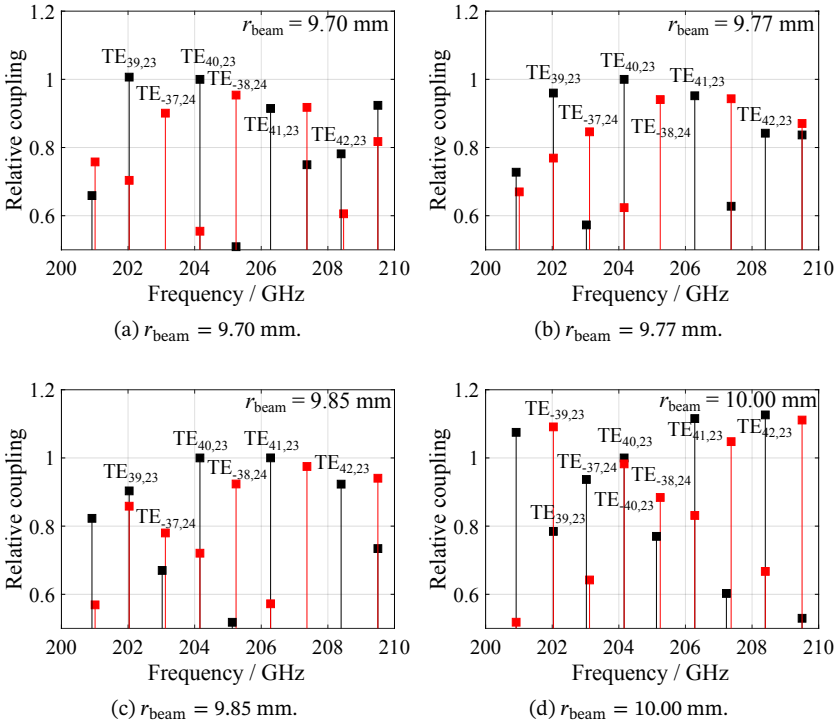

(a) $r_{beam} = 9.70$ mm. (b) $r_{beam} = 9.77$ mm.

(c) $r_{beam} = 9.85$ mm. (d) $r_{beam} = 10.00$ mm.

Fig. 3.23: Mode spectra with varied electron beam radius r_{beam}. The main competitors with a relative coupling higher than 0.5 are considered. The beam radius is varied from 9.70 mm to 10.00 mm. The black bars indicate co-rotating modes and the red bars counter-rotating modes.

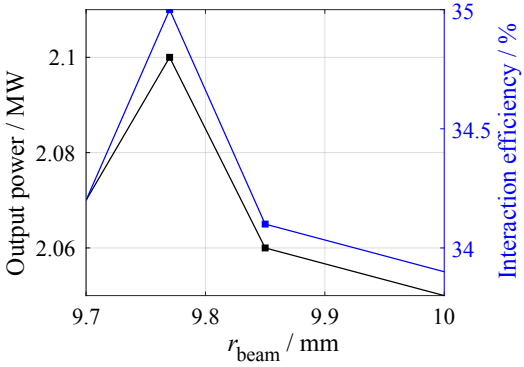

Fig. 3.24: Variation of the electron beam radius at the cavity midsection and its influence in respect to the output power and the interaction efficiency considering the $TE_{40,23}$ mode operating at 204 GHz.

Figure 3.24 shows the output power and the interaction efficiency of the $TE_{40,23}$ mode using the given electron beam radii. Maximum performance is achieved at $r_{beam} = 9.77$ mm because of the maximum coupling according to Eq. (2.24). A deviation from the maximum leads to a reduced performance. However, a slightly increased electron beam radius improves the mode stability. An electron beam radius of $r_{beam} = 9.85$ mm is selected.

A second investigation focuses on the effect of different electron beam parameters on the interaction. Different values for the guiding center, the pitch factor and the kinetic energy spreads are considered in the interaction simulations. A summary of the simulation results is given in Tab. 3.8. The main operating parameters are fixed during the study to $U_{beam} = 91.8$ keV, $I_{beam} = 75$ A and $B_{cav} = 6.88$ T at 170 GHz and $U_{beam} = 89.5$ keV, $I_{beam} = 68$ A and $B_{cav} = 8.27$ T at 204 GHz. The velocity, guiding center radius and energy spread are studied separately. During the variation of a certain spread, the other spreads are fixed to be $\Delta E_{kin} = 0.01$ %, $\Delta\alpha = 6$ % and $\Delta r_{gc} = 1.96$ %. In conclusion, the $TE_{34,19}$ mode and the $TE_{40,23}$ mode are excited even in the worst-case scenario. However, the velocity spread should be < 20 % to guarantee an output power of 2 MW at 204 GHz.

Table 3.8: Summary of the effect of varying the pitch factor $\Delta\alpha$, guiding center radius Δr_{gc} and energy spread ΔE_{kin} on the output power and the interaction efficiency. For comparison the beam energy has been fixed to $U_{\mathrm{beam}} = 91.8$ keV at 170 GHz and 89.5 keV at 204 GHz. The reference values are $\Delta\alpha = 6$ %, $\Delta r_{gc} = 1.96$ % and $\Delta r_{gc} = 0.1$ %.

Mode	$TE_{34,19}$		$TE_{40,23}$	
$\Delta\alpha$ / %	P_{out} / MW	Eff. / %	P_{out} / MW	Eff. / %
3	2.62	37.2	2.15	35.6
6	2.58	36.4	2.12	35.4
10	2.51	35.6	2.06	34.6
15	2.46	34.5	2.03	33.9
20	2.34	33.4	1.86	30.5
Δr_{gc} / %				
1.50	2.62	37.0	2.13	35.5
1.96	2.58	36.4	2.12	35.4
2.00	2.57	36.3	2.13	35.5
4	2.52	35.5	1.85	33.0
ΔE_{kin} / %				
0.05	2.62	36.8	2.14	35.6
0.1	2.58	36.4	2.12	35.4
0.2	2.50	35.5	2.02	34.0

Start-Up Scenario Considering the Coaxial Diode MIG

Finally, the design of the coaxial cavity is verified including the spreads and the pitch factor from the electron beam of the MIG simulations. The three available MIGs are considered in this study.

Firstly, the coaxial-diode MIG will be installed to the pre-prototype for the first proof-of-principle experiments. Figure 3.25a presents the start-up of the counter-rotating $TE_{-34,19}$ mode at 170.01 GHz. The corresponding electron beam parameters from Section 3.3.1 are used in order to be most realistic.

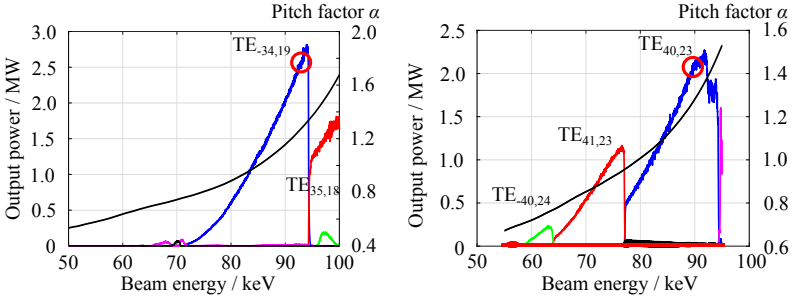

(a) $TE_{-34,19}$ mode at 170.01 GHz.

(b) $TE_{40,23}$ mode at 204.1 GHz.

Fig. 3.25: Output power of the start-up scenario using the electron beam parameters from Section 3.3.1 of the coaxial diode MIG for a) $TE_{-34,19}$ mode at 170 GHz and b) $TE_{40,23}$ mode at 204 GHz. The black curve indicates the pitch factor versus the beam energy.

The simulation includes 63 modes and considers 2565 electrons. There is no need to distinguish between electrons in cross section or volume, given that a beamlet approach is considered. The spread of the pitch factor is between $\Delta\alpha = 5.7\,\%$ rms and $6.2\,\%$ rms during the start-up. The maximum magnetic field is $B_{\mathrm{cav}} = 6.88$ T at the center of the cavity midsection. The nominal mode is the first excited mode. All other modes cannot get dominant because of the very low pitch factor. A wall loading of 2 kW/cm^2 is reached at a beam energy of $U_{\mathrm{beam}} = 92.8$ keV and a beam current of $I_{\mathrm{beam}} = 72$ A. The resulting pitch factor is $\alpha = 1.27$ and the insert loading of 0.17 kW/cm^2 is below the insert loading constraint. An output power of $P_{\mathrm{out}} = 2.54$ MW with an interaction efficiency of $\eta = 38.8\,\%$ is achieved.

The start-up scenario of the $TE_{40,23}$ mode operating at 204.17 GHz and the corresponding pitch factor is depicted in Fig. 3.25b. The simulation considers 74 modes and 2079 electrons. The spread of the pitch factor is between $\Delta\alpha = 5.4\,\%$ rms and $6.5\,\%$ rms during the start-up. The maximum magnetic field is 8.27 T. The pitch factor at 204 GHz is higher at lower beam energy compared to the 170 GHz case. The nominal operating parameters are for a beam energy of $U_{\mathrm{beam}} = 89.9$ keV and a beam current of $I_{\mathrm{beam}} = 68$ A. The resulting pitch factor is $\alpha = 1.25$ and the insert loading of 0.05 kW/cm^2 is far below

the maximum tolerable constraint. An output power of $P_{\text{out}} = 2.08$ MW with an interaction efficiency of $\eta = 34.3$ % is achieved. The output power is increased by ≈ 22 % through optimization of the coaxial cavity.

Start-Up Scenario Considering the cMIG

In the following, the interaction simulations are presented using the electron beam parameters of the cMIG. In contrast to the coaxial diode MIG, the co-rotating $TE_{34,19}$ mode is used as operating mode at 170 GHz. The start-up up is given in Fig. 3.26. The nominal operating point is given by a beam energy of $U_{\text{beam}} = 90.1$ keV, a beam current of $I_{\text{beam}} = 77$ A and a magnetic field strength of $B_{\text{cav}} = 6.86$ T. The resulting pitch factor is $\alpha = 1.3$. The theoretical output power is $P_{\text{out}} = 2.63$ MW with an interaction efficiency of $\eta = 37.8$ %.

The nominal operation point of the $TE_{40,23}$ mode is identified at a beam energy of $U_{\text{beam}} = 87.4$ keV, a beam current of $I_{\text{beam}} = 68$ A and a magnetic field strength of $B_{\text{cav}} = 8.23$ T. The resulting pitch factor is $\alpha = 1.23$. The output power is $P_{\text{out}} = 2.05$ MW with an interaction efficiency of $\eta = 34.5$ %. In summary, the performance using the cMIG and the diode MIG are quite similar according to similar electron beam parameters.

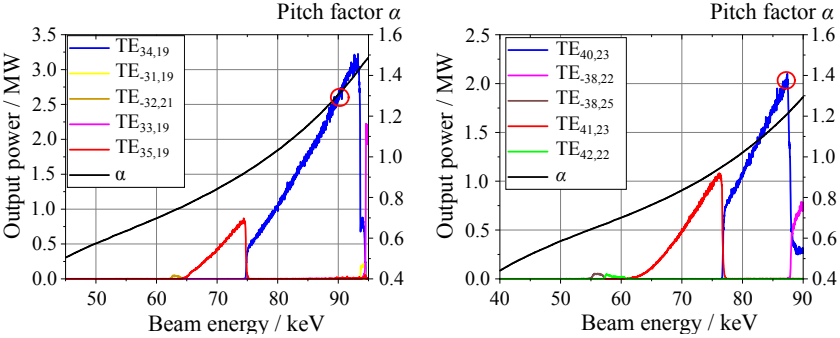

(a) $TE_{34,19}$ mode at 170.01 GHz. (b) $TE_{40,23}$ mode at 204.1 GHz.

Fig. 3.26: Start-up scenario considering the electron beam parameters of the coaxial cMIG for a) $TE_{34,19}$ mode at 170 GHz and b) $TE_{40,23}$ mode at 204 GHz.

Start-Up Scenario Using MIG Parameters of iMIG

Finally, the interaction simulation with the beam parameters of the iMIG are presented for 204 GHz. Figure 3.27 shows the start-up scenario for the $TE_{40,23}$ mode. The nominal operation point is at a kinetic beam energy of $U_{\text{beam}} = 86.4$ keV, a beam current of $I_{\text{beam}} = 68$ A and a magnetic field strength of $B_{\text{cav}} = 8.23$ T. The resulting output power is $P_{\text{out}} = 2.08$ MW with an interaction efficiency of $\eta = 37.8$ %.

In conclusion, three MIGs at KIT have been adapted to the magnetic field profile of the new SC magnet providing sufficient performance. An output power of 2 MW is achieved in theory using each MIG. The best results have been obtained using the iMIG. The resulting output power is only slightly above the required 2 MW and therefore has a small reserve. An increase is possible by either increasing the cavity radius, accepting higher mode eigenvalues or tolerating higher wall loading.

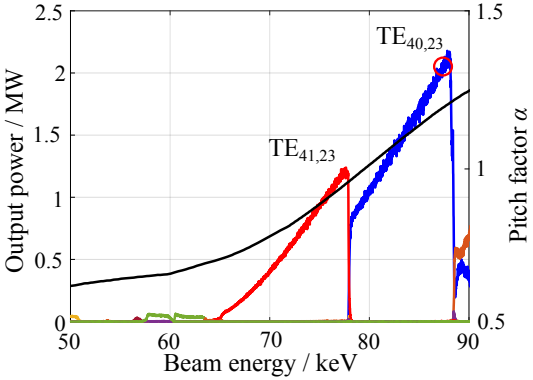

Fig. 3.27: Start-up scenario considering the electron beam parameters of the iMIG for the $TE_{40,23}$ mode at 204 GHz. The black curve shows the corresponding pitch factor.

3.3.3 Design of a 170/204 GHz Quasi-Optical Output Coupler

A quasi-optical output coupler consists of a launcher and several mirrors. It converts the excited high-order rotating gyrotron cavity mode into a linearly polarized Gaussian beam. The existing 170 GHz single-frequency quasi-optical output coupler suffer from a low Gaussian mode content at 204 GHz. A new quasi-optical output coupler is designed considering the following requirements:

(i) the length of the new launcher should be almost identical,

(ii) the Brillouin angle should be almost identical $\theta_B \approx 65.4°$,

(iii) a mirror-line launcher has been identified as optimum (hybrid-type launchers are not possible because of the relative caustic radii of about 0.32 [103]),

(iv) the quasi-optical output coupler must fit into the existing mirror box,

(v) a resulting Gaussian mode content of ≥ 95 % at both frequencies.

The deviation of the relative caustic radii in a mode series should be < 4 % to ensure a proper operation of the launcher at different center frequencies. The two operating modes at 170 GHz and 204 GHz have a deviation of 2 %. The relative caustic radius of the $TE_{34,19}$ mode is $r_c/r_{cav} = 0.3232$ and that of the $TE_{40,23}$ mode is $r_c/r_{cav} = 0.3167$.

A new quasi-optical output coupler is designed, which is optimized for the operation at 170 GHz and 204 GHz [103] using the numerical method described in [90]. First, a dual-frequency launcher has been designed. The launcher input radius is reduced from 32.5 mm to 32.0 mm. In addition, the slope of the inner wall is modified. A graph of the inner contour is plotted in Fig. 3.28. The designed perturbations are in the range of $-0.142 < \Delta R < 0.142$ mm. The resulting Gaussian mode content at the launcher aperture is 96.5 % for the operation at 170 GHz and at 204 GHz. The maximum ohmic wall loading is 560 W/cm^2 at 170 GHz and 540 W/cm^2 at 204 GHz at the launcher tip. The microwave beam radiated by the launcher is focused and

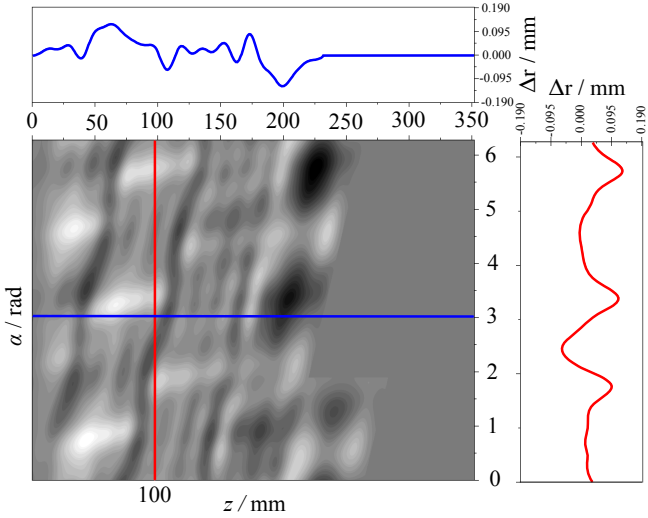

Fig. 3.28: Inner wall profile of the dual-frequency launcher [103].

shaped by a set of three mirrors. This system contains a quasi-elliptical and two beam shaping mirrors. The two beam shaping mirrors are designed according to the method described in [104]. The reduced launcher radius leads to a wider microwave beam pattern. The whole microwave beam can be collected either by a larger mirror or a shift of mirror 1. Since a larger mirror does not fit into the existing mirror box, the quasi-elliptical mirror with similar width is positioned 20 mm closer to the gyrotron axis. The positions of the beam shaping mirrors are adapted accordingly.

The resulting beam waist at the position of the output window should be around 24.5 mm corresponding to half of the window radius of 49 mm. This ensures an almost homogeneous field distribution at the center of the window and low truncation losses. The resulting beam waists are 21.6 mm and 24.6 mm for the $TE_{34,19}$ mode and 19.27 mm and 24.2 mm for the $TE_{40,23}$ mode in the x- and y-direction. The E-field intensity distributions at the window plane are depicted in Fig. 3.29. The calculated stray radiation is given by 1.5 % at 170 GHz and 204 GHz. The components have been man-

ufactured by Reinhold Mühleisen GmbH, Gerlingen, Germany. They are made of high-purity and oxygen-free copper (Cu-OFE) with at least 99.99 % copper. The material does not contain any elements that can evaporate at high temperatures and collapse the vacuum, has a high electrical and thermal conductivity and is therefore suitable for the use in vacuum tubes [105]. Figure 3.30 presents the manufactured components. The manufacturing precision is measured to be $< 20\ \mu m$ for resolving successfully the perturbations.

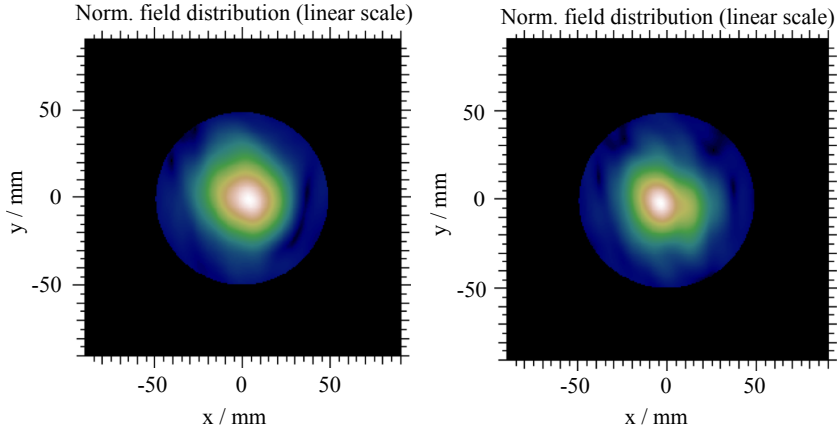

(a) 170 GHz. (b) 204 GHz.

Fig. 3.29: *E*-field intensity distribution of the microwave output beam in the window plane at a) 170 GHz and b) 204 GHz.

Fig. 3.30: Pictures of the manufactured quasi-optical output coupler. Launcher, quasi-elliptical and two beam shaping mirrors from left to right are depicted.

3.4 Frequency Step-Tunability

Frequency step-tunability in a bandwidth of ± 10 GHz around each center frequency (i.e. at 170 GHz and at 204 GHz) is proposed for EU DEMO. This study is the first to consider the insert loading in the mode selection process.

Different Methods for Frequency Tuning

Theoretically, the operating frequency of a gyrotron can be tuned by a mechanical change of the cavity structure [106]. However, this method is not employed because it requires an opening of the tube. A preferred method is to tune the magnetic field B_{cav} and/or the accelerating voltage V_{acc} [44]. According to Eq. 2.2, tuning the accelerating voltage leads to a strong variation of γ. Additionally, it allows frequency tuning only in the range of several ten MHz. Hence, the most effective method to cover a large frequency bandwidth is to use different modes at discrete frequency steps. This can be achieved by tuning the magnetic field strength. Then, the operating points are tuned individually for each mode for maximum performance. The time required for the frequency tuning depends on the maximum possible speed for changing the magnetic field strength of the SC magnet. A first hybrid magnet achieved a tuning speed of 652 mT/s [107]. This corresponds to $\approx$ 15 GHz/s. However, this magnet is only able to operate in 1 ms pulses and a duty cycle of 0.1 %. Another 7 T SC magnet manufactured by Japan Superconductor Technology Inc. (JASTEC), Hyogo, Japan provided a tuning speed of 40 mT/s ($\approx$ 0.96 GHz/s) in a range of ±200 mT [108].

Broadband gyrotron output windows

The proposed frequency bandwidth is not covered by classical gyrotron windows. According to Fig. 3.1, high reflection occurs outside the resonance of the window. Alternative concepts are double-disk windows or Brewster-windows. A double-disk window with variable spacing in between is used at ASDEX Upgrade [109]. The distance between the disks defines the transparency according to Fabry-Perot resonances [110]. However, this

type of window is only transparent at discrete frequencies. Therefore, a gyrotron window under the Brewster angle θ_{Brew} is under investigation [82, 111, 112], which does not show a resonant transmission behavior for a specific polarization. The Brewster angle of CVD-diamond is $\theta_{\mathrm{Brew}} = 67.2°$. The required diameter for a tilted diamond disk has to be consequently larger. The largest diamond disk with a diameter of 180 mm has been manufactured successfully with a thickness of 2 mm, as published in [113].

3.4.1 Mode Selection Process

Equidistant frequency steps can be achieved by a mode series including the azimuthal neighboring modes [114]. This approach is published for hollow-cavity gyrotrons in [31, 42, 44] and for coaxial-cavity gyrotrons in [44]. Azimuthal neighboring modes have a frequency distance of 2.1 GHz in the coaxial-cavity technology, which requires 11 modes to cover the entire bandwidth of $\pm$10 GHz. An initial list of the chosen modes around 170 GHz and 204 GHz is summarized in Tab. 3.9 considering the approach of azimuthal neighboring modes. A detailed list with the important parameters of the modes can be found in Appendix A.2.

Firstly, each mode has been simulated individually to validate its performance and to define the nominal operating parameters. The insert loading strongly increases towards the lower frequencies in both frequency bands. Five modes exceed the insert loading limitation at the mode series around 170 GHz. These modes are the $TE_{33,19}$ at 167.9 GHz, $TE_{32,19}$ at 165.8 GHz, $TE_{31,19}$ at 163.7 GHz, $TE_{30,19}$ at 161.6 GHz and $TE_{29,19}$ at 159.5 GHz. Three modes exceed the insert loading limitation at the mode series around 204 GHz. Here, the modes are the $TE_{37,23}$ at 197.8 GHz, $TE_{36,23}$ at 195.7 GHz and $TE_{37,23}$ at 193.6 GHz. This is due to the decreasing caustic radii and thus the decreasing distance to the insert. Therefore, the covered bandwidth is reduced to in total 10 GHz and 14 GHz around the center frequencies of 170 GHz and 204 GHz. In addition, the caustic radius increases monotonically during the mode series. The deviation of the caustic radius of this mode series exceeds the requirement of 4 %. In conclusion, an azimuthal

Table 3.9: Summary of the initial mode series for frequency step-tunability around 170 GHz and 204 GHz using azimuthal neighboring modes and their frequency distance to the center frequency.

Δf / GHz	Modes around 170 GHz	Modes around 204 GHz
-10.5	$TE_{29,19}$	$TE_{35,23}$
-8.4	$TE_{30,19}$	$TE_{36,23}$
-6.3	$TE_{31,19}$	$TE_{37,23}$
-4.2	$TE_{32,19}$	$TE_{38,23}$
-2.1	$TE_{33,19}$	$TE_{39,23}$
0	$TE_{34,19}$	$TE_{40,23}$
+2.1	$TE_{35,19}$	$TE_{41,23}$
+4.2	$TE_{36,19}$	$TE_{42,23}$
+6.3	$TE_{37,19}$	$TE_{43,23}$
+8.4	$TE_{38,19}$	$TE_{44,23}$
+10.5	$TE_{39,19}$	$TE_{45,23}$

change in the mode index is not sufficient to satisfy the requirements for the coaxial-cavity technology.

Hence, an additional change in the radial mode index is required for frequency step-tunability. A new mode series should provide almost equidistant frequency steps. Figure 3.31 presents a mode spectrum with different possible modes around the center frequency at 170 GHz. Modes highlighted in red either exceed the insert loading constraint or the deviation limit of the caustic radius, or generally show inefficient operation. Modes highlighted in green are suitable candidates for an efficient mode series for frequency-step tunability. The similar study has been performed at 204 GHz.

In conclusion, the best performance can be achieved by a jump of the radial mode index from the $TE_{m,p}$ mode at the center frequency to the $TE_{m+2,n-1}$ mode. The modes before and after these two are changed by the azimuthal mode index for equidistant frequency steps of 2.1 GHz. A frequency step of 1.2 GHz is identified at the mode jump. A summary of the proposed mode series is given in Tab. 3.10.

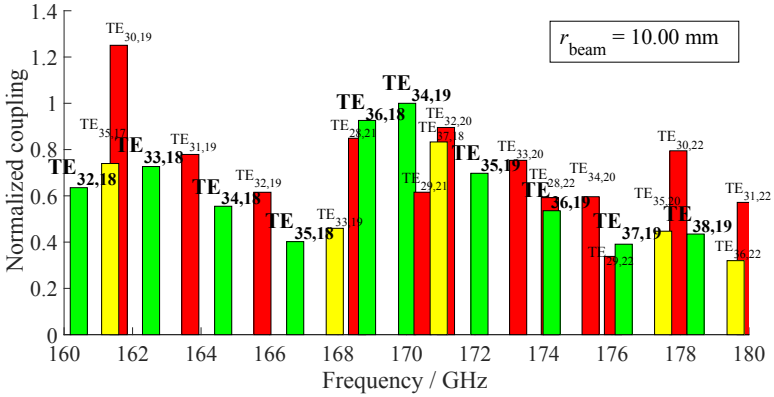

Fig. 3.31: Mode spectrum for the identification of a suitable mode series for efficient frequency step-tunability at the center frequency of 170 GHz. The green bars indicate modes showing in simulations high performance and reliability. The red colored bars indicate modes do not satisfy the requirements.

Table 3.10: Summary of the proposed mode series for frequency step-tunability around 170 GHz and 204 GHz.

Δf / GHz	Modes around 170 GHz	Modes around 204 GHz
-9.6	$TE_{32,18}$	$TE_{38,22}$
-7.5	$TE_{33,18}$	$TE_{39,22}$
-5.4	$TE_{34,18}$	$TE_{40,22}$
-3.3	$TE_{35,18}$	$TE_{41,22}$
-1.2	$TE_{36,18}$	$TE_{42,22}$
0	$TE_{34,19}$	$TE_{40,23}$
+2.1	$TE_{35,19}$	$TE_{41,23}$
+4.2	$TE_{36,19}$	$TE_{42,23}$
+6.3	$TE_{37,19}$	$TE_{43,23}$
+8.4	$TE_{38,19}$	$TE_{44,23}$
+10.5	$TE_{39,19}$	$TE_{45,23}$

Figure 3.32 presents a comparison of the caustic radii of the optimized and initial mode series. The optimized mode series has a reduced total deviation in caustic radius compared to the initial mode series. The deviation of the relative caustic radius of the initial mode series is ±9.0 % around 170 GHz and ±7.7 % around 204 GHz. The optimized mode series shows a deviation in relative caustic radius of ±4.1 % around 170 GHz and ±3.7 % around 204 GHz to the mean value.

The performance of the dual-frequency 170/204 GHz quasi-optical output coupler is validated according to the mode series. The number of modes having a Gaussian mode content (GMC) higher than 95 % is summarized in Tab. 3.11. The number of modes satisfying the EU DEMO requirements are doubled using the optimized mode series. In the frame of this research, the used quasi-optical output coupler is optimized for the operation at the center frequencies of 170 GHz and 204 GHz. It is not optimized for frequency-step tunability. However, this quasi-optical output coupler is working with a high performance for a large number of modes. The simulation results of the quasi-optical output coupler are discussed in Appendix A.2.3. It is postulated that a quasi-optical output coupler designed for a relative caustic radius equal to the mean value of Fig. 3.32 will have even better performance.

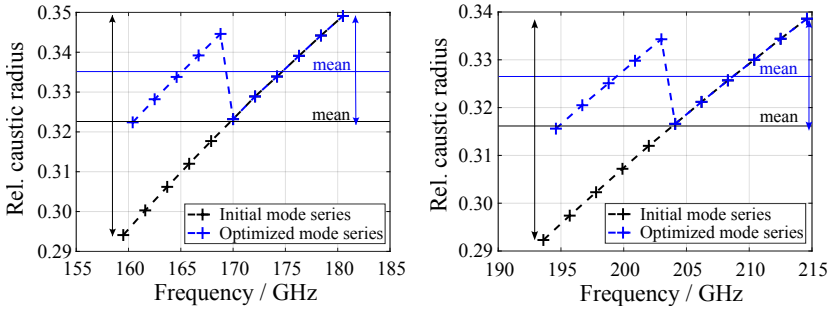

(a) 170 GHz. (b) 204 GHz.

Fig. 3.32: Relative caustic radii of the mode series using the classical approach in black and the optimized mode series colored in blue, at the center frequency bands around a) 170 GHz and b) 204 GHz.

Table 3.11: Number of modes satisfying the specified Gaussian Mode Content (GMC) of the initial and optimized mode series at 170 GHz and 204 GHz. The numbers in parentheses indicate the number of modes that can be operated if the insert loading is considered.

≥ 95 % GMC	170 GHz	204 GHz
Initial mode series	3 (1)	2
Optimized mode series	2	5
≥ 90 % GMC	**170 GHz**	**204 GHz**
Initial mode series	6 (3)	6
Optimized mode series	6	8

3.4.2 Dynamic Step-wise Frequency Tuning

Generally, step-wise frequency tuning has to be divided into a) tuning from high to low and b) from low to high frequencies.

Frequency Tuning from High to Low Frequencies

Continuous magnetic field tuning is an effective method for frequency step-tuning from high to low frequencies as described in [31], [114]. Magnetic field tuning is performed in the range from 7.32 T to 6.54 T around 170 GHz and from 8.80 T to 7.85 T around 204 GHz to cover the entire frequency bandwidth of ±10 GHz. Figure 3.33 presents a multi-mode simulation of continuous frequency step-tuning from high to low frequencies. It ranges from 180.5 GHz to 159.5 GHz and from 214.7 GHz to 194.6 GHz. The beam current is set to be constant to 75 A and 68 A for the frequency band around 170 GHz and 204 GHz. The beam radii are adjusted to maximize the beam coupling to the corresponding modes. The nominal operation parameters are limited by the maximum wall loading constraint of 2 kW/cm^2. The beam energy is modified for each mode to maintain optimized detuning for maximum output power and efficiency. A summary of the nominal parameters and the resulting output powers and efficiencies are summarized in Tab. 3.12 and are highlighted in Fig. 3.33. A velocity spread of $\Delta\alpha = 6.0$ %

and a kinetic energy spread of $\Delta E = 0.1\,\%$ are considered. The insert loading of the chosen modes does not exceed the specified limit. The maximum deviations of the output power in the mode series are given by 5 % and 18 %.

Table 3.12: Nominal operation parameters (beam energy U_{beam}, magnetic field strength B_{cav} at cavity and electron beam radius r_{beam}) and simulation results (output power P_{out} and interaction efficiency η_{elec}) in the frequency band of 170 GHz. and 204 GHz.

Mode	U_{beam} / keV	B_{cav} / T	r_{beam} / mm	P_{out} / MW	η_{elec} / %	f / GHz
$\mathrm{TE}_{32,18}$	95.0	6.53	10.05	2.42	33.5	160.4
$\mathrm{TE}_{33,18}$	93.4	6.60	10.35	2.36	33.6	162.5
$\mathrm{TE}_{34,18}$	92.1	6.68	10.52	2.45	34.6	164.6
$\mathrm{TE}_{35,18}$	93.5	6.77	10.70	2.41	34.8	166.7
$\mathrm{TE}_{36,18}$	93.0	6.85	10.80	2.39	34.8	168.8
$\mathrm{TE}_{34,19}$	91.4	6.88	10.08	2.37	34.8	170.0
$\mathrm{TE}_{35,19}$	92.5	6.98	10.30	2.42	34.5	172.1
$\mathrm{TE}_{36,19}$	93.3	7.07	10.50	2.40	34.1	174.2
$\mathrm{TE}_{37,19}$	91.5	7.14	10.70	2.28	33.3	176.3
$\mathrm{TE}_{38,19}$	92.0	7.24	10.85	2.29	32.9	178.4
$\mathrm{TE}_{39,19}$	91.8	7.32	10.95	2.30	33.3	180.5
$\mathrm{TE}_{38,22}$	91.8	7.89	9.85	2.12	36.7	194.5
$\mathrm{TE}_{39,22}$	91.5	7.98	9.98	2.10	36.0	196.6
$\mathrm{TE}_{40,22}$	90.7	8.07	10.13	2.00	34.8	198.7
$\mathrm{TE}_{41,22}$	90.5	8.16	10.24	1.94	33.7	200.8
$\mathrm{TE}_{42,22}$	90.0	8.24	10.35	1.93	33.6	202.9
$\mathrm{TE}_{40,23}$	89.5	8.25	9.85	2.05	35.3	204.1
$\mathrm{TE}_{41,23}$	92.5	8.40	10.00	1.94	33.1	206.2
$\mathrm{TE}_{42,23}$	93.9	8.50	10.10	1.88	31.9	208.3
$\mathrm{TE}_{43,23}$	92.4	8.57	10.24	1.86	31.5	210.4
$\mathrm{TE}_{44,23}$	93.5	8.70	10.50	1.70	28.7	212.5
$\mathrm{TE}_{45,23}$	95.0	8.80	10.65	1.75	29.0	214.6

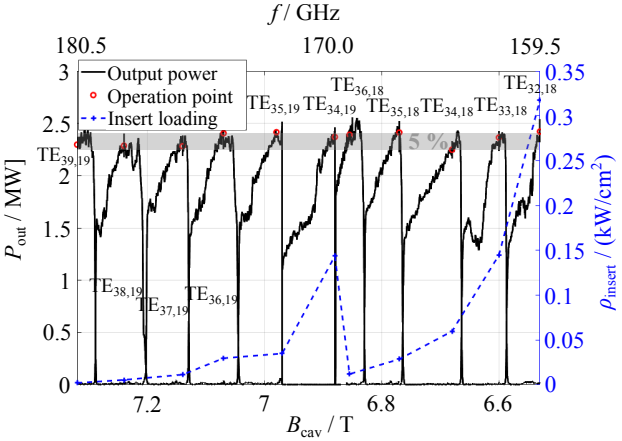

(a) 170 GHz.

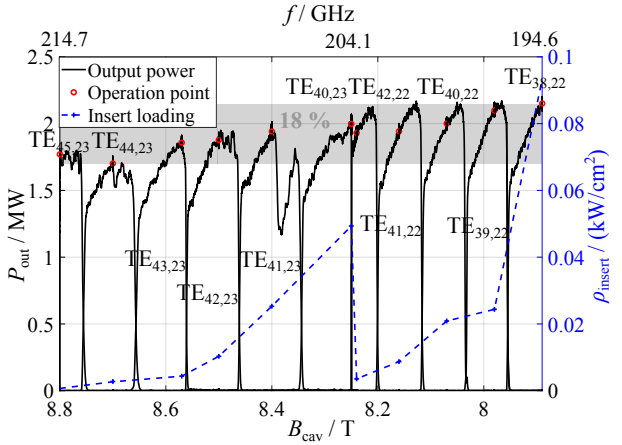

(b) 204 GHz.

Fig. 3.33: Simulation of continuously stepwise frequency tuning using the optimized mode series from high to low frequency around the center frequencies of a) 170.0 GHz and b) 204.1 GHz.

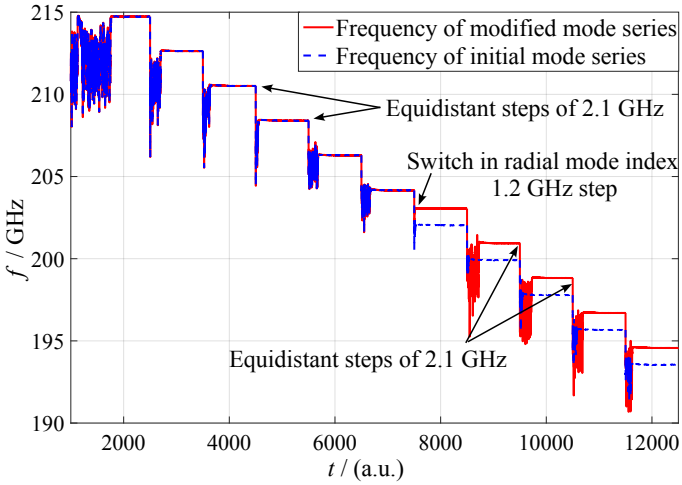

Fig. 3.34: Comparison of the frequency steps of the classical approach and the optimized mode series.

Figure 3.34 depicts the frequency steps along the tuning at 204 GHz. The distances between the operating frequencies are equidistant and correspond to 2.1 GHz. Except, a smaller step of 1.2 GHz, which is due to the jump from the nominal center $TE_{m,p}$ mode to the $TE_{m+2,n-1}$ mode. The flat tops represent the operation at the defined nominal operating parameters.

Frequency Tuning from Low to High Frequencies

Continuous magnetic field tuning is not possible for tuning the frequency from low to high frequencies in terms of hysteresis effects [115, 116]. Increasing the magnetic field does not lead to a jump to the next higher mode. The dominant mode still operates at low detuning and low output power. This effect has already published theoretically in [31] and experimentally in [116]. Figure 3.35 illustrates this effect for the $TE_{40,23}$ and $TE_{41,23}$ modes. The nominal magnetic field for the $TE_{41,23}$ mode is 8.40 T. A simulation is performed considering both modes while increasing the magnetic field strength from 8.21 T to 8.45 T. However, the $TE_{41,23}$ mode is not excited.

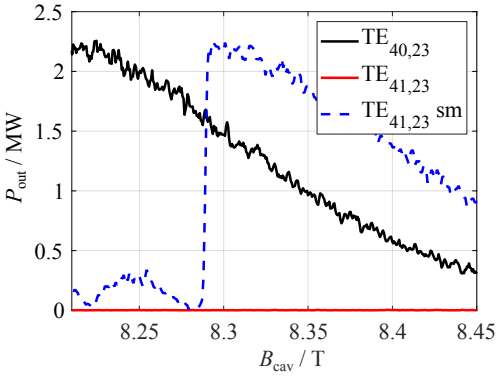

Fig. 3.35: Output power of the $TE_{40,23}$ and $TE_{41,23}$ modes for magnetic field tuning from low to high frequencies. The dashed line indicates the behavior of the $TE_{41,23}$ mode in single-mode calculation.

The dashed line describes for illustration the behavior of the $TE_{41,23}$ mode in single-mode calculation.

An alternative approach is to shut down the gyrotron, change the magnetic field and turn it back on, as published in [31]. Prior to this study, each mode was simulated individually. This coaxial-cavity design is capable to excite each mode with common start-up scenario. Figure 3.36 presents a frequency tuning from low to high frequencies using the $TE_{42,22}$ mode, the $TE_{40,23}$ mode and the $TE_{41,23}$ mode. The graph is limited to 3 modes for better visibility. Each mode is operating at the nominal operation parameter. A shut down can be realized either by ramp down the applied acceleration voltage completely or by reducing the pitch factor [31]. A MIG in triode configuration can vary the pitch factor in a large range. The interaction stops by decreasing the pitch factor to a value of e.g. 0.5. The gyrotron is ramped up in the following by an increase of the pitch factor to its nominal value.

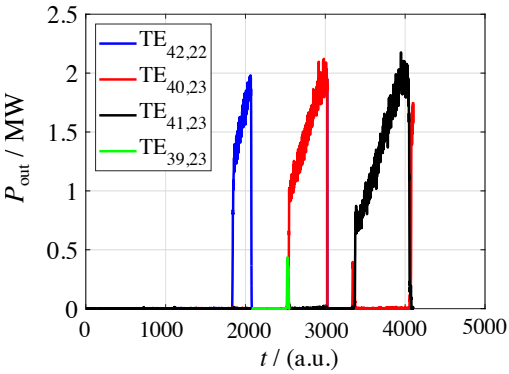

Fig. 3.36: Frequency step-tunability from low to high frequencies. Only the $TE_{42,22}$ mode, the $TE_{40,23}$ mode and the $TE_{41,23}$ mode are plotted in terms of visibility.

3.5 Performance Analysis at 136 GHz

A validation of the performance of the key components at 136 GHz is performed. The key components under investigation are the MIG, the coaxial cavity and the quasi-optical output coupler. A summary of possible operating modes at 136 GHz are summarized in Tab. 3.13. The $TE_{28,15}$ mode satisfies the requirements best. The mode operates at a frequency of 135.8 GHz, resulting in a low window reflection of 0.03 % and has a deviation in caustic radius of 3.09 %.

Table 3.13: Mode candidates and their key parameters for the operation at 136 GHz.

Mode	Rel. caustic radius	Diff. in caustic radius / %	Frequency / GHz
$TE_{28,15}$	0.3332	3.087	135.81
$TE_{25,16}$	0.2998	-7.255	134.78
$TE_{26,16}$	0.3069	-5.054	136.92

3.5.1 Operating the Magnetron Injection Guns at 136 GHz

The MIGs at KIT are being investigated for their applicability at 136 GHz. The selected $TE_{28,15}$ mode has a beam radius of $r_{beam} = 10.35$ mm and a maximum magnetic field strength at the center of the midsection of $B_{cav} = 5.40$ T.

Coaxial diode MIG

The coaxial diode MIG discussed in Section 3.3.1 is not suited to be used at 136 GHz. The velocity spread is well above 20 % and the pitch factor is out of the operating range of $\alpha = 1.1 - 1.3$. There is not a design by changing the anode shape that covers all three frequencies (136, 170 and 204 GHz). The electron beam parameters can be set to nominal values only by modifying the cathode and emitter shapes. This requires re-manufacturing of the emitter ring, which is the most expensive component of a MIG. Therefore, this MIG is skipped as potential candidate at 136 GHz. A triode MIG must be used for this purpose.

iMIG

The influence of the modulation anode on the electron beam parameters using the iMIG is presented in Fig. 3.37. In general, the iMIG satisfies the beam requirements at a voltage of 28 kV applied to the modulation anode. The resulting pitch factor is $\alpha = 1.2$ and the transverse velocity spread is $\delta\beta_t = 3$ % for a magnetic field angle of $\phi_{emt} = 0°$ at the emitter. A study on secondary electrons shows that this design prevents trapped electrons. The iMIG is a suitable candidate to be used at 136 GHz.

cMIG

The triode-type cMIG can be used for operation at 136 GHz. The resulting pitch factor is $\alpha = 1.28$ at a transverse velocity spread of $\delta\beta_t = 2.25$ %. Figure 3.38 presents a study about secondary electrons. Some of the electrons emitted from the rear part and the front part of the cathode nose are collected by the anode and the insert, respectively. The other electrons are

guided to the cavity. Figure 3.38b shows the pitch factor at the cavity versus the emitting position of the corresponding electron. Trapped electrons are prevented because the maximum pitch factor is below $\alpha_{\max} = 3$.

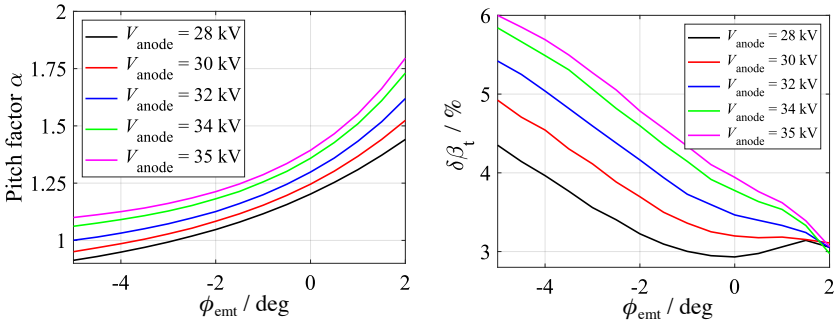

(a) Pitch factor α. (b) Transverse velocity spread $\delta\beta_t$.

Fig. 3.37: Pitch factor α and transverse velocity spread $\delta\beta_t$ over a wide range of the magnetic field angle ϕ_{emt} and applying different voltages at the modulation anode V_{anode} of the iMIG.

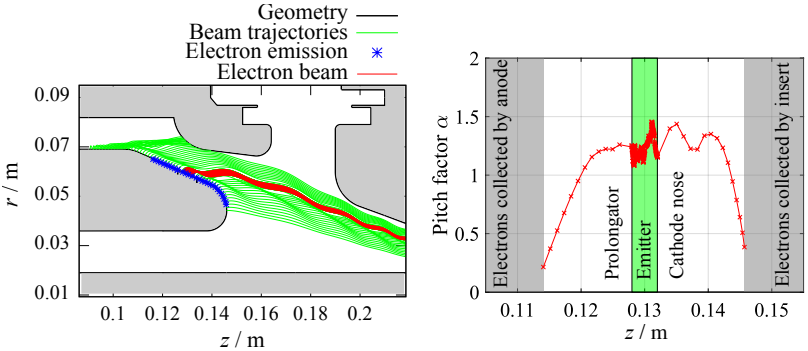

(a) Electron beam trajectories. (b) Pitch factor α

Fig. 3.38: a) Trajectories of electrons emitted from the cathode surface. b) Pitch factor α at the cavity versus the axial position of the emitting point of the cathode which are highlighted with blue crosses in Fig. 3.38a.

3.5.2 Verification of the Interaction Cavity at 136 GHz

The performance of the coaxial cavity using the $TE_{28,15}$ mode is investigated. A velocity spread of $\Delta\alpha = 6$ % and a kinetic energy spread of 0.1 % are considered in the simulations. An adiabatic start-up simulation is presented in Fig. 3.39. The nominal operation point is given by a kinetic energy of the electrons of $U_{\mathrm{beam}} = 82.4$ keV, a beam current of $I_{\mathrm{beam}} = 70$ A and a magnetic field strength of $B_{\mathrm{cav}} = 5.40$ T. The pitch factor is $\alpha = 1.3$. The resulting output power is $P_{\mathrm{out}} = 2.42$ MW with an interaction efficiency of $\eta = 41.9$ %. The wall loading is 1.35 kW/cm^2 and the insert loading is > 0.30 kW/cm^2. Thus, the insert loading exceeds the maximum limit. An output power of 1.1 MW with an interaction efficiency of 20.7 % is achieved considering an insert loading of 0.2 kW/cm^2. This is the technical limitation of this mode given by the loading constraint published in [78]. However, multi-physics simulations have been performed in [99, 100] for an advanced insert cooling system coming to the result that the insert can theoretically withstand a heat flux of up to 0.39 kW/cm^2. In this case, the $TE_{28,15}$ mode can be used considering this assumption.

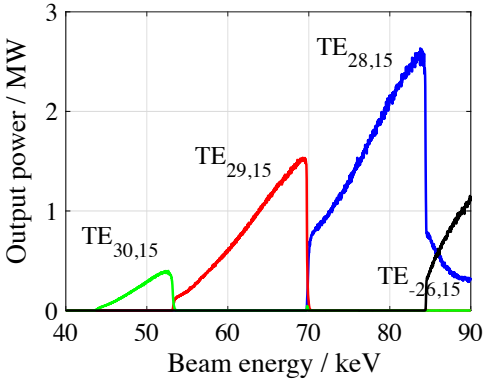

Fig. 3.39: Adiabatic start-up scenario for the $TE_{28,15}$ mode operating at 135.8 GHz.

3.5.3 Operating the Quasi-Optical Output Coupler at 136 GHz

Both available quasi-optical output couplers, namely the 170 GHz single-frequency design and the 170/204 GHz multi-frequency design have been evaluated. The input mode is the $TE_{28,15}$ mode at 135.8 GHz. Both designs provide a Gaussian mode content close to 95 %. Figure 3.40 shows the simulation result of the *E*-field intensity and phase pattern for the 170/204 GHz dual-frequency quasi-optical output coupler at 136 GHz. In conclusion, both designs satisfy the EU DEMO requirements providing a Gaussian mode content of $\geq$ 95 %. However, the microwave output beam is shifted by 8 mm off center.

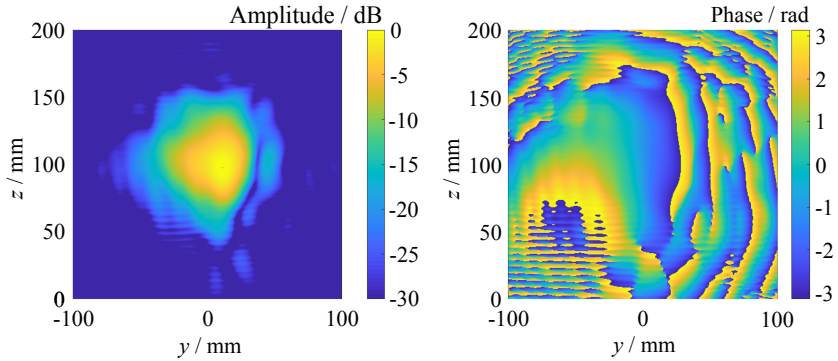

(a) 170 GHz.

(b) 204 GHz.

Fig. 3.40: a) *E*-field intensity and b) phase pattern of the $TE_{28,15}$ mode at 135.8 GHz using the quasi-optical mode converter designed for 170/204 GHz dual-frequency operation.

4 Upgrade of the Gyrotron Test Systems

The test systems used in gyrotron development are divided into two categories, i.e. the low-power "cold"-measurements and the high-power "hot"-measurements. Gyrotron key components are verified in cold-measurements without the usage of a gyrotron nor the necessity of a SC magnet or a high-voltage power supply. Those systems excite the required input mode to supply the dedicated gyrotron key components for verification. In this way, a pre-validation of e.g. the quasi-optical output coupler or the gyrotron output window is performed [81].

The category of "hot"-measurements includes the monitoring of the gyrotron operation. In this way, an in-direct verification of the design and fabrication quality of its sub-components is performed. Examples are the calorimeters for microwave power measurements and the frequency diagnostics for validating the frequency spectrum purity [117]. The existing frequency diagnostics needs to be adapted to higher operating frequencies due to the increasing demand for gyrotrons operating above 200 GHz.

4.1 Measurement of Quasi-Optical Components

The quasi-optical output coupler separates the electromagnetic wave from the electron beam. In addition, it converts the high-order rotating cavity mode into a linearly polarized Gaussian beam. The Gaussian mode has low transmission losses and is used to guide the microwave beam to the plasma vessel [11, 118]. Proper pre-validation of these quasi-optical output couplers is vital before the installation into the gyrotron. The components, and in particular the launcher, are very sensitive to manufacturing tolerances, which are in the range of a few μm. Therefore, the gyrotron cavity mode needs to

be excited at low power levels for the verification in "cold" measurements. There are different methods for the excitation of high-order modes:

(i) using mode conversion from the fundamental mode [119, 120],

(ii) by a point source and a set of m alternating dielectrics [121],

(iii) by a metallic perforated insert of a coaxial cavity [122],

(iv) or by a quasi-optical approach [123, 124].

The method discussed in (i) is not suitable for exciting gyrotron cavity modes with mode indices $m, p \gg 1$. Method (ii) is a purely theoretical design and is not feasible in practice. The excitation of higher order modes by a perforated metal insert of method (iii), is applicable, however, has compared to the quasi-optical method (iv) a lower efficiency for the excitation of very high-order modes. This is due to the need of m holes on the circumference of the insert. In terms of the small insert radius the holes become smaller with increasing azimuthal mode index m. Technical feasibility is combined with high mode purity in the quasi-optical mode generator (method (iv)). In the following, its principle and its upgrade including an automated measurement procedure is presented. Then, the $TE_{34,19}$ mode at 170 GHz and the $TE_{40,23}$ mode at 204 GHz are excited. Finally, the 170/204 GHz dual-frequency quasi-optical output coupler is verified in cold measurements.

4.1.1 Mode Excitation Principle in a Low Power Test Stand

Figure 4.1 shows a photo of the quasi-optical mode generator at KIT. The design is based on [125]. A schematic of the measurement setup is given in Fig. 4.2. A step-tapered horn antenna is used to radiate the signal from a vector network analyzer (VNA) as a Gaussian beam ($TEM_{0,0}$ mode) [124]. Then, a lens system forms an astigmatic Gaussian beam with a plane phase front at the position of a quasi-parabolic (q.-p.) mirror [126]. Spillover losses are reduced by the astigmatism. The quasi-parabolic mirror is adjusted in the vertical and horizontal position and the angle to achieve maximum efficiency. The electromagnetic wave is reflected at the quasi-parabolic mirror and couples through the perforated cavity wall. The beam is focused close to

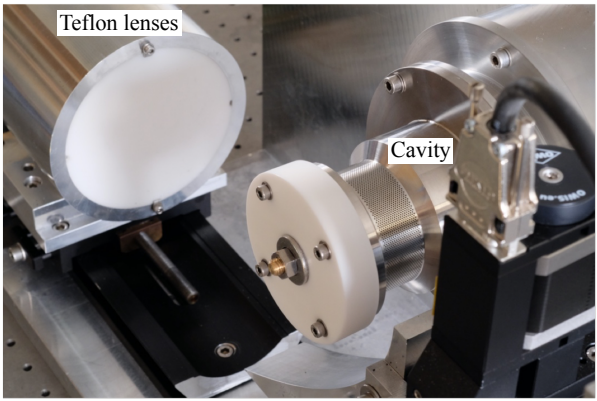

Fig. 4.1: Photo of the mode generator setup used for the $TE_{40,23}$ mode at 204 GHz.

the caustic radius of the desired cavity mode. A coaxial insert is used and the cavity is designed specifically for the low-power tests using a scattering matrix code [127]. The insert improves the separation to competing modes. A non-linear up-taper is assembled to the mode generator setup for the adjustment procedure [128]. This greatly increases the waveguide radius, resolving the measured mode field intensity patterns with higher quality. The non-linear up-taper is removed and replaced by the quasi-optical output coupler for verification after the desired mode has been successfully excited. The output field pattern is measured using a rectangular standard waveguide pick-up antenna with a chamfer of 15°. The chamfered antenna edges reduce reflections back to the mode generator. The antenna is mounted on a 3D measurement arm and samples the pattern of the generated mode point by point [125]. The received signal is evaluated using the VNA.

In the past, the optimization of the mode quality was a time-consuming task. The sub-components were adjusted by manual optimization. In this work, the mode generator setup has been improved with high-precision linear drivers and a goniometer which are controlled via the computer.

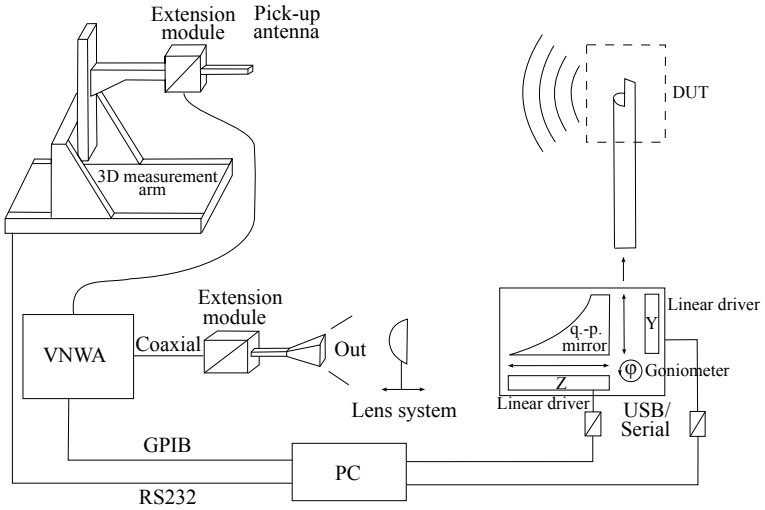

Fig. 4.2: Schematic view of a mode generator setup, VNA, 3D measurement arm and PC. The device under test (DUT) is illustrated in the graph as a launcher. In principle the DUT can be the radiated mode after the non-linear up-taper, the launcher or the complete quasi-optical output coupler.

This upgrade allows the use of new methods for an autonomous mode generator setup.

4.1.2 Key Components of a Mode Generator System

The structure of the quasi-optical mode generator consists of four key components: 1) the horn antenna with lens system, 2) the quasi-parabolic mirror, 3) the coaxial cavity and 4) the non-linear up-taper. The design of the key components for the $TE_{34,19}$ mode at 170 GHz and $TE_{40,23}$ mode at 204 GHz are discussed in the following,

Horn Antenna with Lens System

The mode generator setup requires a Gaussian-like HE_{11} hybrid mode as input mode. A corrugated HE_{11} horn antenna [129] can be used for this purpose. A cheap alternative is a Potter horn antenna [130] with two straight tapers [131]. Figure 4.3 depicts a schematic of the Potter horn. This type of antenna has a low sidelobe level down to -30 dB. This allows an optimal illumination of the quasi-parabolic mirror and avoids reflection artefacts on the mode generator housing. The Potter horn is a dual-mode antenna. The dominant TE_{11} and the high-order TM_{11} modes are excited in a given ratio. Superposing the TE_{11} mode with 85 % of the power, the TM_{11} mode with 15 % of the power and a phase shift of 180° between the modes results in a HE_{11} mode with 99.19 % purity [132]. The conversion of the TE_{11} input mode to the required mode ratio with associated phase shift is not achievable in a wide frequency range. Therefore, a Potter horn is designed at 170 GHz and another at 204 GHz. The geometry is optimized using a scattering-matrix code [133], which is much faster for this purpose in contrast to commercial 3D software tools like CST Microwave Suite [134], since only discretization in axial direction is required. Figure 4.4 and Fig. 4.5 present the simulation results with the parameters given in Tab. 4.1. The ratio at the end of the

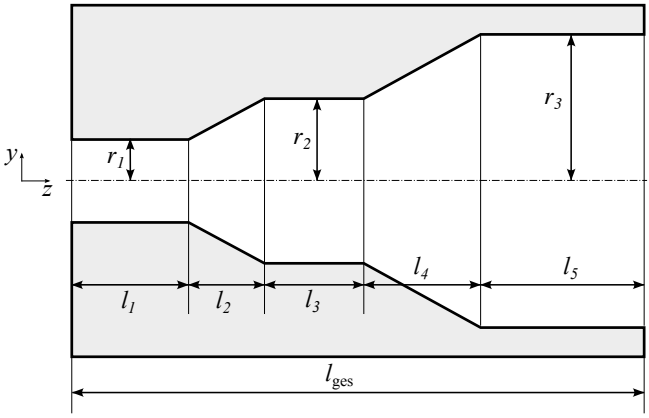

Fig. 4.3: Parametric schematic of a Potter horn.

antenna is 85.4 % and 14.0 % at 170 GHz and 85.0 % and 14.2 % at 204 GHz for the TE_{11} mode and TM_{11} mode, respectively. The phase shift $\Delta\varphi$ between the two modes is $\Delta\varphi = 180°$ by selecting the length l_5 accordingly.

Table 4.1: Parameters of the designed Potter horn antennas operating at 170 GHz and 204 GHz.

Parameter / mm	170 GHz	204 GHz
r_1	0.65	0.65
r_2	1.31	1.09
r_3	2.57	2.06
l_1	2.47	2.06
l_2	2.48	1.89
l_3	1.48	1.40
l_4	5.94	4.95
l_5	18.61	15.35
l_{ges}	30.98	25.65

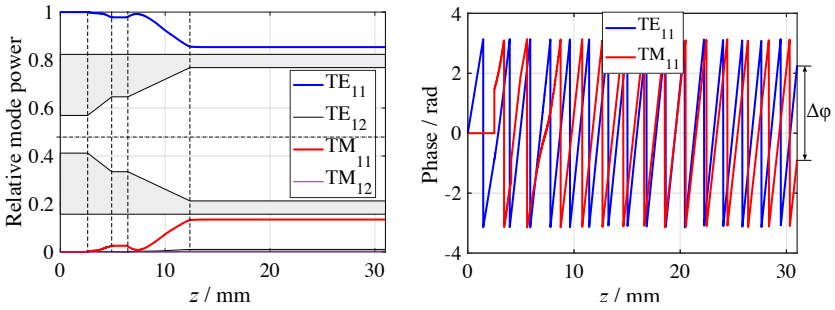

(a) Relative port power.

(b) Phase.

Fig. 4.4: a) Relative mode power and b) phase of the Potter horn at 170 GHz according to the parameters of table 4.1. The schematic of the Potter horn is not in scale. The phase difference corresponds to $\Delta\varphi = 180°$.

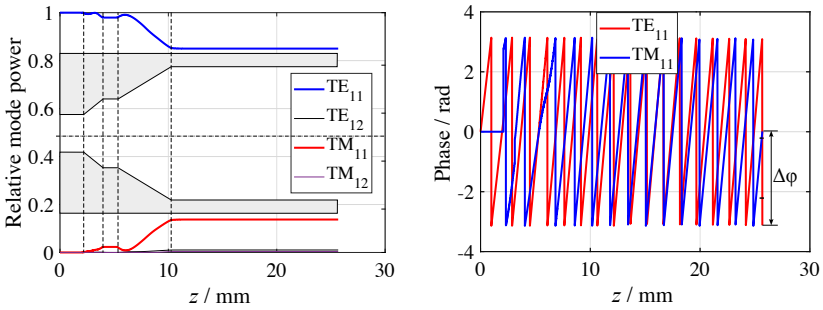

(a) Relative port power.

(b) Phase.

Fig. 4.5: a) Relative mode power and b) phase of the Potter horn at 204 GHz according to the parameters of table 4.1.The schematic of the Potter horn is not in scale. The phase difference corresponds to $\Delta\varphi = 180°$.

The optimum simulation results are validated using CST Microwave Suite. The correct transformation of the input mode into the TE_{11} and TM_{11} modes in the given ratio is depicted in Fig. 4.6a. The E-field distribution at the end of the antenna is perfectly cylindrical, resulting in a transformation into the HE_{11} mode. Figure 4.6b depicts the antenna pattern in the E- and H-plane at 170 GHz and at 204 GHz. The sidelobe level in the E-plane is -30 dB and is in agreement with the theoretical value. The half power beam width is 27.0° and 26.6° for the E- and H-plane at 204 GHz and 26.8° in both planes at 170 GHz. The directivity is 17.2 dBi for both antennas. Nearly identical results were expected and have been demonstrated since the antennas were scaled with the frequency. Except for the input section which had to be matched to the different standardized waveguide flanges. The Potter horns are manufactured using a step driller, which has the specific shape of the inner contour of the Potter horn, as discussed in Appendix A.4.

The radiated beam has to be focused to the quasi-parabolic mirror. This can be achieved by using a metallic reflector [135, 136] or by a lens system [125, 137]. The mode generator with a lens system benefits from a more compact and one-dimensional setup. The quasi-parabolic mirror would be only partially illuminated using a spherical shaped lens. Therefore, and in

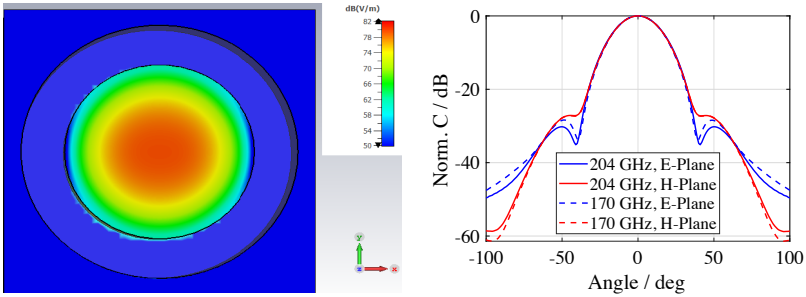

(a) Intensity profile of the radiated field.

(b) Normalized antenna pattern.

Fig. 4.6: a) Intensity profile of the radiated field at 204 GHz and b) far field pattern of the antennas at 170 GHz and 204 GHz in E- and H-plane using CST Microwave Suite.

order to reduce spillover losses, two cylindrical shaped lenses are used to form an astigmatic beam. One lens is orientated along the horizontal and the second along the vertical direction. A measurement using the Potter horn and the lens system is shown in Fig. 4.13.

Quasi-Parabolic Mirror

The quasi-parabolic mirror focuses the astigmatic beam in-phase close to the caustic of the desired mode in the coaxial cavity. A schematic is depicted in Fig. 4.7. The shape of the quasi-parabolic mirror can be derived by the requirement of equal optical length between the plane phase front of the incident beam and the phase front at the caustic [138]. The principle of the quasi-parabolic mirror is described in [76]. In this publication, the quasi-parabolic mirror is used in a gyrotron output coupler to convert the high-order gyrotron cavity mode into a free-space Gaussian beam. Here, the mirror operates in reverse direction, i.e. the Gaussian beam is focused close

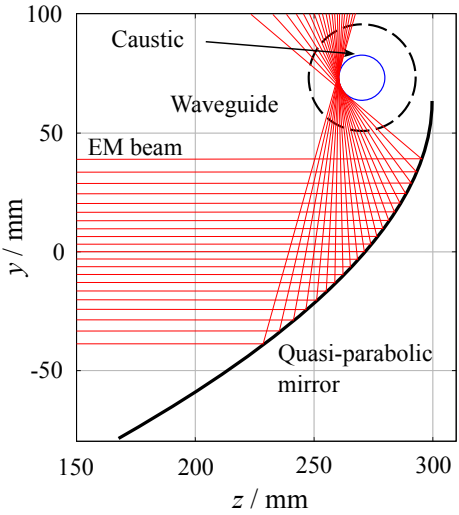

Fig. 4.7: Schematic of the principle of the quasi-parabolic mirror.

to the caustic. The shape of the quasi-parabolic mirror can be calculated as discussed in [76]:

$$z(\alpha) = 2F \tan\left(\frac{\alpha}{2}\right) + r_c \left(1 + \alpha \tan\left(\frac{\alpha}{2}\right)\right) \tag{4.1}$$

$$y(\alpha) = F\left(\tan^2\left(\frac{\alpha}{2}\right) - 1\right) + r_c \left(\frac{\alpha}{2}\tan^2\left(\frac{\alpha}{2}\right) + \tan\left(\frac{\alpha}{2}\right) - \frac{\alpha}{2}\right) \tag{4.2}$$

F is the desired focal length. α is the angle between the incident and reflected wave. r_c is the caustic radius. The width of the quasi-parabolic mirror must be larger than the midsection of the mode generator cavity to minimize diffraction losses. The height is selected based on the limited beam waist of the lens, which is defined by the lens diameter. The caustics of the $TE_{34,19}$ and $TE_{40,23}$ modes are similar. Therefore, the identical quasi-parabolic mirror can be used at 170 GHz and 204 GHz with $F = 30$ mm and $r_c = 9.5$ mm.

Coaxial Cavity of the Mode Generator

The cavity for the mode generator consists of a down-taper, a midsection and an up-taper. An increased quality factor is required in comparison to the gyrotron cavity for a more robust mode excitation. There are two different methods to increase the quality factor. First, a steeper down- or/and up-taper to increase the reflected wave, and second, increasing the midsection length. A wider illumination area of the midsection is selected, in terms of the required geometrical width of the quasi-parabolic mirror. Therefore, the midsection of the cavity of the mode generator is chosen to be 22.0 mm. It is much longer compared to the 13.6 mm of the gyrotron cavity. The schematic is presented in Fig. 4.8. The increased length leads to a quality factor of the mode generator cavity of 3266 compared to 1094 at 170 GHz and 4897 compared to 1647 at 204 GHz of the gyrotron cavity.

The operating frequency depends on the perforated, translucent outer wall. Two different cavities are designed to optimize the coupling for each frequency individually. A derivation of the coupling through a translucent wall

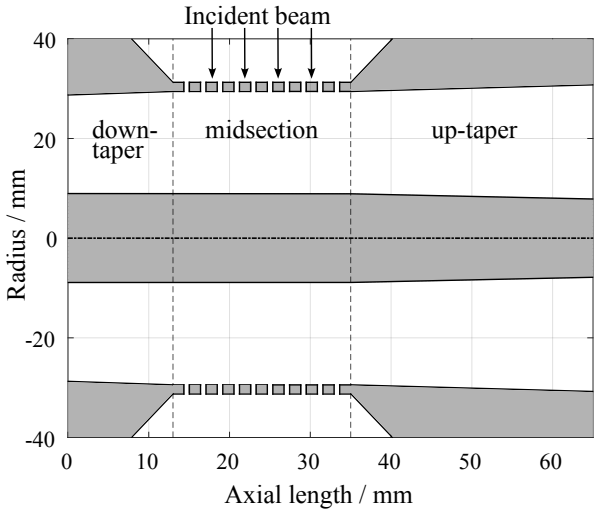

Fig. 4.8: Schematic of the coaxial cavity for the mode generator setup.

is given in Appendix A.5. The diameter of the coupling holes has been set to 0.634 mm at 170 GHz and 0.590 mm at 204 GHz. The diameters are in cut-off and are chosen for a coupling of about -20 dB. Due to the coupling holes the effective cavity radius is slightly larger [138]. In the first publications on quasi-optical mode generators, the coupling holes were placed only in the illuminating region [123, 136]. This results in a cavity without a constant effective cavity radius. The asymmetric cavity leads to an increased counter-rotating amount of the excited mode. Therefore, coupling holes are placed on the complete circumference [137]. The slightly increased effective cavity radius results in a downshift of the frequency. This can be retuned by a reduction of the cavity radius in the design process leading to the cavity radius of 29.415 mm compared to 29.55 mm of the gyrotron cavity.

In the previous work, the outer structure was manufactured from brass, which has good electrical conductivity and therefore low losses compared to other materials. In this work, the cavity is manufactured out of stainless steel, since the cut-off holes in the midsection can be laser cutted. This method has higher precision than the conventionally machining. Therefore, the cut-off holes are almost identical, which reduces also the counter-rotating amount. Later experiments do not show reduced efficiency in terms of the used material.

Each mode generator cavity is built in the coaxial structure containing an additional insert for an improved mode selection process [65, 66]. An estimation about the number of modes that can operate in a waveguide with a fixed radius is given by Eq. (2.37). About 2800 modes at 170 GHz and 4100 modes at 204 GHz are able to propagate considering a cavity radius of $r_{\mathrm{cav}} = 29.415$ mm of the proposed cavity. The mode excitation benefits from a specific choice of the ratio of insert and cavity radius. The ratio is chosen based on the calculated eigenvalue map with the aim to reduce the influence of neighboring modes. The eigenvalue curves for the coaxial setup are given by [65, 66].

$$\frac{Y_m\left(\chi_{m,p}\frac{r_{\text{insert}}}{r_{\text{cav}}}\right)}{Y_m\left(\chi_{m,p}\right)} = \frac{J'_m\left(\chi_{m,p}\frac{r_{\text{insert}}}{r_{\text{cav}}}\right)}{J'_m\left(\chi_{m,p}\right)} \quad . \tag{4.3}$$

J_m and Y_m are the Bessel and Neumann functions of order m. The eigenvalue $\chi_{m,p}$ is the p^{th}-zero of the Bessel function. Figure 4.9 depicts the eigenvalue spectrum at 170 GHz and 204 GHz. An optimal excitation point for the mode generator is at $C = r_{\text{cav}}/r_{\text{insert}} = 3.347$ for the $\text{TE}_{34,19}$ mode at 170 GHz and $C = 3.451$ for the $\text{TE}_{40,23}$ mode at 204 GHz. This corresponds to an insert radius of $r_{\text{insert}} = 8.79$ mm and $r_{\text{insert}} = 8.52$ mm, respectively. It is obvious to see, that the number of modes increase and the distances between adjacent modes decrease with increasing frequency. The inner conductor is still made of brass and mounted with a screw to a Teflon cap which is placed at the end of the down-taper. The benefit of a Teflon cap is a good microwave transparency. Possible unwanted modes are propagating through the Teflon cap and are not reflected back into the cavity. Therefore, those modes do not disturb the excitation and thus do not reduce the purity of the cavity mode.

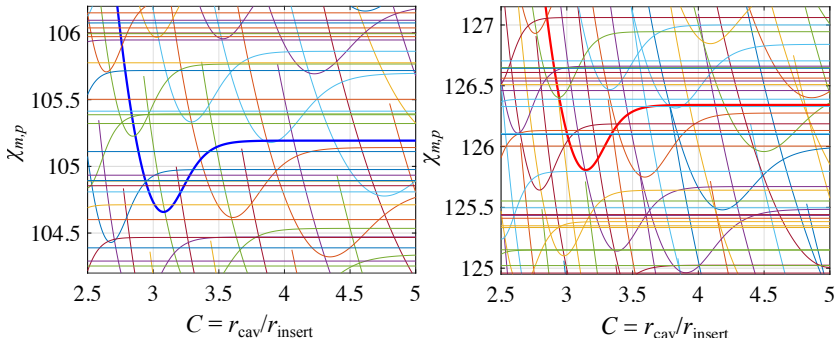

(a) $\text{TE}_{34,19}$ mode. (b) $\text{TE}_{40,23}$ mode.

Fig. 4.9: Eigenvalue spectrum to identify the optimum ratio $C = \frac{r_{\text{cav}}}{r_{\text{insert}}}$ to excite a) $\text{TE}_{34,19}$ mode at 170 GHz (blue) and b) $\text{TE}_{40,23}$ mode at 204 GHz (red).

Non-Linear Up-Taper

A non-linear up-taper is mounted to the end of the cavity for the verification of the generated cavity mode. The shape of the non-linear up-taper is shown in Fig. 4.10. The non-linear up-taper increases the radius of the waveguide without reducing the mode purity [77]. It helps to achieve a sufficient resolution to reliably determine the mode order, because of the limited spatial resolution of the receiving antenna of ≈ 1 mm. The relative mode contents along the non-linear up-taper at 170 GHz and 204 GHz are plotted in Fig. 4.11. The calculations, which have been performed using the scattering matrix code show excellent performance.

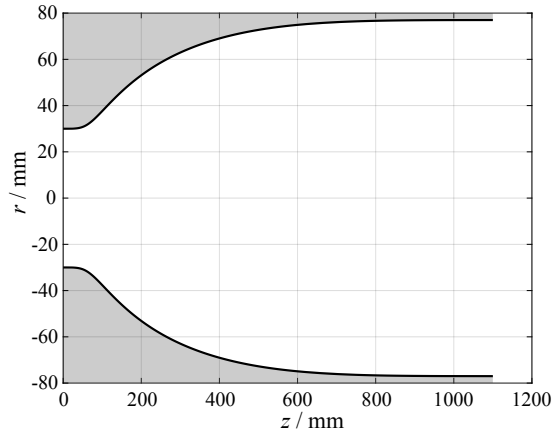

Fig. 4.10: Radius profile of the non-linear up-taper at the output of the quasi-optical mode generator.

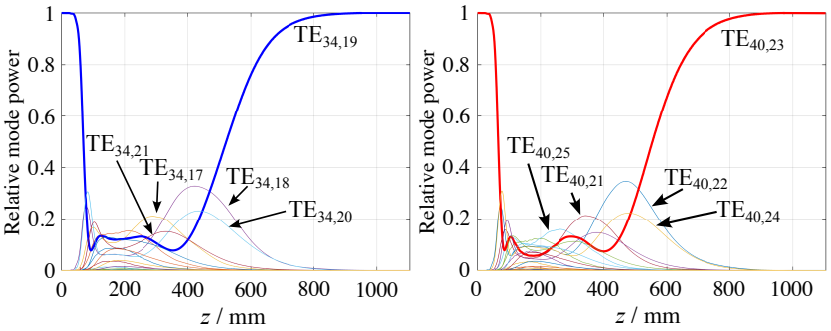

(a) 170 GHz. (b) 204 GHz.

Fig. 4.11: Relative power of the modes along the z-axis of the non-linear up-taper for the a) $TE_{34,19}$ mode at 170 GHz and b) $TE_{40,23}$ mode at 204 GHz.

4.1.3 Novel Automated Measurement Procedure

The most time-consuming and challenging task is to excite the operating high-order cavity mode with high purity and low counter-rotational amount. In former times, the quasi-parabolic mirror was set manually. These manually adjustable sliding units have low accuracy and high repeatability errors. In addition, as the operating frequency increases, the required adjustment accuracy increases. Therefore, the existing sliding units are replaced by electronically movable high-precision linear-drivers (LTM 60-100-HSM [139]) for the horizontal and vertical positioning each and a goniometer (MOGO 65-40-65-HiSM [140]) for the tilt. The high-precision linear drivers have a position error of $< 25\ \mu m/100$ mm and a bidirectional repetition failure of $< 15\ \mu m$. The goniometer has a bidirectional accuracy of $< 0.02°$ in a range of $\pm\ 20°$. These upgrades were the first step of an automation process of the mode generator setup [141]. The flow chart of the automatized mode generator adjustment procedure is given in Fig. 4.12. The steps of the procedure are discussed in detail in the following.

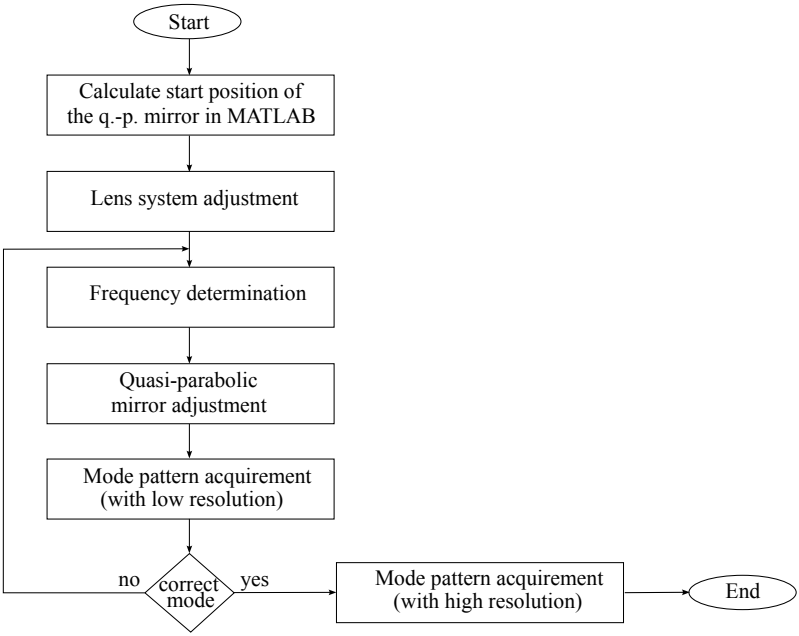

Fig. 4.12: Flow-chart of automatized adjustment of the mode generator setup.

Estimation of Starting Parameters for Automation Process

The feature of the horn antenna, the lens system, the quasi-parabolic mirror and the cavity are implemented in MATLAB [142] as a 2D model. The theoretical distances between 1) the horn antenna and the lens system, 2) the lens system and quasi-parabolic mirror and 3) the quasi-parabolic mirror and cavity are calculated.

To 1): This distance has to be optimized that the complete radiated beam is focused by the lens. This guarantees an illumination of the whole quasi-parabolic mirror and thus increase the efficiency.

To 2): The focused beam can be represented by Gaussian optics. A plane phase front has to be applied at the position of the quasi-parabolic mirror.

The distance between the lens system and the quasi-parabolic mirror is calculated at which this condition is met.

To 3): An initial starting position of the distance between the quasi-parabolic mirror and the cavity is calculated as presented in Fig. 4.7.

Adjustment of the Lens System

The combination of the Potter horn and the lens system has to be verified. The theoretically calculated distances of 1) and 2) from the previous step are validated experimentally. A measurement of the E-field intensity and phase pattern of the Potter horn and the lens system at 204 GHz are depicted in Fig. 4.13. A clear astigmatic field pattern is visible. Therefore, spillover losses are reduced and thus, the efficiency is increased. The relevant illumination part at the quasi-parabolic mirror is 20 mm in horizontal and 30 mm in vertical direction. A phase deviation of 5° in horizontal x-direction and 12° in the vertical y-direction at 204 GHz is measured in the relevant area. Therefore, an almost plane phase front is validated at the position of the quasi-parabolic mirror.

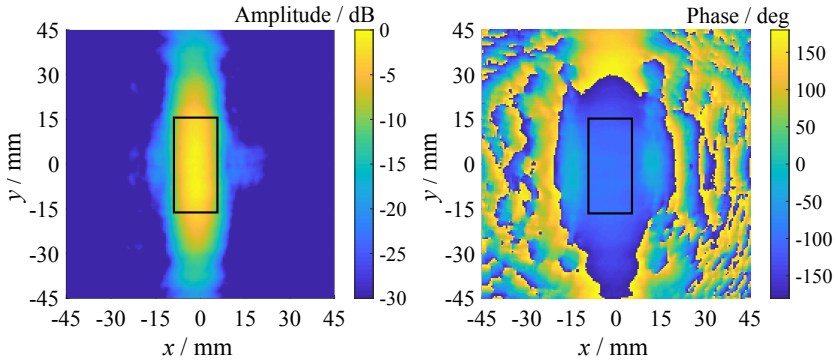

(a) E-field intensity (b) Phase

Fig. 4.13: Measured a) E-field intensity and b) phase pattern generated by the Potter horn and the lens system at 204 GHz.

Determination of the Operating Frequency

The operating frequency can only be estimated at the beginning. It is due to the manufacturing tolerances and the effect of the cut-off holes in the cavity wall. The transmission is measured in a given frequency band to identify resonances, which correspond to operating frequencies of specific modes. A measurement is depicted in Fig. 4.14. Therefore, the quasi-parabolic mirror is set according to the calculations. The receiving standard pick-up antenna is positioned at the caustic of the desired mode. Figure 4.14 shows resonances at 203.37 GHz, 204.07 GHz and 204.86 GHz. However, at this stage of the measurement procedure, it is not known which mode corresponds to the measured resonances. The frequency having the highest amplitude peak (here: 204.071 GHz) is selected for the next step.

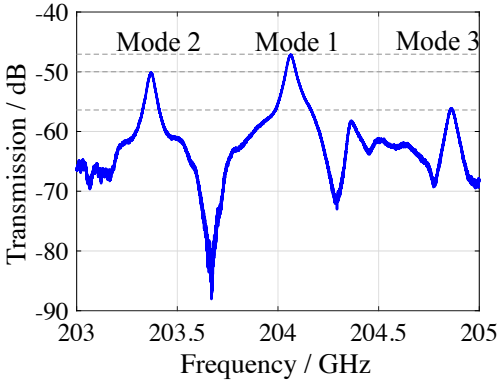

Fig. 4.14: Amplitude measurement in the frequency range around 204 GHz. The receiving standard waveguide antenna is positioned on the field maximum of the desired mode. The quasi-parabolic mirror is not yet optimized in this step.

Adjustment of the Quasi-Parabolic Mirror

The position of the quasi-parabolic mirror is adjusted to excite the cavity mode with a high purity and the correct rotation. The adjustment is highly mode selective. The receiving antenna is positioned at the field maxima of the desired mode. A field intensity pattern is recorded for different positions of the quasi-parabolic mirror, which is varied in x- and y-direction with a step size of $< 100\ \mu$m and the angle is varied in 0.2° steps. Figure 4.15 shows as an example a measurement of the field intensity at two different angles. The position of the high-precision linear drivers is selected to provide the highest field amplitude.

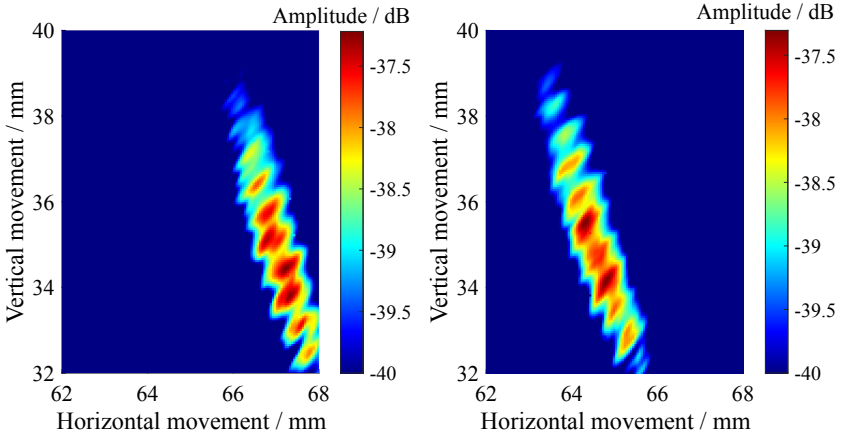

(a) Goniometer set to $\varphi = -1°$.

(b) Goniometer set to $\varphi = -2°$.

Fig. 4.15: E-field intensity pattern at different positions of the quasi-parabolic mirror and angle of the goniometer of a) $\varphi = -1°$ and b) $\varphi = -2°$ at an operating frequency of 204.07 GHz. The receiving standard waveguide antenna is positioned on the field maximum of the desired mode.

Acquisition of the Mode Pattern

First, a low-resolution mode pattern with a pixel size of 0.5 x 0.5 mm is recorded. The selected pixel size is sufficient for successful computer-based mode evaluation because the main characteristics can be resolved. This intermediate step is used to reduce the adjustment time. If the correct mode has been excited, a high-resolution mode pattern with a pixel size of 0.2 x 0.2 mm is recorded. However, if the excited mode is not the correct one, an iterative process is started and the next possible frequency is selected according to Fig. 4.14. The success and time of this procedure depends strongly on the starting position of the quasi-parabolic mirror. In general, three cases can be defined in this procedure. Firstly, the selected operating frequency fits to the desired mode. In this case, the mode is successfully excited after the first iteration. Secondly, the selected operating frequency does not fit to the desired mode. In this case, in minimum two iterations are required and in maximum the number of resonances, which are measured in the frequency bandwidth. Thirdly, the starting value of the position of the quasi-parabolic mirror is outside a range in which the mode cannot be excited. In this case, the measurement procedure will fail. This can be avoided by implementing some kind of knowledge after the first iteration. The measurement in the first iteration is similar to that described before. It is important to excite a mode with sufficient mode quality in the first iteration so that the mode evaluation process can determine the mode order. The procedure is terminated after the first iteration if the correct mode is excited. If not, equation (4.4) can be considered to unambiguously calculate the operating frequency of the desired mode f_{mode}. This formula is approximated by the equation (2.23) taking into account constant mechanical geometrical parameters.

$$\frac{f_{\mathrm{initial}}}{\chi_{\mathrm{initial}}} \approx \frac{f_{\mathrm{mode}}}{\chi_{\mathrm{mode}}} \tag{4.4}$$

f_{initial} is the determined frequency and χ_{initial} is the eigenvalue of the validated mode in the first iteration. χ_{mode} is the eigenvalue of the desired mode and can be calculated since it depends only on the geometrical parameters. A deviation from the theoretical frequency of maximal 1 MHz is obtained using the equation (2.23). This proves the validity of the proposed method.

The effect of the translucent cavity wall can be neglected here, since all eigenvalues in the given frequency range are affected equally. This leaves one unknown in the system, which is the position of the quasi-parabolic mirror, which can be solved uniquely. This upgrade makes the algorithm independent of the choice of starting positions. In addition, the upgrade limits the maximum number of iterations to two for successful excitation of the desired mode. The optimized measurement procedure results in a time saving of more than 94 % for the excitation of the $TE_{28,10}$ mode operating at 140 GHz with high purity compared to the manual adjustment [143].

Mode Evaluation Techniques

The implemented mode evaluation techniques are discussed based on the example of the $TE_{28,8}$ mode operating at 140 GHz. This mode of lower order results in a better readability of the shown graphs. A theoretical depiction of the absolute values of the non-rotating field intensity of the $TE_{28,8}$ mode is shown in Fig. 4.16a and a simulation of the rotating field intensity pattern is presented in Fig 4.16b. The simulation includes the effect of the measurement equipment onto the pattern. The receiving antenna is a standardized waveguide guiding the linear polarized fundamental $TE_{1,0}$ mode. This results in a measurement in cartesian coordinates instead of polar coordinates as described with equations (2.19) and (2.20). The polarization of the receiving antenna affects the mode pattern depending on the orientation, since the receiving antenna measures only one polarization. In the horizontal direction at $\varphi = 0°$ and $\varphi = 180°$ there is a dependence of $J'_m(\frac{\chi_{m,p} \cdot r}{r_{\text{cav}}})$, whereas in the vertical plane at $\varphi = 90°$ and $\varphi = 270°$, there is a dependence of $J_m(\frac{\chi_{m,p} \cdot r}{R})$ [144]. This shows that the graph is not rotational symmetric. The mode pattern in the cross diagonals is blurred, since the field components E_r and E_φ are measured simultaneously.

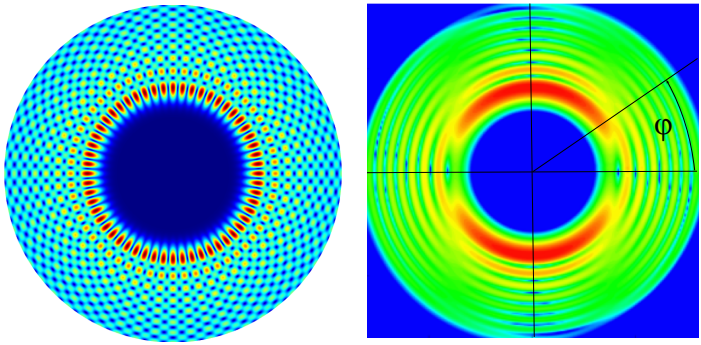

(a) Calculated non-rotating field intensity pattern.

(b) Calculated rotating field intensity pattern.

Fig. 4.16: a) Calculated non-rotating E-field intensity pattern of the $TE_{28,8}$ mode and b) calculated rotating E-field intensity pattern considering the measurement equipment for cold tests of the vertical polarization.

A measurement of the $TE_{28,8}$ mode at 140.0 GHz is presented in Fig. 4.17. Five different evaluation techniques are implemented in the post-processing, to determine

(i) the radial mode index p,

(ii) the azimuthal mode index m,

(iii) the scalar mode content ψ,

(iv) the quality factor $Q_{3\,\mathrm{dB}}$,

(v) the amount of the counter-rotating mode.

To (i): The radial mode index p can be determined by counting the number of rings in the radial direction. A cut through the E-field intensity pattern is shown in Fig. 4.18. The measured and the simulated patterns are compared. The maximum amplitude levels differ ΔE, which is caused by a 12° rotation of the receiving antenna. The rotation is resolved by optimizing the 3D measurement arm.

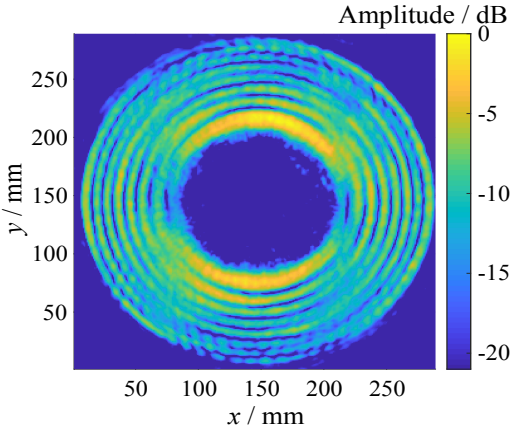

Fig. 4.17: Measured E_y-field intensity pattern of the rotating $TE_{28,8}$ mode operating at 140.0 GHz with a pixel size of 0.25x0.25 mm [144].

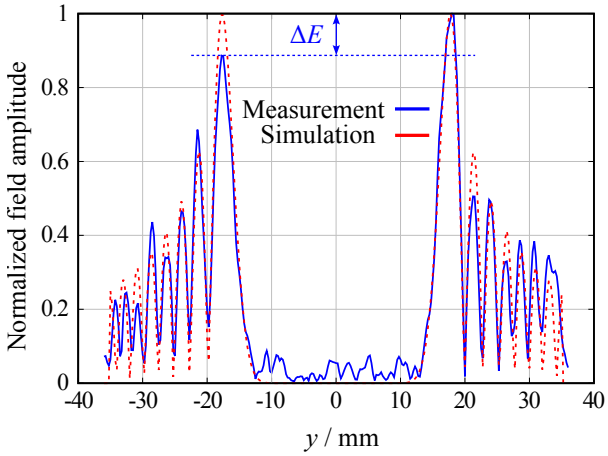

Fig. 4.18: Vertical cut of the E_y-field intensity mode pattern of the $TE_{28,8}$ mode operating at 140.0 GHz [144].

To (ii): The azimuthal mode index m is calculated by evaluating the phase jumps in the azimuth. Figure 4.19 depicts a measured phase pattern of the $TE_{28,8}$ mode. The algorithm can determine whether a co-rotating or counter-rotating mode is excited based on the phase profile. The phase in the center and outside of the mode pattern is random because field components do not exist there. In post-processing, the algorithm counts the number of phase jumps on a given circle. The circle is indicated in black in Fig. 4.19. Two different design criteria are defined for a robust evaluation, 1) counting the number of phase jumps from +180° to -180° and 2) counting the number of zero-crossings divided by two. As published in [128], the counted phase periods are related to the azimuthal mode index m. The number of phase periods is equal to $m - 1$ for measuring one polarization in Cartesian coordinates. In contrast, the number of phase periods is equal to m for a measurement in Polar coordinates. This assumption can be proven starting from the equations (2.19) and (2.20) for E_r and E_φ. The amplitudes are considered to be $a = -m/r \cdot J_m(\chi/r_{cav} \cdot r)$ and $b = \chi/r_{cav} \cdot J'_m(\chi/r_{cav} \cdot r)$. The derivation is done for a fixed z-position at $z = 0$. In the following, the effect

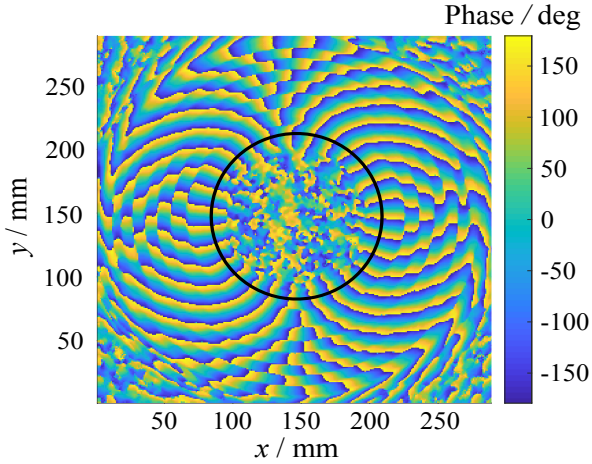

Fig. 4.19: Measured phase pattern of the $TE_{28,8}$ mode operating at 140.0 GHz. The black circle indicates the circle of evaluation.

is demonstrated for the vertical polarization, considering the coordinate transformation resulting in

$$E_y = a \cdot \exp(-j \cdot m \cdot \varphi) \cdot \sin(\varphi) + b \cdot \exp(-j \cdot m\varphi) \cdot \cos(\varphi) \quad . \tag{4.5}$$

The trigonometric terms can be expressed by exponential function and under the assumption $a = b$, which results in

$$\begin{aligned} E_y = a \cdot \exp(-j \cdot m \cdot \varphi) \cdot \frac{\exp(j\varphi) - \exp(-j\varphi)}{2} \\ + a \cdot \exp(-j \cdot m\varphi) \cdot \frac{\exp(j\varphi) + \exp(-j\varphi)}{2} \quad , \end{aligned} \tag{4.6}$$

$$E_y = a \cdot \exp(-j \cdot \varphi(m-1)) \quad . \tag{4.7}$$

The argument of this equation is set to zero for calculation of the zero-crossing given by

$$\arg(E_y) = \arctan\left(\frac{\sin(-\varphi(m-1))}{\cos(-\varphi(m-1))}\right) = 0 \tag{4.8}$$

$$\varphi = \frac{\pi \cdot n}{m-1} \quad n \in \mathbb{Z} \tag{4.9}$$

Equation (4.9) confirms that the E_y-field pattern has $2(m-1)$ zero crossings and $m-1$ phase jumps. In [144], the equation is solved considering $a \neq b$.

The difference between the unwrapped phase around the circle and a linear phase is presented in Fig. 4.20. The mentioned 12° rotation of the receiving antenna is observed in the phase difference. The radial field component E_r is measured in the non-highlighted area. So, the phase difference is almost constant. These areas are around −102° (ideally −90°) and +78° (ideally +90°). The increase and decrease in phase are due to the fact that the azimuthal field component E_φ is additionally measured with a phase difference of 90°.

To (iii): The scalar mode content is calculated using the measured E-field E_{meas} in comparison to the theoretical E_{theory} of the $\text{TE}_{m,p}$ mode using

$$\psi = \frac{\int\int_S |E_{\text{meas}}| \cdot \left|E_{\text{theory}}\right| \, dA}{\sqrt{\int\int_S |E_{\text{meas}}|^2 \, dA \cdot \int\int_S \left|E_{\text{theory}}\right|^2 \, dA}} \tag{4.10}$$

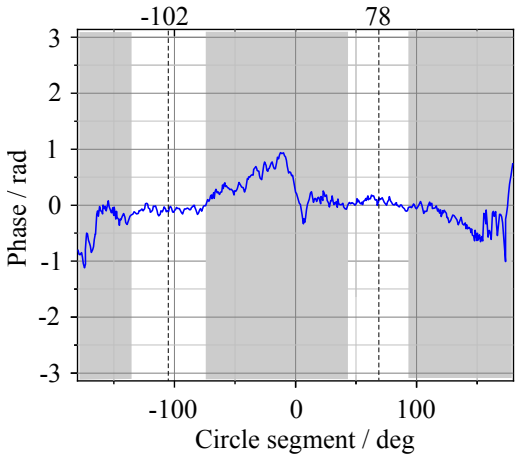

Fig. 4.20: Difference between the unwrapped phase on the given circle and a linear phase [144].

In case of the $TE_{28,8}$ mode the scalar mode content amounts to $\psi = 94.5\,\%$. The mode diverges between the end of the non-linear up-taper and the receiving antenna. This and any rotation of the receiving antenna will affect the scalar mode content.

To (iv): The counter-rotating amount P_-/P_+ is defined by the power ratio between the power of the unwanted counter-rotating P_- and the desired co-rotating mode P_+. It can be calculated by [69]:

$$\frac{P_-}{P_+} = \left(\frac{SWR - 1}{SWR + 1}\right)^2 \tag{4.11}$$

with

$$\Delta = 20 \cdot \log_{10}(SWR) \quad \text{in dB}\,.$$

SWR is the standing wave ratio. Δ is the difference between maximum and minimum power in φ-direction. A high percentage of the counter-rotating mode results in the presence of multiple nodes along the circumference. The number of nodes along the circumference corresponds to the azimuthal mode index m. The counter-rotating amount of the given measurement is 0.33 %. It cannot become zero due to the non-symmetrical mode excitation

To (v): The quality factor $Q_{3\,\mathrm{dB}}$ of the measured coaxial cavity is calculated with the resonance frequency f_{res} to the 3-dB bandwidth $B_{3\,\mathrm{dB}}$.

$$Q_{3\,\mathrm{dB}} = \frac{f_{\mathrm{res}}}{B_{3\,\mathrm{dB}}} = 2548 \tag{4.12}$$

The measured quality factor is in very good agreement with the simulation of 2533 for the $\mathrm{TE}_{28,8}$ mode.

This automatized measurement procedure with the evaluation algorithms is validated successfully. The quasi-optical mode generator is used to excite several modes at different frequencies. Those are the $\mathrm{TE}_{20,8}$ mode at 105 GHz [145], the $\mathrm{TE}_{28,8}$ mode [146] and the $\mathrm{TE}_{28,10}$ mode [36], [144] operating both at 140 GHz, the $\mathrm{TE}_{36,12}$ mode at 175 GHz [143], the $\mathrm{TE}_{34,19}$ mode at 170 GHz and the $\mathrm{TE}_{40,23}$ at 204 GHz [147], [148]. In [144], a time saving of up to 94 % has been calculated for the excitation of the $\mathrm{TE}_{28,10}$ mode using the automatized mode generator compared to manual adjustment.

4.1.4 Tolerance Analysis of the Mode Generator Setup

A tolerance study is performed to investigate the influence of the measurement arm, the temperature changes of the cavity and the influence of covering the quasi-optical mode generator with absorber material.

Influence of Tolerances coming from the 3D Measurement Arm

The 3D measurement arm can operate in continuous and in step mode. The continuous mode provides the shortest measurement time. However, this mode suffers from high pixel position errors and a blurring of the mode patterns due to the averaging of the measurement points. Therefore, the step mode is preferred. In step mode, the 3D measurement arm vibrates due to the permanent start and stop movement. The vibrations of two measuring arms with different lengths of 890 mm and 600 mm are investigated. 600 mm corresponds to the shortest possible length at which the full range of motion can still be used.

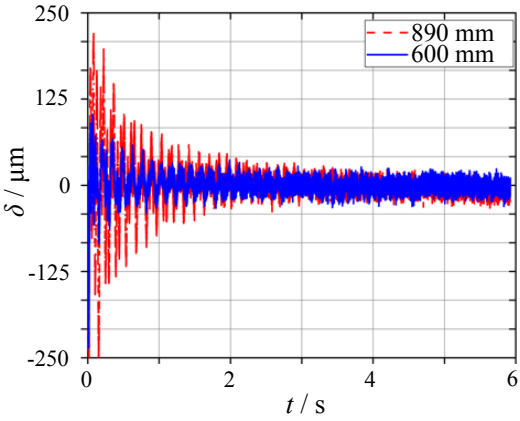

Fig. 4.21: Deflection δ of the measurement arm due to the stepwise driving with step size of 0.25 mm.

The transient behavior of the measurement arm is recorded using a distance measurement tool. The arm moves in steps of 250 µm. The vibration is measured for 6 s after the arm stops at the given position. Figure 4.21 compares the vibrations of the two measurement arms. The vibration fades away at around 2 s. The deflection δ is largest after stopping and corresponds to a maximum of $\approx \pm$ 206 µm. It is a trade-off between vibration and measurement time (time per pixel). At a pause of 0.5 s, the deflection of the 890 mm long arm is $\approx \pm$120.5 µm and that of the 600 mm long arm is $\approx \pm$80 µm. The total deviation of the 600 mm long arm with a pause of 0.5 s is $\approx$ 160 µm and thus less than the step size of 250 µm. The 600 mm long arm is selected.

Influence of a Temperature Variation During a Measurement

A measurement of the radiated mode patterns with a resolution of 250 x 250 µm takes up to 48 h for the $TE_{28,8}$ mode and 120 h for the $TE_{34,19}$ and $TE_{40,23}$ modes. During this time the room conditions may change, e.g. due to direct sunlight. This effect needs to be investigated in relation to the high quality factors of the mode generator cavities. A temperature sensor (BME280) is installed on the cavity. The temperature data is stored on a logging system

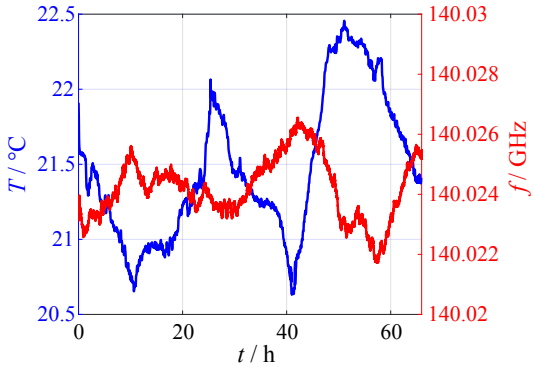

Fig. 4.22: Temperature profile and the resulting resonance frequency change during ≈3 days measurement time.

(Arduino Mega and SD card). A temperature profile is recorded over 3 days. The maximum temperature change is achieved with direct sunlight during the day and open windows at night. This implicit a possible worst-case scenario. In addition to the temperature, the resonance frequency is recorded for the validation. Figure 4.22 shows the effect of a temperature variation on the operating frequency. The characteristic values are summarized in Tab. 4.2. A maximum temperature drift of $\Delta T = 2.1$ °C occurs. This results in a change in operating frequency of 4 MHz. The given frequency drift causes an amplitude drop of 0.07 dB, which is negligible. An effect on the measurement can be seen at a frequency drift of ± 14 MHz, corresponding to a temperature drift of $\Delta T \approx \pm 7.2$ °C.

Table 4.2: Characteristic points for the temperature and the related measured quality factor.

Time/ h	Temperature / °C	Frequency / GHz
10.6	20.7	140.026
25.8	22.0	140.023
41	20.6	140.026
53	22.3	140.022

Covering the Setup with Absorber Material

The translucent cavity wall couples only small fraction of the electromagnetic wave into the cavity due to the dimensions of the holes. The reflected wave can propagate into the setup and disturb the excitation of the desired cavity mode. The effect is enhanced because the quasi-optical mode generator is mainly made of metal. Covering the quasi-optical mode generator with absorber material has a minor effect on the excited mode in the step of its adjustment. However, the assembly is rotated by 90° after adjustment for the verification of the quasi-optical output coupler. Then, the bottom side is also terminated by the metal of the table. Previously, this side was open to free space where the electromagnetic beam could propagate. This assembly strongly affects the mode and therefore the measurement of the quasi-optical output coupler. Figure 4.23 compares the measurement with a) not covering the beam path and b) covering the beam path with absorber material.

In addition, three identical launchers were verified using a quasi-optical mode generator. The patterns of the E-field intensity distribution differ more from launcher to launcher than from different measurements using the same launcher. This concludes that the effect of the manufacturing tolerances of the launcher can be measured.

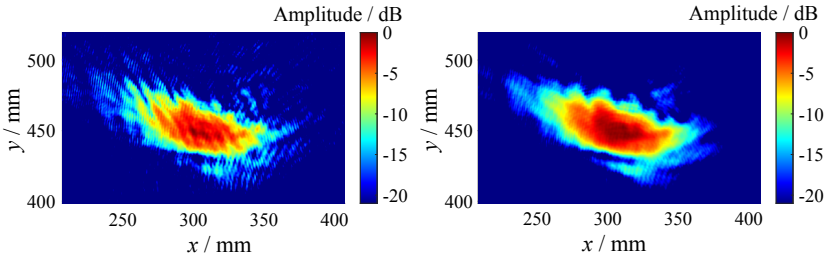

(a) Not covered by absorber material

(b) Covered by absorber material.

Fig. 4.23: Measured E-field intensity of a launcher operating at 105 GHz and a) not covered and b) covered by absorber material.

4.1.5 Verification of the Operating Modes and the Quasi-Optical Mode Coupler at 170 GHz and 204 GHz

Section 4.1.2 discusses a mode generator design for the $TE_{34,19}$ mode at 170 GHz and the $TE_{40,23}$ mode at 204 GHz. Then, the automated process and a tolerance study was presented. In the following, the relevant modes are excited and are used to verify the designed 170/204 GHz quasi-optical output coupler.

Excitation of the $TE_{34,19}$ mode and the $TE_{40,23}$ mode

The automated mode excitation procedure is used to excite the $TE_{34,19}$ and $TE_{40,23}$ modes. In the first step, the nominal operating frequencies are determined to be 170.325 GHz for the $TE_{34,19}$ mode and 204.071 GHz for the $TE_{40,23}$ mode. A full mode pattern can be taken after the automated adjustment of the quasi-parabolic mirror. Figure 4.24 and Fig, 4.25 show the E_y-field intensity and the phase pattern of the $TE_{34,19}$ and $TE_{40,23}$ modes with a pixel size of 250 x 250 µm.

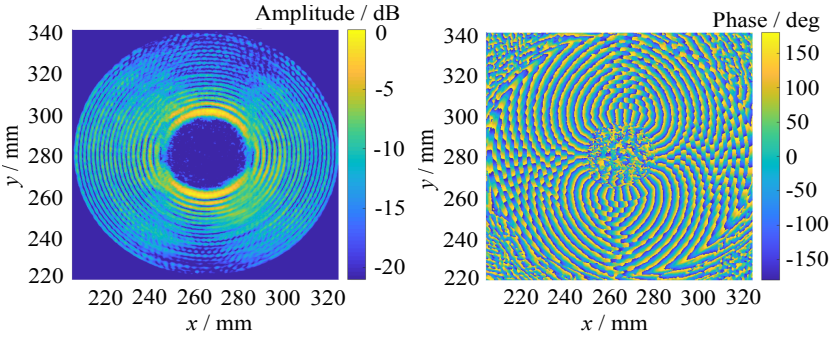

(a) E_y-field intensity pattern (b) Phase pattern

Fig. 4.24: Measured a) E-field intensity and b) phase pattern for vertical polarization of the $TE_{34,19}$ mode operating at 170.325 GHz with a pixel step width of 0.25 mm in both directions.

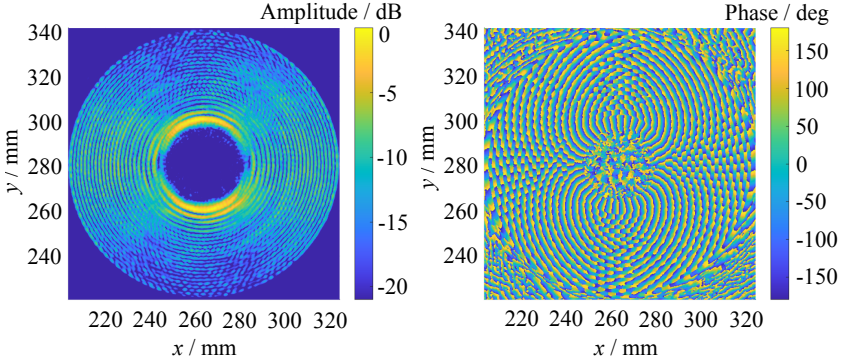

(a) E-field intensity pattern (b) Phase pattern

Fig. 4.25: Measured a) E-field intensity pattern and b) phase for vertical polarization of the $TE_{40,23}$ mode operating at 204.071 GHz with a pixel step width of 0.25 mm in both directions.

The number of rings in the E_y-field intensity patterns correspond to the radial mode index p, which is 19 at 170 GHz and 23 at 204 GHz. The azimuthal mode index m is determined by the number of phase jumps plus one and the azimuthal mode index is determined by 34 and 40, respectively. The scalar mode content ψ and quality factor $Q_{3\,\mathrm{dB}}$ are determined to be $\psi = 92.1$ % and $Q_{3\,\mathrm{dB}} = 3603$ at 170 GHz and $\psi = 91.8$ % and $Q_{3\,\mathrm{dB}} = 4835$ at 204 GHz. The counter-rotating amount has been calculated to be below < 0.5 % at both frequencies. The generation of the $TE_{34,19}$ mode has already been described in [149]. A counter-rotating amount of up to 0.7 % was observed there. The quality of the excited modes is, to the best knowledge of the author, highest using the optimized quasi-optical mode generator. The high-order rotating $TE_{40,23}$ mode is with its eigenvalue of 126.3 the world's highest ever excited rotating mode in cold tests.

Verification of the Dual-Frequency Quasi-Optical Output Coupler

The cavity modes for 170 GHz and 204 GHz are used as input to verify the quasi-optical output coupler described in Section 3.3.3. The non-linear

up-taper is replaced by the launcher, as it is shown in Fig. 4.26. The step size of the 3D measurement arm is set to 1 mm in both directions. The measurements are performed at the selected frequencies of 170.325 GHz for the $TE_{34,19}$ mode and 204.071 GHz for the $TE_{40,23}$ mode. Since the contours of the mirrors follow a quadratic function, the most critical component in the manufacturing process of the quasi-optical output coupler is the launcher. Therefore, the first step is to investigate the performance of the launcher. Figure 4.27a and Fig. 4.28a present the *E*-field intensity of the horizontal polarization (x-direction) of the launcher aperture at 170.325 GHz and 204.071 GHz. The measurements are in very good agreement with the simulations. The vertical disruptions are caused by the counter-rotating part of the excited mode, which cannot be prevented. The measured pattern at the launcher aperture gives a first indication about the performance. Figure 4.27b and Fig. 4.28b show the measured phase distribution.

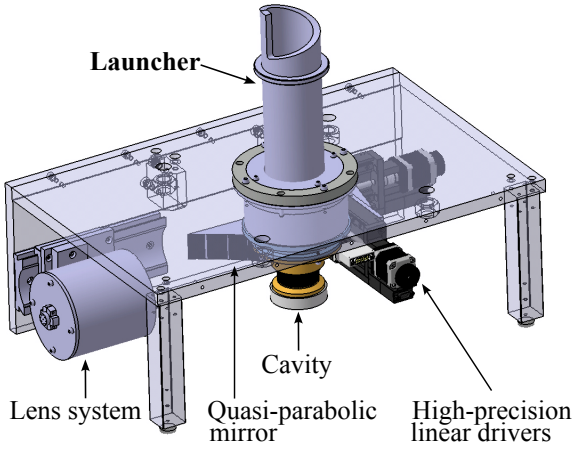

Fig. 4.26: 3D schematic of the measurement setup for verification of the launcher.

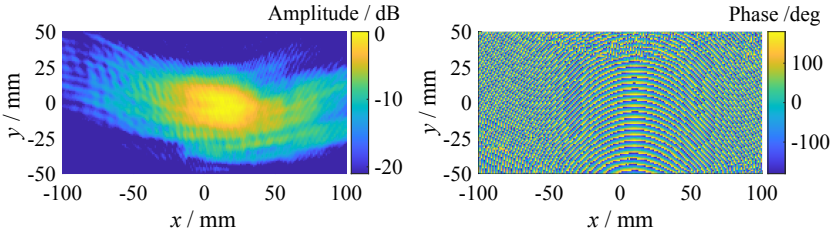

(a) E-field intensity. (b) Phase.

Fig. 4.27: E-field intensity (a) and phase pattern (b) of the x-polarization at 170.33 GHz of the launcher aperture. The pixel step width is selected by 1 mm in both directions.

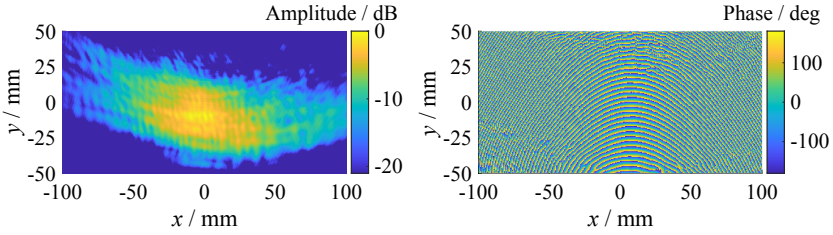

(a) E-field intensity. (b) Phase.

Fig. 4.28: E-field intensity (a) and phase pattern (b) of the x-polarization at 204.07 GHz of the launcher aperture. The pixel step width is selected by 1 mm in both directions.

Figure 4.29 depicts the patterns at the launcher aperture if the counter-rotating mode is excited. The mode is not converted properly and the beam is not focused. It is not possible to compare the amplitude levels of the electromagnetic wave emitted from the launcher by the co-rotating and counter-rotating modes.

A conclusive statement about the performance of the designed quasi-optical output coupler is only possible by using the launcher and all three mirrors. Figure 4.30 presents a photo of the 170/204 GHz dual-frequency quasi-optical output coupler. The alignment of all components and the virtual gyrotron axis is ensured by mounting them on the mirror plate of the gyro-

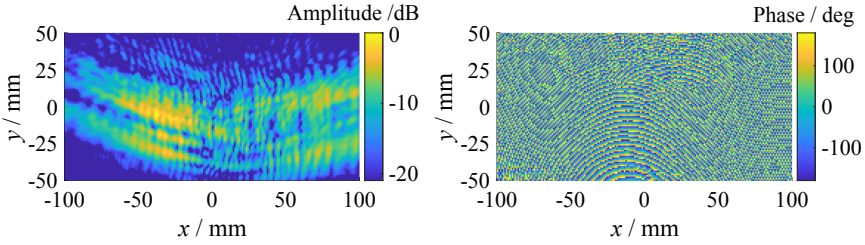

(a) E-field intensity. (b) Phase.

Fig. 4.29: E-field intensity (a) and phase pattern (b) of the x-polarization at 204.07 GHz of the launcher aperture. The pixel step width is selected by 1 mm in both directions. The launcher is fed with the counter-rotating $TE_{-40,23}$ mode.

tron. The measurements at each individual mirror position are discussed in Appendix A.3. Most important is the measurement at the gyrotron window plane. The distance from the gyrotron window plane to the gyrotron axis is 300 mm. The position of the window center in the direction of the gyrotron axis corresponds to the center of the third mirror. Figure 4.31 and Fig. 4.32 compare the E-field intensity and phase patterns of the simulation and the measurement for the quasi-optical output coupler at 170.325 GHz, respectively. Figure 4.33 and Fig. 4.34 compare the E-field intensity and phase patterns of the simulation and a measurement at 204.071 GHz. The measured patterns are in very good agreement with the simulations. The results are summarized in Tab. 4.3. The higher background intensity in the amplitude measurement is due to the fact that a mode with 100 % purity cannot be excited.

Table 4.3: Comparison of measurement results with simulations at 170 GHz and 204 GHz.

Parameter	170 GHz		204 GHz	
	Sim.	Meas.	Sim.	Meas.
Scalar mode content / %	98.8	97.8	98.6	98.5
Vectorial mode content / %	97.5	95.0	96.7	95.0
Beam waist $w_{0,x}$ / mm	21.57	25.66	19.27	24.2
Beam waist $w_{0,y}$ / mm	24.63	24.15	23.65	22.41
Beam shift in x / mm	4.5	2.2	-3.7	-0.1
Beam shift in y / mm	4.0	1.8	-1.8	0.1

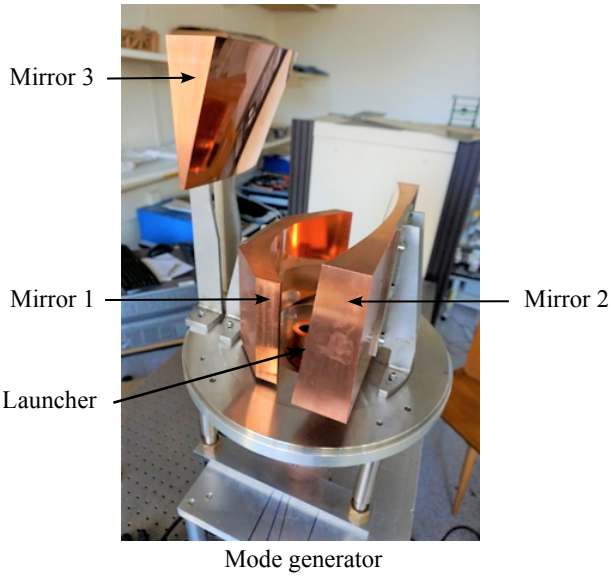

Fig. 4.30: Photo of the assembled quasi-optical output system, consisting of the launcher and three mirrors, on the mode generator.

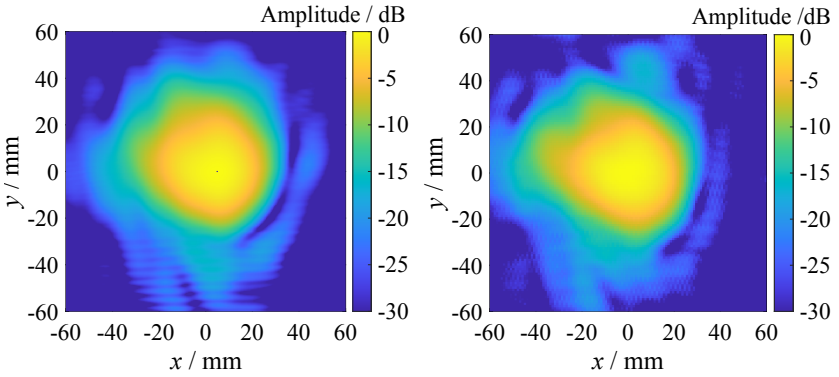

(a) Simulation. (b) Measurement.

Fig. 4.31: Comparison of simulated (a) and measured (b) *E*-field intensity of the horizontal polarization at 170.325 GHz at the position of the gyrotron window with a pixel step width of 1 mm in both directions.

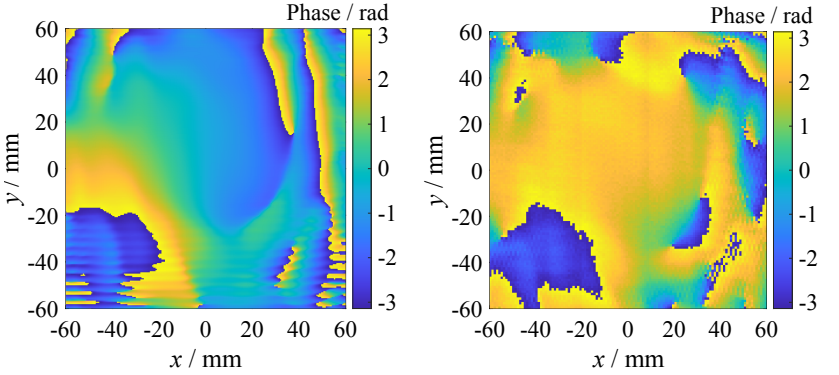

(a) Simulation. (b) Measurement.

Fig. 4.32: Comparison of simulated (a) and measured (b) phase pattern of the horizontal polarization at 170.325 GHz at the position of the gyrotron window with a pixel step width of 1 mm in both directions.

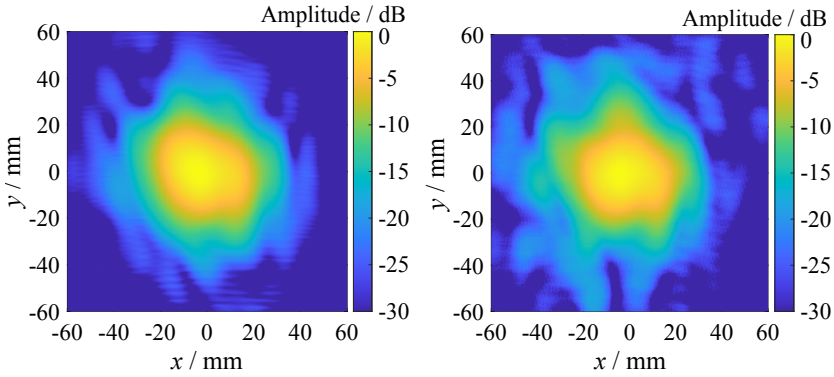

(a) Simulation. (b) Measurement.

Fig. 4.33: Comparison of simulated (a) and measured (b) E-field intensity of the horizontal polarization at 204.071GHz at the position of the gyrotron window with a pixel step width of 1 mm in both directions.

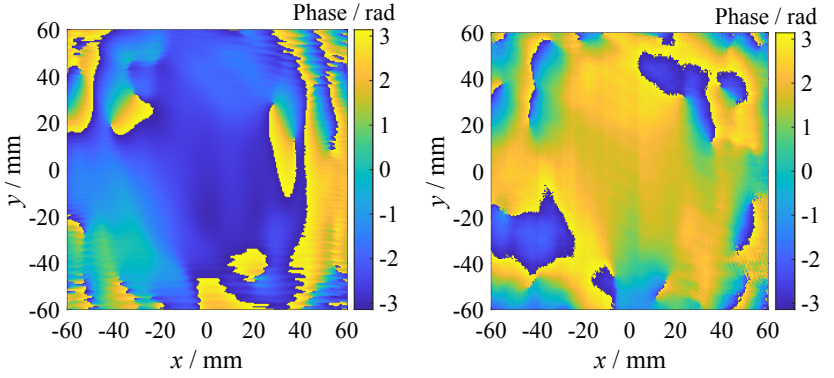

(a) Simulation. (b) Measurement.

Fig. 4.34: Comparison of simulated (a) and measured (b) phase pattern of the horizontal polarization at 204.071 GHz at the position of the gyrotron window with a pixel step width of 1 mm in both directions.

In conclusion, the measurement results confirm that the dual-frequency 170/204 GHz quasi-optical output coupler is expected to operate correctly in gyrotron experiments. The measurements are in excellent agreement with the simulations. The $TE_{40,23}$ mode is the mode with the world's highest eigenvalue ever excited in cold tests. The upgrade of the quasi-optical output system provides the excitation of co- and counter-rotating modes with a high purity. In addition, the measurement tolerances are below the manufacturing tolerances of the launcher.

4.1.6 Possible Future Method for Mode Excitation

Considering e.g. [150, 151], the trend goes towards operating frequencies of gyrotrons above 200 GHz. The eigenvalue of the modes increases with increasing operation frequency at a given cavity radius. This can be seen in the mode series of the KIT 2 MW coaxial-cavity gyrotron. The corresponding eigenvalues are $\chi_{28,15} = 84.0$ at 136 GHz, $\chi_{34,19} = 105.2$ at 170 GHz, $\chi_{40.23} = 126.3$ at 204 GHz and $\chi_{48,26} = 146.8$ at 238 GHz. Excitation of a gyrotron cavity mode with high purity becomes even more challenging with increasing operating frequency due to a denser mode spectrum and thus, increased mode competition. A concept for a cavity to improve the output mode purity is discussed in [152]. The cavity provides a step in the cavity section. This transforms the mode according to the step width into a mode with the same azimuthal mode index but a different radial mode index. The proposed effect is valid for all axial symmetric radius steps [153].

For example, with the already existing $TE_{40,23}$ mode generator operating at 204 GHz the $TE_{40,25}$ mode at also 204 GHz could be excited just with a waveguide radius step. The approach is in terms of its passive structure reciprocal. This means that the same step converts the $TE_{40,25}$ mode into the $TE_{40,23}$ mode. The method could be beneficial for future EU DEMO-relevant cavity modes operating at frequencies above 200 GHz. However, this needs to be verified experimentally.

4.2 Characterization of Gyrotron Windows

A dielectric output window is used in the gyrotron to separate between vacuum and air condition while coupling out the Gaussian microwave beam with minimal absorption and reflection. In the following, a characterization method for dielectric window disks is described.

Other dielectric materials are used in the gyrotron beam tunnel between the indented metal and absorbing ceramic disks for the suppression of parasitic oscillations or in the gyrotron load to dissipate almost the complete produced microwave power in experiments. The manufacturing process and absorption measurements of a thin dielectric layer for a gyrotron load is described in Appendix A.6.

4.2.1 Dielectric Measurement Methods

A dielectric material that is not conductive is defined by its complex relative dielectric permittivity

$$\epsilon_r = \frac{\epsilon}{\epsilon_0} = \epsilon_r' - j\epsilon_r'' \,. \tag{4.13}$$

The imaginary part of ϵ_r describes the losses in the medium in terms of oscillating dipoles. The loss tangent $\tan\delta$ is defined by the ratio between the imaginary and real part of the complex relative permittivity [154]

$$\tan\delta = \frac{\epsilon_r''}{\epsilon_r'} \,. \tag{4.14}$$

One of the most commonly known measurement method is using a coaxial probe measuring liquid and solid dielectrics [155]. This method can be applied up to frequencies in the THz-range. However, it cannot be used for measuring the transmission of the gyrotron window over a large geometric range. Other methods use an open resonator structure [156] or a free space measurement setup [157]. In [158], a measurement setup using an open resonator is presented. The relative permittivity and the loss tangent can

be determined very exactly for selected frequency points. However, it is not applicable for a wide frequency range. Therefore, the free space method is used for measuring the reflection and transmission behavior. Figure 4.35 shows a measurement schematic on the basis of an existing setup published in [83]. The setup is adapted by a vector network analyzer using frequency extension modules (FCM) to cover the high frequency bands. A $TEM_{0,0}$ mode is launched by a corrugated circular horn antenna. A set of mirrors collimate the radiated beam to form a Gaussian beam with identical parameters as in the gyrotron. The microwave beam is focused onto the device under test (DUT) using mirror 2. The received signal is picked up by the additional mirror 1 or 3 and the corrugated horn 1 or 2 depending on the reflection or transmission measurement, respectively. The evaluation is performed using a vector network analyzer. More details about the mirror design is published in [83].

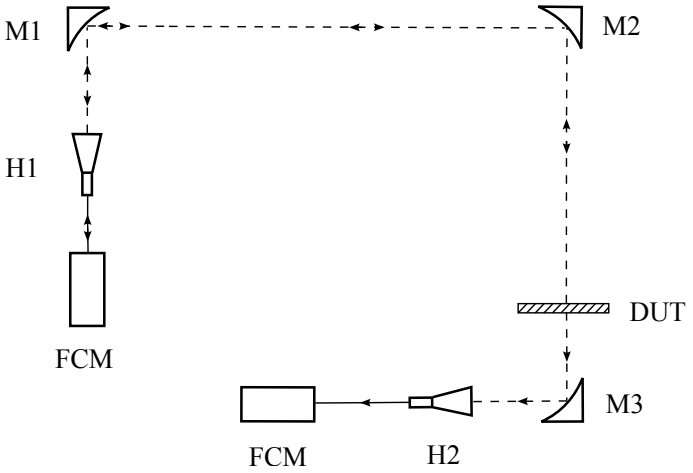

Fig. 4.35: Schematic of the quasi-optical measurement setup for transmission and reflection measurement of a dielectric device under test (DUT).

4.2.2 Measurement of the Gyrotron Output Window

CVD-diamond is used as material for the output window for megawatt-class gyrotrons operating at long pulses. A detailed description is given in Section 3.1.1. CVD-diamond has in the millimeter wavelength range a relative permittivity of $\epsilon_r = 5.67$ and a loss tangent of $\tan\delta \approx 2 \cdot 10^{-5}$ [82].

Measurement of Single Gyrotron Output Windows

The reflection R and transmission T of a single gyrotron output window is given by [83]

$$R = \frac{R_0\left(1 - 2T_0\cos\left(2\beta_{\epsilon\upsilon}d_{\text{window}}\right) + T_0^2\right)}{1 - 2R_0T_0\cos\left(2\beta_{\epsilon\upsilon}d_{\text{window}}\right) + R_0^2T_0^2} \tag{4.15}$$

$$T = \frac{T_0\left(1 - R_0\right)^2}{1 - R_0T_0\cos\left(2\beta_{\epsilon\upsilon}d_{\text{window}}\right) + R_0^2T_0^2} \tag{4.16}$$

$$\text{with} \qquad R_0 = \left|\rho_\upsilon\right|^2 \tag{4.17}$$

$$T_0 = \exp\left(-2\alpha_{\epsilon\upsilon}d_{\text{window}}\right)\,. \tag{4.18}$$

The window thickness is given by d_{window} and the reflection factor by ρ_υ. The complex wave propagation constant is $\underline{\gamma}_{\epsilon\upsilon} = \alpha_{\epsilon\upsilon} + j\beta_{\epsilon\upsilon}$ with the attenuation coefficient $\alpha_{\epsilon\upsilon}$ and the phase constant $\beta_{\epsilon\upsilon}$. The complete derivation of the formulas is discussed in Appendix A.7. The formulas above are valid for windows mounted almost perpendicular to the gyrotron.

An existing CVD-diamond disk with a thickness of $d_{\text{window}} = 1.601$ mm is considered. The measurement setup is calibrated using a short (metal plate with high electrical conductivity) for the reflection measurement and a through (no disk) for the transmission. Only the amplitude values are calibrated using this calibration method [159]. Time gating is applied additionally to resolve multiple reflections that occur in the time domain at 3.54 m. This distance is equal to half of the distance from the transmitting horn to the DUT. In [160], a CVD-diamond window is measured. Figure 4.36 depicts a comparison of the theoretical model and the measurement for the

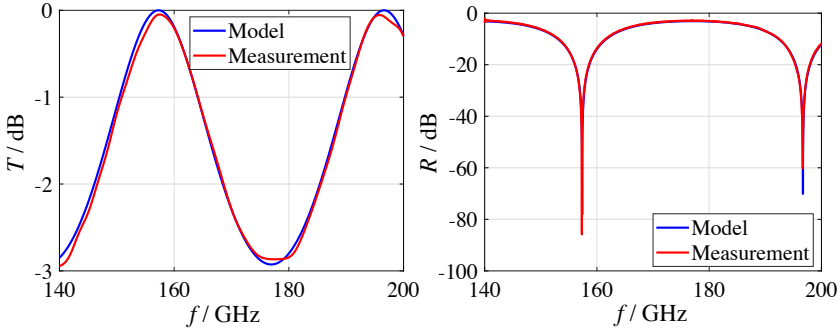

(a) Transmission.

(b) Reflection.

Fig. 4.36: a) Transmission T and b) reflection R of a perpendicularly assembled CVD-diamond disk in a frequency range of 140 – 200 GHz.

reflection and transmission. The measurement and theoretical model are in excellent agreement. The measurement is limited to a frequency range of 140 – 200 GHz, because of the specified frequencies of the isolator and corrugated horn antenna.

4.3 Upgrade of the Frequency Diagnostic Systems

During gyrotron operation different characteristic parameters, like the vacuum condition, the accelerating voltage and current, the output power and the operating frequency, are monitored. The measurement setup discussed in this work is related to frequency detection and frequency spectrum monitoring. Besides the interest in the operating frequency, additionally possible parasitic oscillations, mode switching, low-frequency oscillations, modulation of the output frequency and frequency tuning during long pulses can be investigated. A detailed discussion is given in [161]. The existing frequency diagnostic systems at KIT are limited to an operating frequency of 175 GHz. Those are the FMS (Frequency Measurement System) [162]

and PSA (Pulse Spectrum Analyzer) [163]. Concerning the demand towards higher frequencies above 200 GHz, a re-design is required.

4.3.1 Gyrotron Frequency Measurement Techniques

There are different methods for frequency measurements. In the past, gyrotrons had an axial output, where the propagating mode mixture can be determined by the use of a k-spectrometer [164]. A measurement takes somehow long, because of a mechanical variation of the position of the diode receivers to the direction of the propagated power and determination of the angle. However, nowadays gyrotrons with radial output coupling system are state of the art. An open-ended waveguide is connected to the relief window guiding a certain amount of the stray radiation to the diagnostic systems for frequency measurements. There are different measurement methods for frequency determinations such as using a heterodyne receiver, a Michelson interferometer [165], or dispersive-line systems for analyzing ultra-short pulses [166]. The most appropriate method is to convert the gyrotron frequency with a mixer into a lower frequency band using a heterodyne receiver. Diagnostic equipment operating in these lower frequency ranges around < 20 GHz are more cost-efficient. The requirements for the frequency diagnostic system are:

- Unambiguous reconstruction of the microwave spectrum
- High bandwidth ($14 - 20$ GHz) for mode competition, mode switching and backward waves investigation
- High dynamic range for parasitic oscillation detection
- Frequency resolution for the diagnosis of frequency instabilities or modulation of at least 10 MHz
- Time dependent analysis (effects may differ from pulse to pulse due to its transient nature)
- Almost real-time capability
- Cost-efficient solution

At KIT, the FMS and PSA system have been developed in the past. They are based on the heterodyne concept. In the heterodyne concept, a received signal with a high frequency (RF) is converted using a mixer. The mixer is pumped with a local oscillator (LO) signal into a lower frequency range (intermediate frequency, IF). The mixer converts the microwave signal at the fundamental or at a harmonic h of the LO signal $h \cdot f_{\mathrm{LO}}$. In general, a mixer can be used for down-converting from high to low frequencies and for up-converting from low to high frequencies. In downward mixing, low (LSI) and high side injection (HSI) occurs based on the relative position of the LO and RF frequency [159],

$$f_{\mathrm{IF,\,LSI}} = f_{\mathrm{RF}} - h \cdot f_{\mathrm{LO}} \quad \text{for } f_{\mathrm{RF}} > h \cdot f_{\mathrm{LO}}$$
$$f_{\mathrm{IF,\,HSI}} = h \cdot f_{\mathrm{LO}} - f_{\mathrm{RF}} \quad \text{for } f_{\mathrm{RF}} < h \cdot f_{\mathrm{LO}}$$

In addition, besides the mentioned side bands, all mixing harmonics can convert signals into the desired IF range. Therefore, ambiguities can occur depending on the applied frequencies for the reconstruction of the RF frequency out of the IF and LO signal, because neither the real mixing harmonic nor the side band are known in prior in the gyrotron experiments.

4.3.2 Upgrade of the FMS System

The hardware components are very expensive considering the mentioned requirements for the frequency diagnostic system. Therefore, two independent systems (FMS and PSA) have been developed up to an operating frequency of 175 GHz. Each system has individual objectives to meet finally the overall requirements. In the first step, the FMS system is discussed. The initial design has been published in [162]. The main concern of the FMS setup was a cost-efficient but real-time capable system. The schematic of the FMS system, which has been modified within this work, is presented in Fig. 4.37. An open-ended waveguide is installed at the relief window of the gyrotron to guide a certain amount of the stray radiation towards the frequency diagnostic system. The oversized waveguide has a length at KIT of up to 15 m having an attenuation of up to 15 dB. In addition, several attenuators are installed

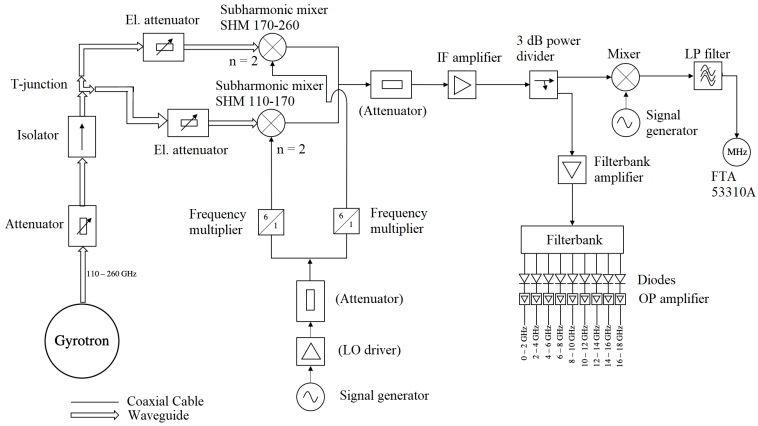

Fig. 4.37: Schematic of the modified FMS system covering a frequency bandwidth from 110-260 GHz [81].

to attenuate the incoming signal for safety reasons of the mixers. The system is modified to cover two waveguide bands from 110 GHz to 260 GHz. Therefore, the input signal is divided into two channels covering each a waveguide band (110 − 170 GHz and 170 − 260 GHz). The existing FMS contains a mixer working on the third harmonic $h = 3$ having a conversion loss of 20 dB. The new diagnostic setup contains a fullband sub-harmonic mixer ($h = 2$) for each channel. In terms of the reduced harmonic, the conversion losses are decreased down to 10 − 15 dB at 110 − 170 GHz and 170 − 260 GHz. Therefore, an increase of the dynamic range of up to 7 dB is achieved (taken also the additional 3 dB power splitter into account). The IF bandwidth is in both versions 18 GHz. There is no diagnostic hardware on the market which is real-time capable for a bandwidth of 18 GHz in a cost-efficient way. Therefore, the IF signal is split into two additional channels. The first channel consists of a filterbank [167] and the second of a FTA (Frequency Time Analyzer) for evaluation of the frequency-time spectra.

Filterbank

The main competing neighboring modes in a coaxial-cavity gyrotron have a frequency separation of ≈ 2 GHz. Therefore, the filterbank divides the input spectrum into 9 adjacent sub-channels with 2 GHz bandwidth each. The insertion losses of the 9 individual sub-channels are plotted in Fig. 4.38b. At each individual sub-channel an RF diode produces a DC voltage, which is proportional to the input RF signal. The DC signals are displayed on an oscilloscope. This setup shows whether a mode is excited in the correct sub-channel, another mode is excited, or even mode switching occurs during a pulse. This channel covers a large bandwidth of 18 GHz in real-time but suffers from a frequency resolution of only 2 GHz.

Frequency Time Analyzer (FTA)

The second channel is equipped with a FTA having a frequency resolution of 10 kHz and covers a bandwidth of up to 2.5 GHz. Therefore, the FTA covers one of the 9 sub-channels for with high resolution in real-time. An additional mixer stage and lowpass filter are used to convert the select frequency band below 2.5 GHz. The new FMS system was built up and installed at the FULGOR test stand and has been successfully tested.

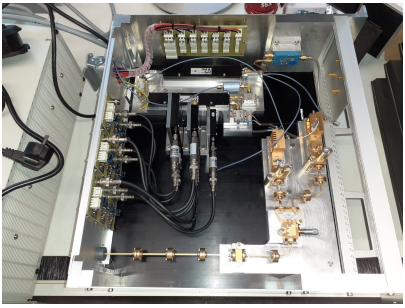

(a) Photo of the FMS from 110 – 260 GHz.

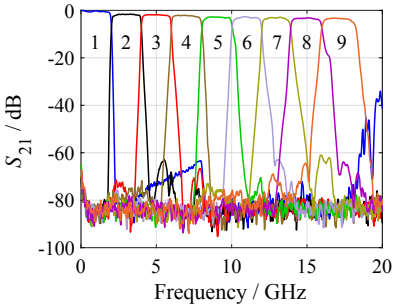

(b) Transmission of the filterbank.

Fig. 4.38: a) Photo of the FMS from 110 – 260 GHz and b) the transmission of the filterbank with the 9 adjacent sub-channels from DC to 18 GHz.

4.3.3 Upgrade of the PSA System

The FMS system gives a sufficient indication, if the gyrotron is operating in the nominal regime. However, it suffers from the fact that possible mixing effects can lead to unwanted frequency ambiguities. In addition, the FMS system has a low dynamic range of up to 27 dB and there is a trade-off between frequency resolution and covered bandwidth. Therefore, an alternative system calling Pulse Spectrum Analysis (PSA) has been developed during a doctoral thesis [161]. The PSA system meets all requirements except real-time capability because of long post-processing of the data.

A schematic view of the PSA system is presented in Fig. 4.39a. The chosen mixers have an IF bandwidth of $\Delta f = 3.5$ GHz. The ambiguity issues could be solved by a single mixer and two successive pulses, changing the LO frequency at the different pulses. By the direction in which the IF frequency shifts and from the knowledge of the LO frequency, an unambiguous reconstruction of the RF band is possible. However, the behavior of the gyrotron may differ from pulse to pulse due to transient effects. So, an unambiguous reconstruction is required for a single pulse. Therefore, a second channel is built up with a second mixer (see Fig. 4.39a). The LO frequency applied to mixer 2 differs from the frequency applied to mixer 1. This setup guarantees an unambiguous reconstruction with a single pulse. The operating harmonics of mixer 1 and 2 are selected differently ($h_{1,d} = 10$ and $h_{2,d} = 12$) to reduce false positives in the reconstruction in the post-processing code [161]. The IF signals are sampled using the oscilloscope RTO1024 from Rohde&Schwarz, Munich, Germany. The sampled signals are transformed using a short-time Fourier transformation into the frequency domain. The resulting spectra of channel 1 $S_1(f, t_i)$ and channel 2 $S_2(f \pm \Delta f_d, t_i)$ with a difference in the LO frequency of Δf_d are used for the reconstruction in the post-processing. It uses a minimum search on numerically shifted and mirrored spectra. The two side bands can be calculated using [161]:

$$R_{\mathrm{LSI}} = \mathrm{Min}(S_1(f, t_i), S_2(f - \Delta f_d, t_i)) \qquad \forall i \tag{4.19}$$

$$R_{\mathrm{HSI}} = \mathrm{Min}(S_1^{\leftrightarrow}(f - \Delta f_d, t_i), S_2^{\leftrightarrow}(f, t_i)) \qquad \forall i \tag{4.20}$$

The symbol "↔" denotes a mirroring of the frequency axis. The resulting reconstructed spectrum has a blind spot between 0 and Δf_D. The blind spot of the spectrum R_x can be eliminated using:

$$R_x = \mathrm{Min}(S_1^{\leftrightarrow}(f + \Delta f_d, t_i), S_2(f, t_i)) \quad \forall i \tag{4.21}$$

A combination of R_{LSI}, R_{HSI} and R_x results in the complete spectrum in the microwave band. In terms of the deviated LO frequency the effective bandwidth is reduced to $2 \cdot \Delta f - \Delta f_d$. An effective bandwidth of ≈ 6 GHz is available by a channel pair. In practice two independent channel pair are implemented having an effective bandwidth of ≈ 12 GHz. The reconstructed spectrum can be visualized in a spectrogram, which displays the frequency behavior over time. An example is given in Fig. 4.39b presenting a gyrotron pulse. The frequency in the start-up is tuned to the nominal value until the flat-top of the power supplies is reached at 260 µs. Mode competition occurs starting from 320 µs ending in a strong modulation and finally a shut down.

The frequency resolution δf and the time resolution is inverse proportional $\delta f = 1/T_{seg}$. Time resolution in a spectrogram is defined by the time segment T_{seg}. A common used frequency resolution in practice is given by $\delta f = 1$ MHz. The time acquisition is limited to 7 ms using both channel pair and maximum sampling rate. The calculated dynamic range is given in [161] by 60 dB up to 2.5 GHz per mixer channel.

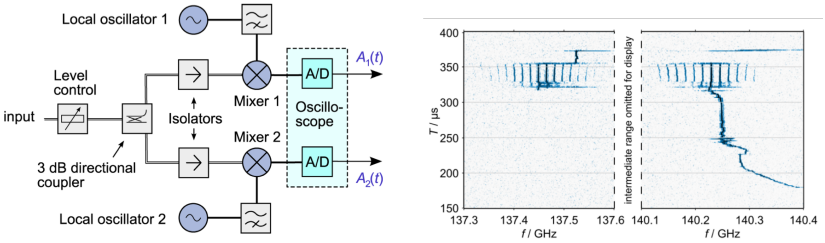

(a) Schematic of PSA.

(b) Spectrogram.

Fig. 4.39: (a) Schematic view of one channel pair and (b) example of a spectrogram using the PSA system [163].

An upgrade of the existing PSA system is performed by installing two additional channel pairs with mixers operating in the frequency band of 170 – 260 GHz. The key element of the setup is the selected choice of operating harmonics of the mixers to reduce the number of possible false positives. Therefore, according to the formulation presented in [161], a calculation about all combinations of harmonics and the resulting number of possible false positives is performed in Fig. 4.40. The mixers on the market are operating typically at $h = 14, 16, 18$ in the given frequency band. Similar harmonics lead to the highest number of false positives. A combination of $h_{1,d} = 14$ and $h_{2,d} = 16$ has been chosen, because of the lower conversion losses than using $h = 18$. The additional channels for the PSA system are currently being assembled.

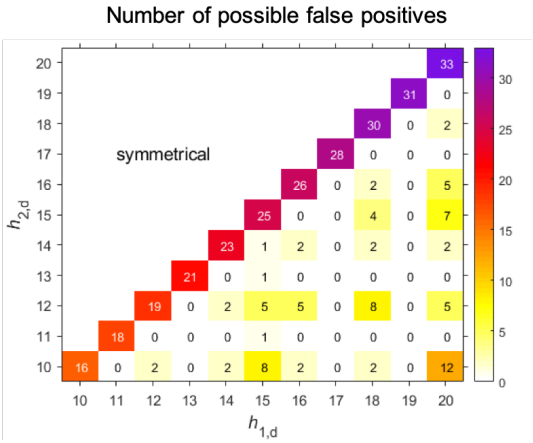

Fig. 4.40: Calculated false positives in the frequency band from 170 – 260 GHz according to the mixer harmonics h of mixer 1 $h_{1,d}$ and mixer 2 $h_{2,d}$ [81].

5 Preparation of the Pre-Prototype Gyrotron for Experiments

In this chapter, the preparation of the 2 MW dual-frequency 170/204 GHz coaxial-cavity pre-prototype is presented. In addition, the assembly and preparation of the in-house manufactured iMIG is discussed.

5.1 Preparation of the 170/204 GHz Pre-Prototype

The 2 MW 170/204 GHz dual-frequency pre-prototype gyrotron will be operated in the Fusion Long Pulse Gyrotron Laboratory (FULGOR) [168] at KIT. FULGOR is equipped with a new high-voltage DC power supply providing up to 10 MW. The power supply allows gyrotron output powers up to approx. 4 MW in long pulses and the possibility to operate with a multi-stage depressed collector. In addition, a 10.5 T SC magnet is ordered for FULGOR to overcome the current frequency limitation of 170 GHz. Section 3.3 discusses the modification required to accommodate to the new test stand and the dual-frequency operation. The following components are manufactured for the first proof-of-principal experiment for 170/204 GHz dual-frequency operation:

(i) New anode with a modified shape and a 33 mm axial elongation to adapt the gyrotron to the new 10.5 T SC magnet.

(ii) Insert elongation by 33 mm that the longitudinal corrugations are positioned at the midsection.

(iii) Optimized coaxial cavity to provide 2 MW at 170 GHz and 204 GHz.

(iv) New oil tank for the cooling of the MIG.

(v) New xy-table to adjust the position of the gyrotron in the magnet.

Figure 5.1 presents a photo of the assembled 2 MW 170/204 GHz coaxial-cavity pre-prototype. The collector is missing in the photo because it is needed in another gyrotron experiment. After installation, a vacuum condition of $\approx 3 \cdot 10^{-8}$ mbar is achieved without baking. First experiments will be performed after the delivery of the 10.5 T SC magnet.

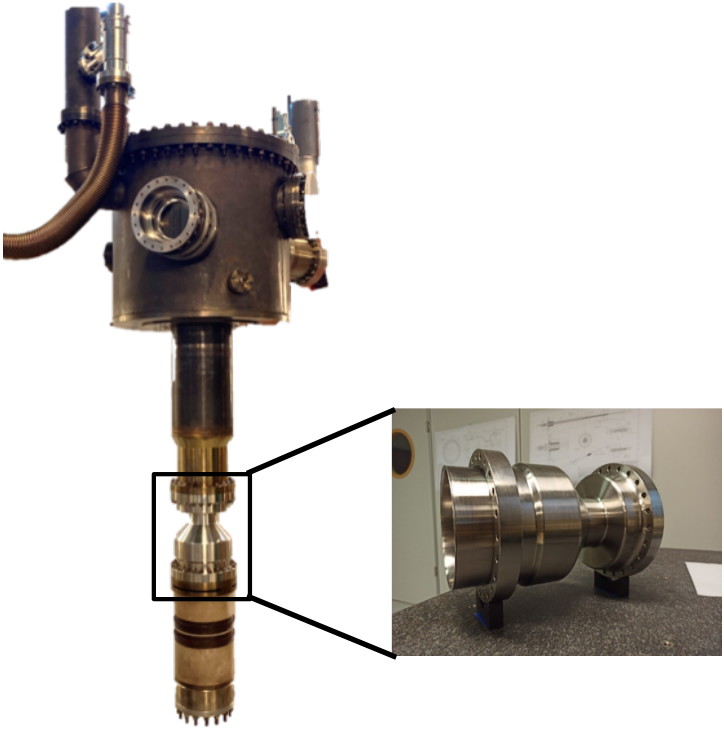

Fig. 5.1: Assembled 2 MW 170/204 GHz dual-frequency coaxial-cavity pre-prototype. It is prepared for proof-of-principal experiments. In this photo the collector is missing.

5.2 Initial Operation of the iMIG

Simulations show promising results for operating the gyrotron with an iMIG. In [59] and [56], the design and fabrication processes of the in-house manufactured iMIG are described. The iMIG has not yet been experimentally validated due to a vacuum leakage.

Electron Beam Welding of the Leaking Connection

The leaky connection between the filament heater of the emitter and the power supply is optimized as part of this work. A new cable feed-through passing through a flange is employed. Electron beam welding is used. A weld between CuCrZn of the iMIG flange and 1.3917 (nickel-iron alloy) of the cable feed-through does not provide a sufficient connection. A nickel sleeve is therefore used as intermediate piece. Two welds are required, one weld between the cable feed-through and the nickel sleeve and a second between the nickel sleeve and the CuCrZn flange. The electron beam parameters are determined by welding a dummy. Figure 5.2 presents a photo of the cut dummy. The quality of the welding in the cutting plane under the microscope is given in Appendix A in Fig. A.29. Afterwards, the original component of the iMIG was successfully welded.

Fig. 5.2: Photo of a test weld of a test piece cutted on the cable feed-through.

Verification of Temperature Homogeneity on Emitter Surface

A uniform temperature distribution over the emitter surface is essential. This ensures the highest quality of the electron beam for optimal interaction. The supplier of the emitter performed a temperature homogeneity test of the emitter at the factory acceptance test showing excellent performance. The measured temperature deviation was ±7 °C at the nominal temperature of 1000 °C and a filament current of 24 A [56]. The homogeneity of the emitter temperature is verified at KIT before the installation to a gyrotron to validate shipping and the assembly. A ZnS window is mounted on the top of the iMIG. This allows a view on the emitter ring with an infrared camera to measure the temperature distribution. A flange for the vacuum pump is mounted on the bottom side. This assembly cannot be placed into an oil tank. Therefore, the emitter cannot be operated at nominal temperature due to the missing oil cooling. Figure 5.3 presents the measurements of the emitter temperature. The measurements are performed at 8 different positions around the emitter circumference applying three different filament currents of 8 A, 9 A and 10 A. The measurements show an excellent homogeneity of less than ±3 °C temperature deviation. Temperatures are slightly lower at position #5. This position corresponds to the feeding point of the heater coil.

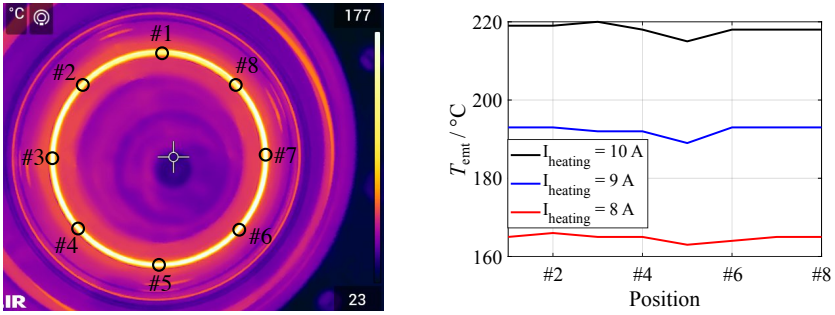

(a) Infrared measurement.

(b) Measurement results.

Fig. 5.3: a) Photo of the infrared measurement and b) validation of the homogeneity of the heated emitter surface with a filament current of 8 A, 9 A and 10 A.

Conditioning and Initial Operation

The iMIG is assembled to the 2 MW 170 GHz coaxial-cavity short-pulse gyrotron. A photo is shown in Fig. 5.4. The evacuated gyrotron has an excellent vacuum of $1 \cdot 10^{-9}$ mbar in cold state (without filament heating) and about $5 \cdot 10^{-9}$ mbar with heated emitter.

The high-voltage tests show that arcing does not occur inside the gyrotron structure. This indicates that the internal geometric construction and the isolators have been designed correctly. In the conditioning phase, the filament of the emitter is heated up to the nominal current of 24 A. The emitter must be activated by overheating to achieve sufficient electron emission. This is done by increasing the filament current above the nominal value for a few minutes. The first operation is carried out with a simplified arrangement, i.e. the modulation anode, the insert and the body are grounded. Simulations are performed accordingly to identify an operating point with the given arrangement. An appropriate electron beam quality is achieved at an accelerating voltage of $V_c = -55$ kV and a maximum magnetic field strength of $B_{cav} = 4$ T. The simplified arrangement is proposed for testing a first emission. A beam current of 3 A is achieved with the first pulses. From the beginning, an emission of the emitter can be detected. Further conditioning is required to operate the gyrotron at the nominal operation parameters. However, this is not possible due to a drop of the voltage at the filament. The ohmic resistance is reduced from 2 Ω to about 0.2 Ω. This implies a short circuit in the filament coil and further emitter heating is not possible. Infrared measurements show that due to the short-circuit at the beginning of the heating coil no energy can be deposited on the subsequent emitter ring. Therefore, this emitter ring cannot longer be used and a new one must be ordered. An investigation into the cause is currently underway before a replacement can be ordered.

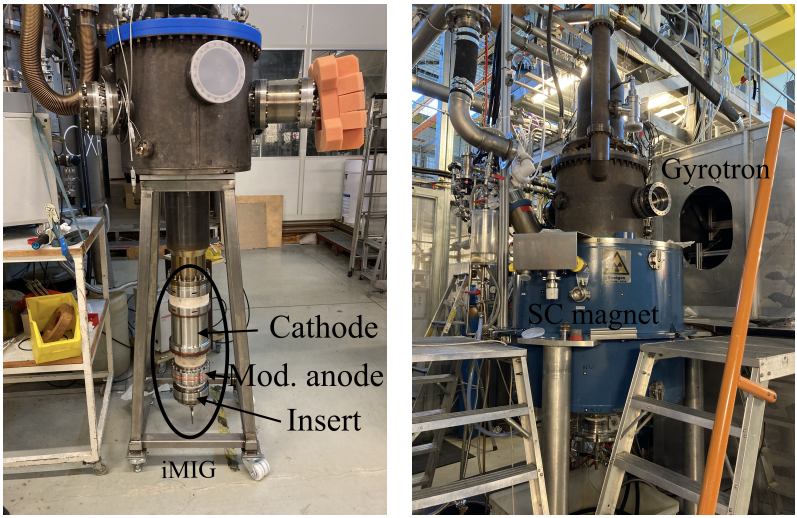

(a) Photo of the 2 MW 170 GHz coaxial-cavity gyrotron.

(b) Installation of the gyrotron into the existing SC magnet.

Fig. 5.4: Photos of the installation process of the Inverse Magnetron Injection Gun (iMIG) to the 2 MW 170 GHz single-frequency pre-prototype and into the existing SC magnet.

6 Towards an Advanced DEMO Gyrotron

The mode series discussed in the present work show a high insert loading at 136 GHz and an output power of 2 MW without much reserve at 204 GHz. Alternative mode series are proposed in [31] and [88] for an EU DEMO-relevant gyrotron in hollow- and coaxial-cavity technology, respectively. However, the hollow-cavity design does not provide 2 MW at the relevant operation frequencies. In addition, modes having higher eigenvalues than the present design are selected in the coaxial-cavity design, e.g. $\chi_{35,21} = 113.1$ compared to $\chi_{34,19} = 105.2$ at 170 GHz. Here, the focus is on a suitable mode series for multi-frequency operation. Therefore, today's design constraints are discussed with regard to their validity.

6.1 Investigation on Alternative Mode Series

Most important requirements in the mode selection process are already described. The insert loading and its diameter are additional important parameters in the coaxial-cavity technology. A statement about the insert loading can be made after interaction simulations have been performed. The first step is to select modes according to their operating frequency and their relative caustic radius. Afterwards, the performance of the mode series is validated according to the output power, efficiency, wall loading and insert loading.

6.1.1 Optimization of the Mode Selection Procedure

A generic mode selection strategy is proposed in [169]. It is implemented in a program called *Design-o-mat*. The code searches for suitable mode series considering the operating frequency and the deviation of the caustic radii of the modes. Figure 6.1 shows the flow chart of the code. A rating system is implemented to identify suitable mode series. However, the defined rating system has several drawbacks. It is 1) very strict for the deviation of the caustic radii, 2) calculates not directly the operating frequency and 3) is restricted to a relative caustic radii of about 0.32.

The first scoring criterion is defined by the normalized standard deviation of the caustic radius σr_c. It is defined in [169]

$$\sigma r_c = \sqrt{\frac{1}{N}\sum_{n}^{N}\left(\frac{m_n}{\chi_{m_n,p_n}\overline{r_c}} - 1\right)^2} \quad . \tag{6.1}$$

This rating system prefers modes with a small deviation defined by an upper limit. The limit was originally set at a deviation of 0.5 %. Therefore, the

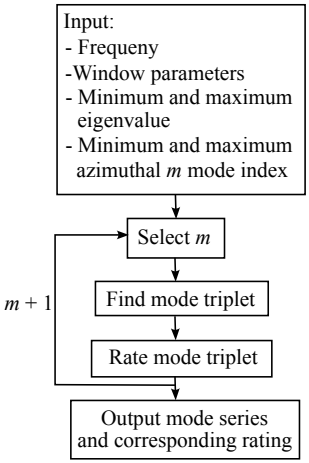

Fig. 6.1: Flow chart of the *Design-o-mat* to identify suitable modes series for multi-frequency operation [169].

rating system identifies mode series with very high eigenvalues, e.g. the mode series published in [88] has an eigenvalue of $\chi_{35,21} = 113.1$ at 170 GHz. In the future, the eigenvalue shall be decreased compared to the eigenvalue of the existing mode series $\chi_{34,19} = 105.2$. An adaption of the rating system is made according to the latest requirements in launcher design. This new rating system considers the upper limit at a deviation of 4 % and reaches the highest score at 0.1 %.

The second criterion is the determination of the operating frequency. The existing rating system uses two rating criteria for this purpose. One to calculate the optimum window thickness to the operating frequencies of the modes and the other to check the linear dependence of the eigenvalue series. These two criteria can lead to a mode series that has perfect linearity, but does not fit to an appropriate window. An optimization is done by implementing Eq. (4.15) and Eq. (4.16). These formulas accurately calculate the behavior of the gyrotron output window. The rating schemes scores if the operating frequencies is in a given bandwidth $\Delta f_{-20\,\mathrm{dB}}$ with a reflection below -20 dB. The highest score is given by a reflection of < -40 dB resulting in a reflected power below 0.01 %.

The performance of the modified rating system is evaluated with the mode series given in [40]. This mode series has been postulated to be optimal in hollow-cavity technology for an output power level of 1 MW. The identified mode series and its parameters are summarized in Tab. 6.1. This mode series has been validated as a suitable candidate using the modified rating scheme. This demonstrates, that the mode selection procedure is properly working.

Table 6.1: Key parameters of the mode series discussed in [40] for a multi-frequency hollow-cavity gyrotron operating at 137, 170 and 203 GHz.

Mode	$TE_{25,9}$	$TE_{31,11}$	$TE_{37,13}$
Relative caustic radius	0.4175	0.4171	0.4168
Deviation of rel. caustic radius / %	+0.09	0	-0.07
Eigenvalue	59.88	74.33	88.77
Oscillating frequency / GHz	137.04	169.98	202.97

6.1.2 Mode Selection Process

The following study includes two aspects: 1) select a mode series that meets the general requirements of today's gyrotrons, and 2) a mode series that meets the gyrotron requirements with modified loading constraints due to anticipated progress in research. An example is an improved cavity cooling system that allows a wall loading constraint of > 2 kW/cm^2. Additional requirements for the mode selection process are:

(i) a reduction of the eigenvalue compared to the existing mode series,

(ii) an output power of minimum 2 MW,

(iii) a maximized interaction efficiency,

(iv) an operation frequency at 136 GHz, 170 GHz and 204 GHz.

The modes are divided into two different categories considering a wall loading of ≤ 2 kW/cm^2 and > 2 kW/cm^2. A mode series is grouped into a wall loading of ≤ 2 kW/cm^2, if the mode at 170 GHz has an eigenvalue close to $\chi_{34,19} = 105.2$.

Mode Series for Wall Loading ≤ 2 kW/cm^2

Two mode series are identified, which have similar scores. The parameters are listed in Tab. 6.2. The two mode series are referred to mode series 1 and 2 in the following for a better overview. In [99], a thermo-hydraulic simulation is given, which postulates an increase of the insert loading to 0.39 kW/cm^2. Assuming this postulation, the existing mode series of the current coaxial-cavity gyrotron can be considered. The postulation needs to be experimentally verified before the insert constraint is extended. A drawback of the existing mode series is the relatively large deviation of the caustic radii of 5 % in total.

Mode Series for Wall Loading up to > 2 kW/cm^2

A mini-channel cooling can increase the allowable wall loading constraint to about 2.5 kW/cm^2 [56, 79, 170]. A first investigation about possible mode

Table 6.2: Key parameters of the identified mode series for possible future EU DEMO-relevant gyrotrons for a wall loading ≤ 2 kW/cm^2.

Mode series 1	$TE_{24,17}$	$TE_{30,21}$	$TE_{36,25}$
Rel. caustic radius	0.2812	0.2817	0.2821
Deviation of rel. caustic radius / %	-0.18	0	+0.14
Eigenvalue	85.35	106.48	127.62
Frequency / GHz	136.43	170.17	203.91
Mode series 2	$TE_{33,13}$	$TE_{41,16}$	$TE_{49,19}$
Rel. caustic radius	0.3942	0.3938	0.3935
Deviation of rel. caustic radius / %	+0.10	0	-0.08
Eigenvalue	83.72	104.13	124.53
Frequency / GHz	136.89	170.16	203.43

series that fit to this requirement is started. Increased wall loading leads to two approaches that can be followed. Firstly, a higher output power can be achieved with almost identical eigenvalues. Secondly, 2 MW output power can still be achieved with a more compact design that has lower eigenvalues. The future trend is towards more compact gyrotrons. The benefit of compact gyrotrons are, e.g. 1.) a SC magnet with a smaller borehole, which drastically reduces the price of the system, and 2.) the mode spectrum is less dense using modes having smaller eigenvalues and thus more robust and reliable operation. The eigenvalue is limited between $90 \leq \chi_{m,p} \leq 105$ for the modes operating at 170 GHz in the following study. In total, three mode series meet the requirements in this category. The different mode series and their key parameters are summarized in Tab. 6.3. For ease of reference, they are referred to mode series 3, 4 and 5, in the following.

Single-mode simulations are performed to investigate the insert loading. The cavity radii are adapted to 28.00 mm, 27.08 mm and 25.60 mm for mode series 3, 4 and 5, respectively, according to Eq. (2.23). The midsection lengths are adjusted to have similar quality factors for comparison. The input θ_1, output θ_2 and insert angle θ_{insert}, the rounding, the length of

Table 6.3: Key parameters of the identified mode series for possible future DEMO relevant gyrotrons allowing a wall loading > 2 kW/cm^2.

Mode series 3	$TE_{20,17}$	$TE_{25,21}$	$TE_{30,25}$
Rel. caustic radius	0.2502	0.2507	0.2510
Deviation of rel. caustic radius / %	-0.20	0	+0.13
Eigenvalue	79.95	99.73	119.52
Mode series 4	$TE_{28,13}$	$TE_{35,16}$	$TE_{42,19}$
Rel. caustic radius	0.3621	0.3628	0.3634
Deviation of rel. caustic radius / %	-0.21	0	+0.14
Eigenvalue	77.33	96.46	115.59
Mode series 5	$TE_{25,13}$	$TE_{31,16}$	$TE_{37,19}$
Rel. caustic radius	0.3404	0.3396	0.3391
Deviation of rel. caustic radius / %	+0.22	0	-0.15
Eigenvalue	73.45	91.28	109.11

the up-taper, down-taper and the total length are identical to the values given in Table 3.6. A fully optimized cavity is not considered for this initial study. Figure 6.2 presents a comparison of the insert loadings of mode series 3, 4 and 5. The selected beam currents are 75 A, 75 A and 68 A and the selected magnetic field strengths are 5.45 T, 6.86 T and 8.23 T for the operation around 136 GHz, 170 GHz and 204 GHz, respectively. The simulations do not include parameter tolerances. The insert radius is selected to $r_{\text{insert}} = 6.5$ mm for a better comparison between the different mode series. This insert radius of 6.5 mm sets the lower limit in terms of acceptable heat loading and vibration due to water flow. Any mode that exceeds the insert load, even if the insert radius is minimal, can be withdrawn. The insert loading constraint of 0.20 kW/cm^2, or even 0.39 kW/cm^2 as stated in [99], is exceeded by mode series 3 (depicted in blue). The modes in mode series 3 are the most volumetric modes with the lowest relative caustic radius and the lowest beam radius of about 8 mm. All other modes do not exceed the insert loading at the minimum insert radius.

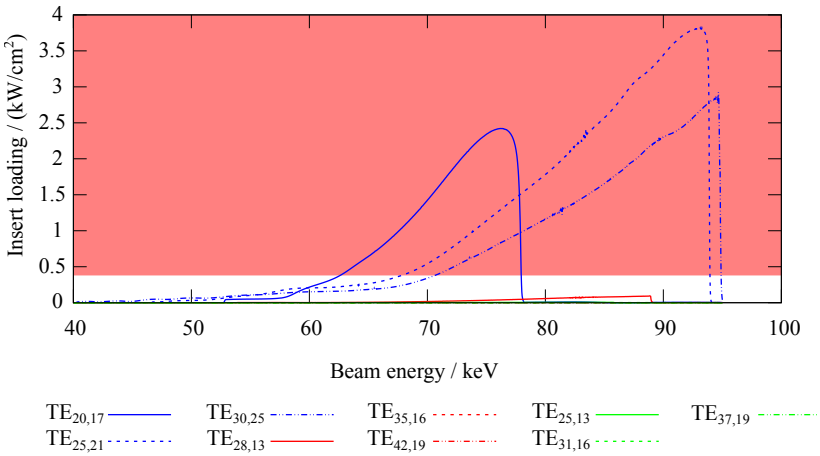

Fig. 6.2: Comparison of the insert loading of mode series 3 (blue), 4 (red) and 5 (green) sweeping the beam energy from 45 keV to 95 keV [171]. The theoretical limit for the insert loading of 0.39 kW/cm^2 is highlighted. An insert radius of 6.5 mm, which is defined to be the minimum, is selected for this study.

6.1.3 Performance Analysis of Alternative Mode Series

The performance analysis of the determined mode series is separated into the two categories. They are not comparable with each other with regard to the different applied wall loadings.

Wall Loading $\leq$ 2 kW/cm^2

The mode spectrum is analyzed for mode series 1 and 2. Therefore, the main competing modes are considered in simulations. A list of the main competitors to the TE$_{m,p}$ mode is summarized in Tab. 6.4. The coupling to neighboring co- and counter-rotating modes is lower in mode series 1 compared to mode series 2.

Multi-mode simulations are performed to investigate the performance of each mode. Table 6.5 summarizes the considered velocity, kinetic energy and

Table 6.4: Main competing modes for a $TE_{m,p}$ mode used in interaction simulation [88].

Co-rotating mode	Counter-rotating mode
$TE_{+m-1,p}$	$TE_{-m,p}$
$TE_{+m-2,p}$	$TE_{-(m-1),p+1}$
$TE_{+m+1,p}$	$TE_{-(m-2),p+1}$
$TE_{+m+2,p}$	$TE_{-(m-3),p+1}$
$TE_{+m+3,p}$	$TE_{-(m-4),p+1}$
$TE_{+m+4,p}$	

guiding center spreads. The insert radius is optimized to $r_{\text{insert}} = 6.5$ mm and $r_{\text{insert}} = 9.7$ mm for mode series 1 and 2, respectively. Mode series 2 benefits from a larger insert radius. It is more robust against vibrations and can withstand higher heat load. The insert radius of mode series 2 is even larger than that of the existing coaxial-cavity gyrotron with $r_{\text{insert}} = 7.9$ mm.

The results of the interaction simulations for mode series 1 are summarized in Tab. 6.6. The loading constraints of today's requirements are selected. The insert loading constraint of 0.2 kW/cm^2 limits the operation of the $TE_{24,17}$ mode at 136 GHz. The resulting cavity wall loading is 1.43 kW/cm^2. An output power of P_{out} =2.21 MW with an interaction efficiency of η =35.7 % is achieved. The insert radius is already set to the minimum value. The performance can be increased by relaxing the cooling constraint. However, the output power at 136 GHz is still above 2 MW. In contrast, the operating points of the $TE_{30,21}$ mode at 170 GHz and the $TE_{36,25}$ mode at 204 GHz are

Table 6.5: Summary of the considered velocity, energy and guiding center spreads used in the interaction simulations.

Parameter	Value
$\Delta\alpha$ / %	6.00
$\Delta\gamma$ / %	0.05
Δr_{beam}	$2 \cdot r_{\text{larmor}}$

Table 6.6: Summary of the simulation results for mode series 1 ($TE_{24,17}$, $TE_{30,21}$ and $TE_{36,25}$).

Parameter	$TE_{24,17}$	$TE_{30,21}$	$TE_{36,25}$
Kinetic beam energy / keV	87.60	92.02	81.66
Beam current / A	75	73	68
Magnetic field / T	5.50	6.89	8.16
Beam radius / mm	9.00	8.95	8.85
Frequency / GHz	136.46	170.17	203.89
Wall loading / (kW/cm^2)	1.43	2.00	2.00
Insert loading / (kW/cm^2)	0.25	0.10	0.01
Output power / MW	2.21	2.53	1.85
Efficiency / %	35.7	37.8	35.4

defined by the maximum wall loading constraint. Interaction simulations show a good performance of the $TE_{30,21}$ at 170 GHz achieving an output power of 2.53 MW with an interaction efficiency of 37.8 %. The output power of the $TE_{36,25}$ mode operating at 204 GHz is calculated to be 1.85 MW, which is below 2 MW. However, it is still higher than with similar midsection length for the $TE_{40,23}$ mode from the initial mode series ($\approx$ 1.7 MW). Full optimization of the coaxial-cavity, which is not considered, can result in a design above 2 MW. In general, the performance of this mode series is quite similar to the existing one. However, the benefit of this mode series is the reduced deviation of the relative caustic radius from in total about 5 % to 0.34 %.

The results of mode series 2 using the $TE_{33,13}$, $TE_{41,16}$ and $TE_{49,19}$ are summarized in Tab. 6.7. Compared to mode series 1, the performance is less considering the wall and insert loading. This effect is obvious regarding the lower eigenvalues. The eigenvalue of mode series 1 at 170 GHz is $\chi_{30,21} = 106.5$ and of mode series 2 is $\chi_{41,16} = 104.1$. Nearly identical results are obtained with a wall loading of 2.15 kW/cm^2 at 170 GHz and 204 GHz. At 136 GHz, the insert loading can be relaxed due to a 1.8 mm larger insert radius. In general, mode series 2 offers less performance given today's loading constraints. But, the advantages of mode series 2 are a larger insert radius of

Table 6.7: Summary of the simulation results for mode series 2 ($TE_{33,13}$, $TE_{41,16}$ and $TE_{49,19}$). The values in the brackets are to be considered if the constraints for wall and insert loading can be relaxed.

Parameter	$TE_{33,13}$	$TE_{41,16}$	$TE_{49,19}$
Kinetic beam energy / keV	89.0 (92.0)	87.5 (88.7)	84.0 (85.0)
Beam current / A	75	73	62
Magnetic field / T	5.52	6.86	8.18
Beam radius / mm	12.10	12.05	12.02
Frequency / GHz	136.89	170.14	203.42
Wall loading / (kW/cm^2)	1.73 (1.96)	2.00 (2.15)	2.00 (2.15)
Insert loading / (kW/cm^2)	0.25 (0.35)	0.13 (0.14)	0.03 (0.05)
Output power / MW	2.27 (2.75)	2.20 (2.40)	1.73 (1.88)
Efficiency / %	35.0 (40.5)	35.7 (37.7)	35.0 (36.1)

9.7 mm and it provides a small deviation of the relative caustic radius of 0.18 %. Mode series 2 is a suitable candidate if the wall loading constraint is extended to 2.15 kW/cm^2. The simulation results allowing higher wall loadings are listed in brackets in Tab. 6.7.

Wall Loading of up to 2.5 kW/cm^2

Even with relaxed constraints, the insert loadings of mode series 3 strongly exceed the limit as presented in Fig. 6.2. Therefore, mode series 3 is not considered as candidate for a future EU DEMO-relevant mode series.

The simulation results of mode series 4 consisting of the $TE_{28,13}$ mode at 136 GHz, the $TE_{35,16}$ mode at 170 GHz and the $TE_{42,19}$ mode at 204 GHz are summarized in Tab. 6.8. The insert radius is selected to be 8 mm, almost identical to the existing one. The beam radii are close to 10.28 mm and are 280 μm larger than in the existing coaxial-cavity gyrotron. This suggests that the existing MIGs at KIT can be used for this mode series without modification. At a wall loading of 2.5 kW/cm^2 an almost identical performance to the original mode series is achieved. A relaxed insert loading is considered in the simulations for the $TE_{28,13}$ mode at 136 GHz. An output power level

Table 6.8: Summary of the simulation results for mode series 4 ($TE_{28,13}$, $TE_{35,16}$ and $TE_{42,19}$).

Parameter	$TE_{28,13}$	$TE_{35,16}$	$TE_{42,19}$
Kinetic beam energy / keV	87.0	89.9	87.1 (88.4)
Beam current / A	75	75	68
Magnetic field / T	5.48	6.88	8.23
Beam radius / mm	10.33	10.28	10.25
Frequency / GHz	136.46	170.18	203.37
Wall loading / (kW/cm^2)	1.95	2.48	2.50 (2.75)
Insert loading / (kW/cm^2)	0.39	0.15	0.03 (0.03)
Output power / MW	2.30	2.30	1.81 (2.13)
Efficiency / %	37.4	35.2	32.2 (36.2)

of > 2 MW at 204 GHz can be achieved with a wall loading constraint of 2.75 kW/cm^2. In addition, improved performance can be achieved considering an optimized coaxial-cavity design. In general, this mode series is a potential candidate for the next step in the gyrotron R&D at KIT. It could be verified in short-pulse operation by modifying the coaxial-cavity and the quasi-optical output system and re-use the insert and the available MIGs. An absolute statement can be made after optimizing the cavity and validating the MIG, which is planned in the next step.

The simulation results of mode series 5 consisting of the $TE_{25,13}$ mode at 136 GHz, the $TE_{31,16}$ mode at 170 GHz and the $TE_{37,19}$ mode at 204 GHz are summarized in Tab. 6.9. This mode series provides the lowest eigenvalues at the corresponding frequencies considered in this work. The insert radius is 6.9 mm and thus 1 mm smaller compared to the initial design. Almost identical performance to the initial mode series is achieved at a wall loading of 2.75 kW/cm^2 for the modes operating at 170 GHz and 204 GHz. Output power of > 2 MW at 204 GHz can be achieved if the wall loading constraint is limited to 2.86 kW/cm^2. In addition, an improved performance can be achieved for an optimized coaxial-cavity design.

Table 6.9: Summary of the simulation results for mode series 5 ($TE_{25,13}$, $TE_{31,16}$ and $TE_{37,19}$).

Parameter	$TE_{25,13}$	$TE_{31,16}$	$TE_{37,19}$
Kinetic beam energy / keV	87.5	90.1	89.8 (90.8)
Beam current / A	75	75	68
Magnetic field / T	5.48	6.86	8.23
Beam radius / mm	9.21	9.16	9.12
Frequency / GHz	136.90	170.05	203.21
Wall loading / (kW/cm^2)	2.25	2.75	2.75 (2.86)
Insert loading / (kW/cm^2)	0.29	0.07	0.02 (0.02)
Output power / MW	2.62	2.50	1.89 (2.14)
Efficiency / %	39.5	38.1	32.0 (35.45)

6.1.4 Conclusions for Future Coaxial-Cavity Designs

Here, the results of the simulations are briefly summarized. The initial mode series provide the highest performance according to today's wall loading requirements. Mode series 2 is a potential candidate if the wall loading constraint is extended to 2.15 kW/cm^2. The benefit of mode series 2 is a significant reduction in the deviation of the relative caustic radii and a comparable large insert radius. If the wall loading constraint is extended to 2.5 kW/cm^2, mode series 4 shows promising results. The mentioned wall loading can be achieved by the mini-channel cooling [56], which is currently being studied in the EU. The mode series has a small deviation of the relative caustic radii of 0.35 % and has a similar insert and electron beam radius compared to the initial mode series. Therefore, this mode series can be easily verified in short-pulse experiments using the existing 170/204 GHz coaxial-cavity housing.

The mode series, which are discussed within this work are limited to eigenvalues in the range of $90 < \chi_{m,p} < 105$ at 170 GHz. Mode series with smaller eigenvalues $\chi_{m,p} < 90$ at 170 GHz have to be considered, if the wall loading constraint is extended to $\approx$ 3 kW/cm^2 or even higher.

In addition, the given simulation results can be used to make general statements about multi-frequency gyrotrons built in coaxial-cavity technology. The nominal operation parameters are limited by the insert loading constraint at 136 GHz and by the wall loading constraint at 170 GHz and 204 GHz. The insert loading constraint has to be adapted for a proper design delivering sufficient performance at 136 GHz. In addition, initial simulations have been carried out at 238 GHz using the mentioned cavity design. The resulting insert loading of 0.005 kW/cm^2 is negligible.

6.2 Dual-Beam Launcher

In [68] a 4 MW, 170 GHz coaxial-cavity is discussed. CVD-diamond disks have a limited power capability of about 2 MW [82, 44] in CW operation. Therefore, two CVD-diamond windows and two microwave beams are used at output power levels above 2 MW [68]. In [68, 172, 173, 174], launchers with two helical cuts forming two microwave beams are described. Figure 6.3 presents the field distribution at the launcher wall at 170 GHz of a launcher with only one helical cut. The first design is limited to the $TE_{34,19}$ mode operating at 170 GHz. The dimensions of the outer geometry are identical to the existing launcher to be compatible. The field distribution of the radiated pattern at the position of the second mirror is simulated using SURF3D. Figure 6.4a depicts a scheme of the validated quasi-optical output coupler. The field distribution at the reference plane is shown in Fig. 6.4b. The Gaussian mode content is calculated to be 97.7 % (left beam) and 98.4 % (right beam) [175]. Additional mirrors must be designed to separate the microwave beams.

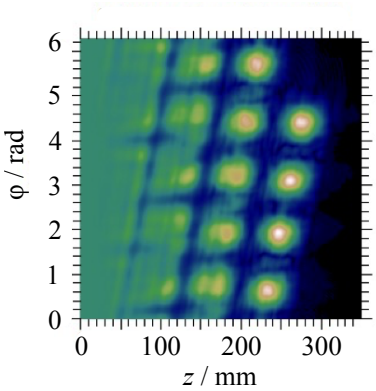

Fig. 6.3: Field distribution at the launcher wall.

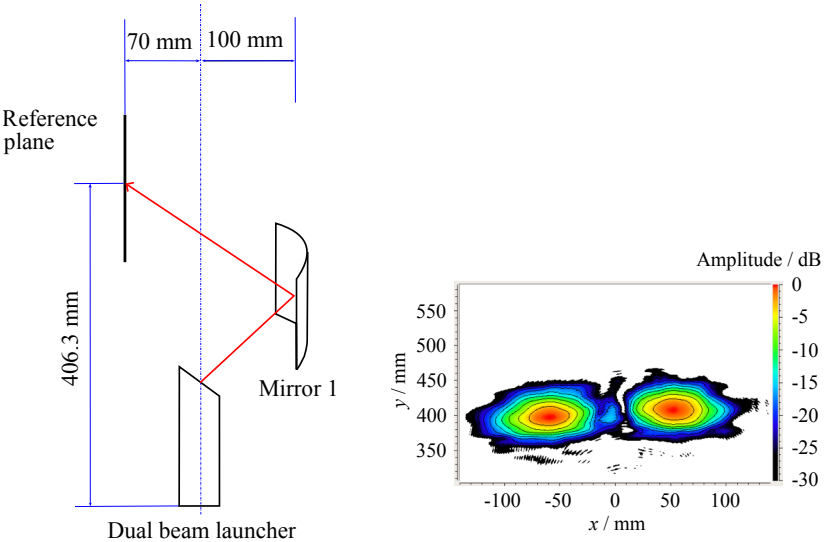

(a) Schematic.

(b) Field intensity pattern.

Fig. 6.4: a) Schematic and b) calculated field intensity pattern of dual beam launcher at 170 GHz using the $TE_{34,19}$ mode.

7 Conclusion and Outlook

A design of a first 2 MW 170/204 GHz multi-frequency / multi-purpose and frequency step-tunable coaxial-cavity short-pulse pre-prototype has been proposed and built up. The design bases on the existing 2 MW 170 GHz single-frequency coaxial-cavity short-pulse pre-prototype. The gyrotron has been built using several existing components, such as the cathode of the Magnetron Injection Gun (MIG). This gyrotron will be the first gyrotron operating at multiple frequencies above 200 GHz in Europe in the new gyrotron test stand FULGOR.

In the design process, there are some restrictions according to the existing pre-prototype, such as the operating mode at 170 GHz, which is fixed to the $TE_{34,19}$ mode. The $TE_{40,23}$ mode was identified as a suitable candidate for operation at 204 GHz. Its parameters fit to the nominal $TE_{34,19}$ mode at 170 GHz. This mode fulfills the criteria of minimum difference in caustic radius and minimum window reflection best. Based on these modes, the gyrotron key components, i. e. the MIG, the coaxial-cavity and the quasi-optical output coupler, were investigated and optimized. An output power of > 2 MW at 170 GHz and 204 GHz must be finally provided.

The existing MIGs at KIT have been studied for the dual-frequency operation to assess whether the required electron beam quality is satisfied. The magnetic field profile of a new 10.5 T SC magnet is considered. This new magnet provides the required field strength for an operation at 204 GHz and above. In conclusion, the coaxial triode iMIG is the favored MIG for future fusion gyrotrons because of its large emitter, the ability of tuning the pitch factor by the modulation anode, the cooling performance and the low velocity spread. The anode configuration of the iMIG is modified for a proper operation in the proposed magnetic field profile. However, the iMIG is still under development. The coaxial triode cMIG can be used too, but is not a suitable MIG for first proof-of-principal experiments because of its

complex handling. Therefore, the coaxial diode MIG is considered in the first experiments because of its reliable operation in other experiments and its easier handling. A modification of the anode shape provides a design that operates at 170 GHz and 204 GHz. This design reuses the cathode, which is one of the most expensive component in the short-pulse gyrotron. The electron beam requirements for the coaxial diode MIG are satisfied using the counter-rotating $TE_{-34,19}$ mode at 170 GHz and the co-rotating $TE_{40,23}$ mode at 204 GHz. In the case of counter-rotating modes a reversion of the magnetic field is required for a proper performance of the quasi-optical output coupler. The designed anode shape has a low effect on the operation due to tolerances. The electron beam parameters of the simulations are considered in the interaction simulations of the coaxial cavity. The design of the existing coaxial cavity provides a maximum output power at 204 GHz of 1.7 MW, which does not satisfy the EU DEMO requirements. Therefore, the coaxial cavity is optimized using a systematic design process, which has been adapted from hollow- to the coaxial-cavity technology. Besides the cavity, a new non-linear up-taper is designed, which provides a mode conversion to neighboring modes of less than 0.1 % at both frequencies. The optimized coaxial cavity achieves in interaction simulations an output power of > 2 MW with an interaction efficiency of > 35 % at both frequencies. The output power is increased by 20 % at 204 GHz. Finally, the quasi-optical output coupler is optimized because of the low vectorial Gaussian mode content of the existing one at 204 GHz. A 170/204 GHz dual-frequency quasi-optical output coupler consisting of a launcher and three mirrors has been designed providing a Gaussian mode content of > 96 %.

In addition, a study about frequency-step tunability in a bandwidth of ± 10 GHz in $2 - 3$ GHz steps at each center frequency has been performed. For the first time, the insert loading was considered in the mode selection process. A mode series as it is state of the art in hollow cavity gyrotrons uses azimuthal neighboring modes. However, several modes exceed the limitation of the insert loading. A novel mode series with a jump of the operating center $TE_{m,p}$ mode to the $TE_{m+2,p-1}$ show a significantly improved performance in both frequency bands. The deviation of the caustic radius

is reduced in total by a factor of two, which results in an increased performance of the launcher for the given modes.

The gyrotron components designed within this work, such as the anode, the insert, the coaxial cavity and the quasi-optical output coupler, have been manufactured. A validation of the manufacturing tolerances have been performed with a high precision 3D measurement arm and a quasi-optical mode generator, respectively. The quasi-optical mode generator is used to verify the quasi-optical output coupler before the installation into the gyrotron, since its manufacturing tolerances are only a few μm to ensure a proper operation. This system excites the gyrotron cavity mode without the need of an electron beam, a SC magnet or high-voltage power supply ("cold" measurements). The test stand has been equipped with a vector network analyzer and frequency extension modules to cover a frequency range from 90 GHz up to 330 GHz. Manually adjustable linear drivers are replaced by electronic movable linear high-precision drivers and a goniometer. All relevant components of the quasi-optical mode generator are controlled electronically in this way. An automated mode excitation procedure with mode evaluation algorithms are developed. Five different evaluation methods are implemented to determine the azimuthal and radial mode index, the quality factor of the cavity, the scalar mode content and the counter-rotating mode amount. The adjustment time of the quasi-optical mode generator is reduced from months to days by the optimizations. The electronic movable linear high-precision drivers and the goniometer make the adjustment reproducible. Nowadays, one quasi-optical mode generator with different coaxial cavities is sufficient to excite the different modes, which reduces the manufacturing effort significantly. The test stand excited during this work 6 different modes at frequencies from 105 GHz to 204 GHz. The relevant $TE_{34,19}$ mode at 170 GHz and the $TE_{40,23}$ mode at 204 GHz have been excited with high purity. The $TE_{40,23}$ mode has the highest eigenvalue, which has ever been excited in cold measurements. The adjusted mode generator is used to verify the 170/204 GHz dual-frequency quasi-optical output coupler. The measurement results are in excellent agreement with the simulations at both frequencies.

After the successful validation, the gyrotron components have been installed to the pre-prototype gyrotron and are waiting for the first proof-of-principal experiments above 200 GHz after the arrival of the 10.5 T SC at KIT. The expected operation frequency is above the current limitation of 175 GHz of the recent frequency diagnostic systems. Therefore, the existing frequency diagnostic systems (FMS and PSA) were modified in preparation for the first experiments. The optimized FMS system has already been installed into FULGOR and verified in experiments. The FMS system was upgraded from 110 GHz to 260 GHz for gyrotron operation and covers two waveguide frequency bands. The design of the PSA system has already been completed and all components have been delivered to KIT.

Finally, the selected gyrotron mode series could be extended to an operation at 136 GHz using the $TE_{28,15}$ mode. Unlike the other modes in the mode series, the operation at 136 GHz is not limited by the wall loading but by the insert loading. The output power is > 2 MW at 136 GHz considering a published insert loading constraint of 0.39 kW/cm^2. There is additional potential in performance, but it is limited by the requirements in using off-the-shelf components. Therefore, a study is started to identify alternative mode series for future EU DEMO-relevant gyrotrons. The study is divided into two categories, 1) considering today's requirements with a wall loading of ≤ 2 kW/cm^2 and 2) > 2 kW/cm^2 considering advanced cooling system like mini-channel cooling. The mode series consisting of the $TE_{28,13}$ mode at 136 GHz, $TE_{35,16}$ mode at 170 GHz and $TE_{42,19}$ mode at 204 GHz has been identified as potential alternative mode series considering a wall loading of 2.5 kW/cm^2. This mode series can be verified in experiments because it is expected that the most critical gyrotron components can be reused.

In this work a first 170/204 GHz coaxial-cavity gyrotron is designed, which will be verified in experiments at KIT. In future R&D, following points have to be considered for an EU DEMO-relevant fusion gyrotron design:

Compact gyrotron design for EU DEMO
The current design is optimized for the operation at 170 GHz and 204 GHz. However, an EU DEMO gyrotron should probably operate at 136 GHz, 170 GHz, 204 GHz and 238 GHz. A principal operation is shown in simula-

tions at all these frequencies with the proposed cavity. However, a design for an optimized cavity at all frequencies needs to be investigated with the realistic requirements given in this work. In addition, it has been identified that the existing mode series does not fit best to the requirements of multi-frequency operation. Depending on the wall loading limitation and possible future gyrotron requirements, a dedicated mode series needs to be selected. The aim is to build more compact gyrotrons using lower order modes. In this work, a new mode series is proposed under certain assumptions. However, further simulations about reliability, insert cooling and insert vibration have to be performed.

Harmonic frequency gyrotrons
A gyrotron can also operate on higher harmonics. One of the main advantages is a reduced magnetic field strength, which can significantly reduce costs for the SC magnet. However, in previous experiments, harmonic gyrotrons achieved output power levels only in the kW range [176]. Performance improvement is in progress to become an alternative to fundamental frequency fusion gyrotrons [177], [178].

Preparation of the 2nd prototype of the iMIG
The iMIG shows excellent results in simulations. In addition, the possibility of an ultra-compact gyrotron using an iMIG is presented in [56]. Regarding the short circuit of the filament heater, a new emitter has to be ordered. A 2nd prototype of the iMIG is being prepared. During the assembly and first operation of the iMIG, necessary optimizations were identified. These are: i) Replacement of the cable feed-through by an alternative, e.g. a 3D printed version is prepared and passed the leakage tests. ii) A new fixture for improved emitter alignment and iii) changing the position of the high-voltage connectors to provide additional space for access.

A Appendix

A.1 Code Package EURIDICE

The interaction simulations are performed with EURIDICE [87], which is a time-dependent, multi-mode, self-consistent code-package. A detailed description of the code is given in [88]. EURIDICE has been verified with the code SELFT from the code package "Cavity" [67]. Both have been benchmarked with the codes TWANG and TWANG-PIC developed at Swiss Plasma Center - École Polytechnique Fédérale de Lausanne (SPC-EPFL) [179, 180]. Additional gyrotron interaction codes are developed at Technical University Hamburg Harburg [38] and MAGY at University of Maryland [181]. These are examples of such codes, a detailed list is presented in [51].

Before the interaction simulation is started, the geometry has to be created in priori with a small discretization of $100 - 200\ \mu m$. The "Coldcav" code which is included in the EURIDICE code package can calculate a mode list of possible competing modes based on the selected frequency range and strength of mode coupling. The eigenvalues of each individual mode are calculated with "CHIMP" presented in [67]. The "Coldcav" code is calculating the frequency, mode coupling, quality factors and axial field-profile without considering the electron beam ("cold" cavity simulations). The interaction simulations are performed with the "Evridiki" code. The equations of electron motion(2^{nd} order Predictor-Corrector scheme) and electromagnetic field (Crank-Nicolson finite difference approach) are solved consistently [31]. The interaction mechanism is described in Section 2.1. A number of in maximum 99 modes can be included in the simulations to investigate the effects of possible mode competition, which is an important issue at these high operating frequencies. As the number of included modes and electrons increases, the calculation becomes longer. This is solved by a parallelized computation. In a start-up simulation the behaviour of the gyrotron can be investigated while increasing the beam energy towards the nominal opera-

tion value. The beam current and the pitch factor are changing according to the adiabatic approximation and the Schottky formula. However, these parameters can be entered individually, including e.g. simulated MIG results to be as realistic as possible.

A.2 Simulation Results of 170/204 GHz Quasi-Optical Output Coupler for Frequency Step-Tunability

In this section, the simulation results of the 170/204 GHz quasi-optical output coupler are listed. First, a summary of the key parameters of the studied modes given in this work are presented. Then, the field patterns and the simulation results are shown.

A.2.1 Mode Selection Process for Frequency Step-Tunability around 170 GHz

The key parameters for a mode series with only azimuthally changing mode index at 170 GHz is summarized in Tab. A.1. A deviation of the caustic radius in the range of -9 % to $+8$ % is investigated. The difference of the caustic radius is given in relation to the nominal mode. It can be stated, that a quasi-optical output coupler for this mode series with only changing the azimuthal mode index is not suitable. A novel mode series for frequency step-tunability for covering a bandwidth of ± 10 GHz is summarized in Tab. A.2. This mode series reduces the difference in the caustic radius in total by a factor of two. The deviation is in the range of 0 % to $+8$ %. A new type of launcher could be designed for the mean value of the relative caustic radius. Thus, a deviation of ± 4 % can be achieved.

Table A.1: Summary of main parameters of the mode series with only change of the azimuthal mode index for frequency step-tunability around 170 GHz.

Mode	Rel. caustic radius	Diff. in caustic radius / %	Frequency / GHz
$TE_{29,19}$	0.2941	-9.0	159.5
$TE_{30,19}$	0.3003	-7.1	161.6
$TE_{31,19}$	0.3062	-5.3	163.7
$TE_{32,19}$	0.3120	-3.5	165.8
$TE_{33,19}$	0.3177	-1.7	167.9
$TE_{34,19}$	0.3232	0	170.0
$TE_{35,19}$	0.3289	+1.7	172.1
$TE_{36,19}$	0.3339	+3.3	174.2
$TE_{37,19}$	0.3391	+4.9	176.3
$TE_{38,19}$	0.3442	+6.5	178.4
$TE_{39,19}$	0.3491	+8.0	180.5

Table A.2: Summary of main parameters of the mode series with jump of the radial mode index for modes higher than the centre mode for frequency step-tunability around 170 GHz.

Mode	Rel. caustic radius	Diff. in caustic radius / %	Frequency / GHz
$TE_{32,18}$	0.3224	-0.2	160.4
$TE_{33,18}$	0.3282	+1.5	162.5
$TE_{34,18}$	0.3338	+3.3	164.6
$TE_{35,18}$	0.3392	+4.9	166.7
$TE_{36,18}$	0.3446	+6.6	168.8
$TE_{34,19}$	0.3232	0	170.0
$TE_{35,19}$	0.3289	+1.7	172.1
$TE_{36,19}$	0.3339	+3.3	174.2
$TE_{37,19}$	0.3391	+4.9	176.3
$TE_{38,19}$	0.3442	+6.5	178.4
$TE_{39,19}$	0.3491	+8.0	180.5

A.2.2 Mode Selection Process for Frequency Step-Tunability around 204 GHz

The key parameters for a mode series with azimuthally changing mode index at 204 GHz is summarized in Tab. A.3. A deviation of the caustic radius in the range of −7.7 % to +6.9 % is observed. The difference of the caustic radius is given in relation to the nominal mode. It can be stated that a mode series with changing the azimuthal mode index is not suitable. A novel mode series for frequency step-tunability for covering a bandwidth of ±10 GHz is summarized in Tab. A.4. This mode series reduces the difference in the caustic radius in total by a factor of two. The deviation is in the range of 0 % to +6.9 %. A new type of launcher could be designed for the mean value of the relative caustic radius. Thus, a deviation of ±3.5 % can be achieved.

Table A.3: Summary of main parameters of the mode series with only change of the azimuthal mode index for frequency step-tunability around 204 GHz.

Mode	Rel. caustic radius	Diff. in caustic radius / %	Frequency / GHz
$TE_{35,23}$	0.2923	-7.7	193.6
$TE_{36,23}$	0.2974	-6.1	195.7
$TE_{37,23}$	0.3023	-4.5	197.8
$TE_{38,23}$	0.3072	-3.0	199.9
$TE_{39,23}$	0.3120	-1.5	202.0
$TE_{40,23}$	0.3166	0	204.1
$TE_{41,23}$	0.3212	+1.5	206.2
$TE_{42,23}$	0.3257	+2.9	208.3
$TE_{43,23}$	0.3300	+4.2	210.4
$TE_{44,23}$	0.3344	+5.6	212.5
$TE_{45,23}$	0.3386	+6.9	214.6

Table A.4: Summary of main parameters of the mode series with jump of the radial mode index for modes higher than the centre mode for frequency step-tunability around 204 GHz.

Mode	Rel. caustic radius	Diff. in caustic radius / %	Frequency / GHz
$TE_{38,22}$	0.3156	-0.3	194.6
$TE_{39,22}$	0.3204	+1.2	196.7
$TE_{40,22}$	0.3251	+2.7	198.8
$TE_{41,22}$	0.3298	+4.2	200.9
$TE_{42,22}$	0.3343	+5.6	203.0
$TE_{40,23}$	0.3166	0	204.1
$TE_{41,23}$	0.3212	+1.5	206.2
$TE_{42,23}$	0.3257	+2.9	208.3
$TE_{43,23}$	0.3300	+4.2	210.4
$TE_{44,23}$	0.3344	+5.6	212.5
$TE_{45,23}$	0.3386	+6.9	214.6

A.2.3 Simulation Results of the 170/204 GHz Dual-Frequency Quasi-Optical Output Coupler used for Frequency-Step Tunability

The tables in the following present the Gaussian mode content (GMC), the shift of the microwave output beam from the centre of the gyrotron output window and the beam waist in x- and y-direction for the initial and novel mode series at 170 GHz and 204 GHz.

Table A.5: Simulation result of 170/204 GHz dual-frequency mode coupler for the initial and optimized mode series at 170 GHz.

Mode	GMC / %	XY-Position / mm	w_{0x}/w_{0y} / mm
$TE_{29,19}$	84.8	3.80/7.44	22.04/28.05
$TE_{30,19}$	88.2	4.74/-5.00	28.05/21.91
$TE_{31,19}$	92.7	3.07/5.21	21.45/27.63
$TE_{32,19}$	95.8	1.79/4.14	21.66/26.99
$TE_{33,19}$	97.2	0.28/2.43	22.30/26.04
$TE_{34,19}$	96.4	-1.37/2.28	23.09/24.99
$TE_{35,19}$	93.7	-3.2/1.01	24.28/24.09
$TE_{36,19}$	90.2	-0.84/4.33	22.96/25.90
$TE_{37,19}$	86.2	-2.41/4.80	22.17/27.30
$TE_{38,19}$	NaN	NaN	NaN
$TE_{39,19}$	78.9	-3.25/4.76	17.61/27.83
$TE_{32,18}$	96.6	-0.89/2.27	23.48/25.97
$TE_{33,18}$	93.9	-2.74/1.15	24.73/24.67
$TE_{34,18}$	90.4	-0.77/3.89	23.73/26.40
$TE_{35,18}$	86.9	-2.57/4.65	22.47/28.06
$TE_{36,18}$	NaN	NaN	NaN

Table A.6: Simulation result of 170/204 GHz dual-frequency mode coupler for the initial and optimized mode series at 204 GHz.

Mode	GMC / %	XY-Position / mm	w0x/w0y / mm
$TE_{35,23}$	78.5	7.58/-4.10	24.92/19.80
$TE_{36,23}$	82.4	6.52/-3.93	26.30/19.39
$TE_{37,23}$	86.6	5.36/-3.45	27.09/19.23
$TE_{38,23}$	90.7	4.46/-2.75	26.87/19.20
$TE_{39,23}$	94.2	3.53/-1.79	25.91/19.46
$TE_{40,23}$	96.4	-0.05/3.43	19.91/24.70
$TE_{41,23}$	95.0	0.38/3.24	22.66/21.86
$TE_{42,23}$	94.3	-3/2.07	21.65/22.89
$TE_{43,23}$	90.7	0.27/4.38	22.30/22.71
$TE_{44,23}$	86.2	-1.28/5.07	21.64/23.74
$TE_{45,23}$	NaN	NaN	NaN
$TE_{38,22}$	96.5	0.04/3.85	20.36/25.24
$TE_{39,22}$	96.9	-1.18/3.04	21.10/24.18
$TE_{40,22}$	95.1	-2.66/2.01	21.97/23.36
$TE_{41,22}$	91.7	0.34/4.04	22.67/23.10
$TE_{42,22}$	86.7	-0.15/6.45	21.71/24.25

A.2.4 Field Intensity and Phase Pattern of the Mode Series around 170 GHz for Frequency-Step Tunability

In the following, the field intensity and phase patterns of the modes given in Tab. A.5 around 170 GHz are presented.

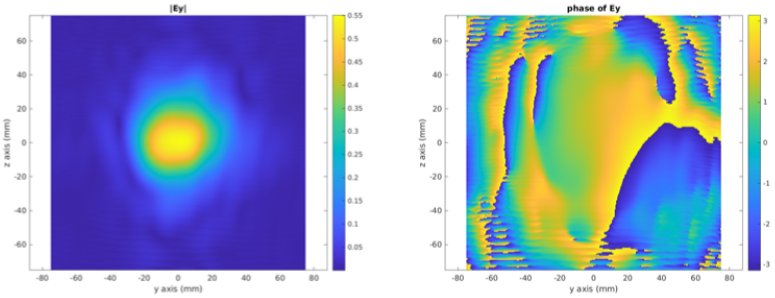

(a) Field intensity pattern. (b) Phase pattern.

Fig. A.1: a) Field intensity pattern and b) phase pattern of the $TE_{32,18}$ mode at 160.4 GHz

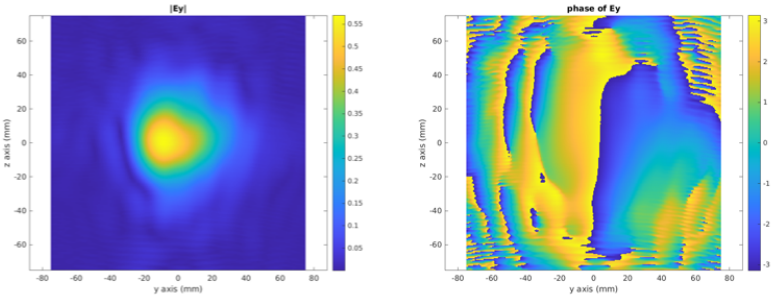

(a) Field intensity pattern. (b) Phase pattern.

Fig. A.2: a) Field intensity pattern and b) phase pattern of the $TE_{33,18}$ mode at 162.5 GHz

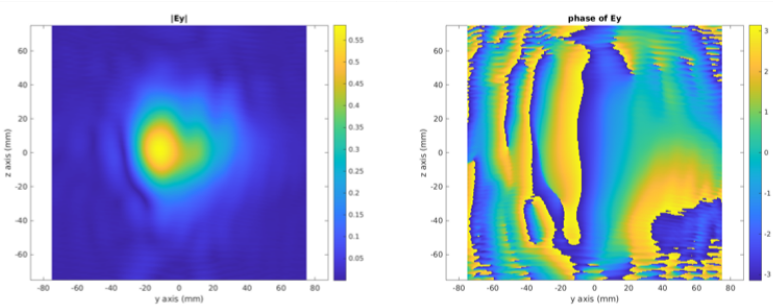

(a) Field intensity pattern. (b) Phase pattern.

Fig. A.3: a) Field intensity pattern and b) phase pattern of the $TE_{34,18}$ mode at 164.6 GHz

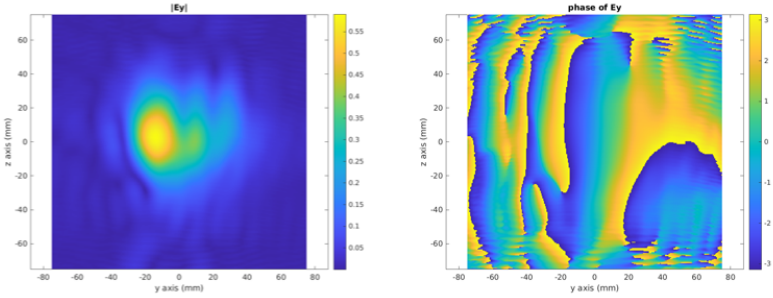

(a) Field intensity pattern. (b) Phase pattern.

Fig. A.4: a) Field intensity pattern and b) phase pattern of the $TE_{35,18}$ mode at 166.7 GHz

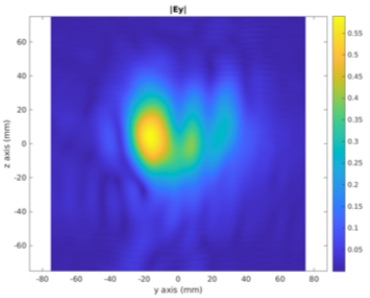

(a) Field intensity pattern.

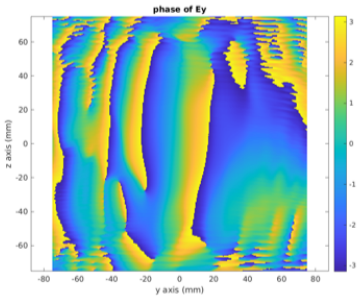

(b) Phase pattern.

Fig. A.5: a) Field intensity pattern and b) phase pattern of the $TE_{36,18}$ mode at 168.8 GHz

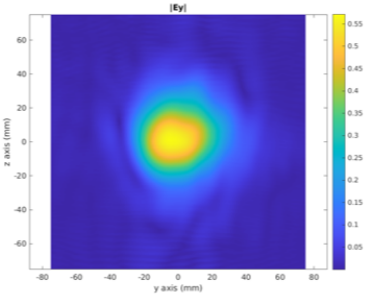

(a) Field intensity pattern.

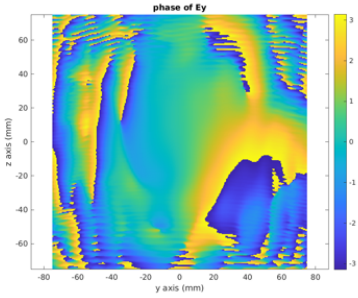

(b) Phase pattern.

Fig. A.6: a) Field intensity pattern and b) phase pattern of the $TE_{34,19}$ mode at 170.0 GHz

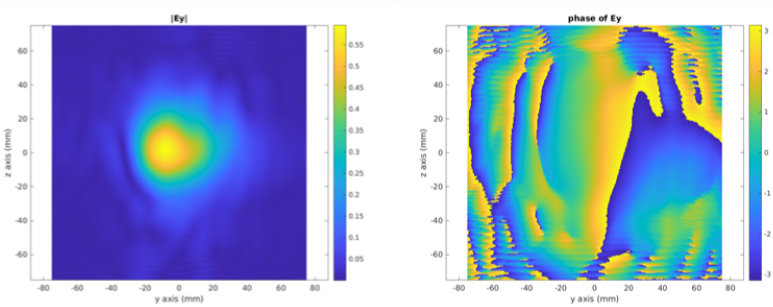

(a) Field intensity pattern. (b) Phase pattern.

Fig. A.7: a) Field intensity pattern and b) phase pattern of the $TE_{35,19}$ mode at 172.1 GHz

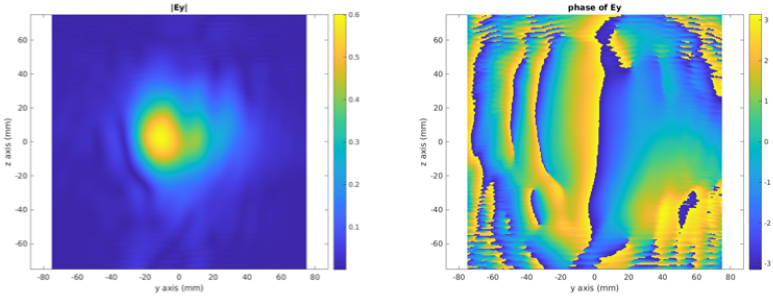

(a) Field intensity pattern. (b) Phase pattern.

Fig. A.8: a) Field intensity pattern and b) phase pattern of the $TE_{36,19}$ mode at 174.2 GHz

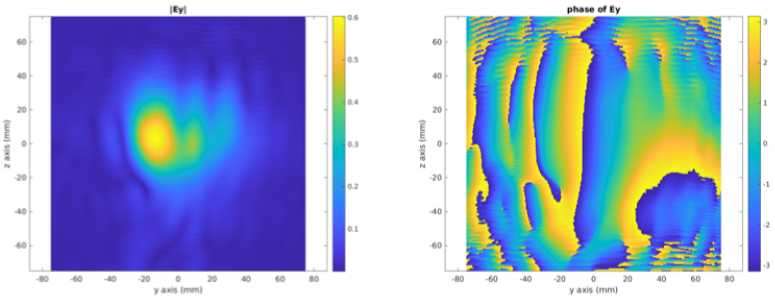

(a) Field intensity pattern. (b) Phase pattern.

Fig. A.9: a) Field intensity pattern and b) phase pattern of the $TE_{37,19}$ mode at 176.3 GHz

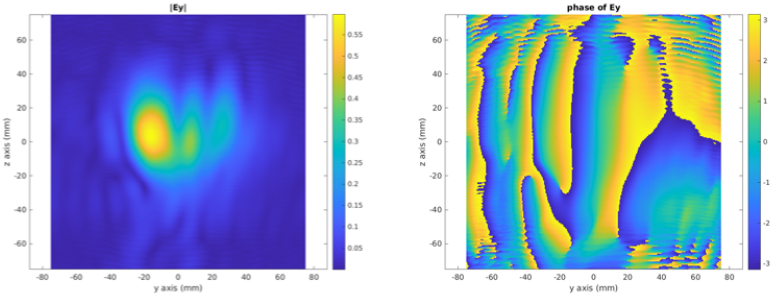

(a) Field intensity pattern. (b) Phase pattern.

Fig. A.10: a) Field intensity pattern and b) phase pattern of the $TE_{38,19}$ mode at 178.4 GHz

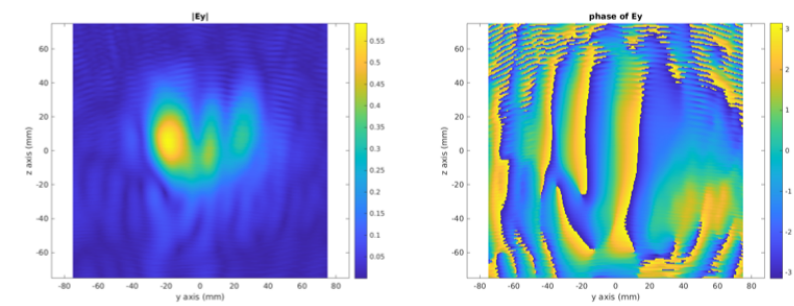

(a) Field intensity pattern.

(b) Phase pattern.

Fig. A.11: a) Field intensity pattern and b) phase pattern of the $TE_{39,19}$ mode at 180.5 GHz

A.2.5 Field Intensity and Phase Pattern of the Mode Series around 204 GHz for Frequency-Step Tunability

In the following, the field intensity and phase patterns of the modes given in Tab. A.6 for the operation around 204 GHz are presented.

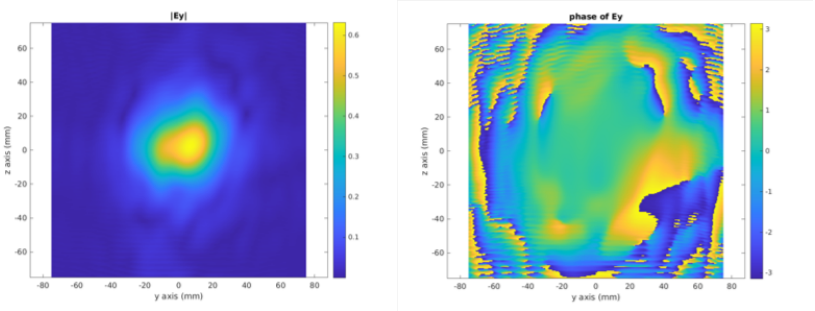

(a) Field intensity pattern. (b) Phase pattern.

Fig. A.12: a) Field intensity pattern and b) phase pattern of the $TE_{38,22}$ mode at 194.6 GHz

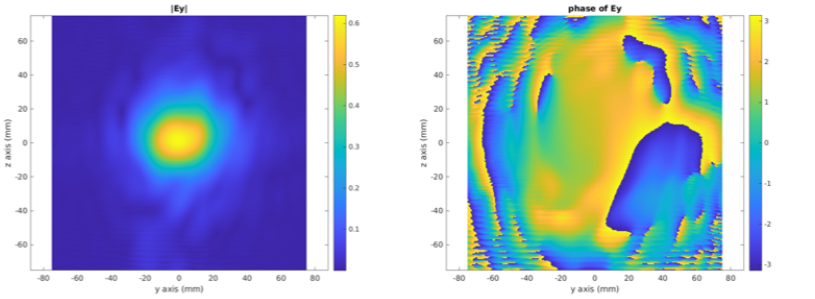

(a) Field intensity pattern. (b) Phase pattern.

Fig. A.13: a) Field intensity pattern and b) phase pattern of the $TE_{39,22}$ mode at 196.7 GHz

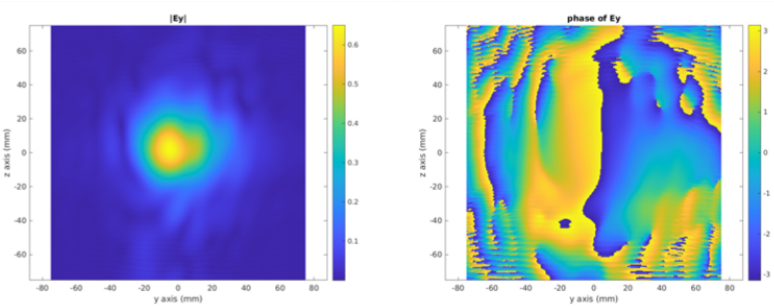

(a) Field intensity pattern. (b) Phase pattern.

Fig. A.14: a) Field intensity pattern and b) phase pattern of the $TE_{40,22}$ mode at 198.8 GHz

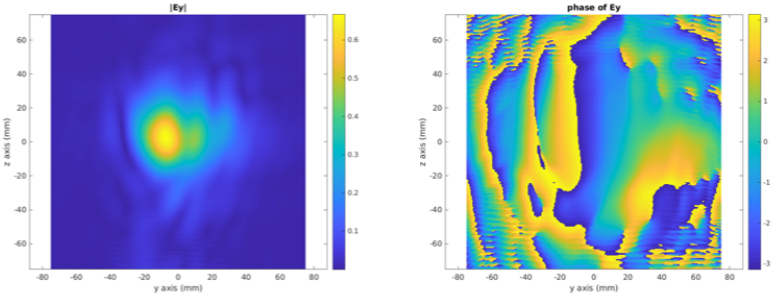

(a) Field intensity pattern. (b) Phase pattern.

Fig. A.15: a) Field intensity pattern and b) phase pattern of the $TE_{41,22}$ mode at 200.9 GHz

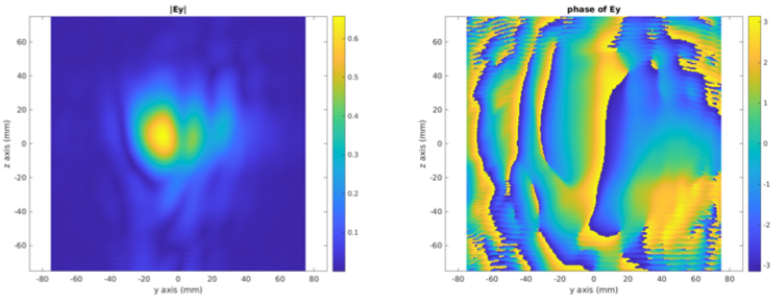

(a) Field intensity pattern. (b) Phase pattern.

Fig. A.16: a) Field intensity pattern and b) phase pattern of the $TE_{42,22}$ mode at 203.1 GHz

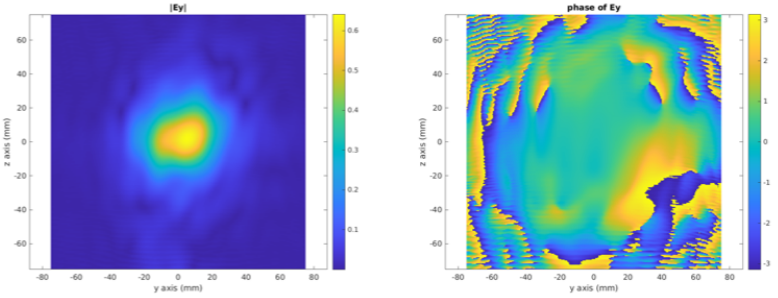

(a) Field intensity pattern. (b) Phase pattern.

Fig. A.17: a) Field intensity pattern and b) phase pattern of the $TE_{40,23}$ mode at 204.1 GHz

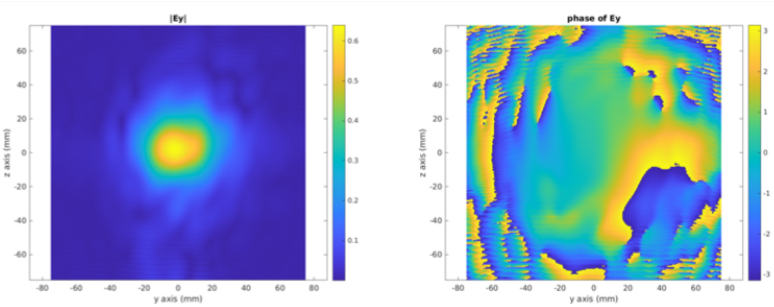

(a) Field intensity pattern. (b) Phase pattern.

Fig. A.18: a) Field intensity pattern and b) phase pattern of the $TE_{41,23}$ mode at 206.3 GHz

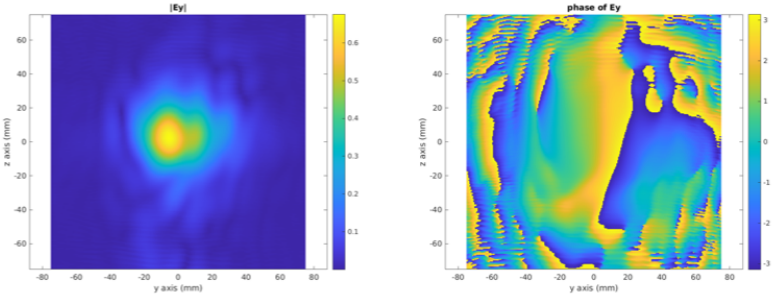

(a) Field intensity pattern. (b) Phase pattern.

Fig. A.19: a) Field intensity pattern and b) phase pattern of the $TE_{42,23}$ mode at 208.4 GHz

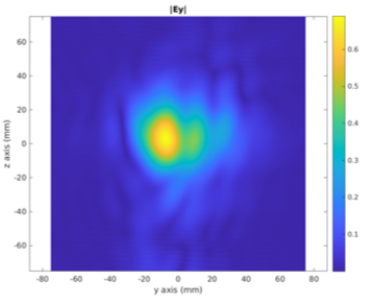

(a) Field intensity pattern.

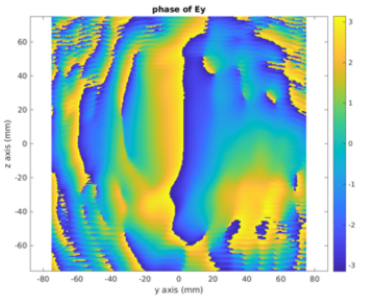

(b) Phase pattern.

Fig. A.20: a) Field intensity pattern and b) phase pattern of the $TE_{43,23}$ mode at 210.5 GHz

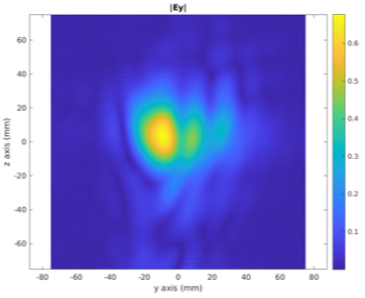

(a) Field intensity pattern.

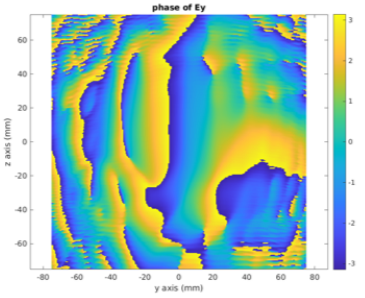

(b) Phase pattern.

Fig. A.21: a) Field intensity pattern and b) phase pattern of the $TE_{44,23}$ mode at 212.6 GHz

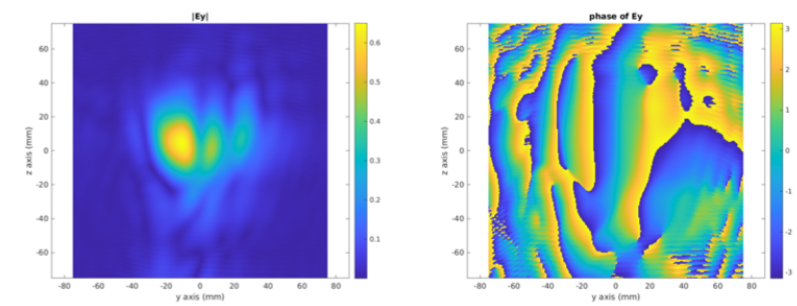

(a) Field intensity pattern.

(b) Phase pattern.

Fig. A.22: a) Field intensity pattern and b) phase pattern of the $TE_{45,23}$ mode at 214.8 GHz

A.3 Measurements of the Quasi-Optical Output Coupler at different Mirror Positions

In the following, the measurements of the quasi-optical output at the position of mirror 2 and 3 at 170 GHz and 204 GHz are presented.

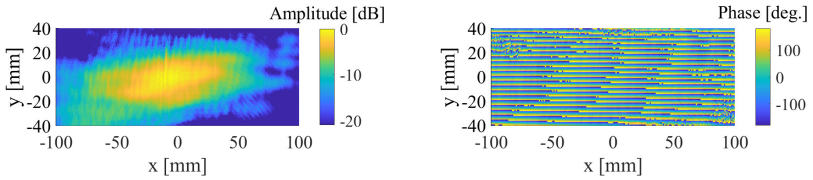

(a) Field intensity pattern. (b) Phase pattern.

Fig. A.23: a) Field intensity pattern and b) phase pattern of the $TE_{34,19}$ mode at 170.325 GHz after the launcher and mirror 1.

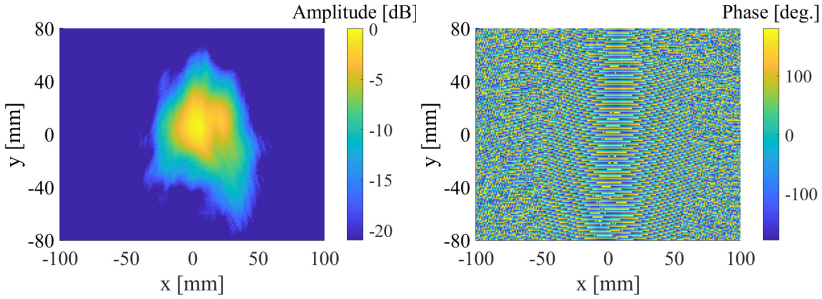

(a) Field intensity pattern. (b) Phase pattern.

Fig. A.24: a) Field intensity pattern and b) phase pattern of the $TE_{34,19}$ mode at 170.325 GHz after the launcher and mirror 2.

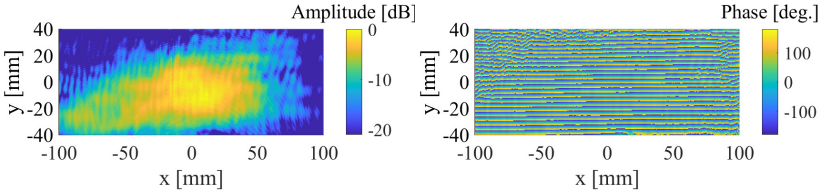

(a) Field intensity pattern. (b) Phase pattern.

Fig. A.25: a) Field intensity pattern and b) phase pattern of the $TE_{40,23}$ mode at 204.071 GHz after the launcher and mirror 1.

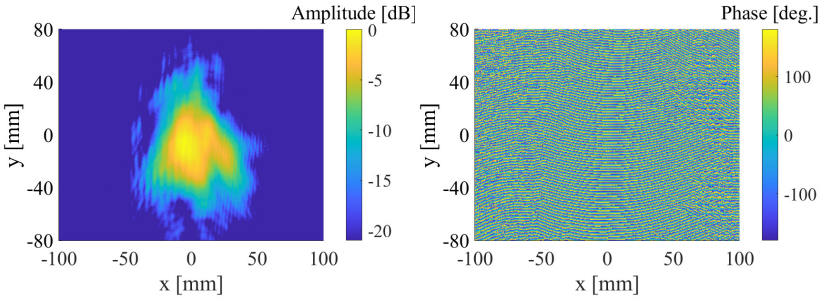

(a) Field intensity pattern. (b) Phase pattern.

Fig. A.26: a) Field intensity pattern and b) phase pattern of the $TE_{40,23}$ mode at 204.071 GHz after the launcher and mirror 2.

A.4 Manufacturing of a Potter Horn

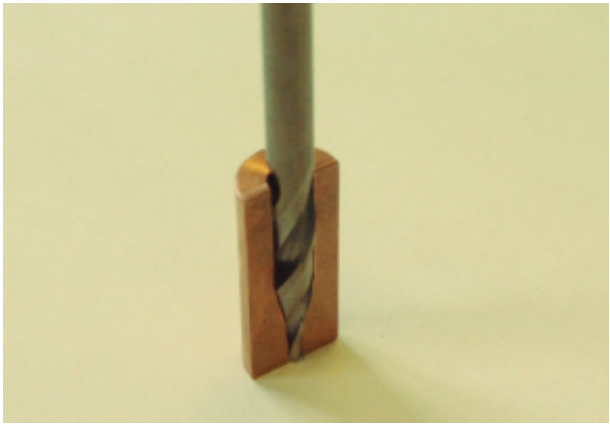

Fig. A.27: Photo of driller and cut of the manufactured Potter horn.

A.5 Coupling through a Translucent Wall

A derivation of the coupling through the perforated, translucent cavity wall is presented. In terms of mutual interaction between several holes, the diffraction theory is taken into account for the coupling [138]. The power balance between the injected beam P_{in} and the power of the beam, which passed through the coupling holes has to be satisfied. In a first approximation, an equation for the coupling through an infinite, periodically perforated plane plate is derived. The transmission is given by [138]

$$|T|^2 = \frac{4\,|\rho|^2}{1 + 4\,|\rho|^2} \quad . \tag{A.1}$$

ρ describes the coupling. The coupling can be calculated, according to Collin [153]. It defines the polarizabilities of a hole. Using the Babinet's principle the polarizability of the periodic system of a plane metallic disk corresponds

to the polarizabilities of a dual periodic system of holes in a metallic plate [138]. Therefore the formula

$$\rho = \frac{k}{2\beta \cdot a \cdot b}(1i \cdot P + 1i \cdot \alpha M) \tag{A.2}$$

can be used to calculate the coupling. P and M characterize the electric and magnetic dipoles for the disk [153]. α and β are described by the cosine and sine of the incident angle of the input beam, and a and b are the distances between the holes in both directions. The electric and magnetic dipole moments can be expressed by [153]

$$M = 8/3 r_{\text{hole}}^3 \tag{A.3}$$

$$M = -4/3 r_{\text{hole}}^3 \alpha \tag{A.4}$$

The interaction between the holes can be included if the electric and magnetic dipole moments are multiplied by $(1 - \alpha_e C_e)^{-1}$ and $(1 - \alpha_m C_m)^{-1}$, respectively, with [153]

$$C_e = \frac{1.2}{\pi \cdot a} - \frac{8\pi}{b^3}\kappa_0\left(\frac{2\pi \cdot b}{a}\right) \tag{A.5}$$

$$C_m = -\frac{1.2}{\pi \cdot a} - \frac{1.2}{\pi \cdot b} + \frac{8\pi}{b^3}\kappa_0\left(\frac{2\pi \cdot b}{a}\right) + \frac{8\pi}{a^3}\kappa_0\left(\frac{2\pi \cdot a}{b}\right) \quad . \tag{A.6}$$

κ_0 is the modified Bessel function of the second kind and $\alpha_e = 16 r_{\text{hole}}^3/3$ and $\alpha_m = -8 r_{\text{hole}}^3/3$.

A.6 Measurement Setup of Dielectric Loaded Disks

In the commissioning phase of a gyrotron, the generated microwave power is transferred to a gyrotron load rather than to the fusion machine. A microwave load should reliably handle powers up to 2 MW in CW operation. The attenuation or even absorption of the microwave beam can be done using a dielectric coating on the inner cylindrical surface of the gyrotron load. The most important characteristics of the dielectric material are according to

[182], high dielectric constant, a reasonable high heat conductivity, high resistance against electromagnetic and thermal loads and a good substrate adhesion. The layer thicknesses are chosen to create almost a resonance structure. This requires around 100 μm thin layers for maximum absorption. Thin coatings are applied by the plasma spraying process. A detailed description of the technology is given in [183]. A common used dielectric material is alumina-titania (AL_2O_3/TiO_2) in a given mixture achieving a high absorption of the microwave beam [182, 184].

Measurement Results of Coated Test Samples

In [184], a mixture of 87/13 wt.% of Al_2O_3/TiO_2 has been used to measured absorption at 140 GHz. In this work, a mixture of 60/40 wt.% is used to be measured at 140 GHz and 170 GHz. Therefore, a set of test samples with different thickness from 30 μm to 150 μm are fabricated on a copper disk with a diameter of 124 mm. A photo of a disk is shown in Fig. A.28a. The measurement results and the values published for the 87/13 wt.% mixture are depicted in Fig. A.28b for comparison. The different graphs show a clear resonance in its behaviour over the thickness. The resonance occurs at a thickness t corresponding to $\lambda_m/4$ using:

$$t = \frac{\lambda_m}{4} = \frac{\lambda_0}{4 \cdot \sqrt{\epsilon_r}} = \frac{c_0}{4 \cdot f \cdot \sqrt{\epsilon_r}}$$

λ_m is the wavelength in the medium. The calculated relative permittivity is $\epsilon_r \approx 17.5$ for the 60/40 wt.% mixture of Al_2O_3/TiO_2 and is in contrast higher than the mixture of 87/13 wt.% having a $\epsilon_r \approx 14.8$. This is due to the larger amount of TiO_2 having a relative permittivity of $\epsilon_r \approx 169$ at 140 GHz [185].

The measurement results are used in the simulation of the gyrotron load. Therefore, a "ballistic" ray-tracing code is used. A large number of single rays are propagated. The powers of the rays are attenuated each time they hit the wall and are reflected according to the specified measured values. After multiple reflections most of the power is attenuated. Different thicknesses over the length are simulated. It was decided to manufacture the gyrotron load with a thin coating having a thickness < 105 μm to avoid any resonance

structures preventing possible arcing. The simulations show the best results when the coating starts with 50 µm, at full power, and is gradually increased to 100 µm. The set of different coating thickness results in simulation, that 2.4 % of the input power is reflected back to the input of the gyrotron load [183]. It has to be mentioned, that in terms of the internal structure of the gyrotron load the remaining microwave beam does not propagate back towards the gyrotron. After the manufacturing process first long pulse tests with a pulse duration of 26 min and an injected microwave power of 500 kW have been successfully performed. Visible inspection afterwards did not reveal any defects [183]. The measurements of this study are performed for a plane incident. A study about changing angles are published in [182].

A.7 Derivation of Reflection and Transmission of Gyrotron Output Windows

A plane wave is reflected at both boundaries (front and rear) of a perpendicular assembled disk. Both boundaries of the gyrotron output window can

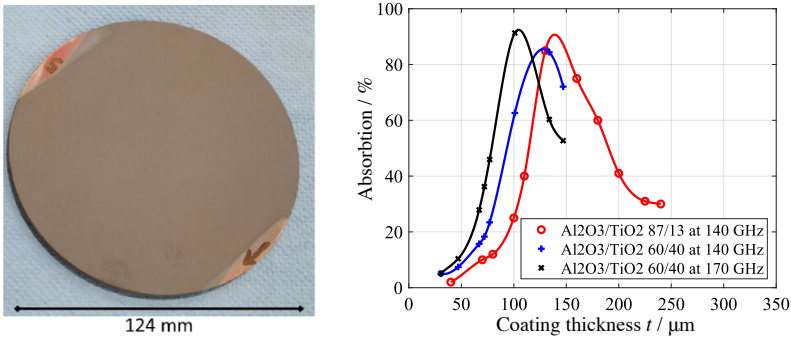

(a) Photo of planar test sample.

(b) Absorbtion.

Fig. A.28: a) Photo of the planar test sample with a coating of Al_2O_3/TiO_2 and b) comparison of the absorption measurements with a mixture of 87/13 wt.% (red) [184] and the measured mixture 60/40 wt.% at 140 GHz (blue) and 170 GHz (black) [183].

be described by a port [83], if the incident beam is not converted and the transversal power density is constant. The reflectivity R and transmission T can be described via the S-parameters of a port. The boundaries of the single-disk can be expressed by [83]:

$$[\underline{S}] = \frac{1}{1-\rho_v^2 \exp(-2\underline{\gamma_{\epsilon v}} d_{\text{window}})} \cdot \begin{bmatrix} \rho_v \left(1-\exp(-2\underline{\gamma_{\epsilon v}} d_{\text{window}})\right) & \left(1-\rho_v^2\right)\exp(-2\underline{\gamma_{\epsilon v}} d_{\text{window}}) \\ \left(1-\rho_v^2\right)\exp(-2\underline{\gamma_{\epsilon v}} d_{\text{window}}) & \rho_v \left(1-\exp(-2\underline{\gamma_{\epsilon v}} d_{\text{window}})\right) \end{bmatrix} . \tag{A.7}$$

d_{window} is the window thickness and ρ_v the reflection factor. The microwave output beam of a gyrotron is linearly polarized, whereas the reflection factor is calculated with the Fresnel equation to [186]:

$$\rho_v = \frac{\sqrt{\epsilon_1'}\cos(\theta_{\text{in}}) - \sqrt{\epsilon_r'}\cos(\theta_{\text{out}})}{\sqrt{\epsilon_1'}\cos(\theta_{\text{in}}) + \sqrt{\epsilon_r'}\cos(\theta_{\text{out}})}. \tag{A.8}$$

θ_{in} and θ_{out} are the angles of the incoming and outgoing/transmitted waves. Equation A.8 can be simplified by considering the vacuum condition in the gyrotron with $\epsilon_1' = 1$, resulting in

$$\rho_v = \frac{1-\sqrt{\epsilon_r'}}{1+\sqrt{\epsilon_r'}} \tag{A.9}$$

The propagation constant $\gamma_{\epsilon v}$ is described by the attenuation $\alpha_{\epsilon v}$ and the phase constant $\beta_{\epsilon v}$ to

$$\gamma_{\epsilon v} = \alpha_{\epsilon v} + j\beta_{\epsilon v} \quad . \tag{A.10}$$

The attenuation and the phase constant can be simplified considering a low loss dielectric material $\tan\delta \ll 1$ to [83]

$$\alpha_{\epsilon\upsilon} \approx \frac{k_0\sqrt{\epsilon_r'}\tan\delta}{2} \quad , \tag{A.11}$$

$$\beta_{\epsilon\upsilon} \approx k_0\sqrt{\epsilon_r'} \quad , \tag{A.12}$$

using the free-space wave number $k_0 = 2\pi f/c_0$. The reflection and transmission can be expressed using the described simplifications and Eq. A.7 to [83]

$$R = \frac{R_0\left(1 - 2T_0\cos\left(2\beta_{\epsilon\upsilon}d_{\text{window}}\right) + T_0^2\right)}{1 - 2R_0T_0\cos\left(2\beta_{\epsilon\upsilon}d_{\text{window}}\right) + R_0^2T_0^2} \tag{A.13}$$

$$T = \frac{T_0\left(1 - R_0\right)^2}{1 - R_0T_0\cos\left(2\beta_{\epsilon\upsilon}d_{\text{window}}\right) + R_0^2T_0^2} \tag{A.14}$$

with

$$R_0 = \left|\rho_\upsilon\right|^2 \tag{A.15}$$

$$T_0 = \exp\left(-2\alpha_{\epsilon\upsilon}d_{\text{window}}\right) \tag{A.16}$$

A.8 Cutting Plane of Electron Beam Welding

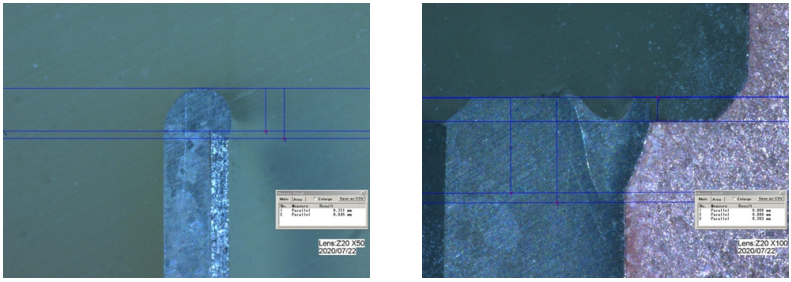

(a) Cutting plane of cable feed-through and nickel sleeve.

(b) Cutting plane of nickel sleeve and CuCrZn flange.

Fig. A.29: Photo of a the cutted planes of the test device under the microscope.

Bibliography

[1] U. Nations, "World population prospects 2019", ST/ESA/SER.A/423: Department of Economic and Social Affairs, Population Division, (2019)

[2] F. F. Chen, "An indispensable truth", Springer New York, NY, (2011), DOI: 10.1007/978-1-4419-7820-2

[3] A. Einstein, "Elementary derivation of the equivalence of mass and energy", in: *Bull. Amer. Math. Soc* 41.4 (1935), pp. 223–230, DOI: bams/1183498131

[4] Y. Gohar, M. Billone, A. Cardella, W. Danner, K. Ioki, T. Kuroda, D. Lousteau, P. Lorenzetto, S. Majumdar, R. Mattas, K. Mohri, R. Raffray, Y. Strebkov, H. Takatsu, and E. Zolti, "ITER breeding blanket design", in: *Proceedings of 16th International Symposium on Fusion Engineering*, vol. 1, (1995), pp. 410–417, DOI: 10.1109/FUSION.1995.534253

[5] J. Lawson, "Some criteria for a power producing thermonuclear reactor", in: *Proceedings of the Physical Society. Section B* 70.1 (1957), pp. 6–10, DOI: 10.1088/0370-1301/70/1/303

[6] O. Mitarai, C. Xiao, D. McColl, M. Drevak, A. Hirose, and M. Peng, "Plasma current start-up by the outer ohmic heating coils in the Saskatchewan TORus Modified (STOR-M) iron core tokamak", in: *Review of Scientific Instruments* 86 (2015), DOI: 10.1063/1.4915316

[7] Y. Kazakov, D. Van Eester, and J. Ongena, "Plasma heating in present-day and future fusion machines", in: *12th Carolus Magnus Summer School on plasma and Fusion Energy Physics* (2015)

[8] F. Mirizzi, A. Cardinali, R. Maggiora, L. Panaccione, G. Ravera, and A. Tuccillo, "Conceptual design of the ICRH and LHCD systems for

FT-3", in: *2007 IEEE 22nd Symposium on Fusion Engineering*, (2007), pp. 1–4, DOI: 10.1109/FUSION.2007.4337936

[9] R. Wolf, S. Bozhenkov, A. Dinklage, G. Fuchert, Y. Kazakov, H. P. Laqua, and S. Marsen, "Electron-cyclotron-resonance heating in Wendelstein 7-X: a versatile heating and current-drive mehtod and a tool for in-depth physics studies", in: *Plasma Phys. Control. Fusion* 61.014037 (2019), DOI: 10.1088/1361-6587/aaeab2

[10] C. Luttrell, E. Coffey, I. Griffith, G. Hanson, A. Lumsdaine, and C. Schaich, "Analysis of the ITER ECH waveguide transmission line expansion unit", in: *Fusion Science and Technology* 72.3 (2017), pp. 312–317, DOI: 10.1080/15361055.2017.1333847

[11] H. P. Laqua, J. Baldzuhn, H. Braune, S. Bozhenkov, K. Brunner, M. Hirsch, U. Hoefel, J. Knauer, A. Langenberg, S. Marsen, D. Moseev, E. Pasch, K. Rahbarnia, T. Stange, R. Wolf, et al., "High-performance ECRH at W7-X: Experience and perspectives", in: *Nuclear Fusion* 61.10 (2021), DOI: 10.1088/1741-4326/ac1a1b

[12] C. Wu, G. Aiello, K. Avramidis, A. Bruschi, E. Fable, T. Franke, G. Gantenbein, S. Garavaglia, G. Granucci, S. Illy, F. Janky, J. Jelonnek, O. Kudláček, A. Moro, E. Poli, et al., "Basic design considerations for a frequency step-tunable electron cyclotron wave system to suppress NTMs in DEMO", in: *Fusion Engineering and Design* 173 (2021), p. 112931, DOI: 10.1016/j.fusengdes.2021.112931

[13] T. Rzesnicki, B. Piosczyk, S. Kern, S. Illy, J. Jin, A. Samartsev, A. Schlaich, and M. Thumm, "2.2-MW record power of the 170-GHz european preprototype coaxial-cavity gyrotron for ITER", in: *IEEE Transactions on Plasma Science* 38.6 (2010), pp. 1141–1149, DOI: 10.1109/TPS.2010.2040842

[14] G. Giruzzi, J. F. Artaud, V. Basiuk, J. Garcia, F. Imbeaux, and M. Schneider, "Integrated modelling of ITER hybrid scenarios with ECCD", World Scientific Publishing Co Pte Ltd, (2009), DOI: 10.1142/9789812814647_0043

[15] S. Korsholm, H. Bindslev, V. Furtula, F. Leipold, F. Meo, P. Michelsen, D. Moseev, S. Nielsen, M. Salewski, and M. Stejner, "Collective thomson scattering capabilities to diagnose fusion plasmas", in: *Nuclear Instruments and Methods in Physics Research Section A: Accelerators, Spectrometers, Detectors and Associated Equipment* 623.2 (2010), 1st International Conference on Frontiers in Diagnostics Technologies, pp. 677–680, DOI: 10.1016/j.nima.2010.05.003

[16] F. M. Poli, E. Fredrickson, M. A. Henderson, N. Bertelli, D. Farina, L. Figini, and E. Poli, "EC power management in ITER for NTM control: the path from the commissioning phase to demonstration discharges", in: *EPJ Web Conf.* 157 (2017), p. 03041, DOI: 10.1051/epjconf/201715703041

[17] H. Braune, H. P. Laqua, S. Marsen, D. Moseev, F. Noke, F. Purps, N. Schneider, T. Schulz, T. Stange, and P. Uhren, "Gyrotron operation during the first W7-X campaign-handling and reliability", in: *2016 41st International Conference on Infrared, Millimeter, and Terahertz waves (IRMMW-THz)*, (2016), pp. 1–2, DOI: 10.1109/IRMMW-THz.2016.7758425

[18] M. Thumm, S. Alberti, A. Arnold, P. Brand, H. Braune, G. Dammertz, V. Erckmann, G. Gantenbein, E. Giguet, R. Heidinger, J.-P. Hogge, S. Illy, W. Kasparek, H. P. Laqua, F. Legrand, et al., "EU megawatt-class 140-GHz CW gyrotron", in: *IEEE Transactions on Plasma Science* 35.2 (2007), pp. 143–153, DOI: 10.1109/TPS.2007.892144

[19] T. Omori, M. Henderson, F. Albajar, S. Alberti, U. Baruah, T. Bigelow, B. Beckett, R. Bertizzolo, T. Bonicelli, A. Bruschi, J. Caughman, R. Chavan, S. Cirant, A. Collazos, D. Cox, et al., "Overview of the ITER EC H&CD system and its capabilities", in: *Fusion Engineering and Design* 86.6 (2011), pp. 951–954, DOI: 10.1016/j.fusengdes.2011.02.040

[20] P. Moreau, S. Bremond, J. Bucalossi, C. Reux, D. Douai, T. Loarer, E. Nardon, R. Nouailletas, F. Saint-Laurent, P. Tamain, C. Bourdelle, N. Fedorczak, E. Tsitrone, and J. F. Artaud, "The commissioning

of the WEST tokamak: experience and lessons learned", in: *IEEE Transactions on Plasma Science* 48.6 (2020), pp. 1376–1381, DOI: 10.1109/TPS.2020.2987160

[21] D. H. Wagner, J. K. Stober, F. Leuterer, G. Sips, G. Grunwald, F. Monaco, M. J. Munich, E. Poli, H. Schutz, F. Volpe, W. Treutterer, H. Zohm, T. Franke, M. Thumm, R. Heidinger, et al., "Progress and first results with the new multifrequency ECRH system for ASDEX Upgrade", in: *IEEE Transactions on Plasma Science* 37.3 (2009), pp. 395–402, DOI: 10.1109/TPS.2008.2011798

[22] G. Granucci, G. Ravera, A. Bruschi, S. Ceccuzzi, P. Agostinetti, S. Garavaglia, A. Romano, and A. Ferro, "The heating & current drive system of divertor tokamak test (DTT)", in: *2020 IEEE 20th Mediterranean Electrotechnical Conference (MELECON)*, 2020, pp. 629–633, DOI: 10.1109/MELECON48756.2020.9140677

[23] J.-P. Hogge, S. Alberti, K. A. Avramidis, A. Bruschi, W. Bin, F. Cau, F. Cismondi, J. Dubray, D. Fasel, G. Gantenbein, S. Garavaglia, J. Genoud, T. P. Goodman, S. Illy, J. Jin, et al., "Megawatt power generation of the dual-frequency gyrotron at TCV at 84 and 126 GHz, in long pulses", in: *AIP Conference Proceedings* (2020), DOI: 10.1063/5.0014343

[24] M. Cengher, R. Brambila, X. Chen, W. Grosnickle, Y. Gorelov, I. Holmes, P. Nesbet, A. Mazzeo, J. Tooker, A. Torrezan, and G. Sips, "DIII-D electron cyclotron heating and current drive system status and plans", in: *IEEE Transactions on Plasma Science* 50.11 (2022), pp. 4069–4073, DOI: 10.1109/TPS.2022.3169058

[25] S. Kim, S. Wang, J. Han, M. Joung, I. Rhee, and J.-g. Kwak, "Progress of high power and long-pulse dual-frequency ECH system in KSTAR", in: *2019 International Vacuum Electronics Conference (IVEC)*, (2019), pp. 1–2, DOI: 10.1109/IVEC.2019.8744875

[26] T. Kobayashi, H. Yamazaki, S. Hiranai, M. Sawahata, M. Terakado, K. Ishita, J. Hinata, F. Sato, K. Wada, N. Toida, R. Ikeda, T. Shinya,

S. Yajima, K. Kajiwara, K. Takahashi, et al., “Development of high-power, long-pulse, multi-frequency ECH/CD system for JT-60SA”, in: *Nuclear Fusion* 62.2 (2022), p. 026039, DOI: 10.1088/1741-4326/ac42f4

[27] D. Xia, X. Chen, D. Xu, J. Fang, J. Zhang, N. Wang, Z. Yang, Z. Chen, Y. Ding, W. Zheng, S. Ma, Z. Wang, and Y. Pan, “Recent progress of the ECRH system and initial experimental results on the J-TEXT tokamak”, in: *Plasma Science and Technology* 24.12 (2022), p. 124010, DOI: 10.1088/2058-6272/aca4b5

[28] P. Khvostenko, I. Anashkin, E. Bondarchuk, A. Chudnovsky, A. Kavin, A. Khvostenko, N. Kirneva, E. Kuzmin, I. Levin, V. Leonov, A. Lutchenko, A. Modyaev, A. Nikolaev, G. Notkin, A. Romannikov, et al., “Current status of tokamak T-15MD”, in: *Fusion Engineering and Design* 164 (2021), p. 112211, DOI: 10.1016/j.fusengdes.2020.112211

[29] G. Federici, C. Bachmann, L. Barucca, W. Biel, L. Boccaccini, R. Brown, C. Bustreo, S. Ciattaglia, F. Cismondi, M. Coleman, V. Corato, C. Day, E. Diegele, U. Fischer, T. Franke, et al., “DEMO design activity in Europe: progress and updates”, in: *Fusion Engineering and Design* 136 (2018), Special Issue: Proceedings of the 13th International Symposium on Fusion Nuclear Technology (ISFNT-13), pp. 729–741, ISSN: 0920-3796, DOI: 10.1016/j.fusengdes.2018.04.001

[30] S. Ciattaglia, M. C. Falvo, A. Lampasi, and M. Proietti Cosimi, “Energy analysis for the connection of the nuclear reactor DEMO to the European electrical grid”, in: *Energies* 13.9 (2020), ISSN: 1996-1073, DOI: 10.3390/en13092157

[31] P. C. Kalaria, “Feasibility and operational limits for 236 GHz hollow-cavity gyrotron for DEMO”, PhD thesis, Karlsruhe Institut of Technology (KIT), (2018), ISBN: 978-3-7315-0717-8

[32] Z. Ioannidis, T. Rzesnicki, F. Albajar, S. Alberti, K. Avramidis, W. Bin, T. Bonicelli, A. Bruschi, I. Chelis, F. Fanale, G. Gantenbein, V. Hermann, J.-P. Hogge, S. Illy, J. Jin, et al., “Report of recent exper-

iments with the European 1 MW, 170 GHz CW and SP prototype gyrotrons for ITER", in: *EPJ Web Conf.* 203 (2019), p. 04006, DOI: 10.1051/epjconf/201920304006

[33] A. Krasilnikov, I. Abdyuhanov, E. Aleksandrov, A. Alekseev, V. Amosov, N. Antonov, N. Arkhipov, A. Burdakov, I. Chugunov, G. Denisov, A. Gervash, M. Ivantsivskiy, Y. Kaschuk, S. Khomyakov, V. Krasilnikov, et al., "Progress with the ITER project activity in Russia", in: *Nuclear Fusion* 55.10 (2015), p. 104007, DOI: 10.1088/0029-5515/55/10/104007

[34] Y. Oda, R. Ikeda, T. Nakai, K. Kajiwara, T. Kobayashi, K. Takahashi, K. Sakamoto, S. Moriyama, C. Darbos, and M. Hendereson, "Completion of 1st ITER gyrotron manufacturing and 1 MW test results", in: *Nuclear Fusion* (2018), DOI: 10.1088/1741-4326/ab22c2

[35] K. Flech, M. Blank, P. Borchard, and S. Cauffman, "Recent tests on 117.5 GHz and 170 GHz gyrotrons", in: *EPJ Web of Conferences* (2015), DOI: 10.1051/epjconf/20158704006

[36] K. A. Avramidis, Z. C. Ioannidis, G. Aiello, P. Bénin, I. Chelis, A. Dinklage, G. Gantenbein, S. Illy, J. Jelonnek, J. Jin, H. P. Laqua, A. Leggieri, F. Legrand, A. Marek, S. Marsen, et al., "Towards a 1.5 MW, 140 GHz gyrotron for the upgraded ECRH system at W7-X", in: *Fusion Engineering and Design* 164 (2021), p. 112173, ISSN: 0920-3796, DOI: 10.1016/j.fusengdes.2020.112173

[37] Z. C. Ioannidis, T. Rzesnicki, K. A. Avramidis, G. Gantenbein, S. Illy, J. Jin, L. Krier, I. G. Pagonakis, S. Ruess, M. Schmid, M. Thumm, and J. Jelonnek, "Operation of the modular KIT 170 GHz – 2 MW longer-pulse coaxial-cavity gyrotron with pulses up to 50 ms", in: *2020 45th International Conference on Infrared, Millimeter, and Terahertz Waves (IRMMW-THz)*, (2020), pp. 01–02, DOI: 10.1109/IRMMW-THz46771.2020.9370698

[38] J. Jelonnek, "Untersuchung des Lastverhaltens von Gyrotrons", Doktorarbeit, TU Hamburg-Harburg, (2000), ISBN: 3183297212; 9783183297214

[39] N. V. Grigorieva and N. M. Ryskin, "Study of injection locking of a gyrotron by using the modified quasilinear theory", in: *2021 14th UK-Europe-China Workshop on Millimetre-Waves and Terahertz Technologies (UCMMT)*, (2021), pp. 1–3, DOI: 10.1109/UCMMT53364.2021.9569876

[40] R. Ikeda, Y. Oda, T. Kobayashi, K. Kajiwara, M. Terakado, K. Takahashi, S. Moriyama, and K. Sakamoto, "Multi-frequency, MW-power triode gyrotron having a uniform directional beam", in: *Journal of Infrared, Millimeter, and Terahertz Waves* 38.5 (2017), pp. 531–537, DOI: 10.1007/s10762-016-0348-8

[41] T. Ruess, K. Avramidis, G. Gantenbein, S. Illy, Z. Ioannidis, J. Jin, P. Kalaria, I. G. Pagonakis, S. Ruess, T. Rzesnicki, M. Thumm, and J. Jelonnek, "Theoretical study on the operation of the EU/KIT TE34,19-mode coaxial-cavity gyrotron at 170/204/238 GHz", in: *EPJ Web Conf.* 203 (2019), p. 04014, DOI: 10.1051/epjconf/201920304014

[42] G. Gantenbein, A. Samartsev, G. Aiello, G. Dammertz, J. Jelonnek, M. Losert, A. Schlaich, T. A. Scherer, D. Strauss, M. Thumm, and D. Wagner, "First operation of a step-frequency tunable 1-MW gyrotron with a diamond brewster angle output window", in: *IEEE Transactions on Electron Devices* 61.6 (2014), pp. 1806–1811, DOI: 10.1109/TED.2013.2294739

[43] A. Samartsev, K. A. Avramidis, G. Gantenbein, G. Dammertz, M. Thumm, and J. Jelonnek, "Efficient frequency step-tunable megawatt-class *D*-band gyrotron", in: *IEEE Transactions on Electron Devices* 62.7 (2015), pp. 2327–2332, DOI: 10.1109/TED.2015.2433016

[44] M. Thumm, A. Arnold, E. Borie, O. Braz, G. Dammertz, O. Dumbrajs, K. Koppenburg, M. Kuntze, G. Michel, and B. Piosczyk, "Frequency step-tunable (114–170 GHz) megawatt gyrotrons for plasma physics

applications", in: *Fusion Engineering and Design* 53.1 (2001), pp. 407–421, ISSN: 0920-3796, DOI: 10.1016/S0920-3796(00)00519-6

[45] L. Krier, K. A. Avramidis, H. Braune, G. Gantenbein, S. Illy, Z. Ioannidis, J. Jelonnek, H. P. Laqua, S. Marsen, D. Moseev, F. Noke, I. G. Pagonakis, T. Ruess, T. Rzesnicki, T. Stange, et al., "Frequency stabilization of megawatt-class 140 GHz gyrotrons at W7-X using an off-the-shelf PLL system", in: *2021 46th International Conference on Infrared, Millimeter and Terahertz Waves (IRMMW-THz)*, (2021), pp. 1–2, DOI: 10.1109/IRMMW-THz50926.2021.9566847

[46] V. L. Bakunin, G. G. Denisov, and Y. V. Novozhilova, "Phase locking of a gyrotron with low-frequency voltage and current fluctuations by an external monochromatic signal", in: *Radiophysics and Quantum Electronics* 63.5 (2020), pp. 392–402, DOI: 10.1007/s11141-021-10064-0

[47] B. Ell, I. G. Pagonakis, C. Wu, G. Gantenbein, S. Illy, T. Rzesnicki, S. Stanculovic, M. Thumm, J. Weggen, and J. Jelonnek, "Mechanical design of the short pulse ExB drift two-stage depressed collector prototype for high power gyrotron", in: *2021 22nd International Vacuum Electronics Conference (IVEC)*, (2021), pp. 1–2, DOI: 10.1109/IVEC51707.2021.9722425

[48] L. Groening, M. Chung, and C. Xiao, "Extension of Busch's theorem to particle beams", in: *29th International Linear Accelerator Conference*, (2018), TUPO078, DOI: 10.18429/JACoW-LINAC2018-TUPO078

[49] N. S. Ginzburg and G. S. Nusinovich, "On the nonlinear theory of a relativistic gyrotron", in: *Radiophysics and Quantum Electronics* 22.6 (1979), pp. 522–528, DOI: 10.1007/BF01081232

[50] J. Flamm, "Diffraction and scattering in launchers of quasi-optical mode converters for gyrotrons", PhD thesis, Karlsruhe Institute of Technology, (2012), ISBN: 978-3-86644-822-3

[51] G. Nusinovich, “The progress in the studies of mode interaction in gyrotrons”, in: *Journal of Infrared, Millimeter, and Terahertz Waves* 43 (2022), pp. 1–47, DOI: 10.1007/s10762-022-00845-7

[52] M. V. Kartikeyan, E. Borie, and M. Thumm, “Gyrotrons: high-power microwave and millimeter wave technology”, Springer Berlin, Heidelberg, (2004), DOI: 10.1007/978-3-662-07637-8

[53] R. Temkin, V. Granatstein, and G. Nusinovich, “Introduction to the physics of gyrotrons”, Johns Hopkins University Press, (2004), DOI: 10.1353/book.62236

[54] H. Jory, S. Evans, K. Felch, J. Shively, and S. Spang, “Gyrotron oscillators for fusion heating”, in: *Heating in Toroidal Plasmas 1982*, ed. by C. Gormezano, G. Leotta, and E. Sindoni, Pergamon, (1982), pp. 1073–1078, ISBN: 978-1-4832-8428-6, DOI: 10.1016/B978-1-4832-8428-6.50126-0

[55] C. J. Edgcombe, “The dispersion equation for the gyrotron amplifier”, in: *International Journal of Electronics* 48 (1980), pp. 471–486, DOI: 10.1080/00207218008901129

[56] S. Ruess, “Pushing the KIT 2 MW coaxial-cavity short-pulse gyrotron towards a DEMOrelevant design”, PhD thesis, Karlsruhe Institute of Technology, (2020), DOI: 10.5445/IR/1000117541

[57] V. K. Lygin, V. N. Manuilov, K. A. N., P. A. B., and B. Piosczyk, “Inverse magnetron injection gun for coaxial 1.5 MW, 140 GHz gyrotron”, in: *International Journal of Electronics* 79.2 (1995), pp. 227–235, DOI: 10.1080/00207219508926264

[58] C. Iatrou, O. Braz, G. Dammertz, S. Kern, M. Kuntze, B. Piosczyk, and M. Thumm, “Design and experimental operation of a 165-GHz, 1.5-MW, coaxial-cavity gyrotron with axial RF output”, in: *IEEE Transactions on Plasma Science* 25.3 (1997), pp. 470–479, DOI: 10.1109/27.597262

[59] S. Ruess, I. G. Pagonakis, G. Gantenbein, S. Illy, T. Kobarg, T. Rzesnicki, M. Thumm, J. Weggen, and J. Jelonnek, "An inverse magnetron injection gun for the KIT 2-MW coaxial-cavity gyrotron", in: *IEEE Transactions on Electron Devices* 63.5 (2016), pp. 2104–2109, DOI: 10.1109/TED.2016.2540298

[60] G. Gaertner, "Historical development and future trends of vacuum electronics", in: *Journal of Vacuum Science & Technology B* 30.6 (2012), p. 060801, DOI: 10.1116/1.4747705

[61] J. A. Eichmeier and M. Thumm, "Vacuum electronics: components and devices", 1st ed., Springer Berlin, Heidelberg, (2008), ISBN: 978-3-540-71929-8, DOI: 10.1007/978-3-540-71929-8

[62] V. N. Manuilov and S. A. Polushkina, "Behavior of helical electron beams in gyrotrons with high pitch factors", in: *Radiophysics and Quantum Electronics* 52.10 (2009), pp. 714–721, DOI: 10.1007/s11141-010-9179-y

[63] F. F. Chen, "Introduction to plasma physics", Springer New York, USA, (1995)

[64] C. J. Edgecombe, "Gyrotron oscillators", CRC Press, (1993), DOI: 10.1201/9781482272369

[65] C. Iatrou, S. Kern, and A. Pavelyev, "Coaxial cavities with corrugated inner conductor for gyrotrons", in: *IEEE Transactions on Microwave Theory and Techniques* 44.1 (1996), pp. 56–64, DOI: 10.1109/22.481385

[66] K. Avramides, C. Iatrou, and J. Vomvoridis, "Design considerations for powerful continuous-wave second-cyclotron-harmonic coaxial-cavity gyrotrons", in: *IEEE Transactions on Plasma Science* 32.3 (2004), pp. 917–928, DOI: 10.1109/TPS.2004.828781

[67] S. Kern, "Numerische Simulation der Gyrotron- Wechselwirkung in koaxialen Resonatoren", 31.04.02; LK 01; Karlsruhe 1996.) Fak. f. Elektrotechnik, Doktorarbeit, (1996), DOI: 10.5445/IR/55396

[68] M. H. Beringer, “Design studies towards a 4 MW 170 GHz coaxial-cavity gyrotron”, 31.30.03; LK 01, PhD thesis, (2011), 197 pp., ISBN: 978-3-86644-663-2, DOI: 10.5445/KSP/1000022514

[69] D. M. Pozar, “Microwave Engineering”, Addison-Wesley, (1990), ISBN: 9780201504187

[70] V. A. Flyagin, A. V. Gaponov, M. I. Petelin, and Y. K. Yulpatov, “The gyrotron”, in: *IEEE Trans. on Microwave Theory and Techniques (MTT)* 25 (1977), pp. 514–521, DOI: 10.1109/TMTT.1977.1129149

[71] S. N. Vlasov, G. M. Zhislin, I. M. Orlova, M. I. Petelin, and G. G. Rogacheva, “Irregular waveguides as open resonators”, in: *Radiophysics and Quantum Electronics* 12.8 (1969), pp. 972–978, DOI: 10.1007/BF01031202

[72] K. E. Kreischer, B. G. Danly, J. B. Schutkeker, and R. J. Temkin, “The design of megawatt gyrotrons”, in: *IEEE Transactions on Plasma Science* 13.6 (1985), pp. 364–373, DOI: 10.1109/TPS.1985.4316447

[73] S. N. Vlasov and I. M. Orlova, “Quasioptical transformer which transforms the waves in a waveguide having a circular cross section into a highly directional wave beam”, in: *Radiophysics and Quantum Electronics* 17 (1974), pp. 115–119, DOI: 10.1007/BF01037072

[74] G. G. Denisov, A. N. Kuftin, V. I. Malygin, N. P. Venediktov, D. V. Vinogradov, and V. E. Zapevalov, “110 GHz gyrotron with a built-in high-efficiency converter”, in: *International Journal of Electronics* 72.5-6 (1992), pp. 1079–1091, DOI: 10.1080/00207219208925634

[75] J. Jin, G. Gantenbein, J. Jelonnek, T. Rzesnicki, and M. Thumm, “Development of mode conversion waveguides at KIT”, in: *EPJ Web of Conferences* 87 (2015), p. 04003, DOI: 10.1051/epjconf/20158704003

[76] S. N. Vlasov, L. I. Zagriadskaia, and M. I. Petelin, “Transformation of a whispering gallery mode, propagating in a circular waveguide, into a beam of waves”, in: *Physics*, (1975)

[77] M. Thumm and A. Möbius, "Gyrotron oscillators, chapter 7: gyrotron output launchers and output tapers", ed. by C. J. Edgecombe, Taylor & Francis, (1993), DOI: 10.1201/9781482272369

[78] J. Jelonnek, G. Aiello, S. Alberti, K. Avramidis, F. Braunmueller, A. Bruschi, J. Chelis, J. Franck, T. Franke, G. Gantenbein, S. Garavaglia, G. Granucci, G. Grossetti, S. Illy, Z. Ioannidis, et al., "Design considerations for future DEMO gyrotrons: A review on related gyrotron activities within EUROfusion", in: *Fusion Engineering and Design* 123 (2017), Proceedings of the 29th Symposium on Fusion Technology (SOFT-29) Prague, Czech Republic, September 5-9, 2016, pp. 241–246, DOI: 10.1016/j.fusengdes.2017.01.047

[79] L. Savoldi, F. Albajar, S. Alberti, K. Avramidis, A. Bertinetti, F Cau, F Cismondi, G Gantenbein, J. Hogge, Z. Ioannidis, et al., "Assessment and optimization of the cavity thermal performance for the European continuous wave gyrotrons", in: *Proceedings of the 27th IAEA Fusion Energy Conference (FEC 2018), Gandhinagar, Indien*, (2018), pp. 22–27

[80] M. Thumm, "State-of-the-art of high-power gyro-devices and free electron masers", in: *Journal of Infrared, Millimeter, and Terahertz Waves* 41.1 (2020), pp. 1–140, DOI: 10.1007/s10762-019-00631-y

[81] T. Ruess, G. Gantenbein, Z. Ioannidis, T. Rzesnicki, D. Wagner, M. Thumm, and J. Jelonnek, "Frequency and mode measurement techniques for megawatt-class gyrotrons", in: *tm - Technisches Messen* 89.2 (2022), pp. 85–96, DOI: doi:10.1515/teme-2021-0039

[82] G. Aiello, T. Scherer, K. Avramidis, N. Casal, T. Franke, G. Gagliardi, G. Gantenbein, M. Henderson, J. Jelonnek, A. Meier, G. Saibene, S. Schreck, D. Strauss, M. Thumm, M. Q. Tran, et al., "Diamond window technology for electron cyclotron heating and current drive: state of the art", in: *Fusion Science and Technology* 75.7 (2019), pp. 719–729, DOI: 10.1080/15361055.2019.1643690

[83] H.-U. Nickel, “Hochfrequenztechnische Aspekte zur Entwicklung rückwirkungsarmer Ausgangsfenster für Millimeterwellengyrotrons hoher Leistung”, in: *Universität Karlsruhe (TH)* (1994)

[84] B. Piosczyk, A. Arnold, H. Budig, G. Dammertz, O. Dumbrajs, O. Drumm, M. Kartikeyan, M. Kuntze, M. Thumm, and X. Yang, “Towards a 2 MW, CW, 170 GHz coaxial cavity gyrotron for ITER”, in: *Fusion Engineering and Design* 66-68 (2003), 22nd Symposium on Fusion Technology, pp. 481–485, ISSN: 0920-3796, DOI: 10.1016/S0920-3796(03)00078-4

[85] J. Jelonnek, G. Aiello, S. Alberti, K. Avramidis, A. Bertinetti, A. Bruschi, J. Chelis, T. Franke, G. Gantenbein, S. Garavaglia, G. Granucci, G. Grossetti, S. Illy, Z. Ioannidis, J. Jin, et al., “European research activities towards a future DEMO gyrotron”, in: *EPJ Web Conf.* 149 (2017), p. 04007, DOI: 10.1051/epjconf/201714904007

[86] G. Li, J. Jin, T. Rzesnicki, S. Kern, and M. Thumm, “Analysis of a quasi-optical launcher toward a step-tunable 2-MW coaxial-cavity gyrotron”, in: *IEEE Transactions on Plasma Science* 38.6 (2010), pp. 1361–1368, DOI: 10.1109/TPS.2010.2043267

[87] K. A. Avramides, I. G. Pagonakis, C. T. Iatrou, and J. L. Vomvoridis, “EURIDICE: a code-package for gyrotron interaction simulations and cavity design”, in: *EPJ Web of Conferences* 32 (2012), p. 04016, DOI: 10.1051/epjconf/20123204016

[88] J. Franck, “Systematic study of key components for a coaxial-cavity gyrotron for DEMO”, PhD thesis, Karlsruhe, (2017), p. 274, ISBN: 978-3-7315-0652-2, DOI: 10.5445/KSP/1000068000

[89] S. Ruess, K. A. Avramidis, M. Fuchs, G. Gantenbein, S. Illy, P. C. Kalaria, T. Kobarg, I. G. Pagonakis, T. Rzesnicki, M. Thumm, J. Weggen, and J. Jelonnek, “KIT coaxial gyrotron development: from ITER towards DEMO”, in: *2017 47th European Microwave Conference (EuMC)*, (2017), pp. 860–863, DOI: 10.23919/EuMC.2017.8230980

[90] J. Jin, M. Thumm, B. Piosczyk, S. Kern, J. Flamm, and T. Rzesnicki, "Novel numerical method for the analysis and synthesis of the fields in highly oversized waveguide mode converters", in: *IEEE Transactions on Microwave Theory and Techniques* 57.7 (2009), pp. 1661–1668, DOI: 10.1109/TMTT.2009.2021878

[91] J. M. Neilson, "Surf3d and LOT : computer codes for design and analysis of high-performance qo launchers in gyrotrons", in: *Infrared and Millimeter Waves, Conference Digest of the 2004 Joint 29th International Conference on 2004 and 12th International Conference on Terahertz Electronics, 2004.* (2004), pp. 667–668, DOI: 10.1109/ICIMW.2004.1422267

[92] I. G. Pagonakis, K. A. Avramidis, G. Gantenbein, S. Illy, Z. C. Ioannidis, J. Jin, P. Kalaria, B. Piosczyk, S. Ruess, T. Ruess, T. Rzesnicki, M. Thumm, and J. Jelonnek, "Triode magnetron injection gun for the KIT 2 MW 170 GHz coaxial cavity gyrotron", in: *Physics of Plasmas* 27.2 (2020), p. 023105, DOI: 10.1063/1.5132615

[93] I. G. Pagonakis, B. Piosczyk, J. Zhang, S. Illy, T. Rzesnicki, J.-P. Hogge, K. A. Avramidis, G. Gantenbein, M. Thumm, and J. Jelonnek, "Electron trapping mechanisms in magnetron injection guns", in: *Physics of Plasmas* 23.2 (2016), p. 023105, DOI: 10.1063/1.4941705

[94] I. G. Pagonakis and J. Vomvoridis, "The self-consistent 3D trajectory electrostatic code ARIADNE for gyrotron beam tunnel simulation", in: *Infrared and Millimeter Waves, Conference Digest of the 2004 Joint 29th International Conference on 2004 and 12th International Conference on Terahertz Electronics, 2004.* (2004), pp. 657–658, DOI: 10.1109/ICIMW.2004.1422262

[95] T. Ruess, K. A. Avramidis, G. Gantenbein, Z. Ioannidis, S. Illy, J. Jin, F.-C. Lutz, I. G. Pagonakis, S. Ruess, T. Rzesnicki, M. Thumm, D. Wagner, and J. Jelonnek, "Operating the KIT 170 GHz 2 MW coaxial-cavity gyrotron at 204 GHz: performance expectations and first cold test of the quasi-optical system", in: *2019 International*

Vacuum Electronics Conference (IVEC), (2019), pp. 1–2, DOI: 10.1109/IVEC.2019.8745094

[96] A. Litvak, K. Sakamoto, and M. Thumm, "Innovation on high-power long-pulse gyrotrons", in: *Plasma Physics and Controlled Fusion* 53.12 (2011), p. 124002, DOI: 10.1088/0741-3335/53/12/124002

[97] G. Denisov, A. Litvak, V. Myasnikov, E. Tai, and V. Zapevalov, "Development in Russia of high-power gyrotrons for fusion", in: *Nuclear Fusion* 48.5 (2008), p. 054007, DOI: 10.1088/0029-5515/48/5/054007

[98] Arti, N. Kumar, U. Singh, V. Gahlaut, and A. Bera, "Inverse magnetron injection gun for megawatt power, sub-THz gyrotron", in: *IEEE Transactions on Plasma Science* 47.2 (2019), pp. 1262–1268, DOI: 10.1109/TPS.2019.2890876

[99] P. C. Kalaria, M. George, S. Illy, K. A. Avramidis, G. Gantenbein, S. Ruess, M. Thumm, and J. Jelonnek, "Multiphysics modeling of insert cooling system for a 170-GHz, 2-MW long-pulse coaxial-cavity gyrotron", in: *IEEE Transactions on Electron Devices* 66.9 (2019), pp. 4008–4015, DOI: 10.1109/TED.2019.2928222

[100] P. C. Kalaria, M. George, S. Illy, K. A. Avramidis, G. Gantenbein, S. Ruess, T. Rzesnicki, M. Thumm, and J. Jelonnek, "Performance analysis of an insert cooling system for long-pulse operation of a coaxial-cavity gyrotron", in: *2018 IEEE International Vacuum Electronics Conference (IVEC)*, (2018), pp. 69–70, DOI: 10.1109/IVEC.2018.8391556

[101] C. T. Iatrou, A. Moebius, and P. Norajitra, "Feasibility study of the EU home team on a 170GHz 1MW CW gyrotron for ECH on ITER", in: *International Journal of Infrared and Millimeter Waves* 16.6 (1995), DOI: 10.1007/BF02068283

[102] W. G. Lawson, "Theoretical evaluation of nonlinear tapers for a high-power gyrotron", in: *IEEE Transactions on Microwave Theory and Techniques* 38.11 (1990), pp. 1617–1622, DOI: 10.1109/22.60007

[103] J. Jin, G. Gantenbein, T. Ruess, M. Thumm, and J. Jelonnek, "Design of a quasi-optical mode converter for a dual-frequency coaxial-cavity gyrotron", in: *2019 44th International Conference on Infrared, Millimeter, and Terahertz Waves (IRMMW-THz)*, (2019), pp. 1–2, DOI: 10.1109/IRMMW-THz.2019.8873692

[104] J. Jin, G. Gantenbein, J. Jelonnek, M. Thumm, and T. Rzesnicki, "A new method for synthesis of beam-shaping mirrors for off-axis incident gaussian beams", in: *IEEE Transactions on Plasma Science* 42.5 (2014), pp. 1380–1384, DOI: 10.1109/TPS.2014.2310903

[105] *https://www.kupferinstitut.de/wp-content/uploads/2019/11/Cu-OFE.pdf*

[106] G. F. Brand and M. Gross, "Continuously tunable, split-cavity gyrotrons", in: *International Journal of Infrared and Millimeter Waves* 6.12 (1985), pp. 1237–1254, DOI: 10.1007/BF01013212

[107] K. Koppenburg, G. Dammertz, M. Kuntze, B. Piosczyk, and M. Thumm, "Fast frequency-step-tunable high-power gyrotron with hybrid-magnet-system", in: *IEEE Transactions on Electron Devices* 48.1 (2001), pp. 101–107, DOI: 10.1109/16.892175

[108] R. Hirose, T. Kamikado, Y. Okui, H. Miyata, K. Shibutani, O. Ozaki, and K. Sakamoto, "Development of 7 T cryogen-free superconducting magnet for gyrotron", in: *IEEE Transactions on Applied Superconductivity* 18.2 (2008), pp. 920–923, DOI: 10.1109/TASC.2008.922296

[109] D. Wagner, G. Grünwald, F. Leuterer, A. Manini, F. Monaco, M. Münich, H. Schütz, J. Stober, H. Zohm, T. Franke, M. Thumm, G. Gantenbein, R. Heidinger, A. Meier, W. Kasparek, et al., "Status of the new multi-frequency ECRH system for ASDEX Upgrade", in: *Nuclear Fusion* 48.5 (2008), p. 054006, DOI: 10.1088/0029-5515/48/5/054006

[110] R. Heidinger, I. Danilov, A. Meier, B. Piosczyk, P. Späh, M. Thumm, W. Bongers, M. Graswinckel, M. Henderson, F. Leuterer, A. Verhoeven, and D. Wagner, "Development of high power window prototypes for ECH&CD launchers", in: *Fusion Enginnering and Design* 82.5 (2007), pp. 693–699, DOI: 10.1046/j.fusengdes.2007.04.043

[111] O. Braz, G. Dammertz, M. Kuntze, and M. Thumm, "D-band frequency step-tuning of a 1 MW gyrotron using a brewster output window", in: *International Journal of Infrared and Millimeter Waves* 18.8 (1997), pp. 1465–1477, DOI: 10.1007/BF02678305

[112] G. Denisov, V. Belousov, A. Pavelev, A. Chirkov, V. Ilin, V. Kurbatov, S. Malygin, V. Myasnikov, V. Orlov, E. Soluyanova, E. Sokolov, and E. Tai, "Multi-frequency gyrotron with BN brewster window", in: *2006 Joint 31st International Conference on Infrared Millimeter Waves and 14th International Conference on Teraherz Electronics*, (2006), pp. 75–75, DOI: 10.1109/ICIMW.2006.368283

[113] G. Aiello, S. Schreck, K. Avramidis, T. Franke, G. Gantenbein, J. Jelonnek, A. Meier, T. Scherer, D. Strauss, M. Thumm, M. Tran, C. Wild, and E. Woerner, "Towards large area CVD diamond disks for brewster-angle windows", in: *Fusion Engineering and Design* 157 (2020), p. 111818, ISSN: 0920-3796, DOI: 10.1016/j.fusengdes.2020.111818

[114] T. Ruess, K. A. Avramidis, G. Gantenbein, S. Illy, T. Rzesnicki, M. Thumm, and J. Jelonnek, "Theoretical study on the possibility for stepwise tuning of the frequency of the KIT 2 MW 170/204 GHz coaxial-cavity gyrotron", in: *2020 45th International Conference on Infrared, Millimeter, and Terahertz Waves (IRMMW-THz)*, (2020), pp. 1–2, DOI: 10.1109/IRMMW-THz46771.2020.9370801

[115] O. Dumbrajs, T. Idehara, Y. Iwata, S. Mitsudo, I. Ogawa, and B. Piosczyk, "Hysteresis-like effects in gyrotron oscillators", in: *Physics of Plasmas* 10.5 (2003), pp. 1183–1186, DOI: 10.1063/1.1561277

[116] O. Dumbrajs and G. S. Nusinovich, "To the theory of high-power gyrotrons with uptapered resonators", in: *Physics of Plasmas* 17.5 (2010), p. 053104, DOI: 10.1063/1.3425876

[117] H. U. Nickel and T. Geist, "Diagnostic and instrumentation for millimetre-wave gyrotrons", in: *Gyrotron Oscillators: Their Principles*

and Practice, ed. by C. J. Edgecombe, Cambridge University Press, (1993), chap. 13, DOI: 10.1201/9781482272369

[118] F. Gandindi, B. B. C. Darbos, T. Gassman, M. Henderson, O. Jean, C. Nazare, T. Omori, D. Purohit, F. Albajar, T. Bonicelli, G. Saibene, T. Bigelow, J. Caughman, D. Rasmussen, G. Denisov, et al., "An overviewof the ITER EC transmission line", in: *Electron Cyclotron Emission and Electron Cyclotron Resonance Heating (EC-16)*, pp. 364–369, DOI: 10.1142/9789814340274_0049

[119] M. Thumm and W. Kasparek, "Passive high-power microwave components", in: *IEEE Transactions on Plasma Science* 30 (2002), pp. 755–786, DOI: 10.1109/TPS.2002.801653

[120] Z. Wu, H. Li, B. Hu, J. Xu, and T. Li, "Design of a circular TE5,1 mode generator for gyrotrons low-power measurements", in: *Journal of Electromagnetic Waves and Applications* 27.13 (2013), pp. 1660–1671, DOI: 10.1080/09205071.2013.822338

[121] B. Huang, C.-H. Du, X.-B. Qi, H.-H. Tang, and P.-K. Liu, "Converting symmetric mode into ultra-high-order asymmetric mode", in: *2016 IEEE International Conference on Mirowave and Millimeter Wave Technology (ICMMT)*, vol. 2, (2016), pp. 836–838, DOI: 10.1109/ICMMT.2016.7762459

[122] Y. Danilov, "Experimental study of perforated coaxil exciter of high-order modes in barrel-shaped cavity", in: *Technical Physics Letters* 33.9 (2007), pp. 738–739, DOI: 10.1134/S1063785007090076

[123] N. L. Aleksandrov, A. V. Chirkov, G. G. Denisov, D. V. Vinogradov, W. Kasparek, J. Pretterebner, and D. Wagner, "Selective excitation of high-order modes in circular waveguides", in: *International Journal of Infrared and Millimeter Waves* 13.9 (1992), pp. 1369–1385, ISSN: 1572-9559, DOI: 10.1007/BF01009994

[124] H. Jory, D. Wagner, M. Blank, S. Chu, and K. Felch, "Compact mode converter system for cold test of assembled gyrotrons", in: *Inter-*

national Journal of Infrared and Millimetere Waves 22.10 (2001), pp. 1395–1407, DOI: 10.1023/A:1015053621109

[125] M. Losert, J. Jin, and T. Rzesnicki, "RF beam parameter measurements of quasi-optical mode converters in the mW range", in: *IEEE Transactions on Plasma Science* 41.3 (2013), pp. 628–632, DOI: 10.1109/TPS.2012.2232942

[126] D. Wagner, M. Thumm, and A. Arnold, "Mode generator for the cold test of step-tunable gyrotrons", in: *27th International Conference on Infrared and Millimeter Waves* (2002), pp. 303–304, DOI: 10.1109/ICIMW.2002.1076205

[127] D. Wagner, J. Pretterebner, and M. Thumm, "Design of coaxial gyrotron cavities using a scattering matrix code", in: *5th Joint Russian-German Meeting on ECRH and Gyrotron* (1993), pp. 555–565

[128] M. Losert, G. Gantenbein, J. Jin, and A. Samartsev, "Low power measurements on a quasi-optical system of an 1MW TE32,9 170GHz gyrotron", in: *2015 German Microwave Conference*, (2015), pp. 256–259, DOI: 10.1109/GEMIC.2015.7107802

[129] C. Mentzer and L. Peters, "Pattern analysis of corrugated horn antennas", in: *IEEE Transactions on Antennas and Propagation* 24.3 (1976), pp. 304–309, DOI: 10.1109/TAP.1976.1141342

[130] P. Potter, "A new horn antenna with suppressed sideolobes and equal beamwidths", in: *Microwave Journal* 6.6 (1963), pp. 71–78

[131] T. Rzesnicki, "Analyse eines neuartigen 1.5 MW, 170 GHz Prototyp-Gyrotrons mit koaxialem Resonator", Doktorarbeit, Forschungszentrum Karlsruhe, (2007)

[132] J. Teniente, "Modern corrugated horn antennas", in: *PhD Thesis, Public University of Navarra* (2003)

[133] T. Itoh, "Numerical techniques for microwave and millimeter-wave passive structures", A Wiley-Interscience publication, John Wiley & Sons Inc., Hoboken, (1989), ISBN: 9780471625636

[134] Dassault Systems, *CST Studio Suite 2021*, version 2021, Nov. 30, 2021

[135] G. Dammertz, S. Alberti, A. Arnold, E. Giguet, Y. LeGoff, and M. Thumm, "Cold test measurements on components of the 1 MW, 140 GHz, CW gyrotron for the stellarator Wendelstein 7-X", in: *Fusion Engineering and Design* 53.1 (2001), pp. 561–569, ISSN: 0920-3796, DOI: 10.1016/S0920-3796(00)00534-2

[136] N. Alexandrov, G. Denisov, D. Whaley, and M. Tran, "Low power excitation of gyrotron-type modes in a cylindrical waveguide using quasi-optical techniques", in: *International Journal of Electronics* 2 (1995), pp. 215–226

[137] A. Arnold, O. Prinz, D. Wagner, and M. Thumm, "Operation of a quasioptical multi-mode generator for 105–150 GHz", in: *2007 Joint 32nd International Conference on Infrared and Millimeter Waves and the 15th International Conference on Terahertz Electronics*, (2007), pp. 434–435, DOI: 10.1109/ICIMW.2007.4516568

[138] M. Pereyaslavets, O. Braz, S. Kern, M. Losert, A. Mobius, and M. Thumm, "Improvements of mode converters for low-power excitation of gyrotron-type modes", in: *International Journal of Electronics* 82.1 (1997), pp. 107–116, DOI: 10.1080/002072197136291

[139] *Precision linear stages LTM 60*, 9012.0253, OWIS GmbH, Oct. 2017

[140] *Goniometer MOGO 65-40-65*, 9012.0352, OWIS GmbH, Jan. 2020

[141] T. Ruess, K. A. Avramidis, M. Fuchs, G. Gantenbein, S. Illy, Z. Ioannidis, F. C. Lutz, S. Ruess, T. Rzesnicki, M. Thumm, D. Wagner, J. Weggen, and J. Jelonnek, "2018 status of the measurement capabilities for fusion gyrotrons at KIT/IHM", in: *EPJ Web Conf.* 187 (2018), p. 01019, DOI: 10.1051/epjconf/201818701019

[142] MATLAB, *version 9.6 (R2018a)*, Natick, Massachusetts: The MathWorks Inc., (2018)

[143] T. Ruess, K. Avramidis, M. Fuchs, G. Gantenbein, S. Illy, F.-C. Lutz, A. Marek, S. Ruess, T. Rzesnicki, M. Thumm, D. Wagner, J. Weggen,

and J. Jelonnek, “Towards fully automated systems for the generation of very high order modes in oversized waveguides”, in: *EPJ Web Conf.* 195 (2018), p. 01030, DOI: 10.1051/epjconf/201819501030

[144] T. Ruess, K. A. Avramidis, G. Gantenbein, Z. Ioannidis, S. Illy, F. C. Lutz, A. Marek, S. Ruess, T. Rzesnicki, M. Thumm, D. Wagner, J. Weggen, and J. Jelonnek, “Computer-controlled test system for the excitation of very high-order modes in highly oversized waveguides”, in: *Journal of Infrared, Millimeter, and Terahertz Waves* 40.3 (2019), pp. 257–268, DOI: 10.1007/s10762-018-0566-3

[145] L. Delpech, S. Alberti, K. Avramidis, A. Ayreault, J. M. Bernard, F. Bouquey, I. Chelis, F. Clairet, E. Corbel, L. Doceul, F. Durand, R. Dumont, T. Fonghetti, G. Gantenbein, P. Garibaldi, et al., “A new 3MW ECRH system at 105 GHz for WEST”, in: *submitted to 21st joint workshop on electron cyclotron emission (ECE) and electron cyclotron resonance heating (ECRH)* (2022)

[146] T. Ruess, K. A. Avramidis, G. Gantenbein, Z. Ioannidis, S. Illy, J. Jin, F.-C. Lutz, A. Marek, S. Ruess, T. Rzesnicki, M. Thumm, D. Wagner, J. Weggen, and J. Jelonnek, “Automated generation of high-order modes for tests of quasi-optical systems of gyrotrons for W7-X stellarator”, in: *2019 12th German Microwave Conference (GeMiC)*, (2019), pp. 226–228, DOI: 10.23919/GEMIC.2019.8698142

[147] T. Ruess, G. Gantenbein, J. Jin, A. Marek, T. Rzesnicki, M. Thumm, D. Wagner, and J. Jelonnek, “Verification of the 170/204 GHz quasi-optical output coupler of the 2 MW coaxial-cavity gyrotron using a mode generator setup”, in: *2022 14th German Microwave Conference (GeMiC)*, (2022), 5 – 8, DOI: 10.5445/IR/1000156179/post

[148] T. Ruess, G. Gantenbein, J. Jin, T. Rzesnicki, S. Stanculovic, M. Thumm, D. Wagner, and J Jelonnek, “170/204 GHz dual-frequency mode generator for verification of the the quasi-optical output coupler of a 2 MW coaxial-cavity gyrotron”, in: *2022 IEEE 2nd Ukrainian Microwave Week (UkrMW), Ukraine*, (2022), pp. 170–175, DOI: 10.1109/UkrMW58013.2022.10036995

[149] T. Rzesnicki, J. Jin, B. Piosczyk, M. Thumm, G. Michel, and D. Wagner, "Low power measurements on the new RF output system of a 170 GHz, 2 MW coaxial cavity gyrotron", in: *International Journal of Infrared and Millimeter Waves* 27.1 (Jan. 2006), pp. 1–11, DOI: 10.1007/s10762-006-9062-2

[150] S. Garavaglia, G. Aiello, S. Alberti, K. Avramidis, A. Bruschi, I. G. Chelis, J. Franck, G. Gantenbein, G. Granucci, G. Grossetti, K. Hizanidis, S. Illy, J. Jelonnek, P. Kalaria, G. Latsas, et al., "EU DEMO EC system preliminary conceptual design", in: *Fusion Engineering and Design* 136 (2018), Special Issue: Proceedings of the 13th International Symposium on Fusion Nuclear Technology (ISFNT-13), pp. 1173–1177, DOI: 10.1016/j.fusengdes.2018.04.097

[151] E. Poli, G. Tardini, H. Zohm, E. Fable, D. Farina, L. Figini, N. Marushchenko, and L. Porte, "Electron-cyclotron-current-drive efficiency in DEMO plasmas", in: *Nuclear Fusion* 53.1 (2012), p. 013011, DOI: 10.1088/0029-5515/53/1/013011

[152] D. Wagner and M. Thumm, "Improvement of the output mode purity of a complex-cavity resonator for a frequency-tunable sub-THz gyrotron", in: *IEEE Transactions on Electron Devices* 68.10 (2021), pp. 5220–5226, DOI: 10.1109/TED.2021.3105955

[153] R. E. Collin, "Periodic structures", in: *Field Theory of Guided Waves*, (1991), pp. 605–643, DOI: 10.1109/9780470544648.ch9

[154] P. Skocik and P. Neumann, "Measurement of complex permittivity in free space", in: *Procedia Engineering* 100 (2015), 25th DAAAM International Symposium on Intelligent Manufacturing and Automation, 2014, pp. 100–104, DOI: 10.1016/j.proeng.2015.01.347

[155] S. Bringhurst and M. Iskander, "Thin sample dielectric properties measurement using open-ended coaxial probes and FDTD calculations", in: *IEEE Antennas and Propagation Society International Symposium. 1995 Digest*, vol. 4, (1995), 1844–1847 vol.4, DOI: 10.1109/APS.1995.530945

[156] I. Kotelnikov, A. Altynnikov, A. Mikhailov, V. Medvedeva, and A. Kozyrev, “Electrodeless measurement technique of complex dielectric permittivity of high-K dielectric films in the millimeter wavelength range”, in: *Progress In Electromagnetics Research M* 52 (2016), pp. 161–167, DOI: 10.2528/PIERM16100505

[157] J. Schultz, “Focused beam methods: measuring microwave materials in free space”, CreateSpace Independent Publishing Platform, (2012), ISBN: 9781480092853

[158] I. Danilov and R. Heidinger, “New approach for open resonator analysis for dielectric measurements at mm-wavelengths”, in: *Journal of the European Ceramic Society* 23.14 (2003), pp. 2623–2626, DOI: 10.1016/S0955-2219(03)00140-7

[159] M. Thumm, W. Wiesbeck, and S. Kern, “Hochfrequenzmesstechnik - Verfahren und Messsysteme”, Vieweg+Teuber Verlag Wiesbaden, (1998), DOI: 10.1007/978-3-663-01599-4

[160] A. Lessmann, “Numerische und experimentelle Untersuchungen von Resonanzen in stark ubermodigen, breitbandigen Gyrotronfenstern”, Bachelorarbeit, Karlsruher Institut fur Technologie, (2022)

[161] A. Schlaich, “Time-dependent spectrum analysis of high power gyrotrons”, 31.03.02; LK 01, PhD thesis, (2015), 286 pp., ISBN: 978-3-7315-0375-0, DOI: 10.5445/KSP/1000046919

[162] H. Prinz, “Frequency measurement system for gyrotron diagnostics”, in: *IEEE Potentials* 26.4 (2007), pp. 25–30, DOI: 10.1109/MP.2007.4280329

[163] A. Schlaich, G. Gantenbein, J. Jelonnek, and M. Thumm, “Transient millimeter-wave signal analysis with unambiguous RF spectrum reconstruction”, in: *IEEE Transactions on Microwave Theory and Techniques* 61.12 (2013), pp. 4660–4666, DOI: 10.1109/TMTT.2013.2283063

[164] W. Kasparek and G. A Müller, "The wavenumber spectrometer—an alternative to the directional coupler for multimode analysis in oversized waveguides", in: *International Journal of Electronics* 64.1 (1988), pp. 5–20, DOI: 10.1080/00207218808962780

[165] M. E. Austin, R. F. Ellis, J. L. Doane, and R. A. James, "Improved operation of the Michelson interferometer electron cyclotron emission diagnostic on DIII-D", in: *Review of Scientific Instruments* 68.1 (1997), pp. 480–483, DOI: 10.1063/1.1147612

[166] J. Benford, J. Swegle, and E. Schamiloglu, "High power microwaves", in: *CRC Press* (2019)

[167] T. Geist, M. Thumm, and W. Wiesbeck, "Continuous filterbank receiver for a pulsed 140 GHz gyrotron", in: *16th International Conference on Infrared and Millimeter Waves*, ed. by M. Q. Tran, vol. 1576, International Society for Optics and Photonics, SPIE, (1991), pp. 329 –330, DOI: 10.1117/12.2297850

[168] M. Schmid, M. Bader, T. Bourgeois, A. Epp, G. Gantenbein, M. Iten, J. Jelonnek, T. Kobarg, W. Leonhardt, D. Mellein, and T Rzesnicki, "The 10 MW EPSM modulator and other key components for the KIT gyrotron test facility FULGOR", in: *Fusion Engineering and Design* (2016), pp. 485–489, DOI: 10.1016/j.fusengdes.2017.02.035

[169] J. Franck, K. Avramidis, G. Gantenbein, S. Illy, J. Jin, M. Thumm, and J. Jelonnek, "A generic mode selection strategy for high-order mode gyrotrons operating at multiple frequencies", in: *Nuclear Fusion* 55.1 (2014), p. 013005, DOI: 10.1088/0029-5515/55/1/013005

[170] S. Stanculovic, R. Difonzo, A. Allio, K. A. Avramidis, P. Brücker, G. Gantenbein, S. Illy, J. Jelonnek, P. C. Kalaria, M. Misko, T. Rzesnicki, and L. Savoldi, "Calibration of the KIT test setup for the cooling tests of a gyrotron cavity full-size mock-up equipped with mini-channels", in: *Fusion engineering and design* 172 (2021), 31.13.02; LK 01, Article no: 112744, ISSN: 0920-3796, DOI: 10.1016/j.fusengdes.2021.112744

[171] J. Eppli, *gyrotron"*Mode selection for a future 136/170/204 GHz multi-frequency coaxial-cavity DEMO*"*, Bachelor thesis, Karlsruhe Institute of Technology, (2021)

[172] M. Thumm, A. Arnold, O. Drumm, J. Jin, G. Michel, B. Piosczyk, T. Rzesnicki, D. Wagner, and X. Yang, "Quasi-optical mode converters in advanced high-power gyrotrons for nuclear fusion plasma heating", in: *Quasi-Optical Control of Intense Microwave Transmission*, ed. by J. L. Hirshfield and M. I. Petelin, Dordrecht: Springer Netherlands, (2005), pp. 325–351, ISBN: 978-1-4020-3638-5

[173] B. Piosczyk, O. Braz, G. Dammertz, C. Iatrou, S. Illy, M. Kuntze, G. Michel, A. Mobius, M. Thumm, V. Flyagin, V. Khishnyak, A. Pavelyev, and V. Zapevalov, "Coaxial cavity gyrotron with dual RF beam output", in: *IEEE Transactions on Plasma Science* 26.3 (1998), pp. 393–401, DOI: 10.1109/27.700770

[174] Y. Novozhilova, V. Bakunin, A. Chirkov, Y. Guznov, G. Denisov, A. A.P. Fokin, A. Shevchenko, N. Zaitsev, and S. Zapevalov, "Influence of mode competition and external wave frequency modulation on gyrotron frequency locking", in: *EPJ Web Conf.* 149 (2017), p. 04021, DOI: 10.1051/epjconf/201714904021

[175] J. Jin and T. Ruess, "internal discussion/document: dual-beam launcher"

[176] T. Saito, N. Yamada, S. Ikeuti, S. Ogasawara, Y. Tatematsu, R. Ikeda, I. Ogawa, T. Idehara, V. Manuilov, T. Shimozuma, S. Kubo, M. Nishiura, K. Tanaka, and K. Kawahata, "Generation of high power sub-terahertz radiation from a gyrotron with second harmonic oscillation", in: *Physics of Plasma* 19.6 (2012), DOI: 10.1063/1.4729316

[177] L. Feuerstein, A. Marek, C. Wu, S. Illy, M. Thumm, and J. Jelonnek, "Design of a second harmonic MW level coaxial gyrotron cavity", in: *submitted to 24th International Vacuum Electronic Conference (IVEC 2023)*, (2023), pp. 1–2

[178] G Denisov, I. Zotova, I. Zheleznov, A. Malkin, N. Ginzburg, A. Sergeev, E. Semenov, and M. Glyavin, "Phase-locking of second-harmonic gyrotrons for providing MW-level output power", in: *IEEE Transactions on Electron Devices* 69.2 (2022), DOI: 10.1109/TED.2021.3134187

[179] S. Alberti, T. M. Tran, K. A. Avramides, F. Li, and J.-P. Hogge, "Gyrotron parasitic-effects studies using the time-dependent self-consistent monomode code TWANG", in: *2011 International Conference on Infrared, Millimeter, and Terahertz Waves*, (2011), pp. 1–2, DOI: 10.1109/irmmw-THz.2011.6105097

[180] F. Braunmueller, T. M. Tran, Q. Vuillemin, S. Alberti, J. Genoud, J.-P. Hogge, and M. Q. Tran, "TWANG-PIC, a novel gyro-averaged one-dimensional particle-in-cell code for interpretation of gyrotron experiments", in: *Physics of Plasmas* 22.6 (2015), p. 063115, DOI: 10.1063/1.4923299

[181] M. Botton, T. Antonsen, B. Levush, K. Nguyen, and A. Vlasov, "MAGY: a time-dependent code for simulation of slow and fast microwave sources", in: *IEEE Transactions on Plasma Science* 26.3 (1998), pp. 882–892, DOI: 10.1109/27.700860

[182] R. Wacker, F. Leuterer, D. Wagner, H. Hailer, and W. Kasparek, "Characterization of absorber materials for high-power millimetre waves", in: *Twenty Seventh International Conference on Infrared and Millimeter Waves*, (2002), pp. 159–160, DOI: 10.1109/ICIMW.2002.1076133

[183] A. Killinger, G. Gantenbein, S. Illy, T. Ruess, J. Weggen, and V. Martinez-Garcia, "Plasma spraying of a microwave absorber coating for an RF dummy load", in: *Coatings* 11.7 (2021), DOI: 10.3390/coatings11070801

[184] M. Floristán, P. Müller, A. Gebhardt, A. Killinger, R. Gadow, A. Cardella, C. Li, R. Stadler, G. Zangl, M. Hirsch, H. P. Laqua, and W. Kasparek, "Development and testing of 140 GHz absorber coatings

for the water baffle of W7-X cryopumps", in: *Fusion Engineering and Design* 86.9 (2011), Proceedings of the 26th Symposium of Fusion Technology (SOFT-26), pp. 1847–1850, DOI: 10.1016/j.fusengdes.2010.12.015

[185] R. T. Schermer and T. H. Stievater, "Millimeter-wave dielectric properties of highly refractive single crystals characterized by waveguide cavity resonance", in: *IEEE Transactions on Microwave Theory and Techniques* 67.3 (2019), pp. 1078–1087, DOI: 10.1109/TMTT.2018.2883107

[186] H. Eugene, "Optik", Berlin, Boston: De Gruyter, (2018), ISBN: 9783110526653, DOI: 10.1515/9783110526653

List of Figures

List of Tables